

---

Electronic Thesis and Dissertation Repository

---

10-24-2016 12:00 AM

## Solvothermal Preparation and Characterization of Superstructures of Nanoscopic CdS and CdSe

Tetyana Levchenko  
*The University of Western Ontario*

Graduate Program in Chemistry

A thesis submitted in partial fulfillment of the requirements for the degree in Doctor of Philosophy

© Tetyana Levchenko 2016

Follow this and additional works at: <https://ir.lib.uwo.ca/etd>

 Part of the [Inorganic Chemistry Commons](#), and the [Materials Chemistry Commons](#)

---

### Recommended Citation

Levchenko, Tetyana, "Solvothermal Preparation and Characterization of Superstructures of Nanoscopic CdS and CdSe" (2016). *Electronic Thesis and Dissertation Repository*. 4245.

<https://ir.lib.uwo.ca/etd/4245>

This Dissertation/Thesis is brought to you for free and open access by Scholarship@Western. It has been accepted for inclusion in Electronic Thesis and Dissertation Repository by an authorized administrator of Scholarship@Western. For more information, please contact [wlsadmin@uwo.ca](mailto:wlsadmin@uwo.ca).

## Abstract

Micrometer-sized superparticles, self-assembled from metallic or semiconducting nanoclusters, can be used as convenient building blocks for preparing functional materials, utilizing the electronic and photophysical properties resulting from the quantum confinement as well as from the coupling between individual nanoscopic constituents.

This research aimed at developing a novel approach utilizing the conversion of a cadmium phenylchalcogenolate precursor  $(Me_4N)_2[Cd(EPh)_4]$  (where E = S or Se) under solvothermal conditions for the preparation of nanoscopic CdE, including both crystalline superlattices of large discrete nanoclusters and superstructures with more complex morphology. In particular, 3D cubic superlattices of molecular CdS nanoclusters of 1.9 and 2.3 nm in diameter were prepared and characterized by a set of techniques, including UV–vis absorption and photoluminescence studies under various conditions, Raman spectroscopy, and thermogravimetric analysis. Structural information was obtained by methods complementary to single crystal X-ray diffraction such as  $^{111}Cd$  SSNMR spectroscopy, electron microscopy, and electron tomographic reconstruction. Observed structural features demonstrate the significance of the prepared materials as a transition point from known families of smaller CdS nanoclusters to unexplored larger ones. Even more unusual 3D superstructures comprised of nanoscopic constituents, *i.e.*, spherical CdS superparticles and porous CdSe single crystal, were reported and possible mechanisms of formation were discussed. The importance of this research lies in improving the ability to manipulate the size and organization of primary nanocluster building blocks into particular superstructures and to tailor the photophysical properties of the resulting material, which enables the creation of new multifunctional systems and broadens potential areas of application.

## Keywords

crystalline superlattices • electron microscopy • metal chalcogenides • nanoclusters • nanoscopic materials • photoluminescence • semiconductor • solvothermal • superstructure

## Acknowledgements

I owe a large debt of gratitude to all those great people who had been helping me during the progress towards my degree. My first thanks go to my two co-supervisors, Prof. John F. Corrigan and Prof. Yining Huang, who constantly supported, guided and encouraged me to move forward to complete my journey in graduate school. Being "split" between two research groups with different focus of interests gave me unique opportunity to view and learn chemistry from diverse perspectives. I also would like to thank all my lab mates in two groups; over the years there were many wonderful people I had been working with, both graduate and undergraduate students. In particular, I am much obliged to Dan MacDonald, Chhatra Khadka, Lu Zhang, and Jun Xu for their help at the early stages of my career to introduce me to new techniques and instruments. I am also very much grateful to Bahar Khalili Najafabadi, Mahmood Azizpoor Fard, Stefan Mitzinger, Maxwell Goldman, Yue (Jason) Zhang, and Bryan Lucier for providing assistance in my research projects and creating a great working atmosphere in the lab.

Within the Department of Chemistry, I do appreciate companionship of my TA-ing mates, especially Preeti Chadah, Mat McCready, and Mahboubeh Hadadpour. Among those graduate students, who helped me with managing instruments and running measurements, I am pleased to mention Allison Brazeau, Ryan Guterman, Augusto Matarazzo, Xiaoxiao (Rachel) Wang, and Kelly Summers; also special thanks to Dr. Chris Levy. I would like to express my sincere gratitude to Prof. Paul J. Ragona, Prof. Robert H. E. Hudson, Prof. Martin J. Stillman, and Prof. François Lagugné-Labarthe for providing access to their instruments and help with measurements. I also would like to thank Undergraduate labs technicians and managers (especially Ron Maslen (retired), Robin Hall, and Robert Harbottle), who answered "yes" countless times to my "Can I please work late tonight?"

The many services of the Department of Chemistry have been of great assistance; in particular, I would like to acknowledge help of Mat Willans (NMR facility), Guerman Popov and Paul Boyle (X-ray diffraction facility), and Warren Lindsay (departmental manager). Yves Rambour (glassblowing shop), John Vanstone, Jon Aukema, and Barakat

Misk (electronic shop) are widely known to possess a special power of fixing anything that was broken or not working properly. I would like to thank to ChemBioStore personnel (Don Yakobchuk (retired), Marylou Hart, Monica Chirigel, Sherrie McPhee, and Yuhua Chen) for their continuous service and support. Similarly, I appreciate kind help and support of Darlene McDonald (graduate coordinator); Anna Vandendries-Barr and Clara Fernandes (departmental administration).

I would like to thank Grace C. Yau and Kim Law (Stable Isotope Lab in the Department of Earth Sciences); Jack Hendriks, Carolyn Cadogan, and Prof. Lyudmila V. Goncharova (Department of Physics and Astronomy); Tim Goldhawk (Nanofabrication facility in the Department of Physics and Astronomy), Ying Zhang (Advanced Analysis and Materials Testing Laboratory, Engineering Department) for their assistance with measurements. I am also grateful to Nadine LeGros (Teaching Support Centre) and Olga Sauer (Society of Graduate Students) for their useful advices and constant encouragement.

Some part of work included in my research projects was carried out with the support of the Karlsruhe Nano Micro Facility (KNMF, [www.kit.edu/knmf](http://www.kit.edu/knmf)), a Helmholtz Research Infrastructure at Karlsruhe Institute of Technology (KIT, <http://www.kit.edu/>). I appreciate great help of Dr. Christian Kübel, Di Wang, and Robby Prang (KNMF, KIT) for their assistance with sample preparation, measurements, and data processing. I would also acknowledge financial support provided by an ASPIRE award to make possible my visit to the KNMF, KIT. I thank to the funding agency NSERC for its financial support in the form of Doctoral Postgraduate Scholarship.

## Co-Authorship Statement

This thesis includes material from three previously published manuscripts presented in Chapters 1, 2 and 3.

The literature review presented in Chapter 1 was co-authored by Levchenko, T. I.; Huang, Y.; Corrigan, J. F. (*Struct Bond*; DOI: 10.1007/430\_2016\_5; Springer Int. Pub., Switzerland, **2016**). The manuscript was written by Tetyana I. Levchenko and edited by Yining Huang and John F. Corrigan.

The manuscript presented in Chapter 2 was co-authored by Levchenko, T. I.; Kübel, C.; Wang, D.; Khalili Najafabadi, B.; Huang, Y.; Corrigan, J. F. (*Chem. Mater.* **2015**, *27* (10), 3666–3682). All of the experimental work was performed by Tetyana I. Levchenko. The electron microscopy imaging (TEM, STEM), SEAD, and data processing were performed together with Christian Kübel and Di Wang. FIB sample preparation and SEM imaging were performed together with Robby Prang. Single crystal X-ray diffraction data were solved by Bahareh Khalili Najafabadi. SEM imaging and EDX analysis were performed together with Tim Goldhawk. RBS measurements and data processing were done together with Jack Hendriks and Lyudmila Goncharova. The manuscript was written by Tetyana I. Levchenko and edited by Christian Kübel (electron microscopy part), Yining Huang, and John F. Corrigan.

The manuscript presented in Chapter 3 represents an extended version of the communication co-authored by Levchenko, T. I.; Kübel, C.; Huang, Y.; Corrigan, J. F. (*Chem.- Eur. J.* **2011**, *17* (51), 14394–14398). Experimental work, except electron microscopy imaging and data processing, was performed by Tetyana I. Levchenko. The electron microscopy imaging (TEM, STEM) and tomographic reconstruction were performed by Christian Kübel. Atomic absorption spectroscopy analysis for Cd was performed together with Kelly L. Summers and discussed with Martin J. Stillman. The manuscript was written by Tetyana I. Levchenko and edited by Christian Kübel (electron microscopy part), Yining Huang and John F. Corrigan.

The draft of the manuscript presented in Chapter 4 is co-authored by Levchenko, T. I.; Lucier, B. E. G.; Huang, Y.; Corrigan, J. F. All of the experimental work was performed by Tetyana I. Levchenko and SSNMR experiments were performed with the assistance of Bryan E. G. Lucier. The draft of the manuscript was written by Tetyana I. Levchenko and edited by Bryan E. G. Lucier, Yining Huang, and John F. Corrigan.

The draft of the manuscript presented in Chapter 5 is co-authored by Levchenko, T. I.; Kübel, C.; Khalili Najafabadi, B.; Cadogan, C.; Goncharova, L. V.; Garreau, A.; Lagugn -Labarhet, F.; Huang, Y.; Corrigan, J. F. Experimental work was performed by Tetyana I. Levchenko, except solid state TRPL measurements (nanosecond time scale), confocal fluorescent microscopy and FLIM, which were performed by Alexandre Garreau and Fran ois Lagugn -Labarhet, and mass-spectrometry, done by Doug Hairsine. Single crystal X-ray diffraction data were solved by Bahareh Khalili Najafabadi. SEM imaging and EDX analysis were performed together with Tim Goldhawk. The electron microscopy imaging (TEM, STEM), SEAD, and data processing were performed together with Christian K bel. FIB sample preparation and SEM imaging were performed together with Robby Prang. Low-temperature PL measurements were performed together with Chris Levy. Solid state PL measurements, including solid state TRPL measurements in microseconds time scale were performed together with Carolyn Cadogan and Lyudmila V. Goncharova. The draft of the manuscript was written by Tetyana I. Levchenko and edited by Yining Huang and John F. Corrigan.

## Table of Contents

<b>Abstract</b> .....	ii
<b>Keywords</b> .....	iii
<b>Acknowledgements</b> .....	iv
<b>Co-Authorship Statement</b> .....	vi
<b>Table of Contents</b> .....	viii
<b>List of Figures</b> .....	xii
<b>List of Schemes</b> .....	xix
<b>List of Tables</b> .....	xx
<b>List of Appendices</b> .....	xxii
<b>List of New Materials Reported</b> .....	xxiii
<b>List of Abbreviations</b> .....	xxiv
<b>Epigraph</b> .....	xxvi
<b>Chapter 1: Introduction: Recent Progress in the Preparations of Large Metal Chalcogenide Clusters and Their Ordered Superstructures <i>via</i> Solvothermal and Ionothermal Syntheses</b> .....	1
<b>1.1 General Introduction to Metal Chalcogenide Clusters</b> .....	1
<b>1.2 Bonding in Metal Chalcogenide Clusters</b> .....	3
<b>1.2.1 Metal-Chalcogen Bonding</b> .....	3
<b>1.2.2 Local Electroneutrality in the Cluster Core</b> .....	5
<b>1.2.3 Series of Tetrahedral Clusters</b> .....	6
<b>1.2.4 Ligands on Tetrahedral Clusters</b> .....	13
<b>1.2.5 Non-Tetrahedral Clusters</b> .....	16
<b>1.3 Bonding in Materials Containing Metal Chalcogenide Clusters</b> .....	17
<b>1.3.1 Bonding in Cluster Superstructures</b> .....	17
<b>1.3.2 Topology of Superstructures</b> .....	20
<b>1.3.3 Total Electroneutrality in Superstructures</b> .....	22
<b>1.4 Synthetic Approaches: Solvothermal and Ionothermal Routes</b> .....	24



<b>1.5 Structures of Materials Containing Metal Chalcogenide Clusters</b> .....	26
<b>1.5.1 General Comments</b> .....	26
<b>1.5.2 Tetrahedral Clusters with M<sup>2+</sup> Cations</b> .....	26
<b>1.5.3 Tetrahedral Clusters with M<sup>3+</sup> and Mixed Cations</b> .....	33
<b>1.5.4 Reactions of Large Tetrahedral Clusters</b> .....	43
<b>1.5.5 Non-Tetrahedral Clusters with M<sup>2+</sup> Cations</b> .....	45
<b>1.5.6 Ring- or Cage-Like Clusters with M<sup>3+</sup>, M<sup>4+</sup> and Mixed Cations</b> .....	46
<b>1.6 Scope of the Thesis</b> .....	52
<b>1.7 References</b> .....	54
<b>Chapter 2: Controlled Solvothermal Routes to Hierarchical 3D Superparticles of Nanoscopic CdS</b> .....	61
<b>2.1 Introduction</b> .....	61
<b>2.2 Results and Discussion</b> .....	64
<b>2.3 Conclusions</b> .....	95
<b>2.4 Experimental Section</b> .....	96
<b>2.4.1 Syntheses</b> .....	96
<b>2.4.2 Characterization</b> .....	98
<b>2.4.3 Single-Crystal X-ray Diffraction</b> .....	101
<b>2.5 References and Notes</b> .....	102
<b>Chapter 3: From Molecule to Materials: Crystalline Superlattices of Nanoscopic CdS Clusters</b> .....	108
<b>3.1 Introduction</b> .....	108
<b>3.2 Results and Discussion</b> .....	108
<b>3.3 Conclusions</b> .....	114
<b>3.4 Experimental Section</b> .....	115
<b>3.4.1 Syntheses</b> .....	115
<b>3.4.2 Characterization</b> .....	116
<b>3.5 References</b> .....	117

<b>Chapter 4: Crystalline Superlattices of Nanoscopic CdS Molecular Crystals: an X-ray Crystallography and <sup>111</sup>Cd SSNMR Spectroscopy Study</b> .....	120
4.1 Introduction .....	120
4.2 Results and Discussion .....	126
4.2.1 Short-Range and Long-Range Structures .....	126
4.2.2 PXRD Data .....	131
4.2.3 Local Environment .....	140
4.2.4 SSNMR Data .....	142
4.3 Conclusions .....	171
4.4 Experimental Section .....	172
4.4.1 Syntheses .....	172
4.4.2 Characterization .....	173
4.5 References and Notes .....	177
<b>Chapter 5: Superstructures of Nanoscopic CdSe: Solvothermal Routes to a Superlattice of Large Nanoclusters and a Nanoporous Single Crystal</b> .....	180
5.1 Introduction .....	180
5.2 Results and Discussion .....	182
5.3 Conclusions .....	219
5.4 Experimental Section .....	221
5.4.1 Syntheses .....	221
5.4.2 Single-Crystal X-ray Diffraction .....	224
5.4.3 Characterization .....	225
5.5 References .....	229
<b>Chapter 6: Conclusions and Future Directions</b> .....	235
6.1 Summary of the synthetic approach: Towards elucidating the mechanism of precursor conversion and finding parameters that govern product structure formation	235
6.2 New materials prepared .....	236
6.3 New properties reported .....	237
6.4 Future Directions .....	239

<b>6.5 References</b> .....	239
<b>Appendix A</b> .....	240
<b>Appendix B</b> .....	245
<b>Curriculum Vitae</b> .....	251

## List of Figures

- Figure 1.1:** Adamantoid or cubic (*left*), barrelanoid or hexagonal (*right*) crystalline cages ..... 4
- Figure 1.2:** The core structures of the largest discrete clusters prepared in the three tetrahedral clusters series: (basic) supertetrahedral cluster  $[\text{Cd}_{13}\text{In}_{22}\text{S}_{52}(\text{mim})_4]^{12-}$  (*left*); penta supertetrahedral cluster  $[\text{Cu}_{11}\text{In}_{15}\text{Se}_{16}(\text{SePh})_{24}(\text{PPh}_3)_4]$  (*centre*); capped supertetrahedral clusters  $[\text{Cd}_{54}\text{S}_{32}(\text{SPh})_{48}(\text{H}_2\text{O})_4]^{4-}$  (*right*) ..... 5
- Figure 1.3:** Tetrahedrally-shaped fragments of regular zinc blende (cubic) crystalline lattice as idealized structures of supertetrahedral  $T_n$  clusters ..... 7
- Figure 1.4:** Hierarchical  $T_{4,2}$  cluster  $[\text{Cd}_{16}\text{In}_{64}\text{S}_{134}]^{44-}$  ..... 8
- Figure 1.5:** Stuffed supertetrahedral cluster  $[\text{Sn}_{10}\text{S}_{20}\text{O}_4]^{8-}$  ..... 9
- Figure 1.6:** Anti- $T_2$  building unit  $\{\text{E}_4\text{M}_{10}\}$  (*top left*). Face-to-face coupling of a  $T_2$  and an anti- $T_2$  supertetrahedral units (*top centre*). Penta supertetrahedral cluster  $P_2$  (*top right*). Anionic  $P_2$  cluster  $[\text{Li}_4\text{In}_{22}\text{S}_{44}]^{18-}$  (*bottom*) ..... 10
- Figure 1.7:** The core  $T_3$  unit (*top left*), a single cubic sheet (*top centre*) that covers each face of the central tetrahedron and a hexagonal cage (*top right*) that caps each vertex in the  $C_3$  cluster  $[\text{Cd}_{54}\text{Se}_{32}(\text{SPh})_{48}(\text{H}_2\text{O})_4]^{4-}$  (*bottom*) ..... 12
- Figure 1.8:** A fragment of the 1D covalently bonded cluster chain of  $[\text{Zn}_8\text{S}(\text{SPh})_{13}\text{L}(\text{H}_2\text{O})]$  with L = 3-carboxypyridyl ..... 15
- Figure 1.9:** Two-cluster anion  $[\text{Ga}_{10}\text{S}_{17}\text{HL}_2\text{-dpeGa}_{10}\text{S}_{17}\text{HL}_2]^{6-}$ , where L = 3,5-dimethylpyridine ..... 18
- Figure 1.10:** Two-cluster doubly-bridged neutral aggregate  $[\text{Cd}_{17}\text{Se}_4(\text{SPh})_{26}\text{-}(dpp)_2\text{-Cd}_{17}\text{Se}_4(\text{SPh})_{26}]$  ..... 18
- Figure 1.11:** Examples of 3D superstructure topologies formed from discrete tetrahedral clusters: idealized cubic diamond (*left*) and hexagonal diamond (*right*) superstructures ..... 21
- Figure 1.12:** Neutral  $P_1$  cluster  $[\text{Zn}_8\text{S}(\text{SPh})_{14}\text{L}_2]$ , where L = 3-(2-thienyl)pyridine ..... 28
- Figure 1.13:** Fragments of cubic superlattices of  $C_3$  clusters: primitive for  $[\text{Cd}_{54}\text{Se}_{32}(\text{SPh})_{48}(\text{H}_2\text{O})_4]^{4-}$  with space group  $P23$  (*left*) and face-centered for  $[\text{Cd}_{54}\text{S}_{32}(\text{SPh})_{48}(\text{H}_2\text{O})_4]^{4-}$  with space group  $F-43c$  (*right*) ..... 29
- Figure 1.14:**  $\text{Cd}_{54}\text{Se}_{80}$  structure of the anionic  $C_3$  cluster  $[\text{Cd}_{54}\text{Se}_{32}(\text{SePh})_{48}(\text{dmf})_4]^{4-}$  .. 30
- Figure 1.15:** Ion-pair charge transfer salt  $[\text{C}_{15}\text{H}_{16}\text{N}_3][\text{Zn}_8\text{S}(\text{SPh})_{15}\text{H}_2\text{O}]$  ..... 31

- Figure 1.16:** Ion-pair charge transfer salt  $[\text{Fe}(\text{phen})_3]_2[\text{Cd}_{32}\text{S}_{14}(\text{SPh})_{40}]$  ..... 32
- Figure 1.17:** Anionic  $T_3$  cluster  $[\text{Ga}_{10}\text{S}_{16}\text{L}_4]^{2-}$  charge-balanced and stabilized by  $2\text{H}^+\text{-L}$ , where  $\text{L} = 3,5\text{-dimethylpyridine}$  ..... 34
- Figure 1.18:** Anionic  $T_4$  cluster  $[\text{Cd}_4\text{In}_{16}\text{S}_{31}\text{L}_4]^{6-}$  charge-balanced and stabilized by  $\text{H}^+\text{-L}$  species ..... 35
- Figure 1.19:**  $[\text{Bmmim}]^+$  cations between two anionic  $T_5$  clusters  $[\text{Cu}_5\text{In}_{30}\text{S}_{52}(\text{SH})_2\text{Cl}_2]^{13-}$  ..... 37
- Figure 1.20:** The neutral cluster with covalently-bonded metal complexes  $[\text{Mn}(\text{tepa})]_4[\text{Zn}_2\text{Ga}_4\text{Sn}_4\text{Se}_{20}]$  ..... 38
- Figure 1.21:** The anionic  $T_3$  cluster  $[\text{Mn}_2\text{Ga}_4\text{Sn}_4\text{S}_{20}]^{8-}$  with metal-complex cations  $[\text{Mn}(\text{dien})_2]^{2+}$  ..... 39
- Figure 1.22:** The anionic  $T_3$  cluster  $[\text{In}_{10}\text{S}_{20}\text{H}_4]^{6-}$  with three metal-complex cations  $[\text{Ni}(\text{phen})_3]^{2+}$  (*left*); superstructure of the clusters, charge-balanced, templated and stabilized by metal-complexes (*right*) ..... 39
- Figure 1.23:** The anionic  $T_4$  cluster  $[\text{Cu}_2\text{Ga}_{16}\text{Sn}_2\text{Se}_{35}]^{12-}$  surrounded by 24 protonated piperidine molecules: those bonded to cluster vertexes (*left*) and the centers of edges (*right*) through  $\text{N-H}\cdots\text{Se}$  hydrogen bonding are shown separately ..... 41
- Figure 1.24:** The anionic  $\text{TO}_2$  cluster  $[\text{In}_{38}\text{S}_{65}(\text{H}_2\text{O})_6]^{16-}$  (*left*); separately shown is the octahedral core unit  $\{\text{In}_{10}\text{S}_{13}\}$  in the same orientation (*right*) ..... 42
- Figure 1.25:** Tetrahedral  $T_4$   $[\text{Cu}_4\text{In}_{16}\text{S}_{35}\text{H}_4]^{14-}$  and cubic  $[\text{Cu}_{12}\text{S}_8]^{4-}$  discrete anionic clusters (*left*); fragment of packing in binary superstructure, where cubic  $[\text{Cu}_{12}\text{S}_8]^{4-}$  reside in hexagonal spaces formed by tetrahedral  $[\text{Cu}_4\text{In}_{16}\text{S}_{35}\text{H}_4]^{14-}$  clusters from different layers (*right*) ..... 43
- Figure 1.26:** Discrete coreless  $T_5$   $[\text{Cd}_6\text{In}_{28}\text{S}_{52}(\text{SH})_4]^{12-}$  (*left*) as a host cluster and discrete  $T_5$  cluster  $[\text{CuCd}_6\text{In}_{28}\text{S}_{52}(\text{H}_2\text{O})_4]^{7-}$  (*right*) as a product of “solvothermal insertion” reaction ..... 45
- Figure 1.27:** Cationic cubic  $[\text{Cd}_8(\text{SPh})_{12}]^{4+}$  cluster in 3D covalently bonded coordination polymer ..... 46
- Figure 1.28:** Ring-shaped anionic clusters  $[\text{Sb}_6\text{S}_{12}]^{6-}$  with metal-complex cation  $[\text{Ni}(\text{aepa})_2]^{2+}$  ..... 47
- Figure 1.29:** Two different orientations of wheel-shaped  $[\text{In}_{18}\text{Te}_{30}(\text{dach})_6]^{6-}$  anionic cluster with  $\text{H}_2\text{O}$  molecule in the central  $2\text{H}^+\text{-dach}\cdot\text{H}_2\text{O}$  unit ..... 48

<b>Figure 1.30:</b> Fragment of packing of anionic clusters $[\text{In}_{18}\text{Te}_{30}(\text{daph})_6]^{6-}$ and metal-complex cations $[\text{Ni}(\text{phen})_3]^{2+}$ .....	49
<b>Figure 1.31:</b> Triangular ring-shaped anionic cluster $[\text{Mn}_9\text{In}_{33}\text{Se}_{60}(\text{dach})_{24}]^{3-}$ with the central $\text{Mn}^{2+}$ cation ( <i>left</i> ). A fragment of packing in the binary superstructure combining larger $[\text{Mn}_9\text{In}_{33}\text{Se}_{60}(\text{dach})_{24}]^{3-}$ and smaller $[\text{In}_{18}\text{Se}_{30}(\text{dach})_6]^{6-}$ ring-shaped clusters ( <i>right</i> ) .....	50
<b>Figure 1.32:</b> Building units of discrete cage-like clusters: $\{\text{M}_3\text{Se}_9\}$ ( <i>top left</i> ) and $\{\text{M}_6\text{Se}_{18}\}$ ( <i>top right</i> ). The discrete cage-like cluster $[\text{Sn}_{36}\text{Ge}_{24}\text{Se}_{132}]^{24-}$ ( <i>bottom left</i> ), composed of eight $\{\text{Ge}_3\text{Se}_9\}$ and six $\{\text{Sn}_6\text{Se}_{18}\}$ units. A fragment of packing of cage-like anions and charge-balancing $[\text{Bmim}]^+$ cations ( <i>bottom right</i> ) .....	52
<b>Figure 2.1:</b> SEM images of cubic crystals of <b>1</b> .....	64
<b>Figure 2.2:</b> Powder X-ray diffraction pattern and UV–vis absorption spectrum of DMF solution of <b>1</b> .....	65
<b>Figure 2.3:</b> Powder X-ray diffraction patterns of <b>1</b> , <b>3</b> , and <b>4</b> samples with reference diffractograms: hexagonal and cubic crystalline CdS .....	66
<b>Figure 2.4:</b> UV–vis absorption spectra of solutions and diffuse reflection spectra of solid samples of <b>1</b> , <b>3</b> and <b>4</b> .....	67
<b>Figure 2.5:</b> Normalized room temperature PL and PLE spectra of saturated DMF solutions of <b>1</b> and <b>4</b> .....	68
<b>Figure 2.6:</b> HAADF STEM image showing individual nanoclusters from DMF solution of <b>1</b> and the corresponding particle size distribution .....	69
<b>Figure 2.7:</b> TEM image of <b>1</b> : aggregate of micron-sized cubes, general view ( <i>left</i> ); with smaller ordered domains visible at the edge of the cube, high resolution ( <i>right</i> ); “wet” sample preparation .....	70
<b>Figure 2.8:</b> BF TEM ( <i>left</i> ) and HAADF STEM ( <i>right</i> ) images of <b>1</b> with an extended nanocluster superlattice in the micron-sized cube; “FIB” sample preparation .....	71
<b>Figure 2.9:</b> SAED of <b>1</b> : single crystal low-angle and wide-angle reflections .....	72
<b>Figure 2.10:</b> Powder X-ray diffraction pattern and UV–vis absorption spectrum of DMF solution of <b>2</b> .....	73
<b>Figure 2.11:</b> The $\text{Cd}_{54}\text{S}_{80}$ core structure of <b>2</b> .....	74
<b>Figure 2.12:</b> TGA curves for <b>1</b> , <b>3</b> and <b>4</b> samples .....	76

<b>Figure 2.13:</b> Raman spectra of <b>1</b> , <b>3</b> and <b>4</b> samples: general view and low-frequency part .....	77
<b>Figure 2.14:</b> Room temperature $^1\text{H}$ NMR spectra for soluble species after one day solvothermal treatment of $(\text{Me}_4\text{N})_2[\text{Cd}(\text{SPh})_4]$ in $\text{CH}_3\text{CN}-d_3$ at different temperatures .....	81
<b>Figure 2.15:</b> SEM image of spheres of <b>3</b> .....	83
<b>Figure 2.16:</b> Powder X-ray diffraction pattern and UV–vis absorption spectrum of DMF solution of <b>3</b> .....	84
<b>Figure 2.17:</b> STEM images of <b>3</b> : sphere, general view and edge of sphere at high resolution; “wet” sample preparation .....	85
<b>Figure 2.18:</b> HAADF STEM images of <b>3</b> : CS-sphere, general view ( <i>top left</i> ); edge of sphere, high resolution ( <i>top right</i> ); core-to-shell transition, high resolution ( <i>bottom right</i> ); core, high resolution ( <i>bottom left</i> ); “FIB” sample preparation .....	87
<b>Figure 2.19:</b> Wide-angle SAED of <b>3</b> , obtained from the areas at the edge ( <i>left</i> ), core-to-shell transition ( <i>middle</i> ) and core ( <i>right</i> ) of CS-sphere .....	87
<b>Figure 2.20:</b> TEM images of <b>3</b> : H-sphere, general view ( <i>left</i> ); edge of sphere, high resolution ( <i>right</i> ); “FIB” sample preparation .....	88
<b>Figure 2.21:</b> SEM image of mixed species of <b>4</b> .....	91
<b>Figure 2.22:</b> Powder X-ray diffraction pattern and UV–vis absorption spectrum of DMF solution of <b>4</b> .....	92
<b>Figure 2.23:</b> Rutherford backscattering spectra for <b>1</b> , <b>3</b> and <b>4</b> samples .....	94
<b>Figure 3.1:</b> Powder X-ray diffraction patterns and UV–vis absorption spectrum of <b>5</b> .....	110
<b>Figure 3.2:</b> HAADF-STEM images of <b>5</b> and their packing into 3D crystalline superlattice .....	111
<b>Figure 3.3:</b> HRTEM and HAADF-STEM images of <b>5</b> . Insert: Fourier transform of the HRTEM image .....	112
<b>Figure 3.4:</b> Volume rendering showing the 3D packing of the CdS nanoclusters along $\langle 100 \rangle$ orientation .....	112
<b>Figure 3.5:</b> TGA curves for <b>5</b> .....	113
<b>Figure 3.6:</b> Raman spectrum of <b>5</b> .....	114

<b>Figure 4.1:</b> Structures of molecular cadmium thiophenolate complexes and tetrahedral nanoclusters with thiophenolate ligand shell $Cd_xS_y(SPh)_z$ .....	129
<b>Figure 4.2:</b> Configuration of substituents on the bridging ( $\mu$ -SPh) thiophenolate ligands in two configurational isomers of $(Me_4N)_4[Cd_{10}S_4(SPh)_{16}]$ , <b>Cd10(I-4)</b> and <b>Cd10</b> .....	130
<b>Figure 4.3:</b> Measured (dried material) and simulated PXRD patterns for <b>Cd1</b> .....	131
<b>Figure 4.4:</b> PXRD patterns measured for dried <b>Cd4</b> .....	132
<b>Figure 4.5:</b> Measured (dried material) and simulated PXRD patterns for <b>Cd10</b> .....	133
<b>Figure 4.6:</b> Measured (dried material) and simulated PXRD patterns for <b>Cd17</b> .....	134
<b>Figure 4.7:</b> Measured (fresh material in paraffin oil and dried material) and simulated PXRD patterns for <b>Cd54</b> .....	136
<b>Figure 4.8:</b> Measured (fresh material in paraffin oil and dried material) PXRD patterns for <b>CdS-1.9 nm</b> .....	139
<b>Figure 4.9:</b> $^1H$ - $^{111}Cd$ VACP/MAS SSNMR and static $^1H$ - $^{111}Cd$ VACP echo SSNMR spectra of <b>Cd1</b> ( <i>left</i> ). The inorganic framework of <b>Cd1</b> ( <i>right</i> ) .....	143
<b>Figure 4.10:</b> $^1H$ - $^{111}Cd$ VACP/MAS SSNMR spectra of <b>Cd4</b> processed using 200 and 500 Hz of line broadening ( <i>left</i> ). The inorganic framework of <b>Cd4</b> ( <i>right</i> ).....	145
<b>Figure 4.11:</b> Static $^1H$ - $^{111}Cd$ VACP echo SSNMR spectrum of <b>Cd4</b> .....	146
<b>Figure 4.12:</b> $^1H$ - $^{111}Cd$ VACP/MAS echo and $^1H$ - $^{111}Cd$ VACP echo SSNMR spectra of <b>Cd10</b> ( <i>left</i> ). The inorganic framework of <b>Cd10</b> ( <i>right</i> ) .....	148
<b>Figure 4.13:</b> $^1H$ - $^{111}Cd$ VACP/MAS echo SSNMR spectra <b>Cd17</b> processed using 200 and 500 Hz of line broadening ( <i>left</i> ). The inorganic framework of <b>Cd17</b> ( <i>right</i> ) .....	152
<b>Figure 4.14:</b> Static $^1H$ - $^{111}Cd$ VACP echo SSNMR spectrum of <b>Cd17</b> .....	156
<b>Figure 4.15:</b> $^1H$ - $^{111}Cd$ VACP/MAS echo SSNMR spectra of <b>Cd17</b> and <b>Cd54</b> ( <i>left</i> ). The inorganic framework of <b>Cd54</b> ( <i>right</i> ) .....	160
<b>Figure 4.16:</b> $^1H$ - $^{111}Cd$ VACP/MAS echo SSNMR spectra of <b>CdS-1.9 nm</b> at 15.5 and 11.0 kHz .....	167
<b>Figure 4.17:</b> $^1H$ - $^{111}Cd$ VACP/MAS echo SSNMR spectra of <b>Cd54</b> and <b>CdS-1.9 nm</b> .....	168



<b>Figure 4.18:</b> $^1\text{H}$ - $^{111}\text{Cd}$ VACP/MAS echo SSNMR spectra of <b>Cd54</b> and <b>CdS-1.9 nm</b> at different contact times .....	170
<b>Figure 4.19:</b> Static $^1\text{H}$ - $^{111}\text{Cd}$ VACP echo SSNMR spectra of <b>Cd54</b> and <b>CdS-1.9 nm</b> .....	171
<b>Figure 5.1:</b> $\text{Cd}_{54}\text{Se}_{80}$ core structure of <b>6</b> .....	183
<b>Figure 5.2:</b> Measured (fresh material in paraffin oil and dried) and simulated powder X-ray diffraction patterns for <b>6</b> .....	184
<b>Figure 5.3:</b> Microscopy images of dried <b>6</b> : optical micrograph ( <i>left</i> ), SEM ( <i>center</i> ) and TEM ( <i>right</i> ). Inset: low-angle SAED reflections of <b>6</b> .....	185
<b>Figure 5.4:</b> Raman spectra of <b>6</b> and <b>7</b> .....	188
<b>Figure 5.5:</b> TGA curve for <b>6</b> .....	189
<b>Figure 5.6:</b> Negative ion mode electrospray mass spectrum of <b>6</b> .....	190
<b>Figure 5.7:</b> Transmission optical ( <i>left</i> ) and confocal fluorescent microscopy ( <i>right</i> ) images of <b>6</b> .....	191
<b>Figure 5.8:</b> UV-vis absorption diffuse reflection spectra of <b>6</b> .....	193
<b>Figure 5.9:</b> UV-vis absorption spectra of DMF-diluted mother liquor before and after crystallization of <b>6</b> .....	194
<b>Figure 5.10:</b> UV-vis absorption spectra of <b>6</b> in DMF and acetonitrile .....	195
<b>Figure 5.11:</b> Normalized PL and PLE spectra of <b>6</b> in DMF at 77 K and room temperature; PL spectrum of <b>6</b> in solid state .....	196
<b>Figure 5.12:</b> Normalized PL and PLE spectra of <b>6</b> in DMF, obtained at different excitation and detection wavelengths .....	197
<b>Figure 5.13:</b> Room-temperature PL and PLE spectra of <b>6</b> in DMF at different concentrations .....	198
<b>Figure 5.14:</b> Normalized time-resolved PL decay traces and FLIM micrographs for <b>6</b> and <b>7</b> .....	201
<b>Figure 5.15:</b> Snapshot of X-ray diffraction image of a single hexagonal prism from <b>7</b> .....	204
<b>Figure 5.16:</b> SEM images of hexagonal prisms in <b>7</b> .....	205
<b>Figure 5.17:</b> High resolution SEM images of surface of <b>7</b> .....	205

<b>Figure 5.18:</b> Powder X-ray diffraction patterns of dried <b>6</b> and <b>7</b> .....	206
<b>Figure 5.19:</b> UV–vis diffuse reflection and room temperature solid state PL spectra of <b>7</b> .....	207
<b>Figure 5.20:</b> Transmission optical ( <i>left</i> ) and confocal fluorescent microscopy ( <i>right</i> ) images of hexagonal prisms of <b>7</b> .....	209
<b>Figure 5.21:</b> SEM images of small hexagonal prism <b>7</b> in the process of FIB preparation .....	210
<b>Figure 5.22:</b> STEM and TEM images of thin slice through hexagonal prism <b>7</b> . Insert: Fourier transform of TEM image .....	211
<b>Figure 5.23:</b> SAED of the thin slice of hexagonal prism <b>7</b> .....	212
<b>Figure 5.24:</b> Bright-field ( <i>left</i> ) and dark-field ( <i>right</i> ) TEM of the thin slice of hexagonal prism <b>7</b> .....	212
<b>Figure 5.25:</b> Schematic representation of a possible pathway for stepwise formation of 3D CdSe network in hexagonal prisms <b>7</b> .....	216
<b>Figure 5.26:</b> SEM images of heavily distorted hexagonal prisms .....	217
<b>Figure 5.27:</b> Schematic representation of a possible nature for the CdSe wall thickness gradient in hexagonal prisms <b>7</b> .....	219
<b>Figure 5.28:</b> Schematic of the experimental setup used for TRPL measurements .....	229

## List of Schemes

<b>Scheme 2.1:</b> Solvothermal route to CdS superstructures .....	64
--	----

## List of Tables

<b>Table 1.1:</b>	Series of tetrahedral metal chalcogenide clusters .....	7
<b>Table 2.1:</b>	Average lattice distances measured from HR TEM of nanocluster aggregates of <b>1</b> in DMF and calculated using SAED of FIB prepared superparticle cross-sections .....	69
<b>Table 2.2:</b>	Summary of EDX data for <b>1</b> , <b>3</b> , and <b>4</b> .....	70
<b>Table 4.1:</b>	Selected crystal data for molecular cadmium thiophenolate complexes and tetrahedral nanoclusters $Cd_xS_y(SPh)_z$ .....	127
<b>Table 4.2:</b>	Measured (dried material) and simulated low-angle reflections for <b>Cd1</b> .....	132
<b>Table 4.3:</b>	Measured in this work (dried material) and previously reported low-angle reflections for <b>Cd4</b> .....	132
<b>Table 4.4:</b>	Measured (dried material) and simulated low-angle reflections for <b>Cd10</b> ....	133
<b>Table 4.5:</b>	Measured (dried material) and simulated low-angle reflections for <b>Cd17</b> .....	134
<b>Table 4.6:</b>	Measured (fresh material) and simulated low-angle reflections for <b>Cd54</b> .....	136
<b>Table 4.7:</b>	Composition of molecular cadmium thiophenolate complexes and tetrahedral nanoclusters $Cd_xS_y(SPh)_z$ .....	141
<b>Table 4.8:</b>	Chemical shifts and proposed assignment for different resonances of <b>Cd1</b> , <b>Cd4</b> , <b>Cd10</b> and <b>Cd17</b> .....	150
<b>Table 4.9:</b>	Literature data on the chemical shifts for selected cadmium compounds .....	154
<b>Table 4.10:</b>	Chemical shifts and proposed assignment for different groups of resonances of <b>Cd54</b> and <b>CdS-1.9 nm</b> .....	161
<b>Table 4.11:</b>	Literature data on the chemical shifts for resonances from different cadmium sites in CdS nanoparticles .....	164
<b>Table 4.12:</b>	Summary of conditions and parameters for $^1H$ - $^{111}Cd$ VACP/MAS SSNMR experiments .....	175

<b>Table 4.13:</b> Summary of conditions and parameters for static $^1\text{H}$ - $^{111}\text{Cd}$ VACP echo SSNMR experiments .....	176
<b>Table 4.14:</b> Summary of conditions and parameters for $^1\text{H}$ - $^{111}\text{Cd}$ VACP/MAS echo NMR experiments performed at a spinning frequency of 15.5 kHz using short contact times .....	176
<b>Table 4.15:</b> Literature data on the chemical shifts used for conversion to the scale with 0.1 M aqueous solution of $\text{Cd}(\text{ClO}_4)_2$ set as a standard ( $\delta = 0$ ) .....	177
<b>Table 5.1:</b> Composition of the members of capped tetrahedral nanocluster series .....	202

## List of Appendices

Appendix A .....	240
Appendix B .....	245

## List of New Materials Reported

material	formula (when applicable) and description		Chapter(s) #; page(s) # <sup>a</sup>
	primary framework	superstructure	
<b>1<sup>b</sup></b>	1.9 nm <sup>c</sup> CdS clusters	cubes	Ch. 2; p. 64 Ch. 4; p. 138
<b>2<sup>b</sup></b>	(Me <sub>4</sub> N) <sub>4</sub> [Cd <sub>54</sub> S <sub>32</sub> (SPh) <sub>48</sub> (dmf) <sub>4</sub> ] clusters	cubes	Ch. 2; p. 73 Ch. 4; p. 135
<b>3</b>	≥2.3 nm <sup>c</sup> CdS particles	spheres	Ch. 2; p. 83
<b>4</b>	2.3 nm <sup>c</sup> CdS clusters	cubes <sup>d</sup>	Ch. 2; p. 90
<b>5</b>	2.3 nm <sup>c</sup> CdS clusters	cubes	Ch. 3; p. 109
<b>6</b>	(Me <sub>4</sub> N) <sub>4</sub> [Cd <sub>54</sub> Se <sub>32</sub> (SePh) <sub>48</sub> (dmf) <sub>4</sub> ] clusters	cubes	Ch. 5; p. 182
<b>7</b>	porous single crystal CdSe	hexagonal prisms	Ch. 5; p. 204

<sup>a</sup> Chapter(s) # where described; page(s) # where discussion of characterization results begins.

<sup>b</sup> The materials **1** and **2** are denoted in the Chapter 4 as **CdS-1.9 nm** and **Cd54**, respectively, in the interest of consistency with notations for smaller clusters characterized in the Chapter 4.

<sup>c</sup> Diameter from electron microscopy data.

<sup>d</sup> Co-exist with some mixed species.

## List of Abbreviations

1D	one-dimensional
2D	two-dimensional
3D	three-dimensional
Å	angstrom
Ac, OAc	acetate
bpy	bipyridine
C <sub>n</sub> , C <sub>n</sub>	capped supertetrahedral (cluster series)
CTAB	cetyltrimethylammonium bromide
DFT	density functional theory
<i>dmf</i>	N,N'-dimethylformamide, ligand
DMF	N,N'-dimethylformamide, solvent
DMSO	dimethylsulfoxide
E	chalcogen (S, Se, Te) atom
<i>e.g.</i>	<i>exempli gratia</i> (for example)
EDX	energy dispersive X-ray
<i>et al.</i>	<i>et alii</i> (and others)
eV	electron volts
fc	ferrocene
FIB	focused ion beam
FLIM	fluorescence-lifetime imaging microscopy
g	gram
h	hour
Hal	halogen, halide
<i>i.e.</i>	<i>id est</i> (that is)
<i>in situ</i>	in the original place
IR	infrared
L	(neutral) organic ligand
M	metal atom
<i>m</i>	metha
M	molar
m/z	mass to charge ratio
Me	methyl
min	minute
mL	millilitre
mm	millimetre
mmol	millimole
n	integer number
<sup>n</sup> Bu	<i>n</i> -butyl
nm	nanometer
NMR	nuclear magnetic resonance
K	Kelvin
<sup>n</sup> Pr	<i>n</i> -propyl
<i>o</i>	ortho



° C	degree Celsius
<i>p</i>	<i>para</i>
Ph	phenyl
phen	phenanthroline
PL	photoluminescence
PLE	photoluminescence excitation
$P_n, P_n$	penta supertetrahedral (cluster series)
ppm	parts per million
R	organic substituent
SAED	selected area electron diffraction
SEM	scanning electron microscopy
SS	solid state
T	temperature
TEM	transmission electron microscopy
TGA	thermogravimetric analysis
$T_n, T_n$	supertetrahedral (cluster series)
TR	time-resolved
UV	ultraviolet
<i>vide infra</i>	see below
vis	visible
<i>viz.</i>	<i>videlicet</i> (namely)
vs.	versus
$\delta$	chemical shift

You boil it in sawdust, you salt it in glue,  
You condense it with locusts and tape,  
Still keeping one principal object in view –  
To preserve its symmetrical shape.

*(from The Hunting of the Snark by Lewis Carroll)*

## Chapter 1

# Introduction: Recent Progress in the Preparations of Large Metal Chalcogenide Clusters and Their Ordered Superstructures *via* Solvothermal and Ionothermal Syntheses<sup>α</sup>

### 1.1 General Introduction to Metal Chalcogenide Clusters

Polynuclear metal chalcogenides ME (where M = metal, E = group 16 element heavier than oxygen) often possess unique structures due to the bonding modes inherent to the chalcogen sites.<sup>1-7</sup> Metal chalcogenide clusters with well-defined sizes and chemical composition can contain tens to hundreds of metal core atoms, organized with a high level of symmetry, and reaching several nanometres in size.<sup>6,8-10</sup> Many of these nanoclusters can be prepared and isolated as single crystals, making it possible to obtain complete structural information through single crystal X-ray diffraction.<sup>11</sup> Other powerful tools, such as electron tomography, can help significantly in the analysis of cluster (super)structures.<sup>12-15</sup> Knowledge of the exact structure of such clusters provides valuable insight into structure-property relationship in nanodimensional systems without the obscuring effects of size polydispersity and structure ambiguity, often inherent to colloidal nanoparticles. Generally, clusters of semiconductor metal chalcogenides have size-related electronic and photophysical properties due to quantum confinement effects.<sup>16-18</sup> Thus, a systematic blue shift for both optical absorption and emission band is observed with decreasing CdSe cluster size.<sup>19,20</sup> The properties of the clusters can also be tuned by the substitution of M and E, by combining several different metals or chalcogens, with site-selective distribution of the components in a cluster core, and/or fitting organic ligands on a cluster surface. Long range order is present with certain secondary structures (1D, 2D and 3D arrangements), maintained by electrostatic (Coulomb) interactions and/or relatively weak (*e.g.*, van der Waals) forces or, alternatively, by covalent bonding (with or without auxiliary organic linkers) between metal chalcogenide clusters.<sup>21</sup> Such multilevel, hierarchical structures of metal-chalcogenide clusters have multiple attractive features: materials containing metal chalcogenide clusters can be engineered at several different length scales, from atomic level (size and composition of cluster core) to the

---

<sup>α</sup> A version of this literature review has been published in Levchenko, T. I.; Huang, Y.; Corrigan, J. F. In *Structure and Bonding*; Springer, 2016. DOI: 10.1007/430\_2016\_5 and has been reproduced with permission.

superstructure level (intercluster bonding type and connectivity patterns), which provides an additional opportunity to control their properties.<sup>22</sup> Moreover, hybrid materials can be created based on molecular-level integration of anionic metal chalcogenide clusters with cations having special functions,<sup>23,24</sup> or even by the combination (crystallization) of cluster superstructures with other advanced materials. One of the recent examples of the latter is the clusters  $Zn_xGa_{18-x}Sn_2S_{35}@reduced\ graphene\ oxide$ .<sup>25</sup> The properties of the materials containing metal chalcogenide clusters encompass such research areas as photophysics, photoelectrochemistry, photocatalysis, *etc.*, as they are promising candidates for application as advanced energy conversion materials and bio-labels.<sup>26–30</sup>

Historically, a coordination chemistry approach has been used for the preparation and crystallization of metal chalcogenide clusters from solutions.<sup>1,6,9</sup> This powerful approach utilizes different sources of chalcogenides and surface chalcogenolates (among them silylated reagents  $E(SiMe_3)_2$  and  $RESiMe_3$ )<sup>11</sup> and has been proven to give access to, for instance, unprecedented large sizes (*e.g.*,  $[Ag_{490}S_{188}(S^{\prime}C_5H_{11})_{114}]$ )<sup>31</sup> as well as opportunities for unique surface functionalization (*e.g.*, ferrocene (fc) decorated  $[Ag_{74}S_{19}(dppp)_6-(fc(C\{O\}OCH_2CH_2S)_2)_{18}]$ , where  $dppp = 1,3-bis(diphenylphosphino)propane$ )<sup>32</sup> to group 11 metal chalcogenide clusters. Materials containing metal chalcogenide clusters have also been prepared by solid-state chemistry approaches from high-temperature reactions in polychalcogenide flux (*e.g.*, a series of discrete clusters  $[M_4Sn_4S_{17}]^{10-}$  with  $M = Mn, Fe, Co, Zn$  in a  $K_2S_x$  flux).<sup>33,34</sup> More recently, solvothermal approaches have been exploited,<sup>35,36</sup> conducting synthesis using relatively simple reagents (*e.g.*, elemental forms and inorganic salts) in an appropriate organic solvent in a sealed vessel at moderately high temperature and autogenous pressure. A related approach, utilizing ionic liquids as reaction media is also a focus of research efforts for the preparation of metal chalcogenide clusters.<sup>37</sup> During the last decade solvothermal and ionothermal approaches have yielded, for example, new metal chalcogenide clusters with unprecedented structures,<sup>38–40</sup> the ability for precise and uniform one-atom-doping of clusters with vacant sites,<sup>41,42</sup> and the preparation of large, discrete clusters, previously accessible only in covalently-bonded 2D and 3D superlattices.<sup>43,44</sup>

Several research groups have been developing solvothermal and ionothermal approaches towards the preparation of large metal chalcogenide clusters and materials derived from

their regular spatial organization. The general synthetic routes and the structures and properties of these materials will be summarized in this chapter. Note that the main focus is on discrete clusters (mainly tetrahedral) and their non-covalent 3D superstructures; while extended framework superstructures (both zeolite and metal-organic framework analogues with inorganic linkers and organic ligand connection between clusters, respectively) were previously covered in several reviews.<sup>45-48</sup> Relatively large metal chalcogenide clusters, mainly containing  $\geq 8$  metal sites in the core, are the focus herein.

## 1.2 Bonding in Metal Chalcogenide Clusters

### 1.2.1 Metal-Chalcogen Bonding

Chalcogenides  $E^{2-}$  form stable bonds with many metals, adopting several different bridging coordination modes, with  $\mu_3$  and  $\mu_4$  being the most common.<sup>4,6,2</sup> Thus, the coordination number of sulfur reaches 4 even with a relatively large metal cation such as  $Cd^{2+}$ . The ability to bridge metals with high coordination numbers is attributed to the large ionic radii, high polarizability, more delocalized electron orbitals, and the anionic nature of chalcogenide ligands.<sup>6</sup> The bridging ability increases on going down group 16 from sulfur to selenium to tellurium.<sup>3,5,7</sup> Metal cations in cluster chalcogenides can be in one particular oxidation state ( $M^{2+}$ ,  $M^{3+}$ , or  $M^{4+}$ ), combinations of two cations (*e.g.*,  $M^{3+}/M^+$  or  $M^{4+}/M^{2+}$ ) or exhibit even more complex composition. A recent example of such multinary compounds is a family of discrete  $M_{20}E_{35}$  clusters, combining, for instance, five metals with different oxidation states (*i.e.*, Cu, Zn, Mn, Ga, and Sn) in one cluster as it was confirmed by EDX analysis; for clusters with less exotic quaternary composition (*e.g.*,  $[Cu_2Ga_{16}Sn_2Se_{35}]^{12-}$  or  $[Zn_4Ga_{14}Sn_2Se_{35}]^{12-}$ ) single-crystal structure refinement results are in good agreement with atomic absorption spectroscopy analysis.<sup>49</sup> As a consequence of the high bridging ability of  $E^{2-}$  with high coordination numbers for  $M^{x+}$ , in many metal chalcogenide frameworks cations and anions both adopt tetrahedral coordination, which makes tetrahedral unit  $\{ME_4\}$  the most basic building block in these materials. A distinct structural feature is the overall tetrahedral shape of many such clusters. The covalent character of bonding in the tetrahedral units  $\{ME_4\}$  reflects the relative position of the composing metals in the periodic table. Most often, metals in these tetrahedral clusters

belong to groups 12, 13, and 14 (*e.g.*, Zn, Cd, Hg; Ga, In; Ge, and Sn) and late first-row transition metals (*e.g.*, Mn, Fe, Co, and Cu); however, this does not exclude the possibility of doping by other metal(s) (*e.g.*, Li). Many of the tetrahedral metal chalcogenide clusters, originally prepared by other approaches, have been reproduced solvothermally. Even more clusters have proven accessible by solvothermal and ionothermal approaches, including those with completely new structure types. The group 11 metal chalcogenide clusters, prepared by coordination chemistry approaches, are numerous and structurally diverse,<sup>50–52</sup> but such discrete clusters are typically not accessible *via* solvothermal or ionothermal approaches. Although large cluster cores composed of tetrahedral units  $\{ME_4\}$  and having an overall tetrahedral shape are characteristic to metal chalcogenides, some examples are also known for oxides (*e.g.*, tetrahedral clusters  $[Mn^{II}_{29}Mn^{III}_6O_{56}]^{36-}$  or  $[Ln_{20}O_{11}]^{38+}$ , where Ln = lanthanoid metal).<sup>53,54</sup> With adamantoid (cubic) (Figure 1.1, left) and barrelanoid (hexagonal) (Figure 1.1, right) crystalline cages both being possible with the tetrahedral coordination of atoms (corresponding to zinc blende and wurtzite crystal structures, respectively, well known for bulk crystalline metal chalcogenides), the recognized structural variations of tetrahedral metal chalcogenide cluster arise from different combinations of cubic and hexagonal cages in the ME frameworks. Thus, by the nature of intra-cluster connectivity, tetrahedral metal chalcogenide clusters can be classified as belonging to three particular structural series: (basic) supertetrahedral, penta supertetrahedral and capped supertetrahedral (Figure 1.2);<sup>47,55</sup> these are considered in detail below in Sections 1.2.3, 1.5.2 and 1.5.3. Although large, non-tetrahedral clusters<sup>6,9</sup> are less often prepared *via* solvothermal and ionothermal syntheses, some fascinating examples of discrete ring- and cage-like frameworks formed by vertex- and edge-sharing of basic tetrahedra  $\{ME_4\}$  have been reported recently. These clusters are discussed below in Sections 1.2.5, 1.5.5 and 1.5.6.



**Figure 1.1:** Adamantoid or cubic (*left*), barrelanoid or hexagonal (*right*) crystalline cages. M sites are shown as green spheres and E as yellow-orange.

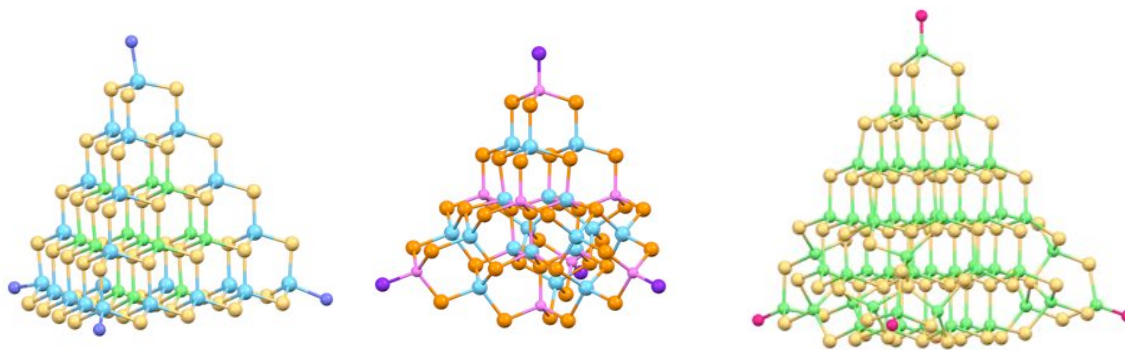


**Figure 1.2:** The core structures of the largest discrete clusters prepared in the three tetrahedral clusters series: (basic) supertetrahedral cluster  $[\text{Cd}_{13}\text{In}_{22}\text{S}_{52}(\text{mim})_4]^{12-}$ , where *mim* = 1-methylimidazole (*left*); penta supertetrahedral cluster  $[\text{Cu}_{11}\text{In}_{15}\text{Se}_{16}(\text{SePh})_{24}(\text{PPh}_3)_4]$  (*centre*); capped supertetrahedral clusters  $[\text{Cd}_{54}\text{S}_{32}(\text{SPh})_{48}(\text{H}_2\text{O})_4]^{4-}$  (*right*).<sup>43,56,57</sup>

If not stated otherwise,  $\text{M}^{2+}$  sites are shown as green;  $\text{M}^{3+}$  – light blue;  $\text{M}^{4+}$  – blue;  $\text{M}^+/\text{M}^{2+}$  transition metal sites – magenta; S – yellow-orange; Se – orange; Te – brown; C – light grey; O – pink; N – violet; P – purple in all figures throughout the Chapter 1. Atoms and bonds in the cluster core are typically shown as spheres and sticks, respectively, while in ligands and other species atoms and bonds are shown as capped sticks.

### 1.2.2 Local Electroneutrality in the Cluster Core

One of the most important factors affecting the size and connectivity of metal chalcogenide clusters is the charge on the constituent metal cations. As the tetrahedral clusters display a clear structural relationship with the corresponding crystalline solids, they are found to obey the same rules surrounding their bonding. Generally, the charge of metal cations appearing in particular sites of tetrahedral metal chalcogenide clusters is found to follow Pauling's electrostatic valence rule. According to this rule, in order to keep *local electroneutrality* (local charge balance) the sum of the strengths of the electrostatic bonds to  $\text{E}^{2-}$  anion should be equal to the charge on the anion, *i.e.*, 2. The electrostatic bond strength can be calculated as the ratio of the charge on adjacent metal cations to its coordination number. From this it follows, for example, that each tetrahedral  $\text{E}^{2-}$  site could be either surrounded by four tetrahedral  $\text{M}^{2+}$  or two tetrahedral  $\text{M}^{3+}$  plus two tetrahedral  $\text{M}^+$ . More specific cases are addressed below when considering the tetrahedral cluster series. Pauling's electrostatic valence rule works most obviously for the inner sites in the cluster,

although it is not always applicable to surface sites (at vertexes, edges and faces of tetrahedral clusters). This is because  $E^{2-}$  sites on the surface may receive additional bond valence from cationic species that are not part of the cluster. A few exceptions to Pauling's electrostatic valence rule (*e.g.*, a tetrahedral cluster with a core  $E^{2-}$  site bonded to four  $M^{3+}$ )<sup>58</sup> can be rationalized considering cluster stabilization from additional lattice species.

### 1.2.3 Series of Tetrahedral Clusters

In a basic *supertetrahedral* series, each molecular cluster consists of a regular tetrahedral shaped fragment of the zinc blende-type lattice (cubic; adamantoid cages) (Figure 1.3). Larger clusters in this series are formed by fusion of adamantoid cages only. This is the most fundamental type of connectivity; other series of clusters can be geometrically derived from the basic supertetrahedral building units. The difference between clusters within the series lies in the size of the framework. This is reflected in conventional notation for the clusters in the supertetrahedral series,  $T_n$ , where the integer  $n$  indicates the number of individual  $\{ME_4\}$  tetrahedra along each edge (Figure 1.3). The integer  $n$  is also equivalent to the number of metal layers within a particular cluster. Thus, a  $T_3$  cluster with a  $M_{10}E_{20}$  core contains four fused adamantoid cages and has three  $\{ME_4\}$  tetrahedra along each edge (or three metal layers) (Figure 1.3, top right). The composition of an idealized core  $M_xE_y$  of any  $T_n$  cluster is strictly defined (see formulae in Table 1.1). It can be seen that the number of E sites in a  $T_n$  cluster is equal to the number of M sites in the next larger  $T_{(n+1)}$  cluster. The peculiarity of large  $T_n$  clusters is the presence of tetrahedrally coordinated (inner) anions, while smaller clusters ( $T_1$ ,  $T_2$ , and  $T_3$ ) consist of  $\mu^-$  and  $\mu_3^-$  anions only. To maintain the local electroneutrality, in large metal chalcogenide clusters containing two or more types of metal cations, site-selective distribution of metals will be one that better balances the tetrahedrally coordinated anion sites  $E^{2-}$ , which occur inside clusters  $\geq T_4$ . In multinary clusters with more than one type of chalcogenide (*e.g.*, both Se and S) the appearance of E, E', M, and M' at inner or surface sites may be governed by multiple factors.<sup>59</sup> The largest reported discrete supertetrahedral clusters are  $T_5$ ; for instance,  $[Cd_{13}In_{22}S_{52}L_4]^{12-}$  cluster, where L – neutral organic ligand 1-methylimidazole, *mim*, capping four cluster vertexes through In–N coordination bonds (Figure 1.2, left); this was prepared using solvothermal methods.<sup>43</sup>



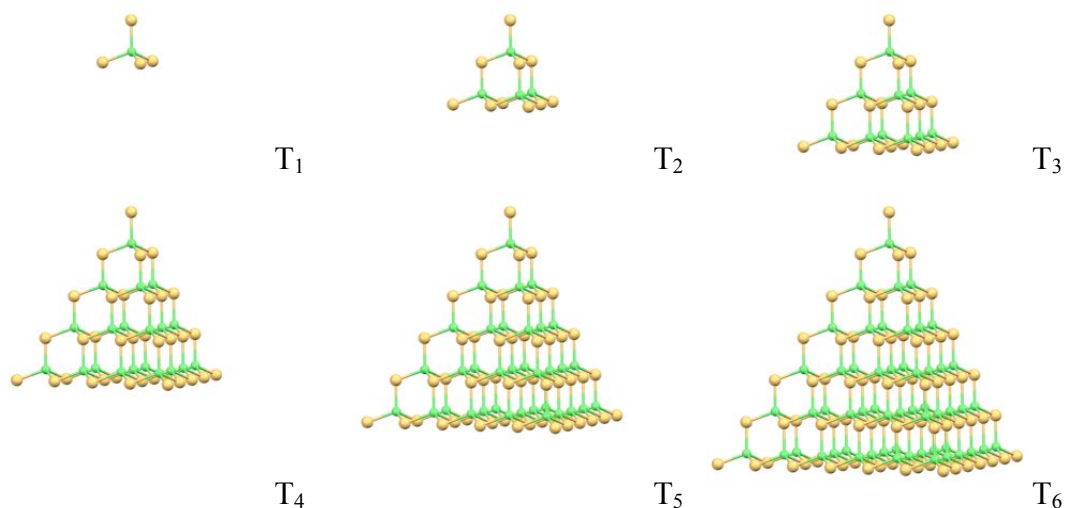


**Figure 1.3:** Tetrahedrally-shaped fragments of regular zinc blende (cubic) crystalline lattice as idealized structures of supertetrahedral  $T_n$  clusters. Such clusters up to  $T_5$  were synthesized and structurally characterized, while  $T_6$  remains a hypothetical structure.

**Table 1.1:** Series of tetrahedral metal chalcogenide clusters.<sup>a</sup>

Name	(Basic) Supertetrahedral	Penta Supertetrahedral	Capped Supertetrahedral
Notation	$T_n$	$P_n$	$C_n$
$n = 1$	$ME_4$	$M_8E_{17}$	$M_{17}E_{32}$
$n = 2$	$M_4E_{10}$	$M_{26}E_{44}$	$M_{32}E_{54}$
$n = 3$	$M_{10}E_{20}$		$M_{54}E_{84}$
$n = 4$	$M_{20}E_{35}$		
$n = 5$	$M_{35}E_{56}$		
Cluster stoichiometry <sup>b</sup>	$M_xE_y$ , <sup>c</sup> where $x = [n(n+1)(n+2)]/6$ ; $y = [(n+1)(n+2)(n+3)]/6$	$M_xE_y$ , where $x = 4[n(n+1)(n+2)]/6$ $+ [(n+1)(n+2)(n+3)]/6$ ; $y = 4[(n+1)(n+2)(n+3)]/6$ $+ [n(n+1)(n+2)]/6$	$M_xE_y$ , where $x = [n(n+1)(n+2)]/6$ $+ [4(n+1)(n+2)]/2 + 4$ ; $y = [(n+1)(n+2)(n+3)]/6$ $+ [4(n+2)(n+3)]/2 + 4$

<sup>a</sup> Adapted from ref. 47

<sup>b</sup> Stoichiometry of discrete clusters is summarized. The overall stoichiometry of the superstructures of covalently connected clusters (*e.g.*, corner-sharing case) varies depending on the pattern of connectivity.

<sup>c</sup> Colours in formulae are used to emphasize the structural relation between clusters with the same  $n$  in the different series: the parts of expression correspond to the number of metal (green) and chalcogen (orange) atoms in the idealized basic supertetrahedral  $T_n$  unit  $M_xE_y$ . For instance, the composition of an idealized penta supertetrahedral  $P_n$  cluster can be derived by taking four times the expression for a  $T_n$  unit and one for an anti- $T_n$  unit, where the latter has the metal and chalcogen positions exchanged in comparison to a regular one.

Clusters with a void or cavity in the core, *i.e.*, hierarchical and coreless clusters, can be considered as structure variations of a supertetrahedral series rather than a separate connectivity type. **Hierarchical** supertetrahedral clusters (denoted  $T_{p,q}$ ) consist of four supertetrahedral  $T_p$  units assembled (through vertex-sharing by bridging  $E^{2-}$  or  $ER^-$  sites) into a self-closed  $T_q$  cluster with a central void of size  $T_p$ . Hierarchical  $T_{p,q}$  clusters can also be viewed as  $T_n$ -like clusters of a larger size ( $n = p \cdot q$ ) with a well-defined tetrahedral void in a core, created by the systematic absence of M and E atoms. In hierarchical clusters, the presence of an inner tetrahedral void ensures a decrease of the coordination number of some of the internal anions; the structure is favourable under conditions of an appropriate combination of constituent elements and a structure-directing agent that optimizes both local and total charge balance. Hierarchical clusters with large  $T_p$  units (and, consequently, large voids) are rare, as  $T_n$  clusters preferentially self-assemble into extended lattices (an extra-ordinary example is dual hierarchical covalently-bonded 3D superstructure  $T_{5,\infty}$ )<sup>60</sup> instead of forming discrete self-closed  $T_{p,q}$  clusters. An example of large hierarchical cluster is the solvothermally prepared discrete  $T_{4,2}$   $[\text{Cd}_{16}\text{In}_{64}\text{S}_{134}]^{44-}$  (Figure 1.4).<sup>61</sup> More recently, solvothermal synthesis also resulted in the preparation of the anionic  $T_{2,2}$  cluster  $[\text{M}_{16}\text{Se}_{34}]^{x-}$  (M = Ge/In mixed sites) covalently linked with  $T_3$  clusters in a 3D framework.<sup>62</sup> Hierarchical supertetrahedral clusters can be prepared while systematically hosting a particular chemical species (*e.g.*, alkali metal cations).<sup>63</sup>

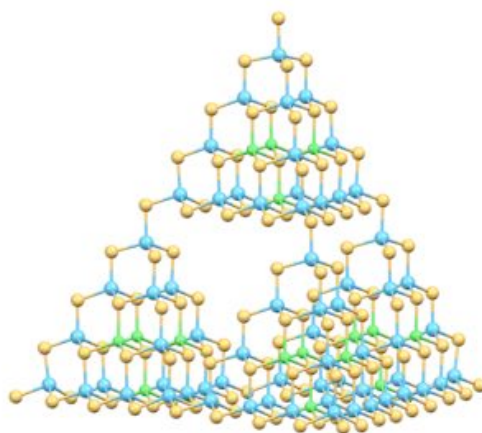


**Figure 1.4:** Hierarchical  $T_{4,2}$  cluster  $[\text{Cd}_{16}\text{In}_{64}\text{S}_{134}]^{44-}$  as an example of clusters with a void in the core; it can be viewed as four  $T_4$  units covalently-assembled into  $T_2$  cluster or as  $T_8$  cluster with the void of  $T_4$  size inside.<sup>61</sup>

The other set of clusters with a central void are *coreless* clusters, having in their otherwise regular  $T_n$  lattice a single metal tetrahedral site vacant, surrounded by four core  $E^{2-}$  ions. Examples are the solvothermally prepared coreless  $T_5$   $[\text{Cd}_6\text{In}_{28}\text{S}_{56}]^{12-}$  which are arranged in a covalently-bonded 2D superstructure<sup>64</sup> and coreless  $T_5$   $[\text{In}_{34}\text{S}_{56}]^{6-}$  which form a covalently-bonded 3D co-assembly with regular  $T_3$   $[\text{In}_{10}\text{S}_{18}]^{6-}$  units.<sup>65</sup> These large clusters with one metal cation missing appear since such a structure allows for a reduction in the coordination number of four inner chalcogenide anions from four to three, helping to maintain local electroneutrality. The void in as-prepared coreless clusters is occupied by various (highly disordered) guest species.<sup>64</sup> At the same time, a coreless structure provides a unique possibility for precise doping with carefully chosen metal cations (*e.g.*, by  $\text{Cu}^+$  or  $\text{Mn}^{2+}$ ), which was shown to change dramatically the photophysical properties versus the pristine metal chalcogenide frameworks.<sup>41,42</sup>

Similar to the main structural feature in coreless clusters that results from metal atom elimination, uncommon *stuffed* clusters can be viewed as a product of the addition of extra atoms to regular  $T_n$  frameworks. Recent examples of solvothermally prepared stuffed clusters include  $[\text{Sn}_{10}\text{S}_{20}\text{O}_4]^{8-}$  and  $[\text{Sn}_{10}\text{Se}_{20}\text{O}_4]^{8-}$  with extra oxygen atoms in each cubic cage of the  $T_3$  units (Figure 1.5); both S- and Se-containing analogues are covalently linked in co-assemblies of clusters of different sizes.<sup>66,67</sup> The formation of such oxychalcogenide units allows for the stabilization of a  $\text{Sn}^{4+}$ -containing  $T_3$  framework, which is otherwise unlikely to form: according to Pauling's electrostatic valence rule,  $\mu_3\text{-E}^{2-}$  sites don't match with tetrahedral  $\text{Sn}^{4+}$  sites and the largest possible supertetrahedral cluster in the pure system  $\text{M}_x^{4+}\text{E}_y$  is  $T_2$ .

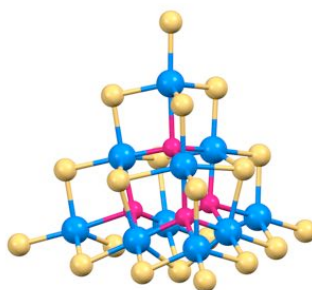


**Figure 1.5:** Stuffed supertetrahedral cluster  $[\text{Sn}_{10}\text{S}_{20}\text{O}_4]^{8-}$ : an extra O atom is present in each of the four cubic cages of the regular  $T_3$  unit.<sup>66</sup>

**Penta** supertetrahedral series clusters (denoted  $P_n$ ) are formed by coupling four  $T_n$  supertetrahedral units onto the faces of an anti-supertetrahedral unit of the same order. The central anti-supertetrahedral unit has the M and E positions exchanged in comparison to a regular one; *e.g.*, anti- $T_2$  unit has composition  $\{E_4M_{10}\}$  (Figure 1.6, top left). In this way,  $P_n$  clusters contain both cubic and hexagonal cages, and the latter appear on fused faces (Figure 1.6, top centre). Thus, in a  $P_1$  cluster four hexagonal cages are sharing a single tetrahedral E site, also each containing three M sites of the same  $\{EM_4\}$  unit. In a  $P_2$  cluster there are three hexagonal cages on each of four faces of anti- $T_2$  unit, twelve in total (Figure 1.6, top right).

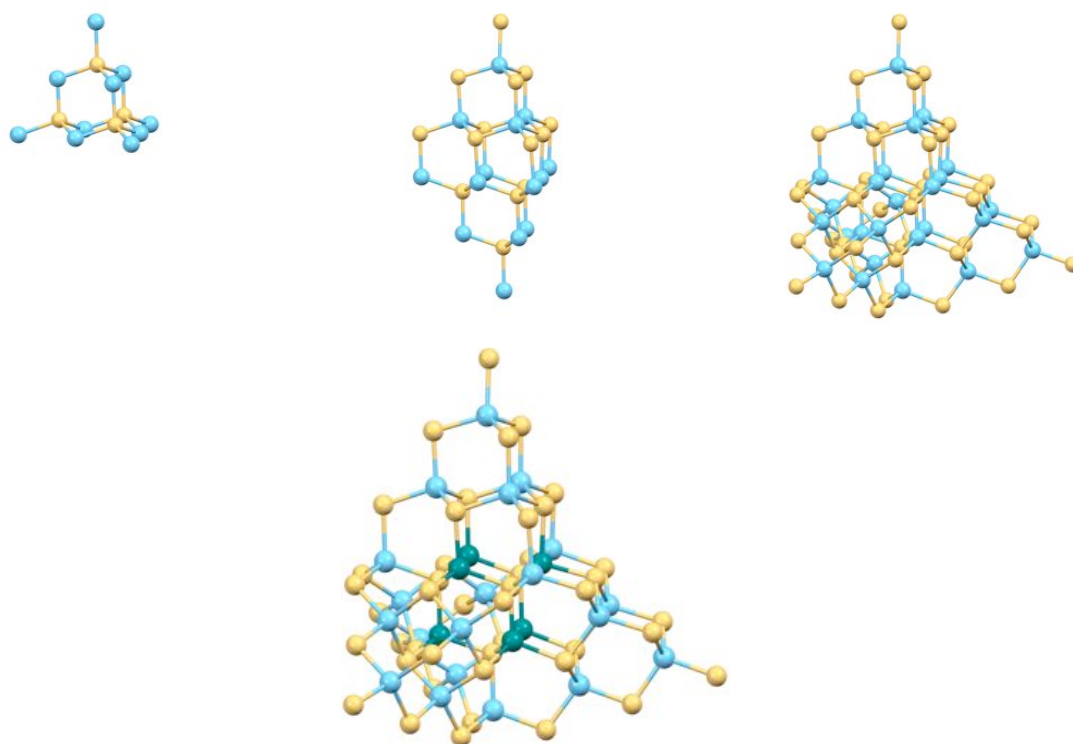


**Figure 1.6:** Anti- $T_2$  building unit with a composition  $\{E_4M_{10}\}$  (*top left*), in which the M and E positions are exchanged in comparison to a regular  $T_2$  unit  $\{M_4E_{10}\}$ . Face-to-face coupling of a  $T_2$  and an anti- $T_2$  supertetrahedral units (each containing a cubic cage) creates three hexagonal cages (*top centre*). Penta supertetrahedral cluster  $P_2$  (*top right*) can be viewed as a combination of four  $T_2$  units and one central anti- $T_2$  unit; partial occupancy of some sites by metals of different valence is ignored here. Anionic  $P_2$  cluster  $[Li_4In_{22}S_{44}]^{18-}$  (*bottom*) contains six inner metal sites with partial occupancy Li/In (shown as dark cyan) to satisfy Pauling's electrostatic valence rule.<sup>68</sup>

The structural relation between  $P_n$  and  $T_n$  with the same  $n$  is reflected in the composition of an idealized  $P_n$  core  $M_xE_y$  (see formulae in Table 1.1), as formulae can be derived using the known composition law for  $T_n$ . The largest solvothermally prepared penta supertetrahedral cluster  $P_2$  with composition  $[\text{Li}_4\text{In}_{22}\text{S}_{44}]^{18-}$  exhibits corner-sharing in a covalently-bonded 3D structure.<sup>68</sup> This large cluster contains four tetrahedrally coordinated  $\text{S}^{2-}$  sites, located in the central anti- $T_2$  unit. To satisfy Pauling's electrostatic valence rule, each such  $\text{S}^{2-}$  site should be surrounded by two  $\text{Li}^+$  and two  $\text{In}^{3+}$ , giving together a bond valence sum of +2. These two metals are statistically distributed over six symmetry equivalent inner metal sites (located in central anti- $T_2$  unit) with 2/3 occupancy by  $\text{Li}^+$  and 1/3 occupancy by  $\text{In}^{3+}$  (Figure 1.6, bottom).<sup>68</sup> In the discrete cluster of the same size  $P_2$ , prepared using a coordination chemistry approach,<sup>56</sup> a statistical distribution of  $\text{Cu}^+$  and  $\text{In}^{3+}$  cations over six symmetry equivalent inner metal sites was also found (Figure 1.2, centre). With four vertex metal positions in the central anti- $T_2$  unit, as well as four metal positions at  $P_2$  cluster vertexes solely occupied by  $\text{Cu}^+$ , results of elemental analysis are in a good agreement with the disordered model and a neutral formula  $[\text{Cu}_{11}\text{In}_{15}\text{Se}_{16}(\text{SePh})_{24}(\text{PPh}_3)_4]$ , featuring  $\text{PhSe}^-$  ligands on edges and  $\text{PPh}_3$  ligands at cluster vertexes.<sup>56</sup>

**Capped** supertetrahedral series clusters (denoted  $C_n$ ) consist of a core, which is a regular fragment of the cubic lattice, and four hexagonal (barrelanoid) cages capping the vertexes. Another way to view clusters of the  $C_n$  series, better showing their relation with  $T_n$  series, is as follows: a regular supertetrahedral unit  $T_n$  at the core is covered on each face with a single "layer" of vertex-sharing basic  $\{\text{ME}_4\}$  units (see Figure 1.7, top centre) and each vertex is completed by a  $\{\text{M}_4\text{E}_4\}$  group to form a hexagonal cage. In this way, the composition of an idealized  $C_n$  core can be derived using formulae for  $T_n$  with the same  $n$  (Table 1.1). The structural feature of  $C_n$  clusters is the open cleft that runs along each of the tetrahedral edges (see Figure 1.7, bottom). Like in  $T_n$  clusters, the number of E sites in a  $C_n$  cluster is equal to the number of M sites in the next larger  $C_{(n+1)}$  in the series. In  $C_n$  clusters, each hexagonal cage (more precisely, a  $\text{M}_4\text{E}_5$  unit) at one of four vertexes can also be independently rotated (around the threefold axis of the tetrahedron) by  $60^\circ$ . This results in additional variation (isomerism) in the capped supertetrahedral series, denoted as  $C_{n,m}$  where  $m$  refers to the number of corners that have been rotated from their original position in the parent  $C_n$ . This variant does not usually change either cluster or

superstructure properties significantly, so vertex rotation will not be mentioned below while referring the cluster type and size. Discrete capped supertetrahedral clusters with sizes up to  $C_3$  were synthesized solvothermally; some examples are  $[\text{Cd}_{54}\text{S}_{32}(\text{SPh})_{48}(\text{H}_2\text{O})_4]^{4-}$  (Figure 1.2, right),  $[\text{Cd}_{54}\text{Se}_{32}(\text{SPh})_{48}(\text{H}_2\text{O})_4]^{4-}$  (Figure 1.7, bottom).<sup>57</sup> The core of these  $C_3$  clusters is formed by ten tetra-coordinated cadmium and twenty tetra-coordinated chalcogenide sites in a cubic arrangement (forming a regular  $T_3$  unit) (Figure 1.7, top left). The inner tetrahedron is covered on each face with seven  $\{\text{CdE}_4\}$  units fused through vertexes by rows 2-3-2 to form a single cubic sheet (Figure 1.7, top centre), resulting in four times three  $\mu_3\text{-E}^{2-}$  sites (twelve in total). Capping each vertex with a hexagonal cage (Figure 1.7, top right) increases the number of edge  $\mu\text{-PhS}^-$  sites to eight per each of the six edges (forty-eight in total).

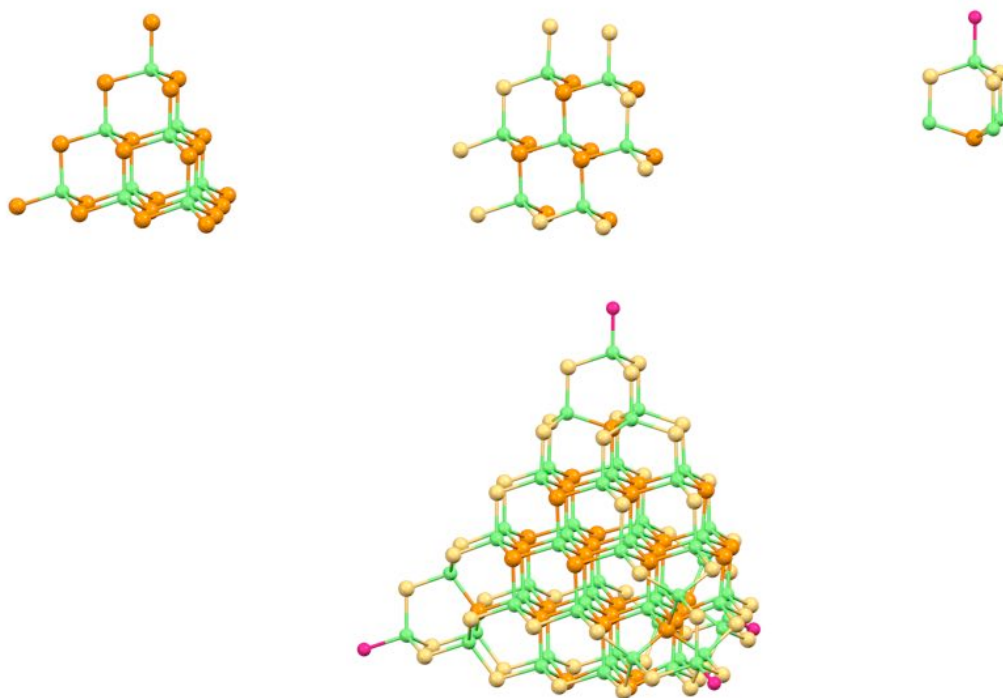


**Figure 1.7:** The core  $T_3$  unit (*top left*), a single cubic sheet (*top centre*) that covers each face of the central tetrahedron and a hexagonal cage (*top right*) that caps each vertex in the  $C_3$  cluster  $[\text{Cd}_{54}\text{Se}_{32}(\text{SPh})_{48}(\text{H}_2\text{O})_4]^{4-}$  (*bottom*). The open cleft along each of the six edges of the tetrahedral  $C_3$  cluster is formed by S (shown as yellow-orange spheres) and Cd (green) atoms. Carbon atoms of  $\text{PhS}^-$  ligands are omitted for clarity.<sup>57</sup>

From the description above it can be seen that in the vast majority of these tetrahedral clusters the number of E sites exceeds the number of M sites; this follows from having the tetrahedral  $\{ME_4\}$  unit as a building block. The presence of an inner anti- $T_n$  unit (derived from a  $\{EM_4\}$  unit) in the structure of  $P_n$  clusters series is an exception. Interestingly, the preparation and structural characterization of several large tetrahedral “quantum dots” with crystalline CdSe cores corresponding entirely to anti- $T_n$  clusters was recently reported.<sup>69</sup> The metal chalcogenide core structure with unusual metal-terminated  $\{111\}$  facets was derived using a combination of single and powder X-ray diffraction data, and atomic pair distribution function analysis. These quantum dots have approximate formulae  $Cd_{35}Se_{20}X_{30}L_{30}$ ,  $Cd_{56}Se_{35}X_{42}L_{42}$ ,  $Cd_{84}Se_{56}X_{56}L_{56}$  with benzoate and *n*-butylamine ligands ( $X = O_2CPh$ ,  $L = H_2N-Bu$ ), and can be viewed as anti- $T_4$ , anti- $T_5$ , and anti- $T_6$ , respectively.

#### 1.2.4 Ligands on Tetrahedral Clusters

Some metal chalcogenide clusters, such as those with groups 13 and 14 metals, may be prepared as purely inorganic (anionic) frameworks. This is in accordance with Pauling’s electrostatic valence rule, as tetrahedrally coordinated  $M^{3+}$  or  $M^{4+}$  cations can balance edge or corner  $E^{2-}$  anions with low coordination numbers. For metal chalcogenide clusters with surface  $M^{2+}$  sites, the sum of the strengths of the electrostatic bonds to edge or vertex  $E^{2-}$  sites is too low to reach local electroneutrality. To overcome this, the coordination numbers of such  $E^{2-}$  sites are found to increase. In other words, clusters require the incorporation of an encapsulating and stabilizing shell of organic ligands. The ligands on a metal chalcogenide core also kinetically protect the cluster and prevent further condensation to the thermodynamically favoured infinite crystalline lattice of the related solid. Organic ligands serving in this capacity include various phosphines  $PR_3$ , amines (especially, N-containing aromatic heterocycles), halides (Hal), and organochalcogenolate anions  $RE^-$ .<sup>6,9</sup> While the majority of these ligands replace surface  $E^{2-}$  sites, creating M–P, M–N, and M–Hal coordination, chalcogenolates at edges and vertexes do not alter the  $M_xE_y$  stoichiometry of the idealized cluster core. For chalcogenolate ligands the most common bonding mode is the doubly bridging  $\mu$ ; triply and higher bridging coordination modes are more often observed for selenolate and tellurolate ligands than for thiolates, reflecting their larger size. In discrete metal

chalcogenide systems with mixed ligands, bridging chalcogenolate ligands preferentially occupy edge positions, while other ligands are bonded to metals at vertex positions.

In coordination chemistry approaches for cluster formation, the use of coordinating and chelating solvents to increase the solubility of reactants and/or products simultaneously can lead to the preparation of metal chalcogenide clusters containing solvent molecules as ligands (*e.g.*, pyridine, *dmf*).<sup>70,71</sup> Higher reactivity under solvothermal or ionothermal conditions may also cause some side reactions to occur. Consequently, products of the decomposition/conversion of solvent (or additive) may serve as ligands. Examples include the coordination of dimethylamine from DMF; piperidine from dipiperidinomethane and 1-butyl-2-methyl-imidazole, Bim, from 1-butyl-2,3-dimethylimidazolium chloride, [Bmmim]Cl.<sup>44,49,72,73</sup> An interesting case of ligand conversion during hydrothermal synthesis is the hydrolysis of the cyano group of 3-pyridinecarbonitrile, which resulted in the preparation of the 1D covalently bonded clusters [Zn<sub>8</sub>S(SPh)<sub>13</sub>L(H<sub>2</sub>O)], with bidentate L = 3-carboxypyridyl bridging two adjacent clusters *via* M–N and M–O coordination (Figure 1.8).<sup>74</sup> Another possibility for “by-product” ligands to appear in the coordination sphere of metals is from the reaction of solvent with some precursor (*e.g.*, MeOCS<sub>2</sub><sup>–</sup> ligand formed from reaction of MeOH and CS<sub>2</sub>, used as sulfur source).<sup>75</sup> The concept of intentional ligand modification during the assembly of metal chalcogenide clusters *via* solvothermal and ionothermal approaches has been developed recently, aiming at broadening the range of possible ligands and gaining access to new moieties that are unreachable under milder synthetic conditions. In this vein, a C–S cross-coupling reaction under hydrothermal conditions was systematically studied for *in situ* ligand reactions between mono halide-substituted pyridines (L = Hal–C<sub>5</sub>H<sub>4</sub>N) and thiophenol during the preparation of [Zn<sub>8</sub>S(SPh)<sub>14</sub>L<sub>2</sub>].<sup>76</sup> Varying the nature and position of the halide substituent allowed to observe that ligands containing iodine as a substituent were, unexpectedly, unreactive under the conditions explored, despite the fact that iodide is the best leaving group in comparison to F<sup>–</sup>, Cl<sup>–</sup>, or Br<sup>–</sup>. The lack of reactivity of iodide-substituted pyridines was attributed to the higher energy barrier for iodide elimination during the hydrothermal process in comparison to the other halide-substituted pyridines. It was also found that with a ligand containing the substituent in the ortho-position, no crystalline product was obtained, whereas the use of ligands with substituents in meta- and para- positions (*e.g.*, 3-chloropyridine and 4-



chloropyridine) led to the crystallization of clusters with *in situ* prepared ligands at the vertexes ( $L = m\text{-C}_6\text{H}_5\text{SC}_5\text{H}_4\text{N}$  and  $p\text{-C}_6\text{H}_5\text{SC}_5\text{H}_4\text{N}$ , respectively). Such selectivity was attributed to the spatial hindrance induced by the cluster  $[\text{Zn}_8\text{S}(\text{SPh})_{14}\text{L}_2]$ . Overall, the successful one-pot-synthesis of clusters with tailored ligands demonstrates the potential of *in situ* ligand-generating reactions under solvothermal and ionothermal conditions in constructing functional metal chalcogenide clusters, simultaneously building a new bridge between coordination chemistry and synthetic organic chemistry.

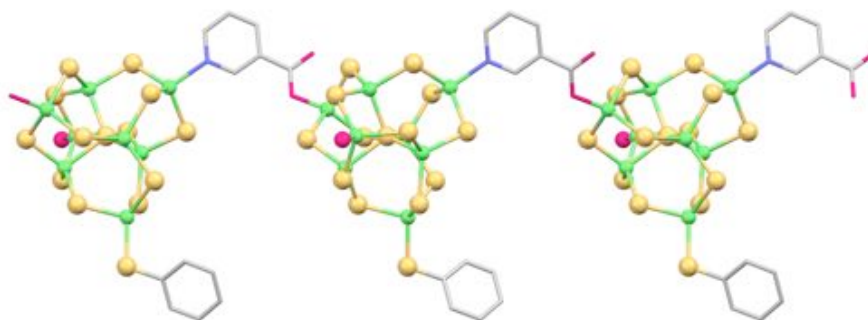


**Figure 1.8:** A fragment of the 1D covalently bonded cluster chain of  $[\text{Zn}_8\text{S}(\text{SPh})_{13}\text{L}(\text{H}_2\text{O})]$  with  $L = 3\text{-carboxypyridyl}$ , a bidentate ligand formed *in situ* by hydrolysis of the cyano group of 3-pyridine-carbonitrile. Carbon atoms of  $\text{PhS}^-$  ligands, except the one on the cluster vertex, are omitted for clarity.<sup>74</sup>

The selection and *in-situ* design of ligands provides potential to modify metal chalcogenide clusters on several levels, tailoring cluster size and composition by adjusting the coordinating ability of the ligands and regulating superstructure topology by changing cluster-cluster interactions. The later can be illustrated on the example of the neutral  $\text{C}_2$  clusters  $[\text{Cd}_{32}\text{S}_{14}(\text{SR})_{36}\text{L}_4]$ , where R is either the phenyl<sup>70</sup> or the 2-hydroxypropyl<sup>77</sup> group, and L is *dmf* or water, respectively. The strong influence of ligands on the superstructure packing is such that the thiophenolate-stabilized  $\text{Cd}_{32}$  clusters crystallize into cubic superstructure (space group  $P32$ ) sustained by van der Waals ligand-ligand intercluster interactions, whereas the thiopropanol-stabilized  $\text{Cd}_{32}$  clusters crystallize into a double layer superstructure (space group  $R-3$ ) with a continuous network of hydrogen bonding. As another important function, an increased solubility of clusters due to the presence of organic surface ligands (especially those with modified properties, such as fluorinated ligands)<sup>78-80</sup> can also enhance the crystallization of clusters into superlattices.<sup>81</sup> The recent preparation of various mononuclear metal complexes with the perfluorinated

chalcogenolate ligands<sup>82,83</sup> that potentially can be used as precursors for the large clusters synthesis, lays the foundation for future progress in this field.

Ligands are also known to influence the photophysical properties of metal chalcogenide clusters. For instance, phenylchalcogenolate ligands were reported to quench CdE clusters emission at room temperature, which was attributed to existence of non-radiative relaxation mechanism that involves vibrating modes of the bridging  $\mu$ -PhE<sup>-</sup> ligands.<sup>20</sup> In contrast to this, the replacement of PhE<sup>-</sup> by Hal<sup>-</sup> ligands results in red shifts and significant enhancements of the emission<sup>84</sup> and absorption<sup>85</sup> peaks. Moreover, optical properties of clusters can be affected by trapping of organic species in ligand shell *via* cation- $\pi$  interactions,<sup>86</sup> that may potentially be used in various sensing systems. Generally, electronic and photophysical properties of smaller clusters were found to be more sensitive to changes in ligand shell. The influence of ligands becomes less pronounced with increasing cluster sizes, as it was observed experimentally and confirmed by theoretical calculations on DFT and TDDFT level for tetrahedral clusters belonging to different series (see, for example, ref. 87). The incorporation of ligands with special functionality (such as those containing ferrocene derivatives) can also introduce electrochemical functionality onto the clusters.<sup>88-90</sup> Ligand exchange reactions provide even more opportunities for tailoring metal chalcogenide clusters; the approach was proven to be efficient for the preparation of neutral Cd<sub>10</sub>E<sub>x</sub> clusters with dendritic thiolate ligands<sup>91</sup> or with poly(ethylene glycol) units directly attached to the core,<sup>92</sup> featuring high solubility in organic solvents and water, respectively, as well as modified photophysical properties.

### 1.2.5 Non-Tetrahedral Clusters

Non-tetrahedral clusters possess diverse frameworks and have no obvious structural similarity with the corresponding bulk crystalline metal chalcogenides.<sup>6,9</sup> In this chapter (see Sections 1.5.5 and 1.5.6) the focus will be on the discrete assemblies where basic tetrahedral {ME<sub>4</sub>} units are joined together into polymeric fragments through sharing of vertexes and/or edges so as to form one or several rings. For instance, large, “double-decker” rings and complex cages have been prepared recently using solvothermal and ionothermal approaches. Metal cations here belong to groups 13 (In<sup>3+</sup>) and 14 (Ge<sup>4+</sup>, Sn<sup>4+</sup>), or transition metals (Mn<sup>2+</sup>) and E is a heavier (Se, Te) chalcogen. Such clusters can

be viewed as molecular analogs of polymeric 1D chains,<sup>93,94</sup> typical for compounds of groups 13 and 14 elements, and more unusual 1D ribbons,<sup>95</sup> also prepared under solvothermal and ionothermal conditions. Complex vertex-linkage or the co-existence of vertex- and edge-linked basic tetrahedral  $\{ME_4\}$  units was previously also found in some 3D metal chalcogenides.<sup>96,97</sup> The tendency of the repeating fragments, composed of linked  $\{MSe_4\}$  or  $\{MTe_4\}$  units, to cyclize can be attributed to the larger atomic size and, as a consequence, the higher structural flexibility of  $Se^{2-}$  and  $Te^{2-}$  in comparison with  $S^{2-}$ . These clusters are typically charge-balanced, templated and stabilized by bulky imidazolium-based cations or other organic amines (see Section 1.5.6).

### 1.3 Bonding in Materials Containing Metal Chalcogenide Clusters

#### 1.3.1 Bonding in Cluster Superstructures

Crystalline solids containing spatially organized metal chalcogenide clusters can be categorized into several classes depending on the nature of the bonding in the superstructure. Clusters may form covalently linked “continuous” frameworks of various types (*i.e.*, 3D networks, 2D layers, or 1D chains) or, alternatively, with an absence of such interconnected species, metal chalcogenide clusters are “isolated” or “discrete” (0D) in their crystalline superstructures.

The covalent linkage of clusters can be realized through inorganic bridges (most often, corner-sharing clusters connected at vertexes with a single  $E^{2-}$  or  $RE^-$  bridge)<sup>98,99</sup> or through the use of organic multidentate ligands (*e.g.*, bi- or even tetradentate tetrahedral linkers).<sup>100–102</sup> In some superstructures, both inorganic and organic connectivities can coexist,<sup>103</sup> and such covalent linkages can also be realized *via* more unusual species, *e.g.*, metal complexes.<sup>104,105</sup> Superstructures with covalent linkages between tetrahedral clusters have been extensively studied and several reviews were published.<sup>47,48</sup> They are not the main subject of this review and only selected cases (featuring exceptional clusters, prepared under solvothermal or ionothermal conditions) are discussed in the following sections. Large tetrahedral metal chalcogenide clusters (*e.g.*,  $T_4$  and  $T_5$ ), covalently linked into superstructures, are well established, while the preparation of the corresponding discrete analogues remained a formidable challenge until recently.

An interesting type of bonding in such superstructures is realized when metal chalcogenide clusters form dimers, *i.e.*, two clusters are linked *via* covalent bonds, and then such dimers are self-assembled into a non-covalent superstructure. This type of bonding of two clusters was achieved, for example, under solvothermal conditions using 1,2-di(4-pyridyl)ethylene (*dpe*) ligands as the organic linker, covalently bonding two vertices of two  $T_3$  clusters (Figure 1.9).<sup>106</sup> In each “half” of such  $T_3$ - $T_3$  two-cluster anion  $[\text{Ga}_{10}\text{S}_{17}\text{HL}_2\text{-dpe-Ga}_{10}\text{S}_{17}\text{HL}_2]^{6-}$ , the remaining two vertexes are terminated by  $L = 3,5$ -dimethylpyridine, while the fourth vertex contains a  $\text{SH}^-$  anion. Total electroneutrality is achieved *via* 3,5-dimethylpyridinium cations. The self-assembly into a non-covalent superstructure (space group  $P-1$ ) is realized through  $\pi$ - $\pi$  interactions between aromatic rings and  $\text{N-H}\cdots\text{S}$  hydrogen bonding between protonated organic cations and surface S atoms in clusters. Even more sophisticated coupling is realized in solvothermally prepared crystalline solids containing a  $C_1$ - $C_1$  two-cluster neutral component, double-bridged by the more flexible bifunctional organic ligand 1,3-di(4-pyridyl)propane (*dpp*)  $[\text{Cd}_{17}\text{Se}_4(\text{SPh})_{26}\text{-}(\textit{dpp})_2\text{-Cd}_{17}\text{Se}_4(\text{SPh})_{26}]$  (Figure 1.10).<sup>107</sup> Such dimers are subsequently assembled into a non-covalent superstructure (space group  $P2_1/c$ ). Non-covalent superstructures, containing cluster dimers, allow the intercluster connectivity with organic linkers to adjust system performance (through the combination of the size-related properties of nanodimensional clusters with functionality of bifunctional ligands), at the same time preserving the solubility of individual components.

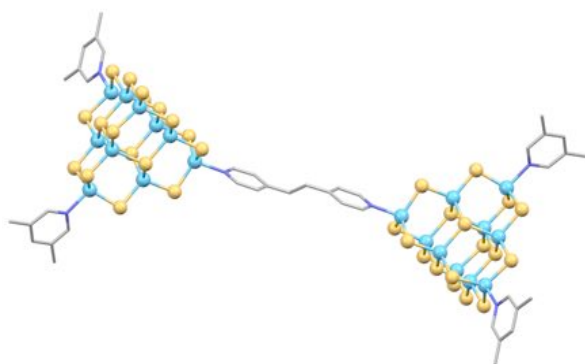


**Figure 1.9:** Two-cluster anion  $[\text{Ga}_{10}\text{S}_{17}\text{HL}_2\text{-dpe-Ga}_{10}\text{S}_{17}\text{HL}_2]^{6-}$ , where  $L = 3,5$ -dimethylpyridine.<sup>106</sup>

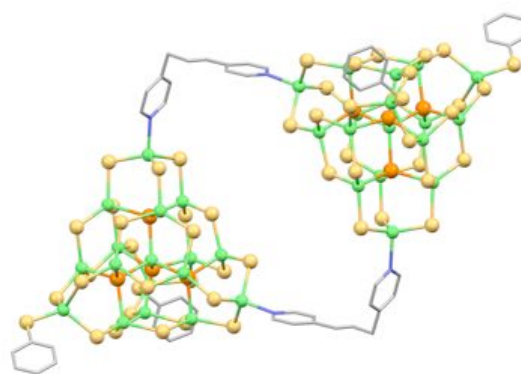


**Figure 1.10:** Two-cluster doubly-bridged neutral aggregate  $[\text{Cd}_{17}\text{Se}_4(\text{SPh})_{26}\text{-}(\textit{dpp})_2\text{-Cd}_{17}\text{Se}_4(\text{SPh})_{26}]$ . Carbon atoms of  $\text{PhS}^-$  ligands, except those on vertexes, are omitted for clarity.<sup>107</sup>

As opposed to covalent intercluster bonding, metal chalcogenide clusters can be considered as being discrete molecular entities when the superstructure is formed only *via* electrostatic bonding and/or other cluster-cluster interactions, *e.g.*, hydrogen bonding and dispersion (van der Waals) forces. In such cases, the superstructures of metal chalcogenide clusters can be referred to as molecular crystals.<sup>21</sup> Such superstructures of smaller clusters prepared by a coordination chemistry approach are especially well documented.<sup>70,77,108–117</sup> In contrast, the preparation of progressively larger, discrete metal chalcogenide clusters (with several composition restrictions related with maintaining both local and total electroneutrality, in addition to low solubility of formed clusters) requires special conditions for superlattice formation. Recent successes (*e.g.*, a superlattice of discrete “full-core” T<sub>5</sub> clusters)<sup>43,44</sup> are closely connected with developing solvothermal and ionothermal approaches together with a better understanding of the role of various factors associated with these synthetic routes.

Since anionic clusters dominate this area, discrete ionic superstructures are most likely to form. Less common, neutral metal chalcogenide clusters, typically with phenylchalcogenolate ligands and/or aromatic ring(s)-containing structure-directing and stabilizing species, can form discrete superstructures through relatively weak ligand-ligand and ligand-template-ligand interactions. The intercluster bonding (for instance, hydrogen or  $\pi$ - $\pi$  interactions) is such that connection between the building blocks into a superstructure is reversible.<sup>118–121</sup> The key factor is whether superstructure disassembly (*e.g.*, *via* dissolving in a suitable solvent) would be possible in such a way that the core and ligand shell of individual clusters does not change. Several cases of complete re-crystallization of superstructures consisting of large discrete clusters were reported under relatively mild solvothermal conditions. Disassembly of the crystalline solid, while clusters went into solution at elevated temperature and pressure, was followed by recurring superstructure formation upon cooling.<sup>41,122</sup>

The solubility of the discrete large tetrahedral clusters broadens their potential for application, making possible, for instance, solution processing to achieve new advanced materials. Thus, mesostructured materials and even porous gels and aerogels were prepared using small metal chalcogenide clusters (*e.g.*, [Ge<sub>4</sub>S<sub>10</sub>]<sup>4-</sup>) as building blocks; such materials may be useful in photocatalysis or in the removal of heavy metals from

water.<sup>123</sup> The production of semiconductor-doped thin film materials for optics and electronics has also been proposed.<sup>70</sup> Thus, polyvinylcarbazole films, functionalized by  $[\text{Cd}_{32}\text{S}_{14}(\text{SPh})_{36}(\text{dmf})_4]$ , can be spin-coated from a pyridine solution.

The nature of the bonding in superstructures is known to influence the physical properties of cluster assembly. In some cases, the effect of connectivity of the clusters is less pronounced in comparison with the effect of cluster size and composition, as it can be followed, for example, for the optical properties of the systems.<sup>41,49</sup> In other cases, these (inter)cluster features are found to be of comparable importance: it was shown that the photocurrent response of solvothermally prepared material containing a 3D covalent framework of  $[\text{Cd}_{32}\text{S}_{14}(\text{SPh})_{40}]^{4-}$  clusters (corner-sharing through  $\text{PhS}^-$  ligands) synthetically integrated with a metal-complex dye is seven times larger than that of the material where the identical clusters are discrete. This was attributed to the facilitated transfer of photo-induced electrons in the 3D framework.<sup>75</sup>

### ***1.3.2 Topology of Superstructures***

For topological consideration on the level of superstructure it is convenient to view each tetrahedral cluster as a tetrahedral pseudo-atom (T) or, alternatively, to consider only the positions of the barycentres of the clusters. The covalent linkage of four-vertexes-connected tetrahedral clusters (often realized by a single  $\text{E}^{2-}$  bridge) is known to give a limited number of topologies for 3D superstructures,<sup>47</sup> which is related to the limited flexibility of the T–E–T angles.<sup>46,124</sup> The common topological types for covalently linked large tetrahedral clusters are (cubic) single and double diamond, as well as cubic carbon nitride. In the latter, four-connected clusters are combined with tri-connected  $\text{S}^{2-}$  sites that bridge the corners of three adjacent clusters.<sup>125</sup> The covalent linkage of tetrahedral clusters with auxiliary organic ligands L, most often pyridyl-based ones, helps to increase the flexibility of the T–L–T connection, which potentially broadens the range of the possible topologies. The cluster connectivity in such cases rarely reaches four and the coordination polymers are most often prepared as 1D and 2D superstructures. An exception is a series of 3D four-connected covalent superlattices where  $\text{T}_3$  or  $\text{T}_4$  units are linked by imidazolate ligands.<sup>126</sup>

The wide variety of the nature and relative weakness of interactions leading to the formation of superstructures from discrete clusters leads to the remarkable diversity in connectivities and makes it more difficult to generalize corresponding topological types. Various distortions also complicate this assignment. For instance, considering the barycentre positions, superlattices with distorted cubic diamond and hexagonal diamond topologies have been often reported for large anionic tetrahedral clusters (Figure 1.11) (*e.g.*, see ref. 44). This means, that intra- and inter-cluster connectivities are the same, and the clusters behave like artificial atoms in zinc blende- and wurtzite-like crystal structures.

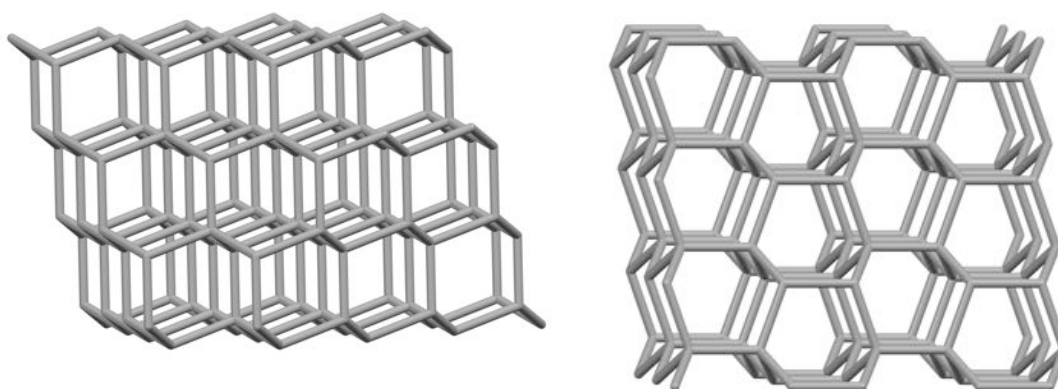


**Figure 1.11:** Examples of 3D superstructure topologies formed from discrete tetrahedral clusters: idealized cubic diamond (*left*) and hexagonal diamond (*right*) superstructures. Clusters are not shown; lines are connecting the barycentres of the clusters.

Unlike 2D and 3D covalent superstructures formed *via* corner-sharing through inorganic linker, where topologies combining two tetrahedral clusters of different size, structure or composition are not that rare (*e.g.*,  $P_1$ - $T_2$ ,  $T_2$ - $T_5$ , or  $T_{2,2}$ - $T_3$  hybrid covalent superstructures),<sup>58,62,65,127–129</sup> there is a limited number of examples of superstructures combining two different discrete clusters. Thus, ionic superstructure with a cubic  $[Cd_8L_{12}(NO_3)(dmf)_8]^{3+}$  cluster as a cation and a dumbbell-shaped  $[Cd_6L_{14}]^{2-}$  cluster as an anion ( $L = 2,5$ -dimethylphenylthiolate) was prepared under ambient conditions.<sup>130</sup> Even more unusual cases of two-cluster-anions superstructures *via* solvothermal preparation (*e.g.*, co-crystallization of tetrahedral  $T_4$   $[Cu_4In_{16}S_{35}H_4]^{14-}$  and cubic  $[Cu_{12}S_8]^{4-}$  discrete anionic clusters)<sup>122</sup> are considered below.

In the superstructures of neutral discrete clusters multi-level organization often takes place with the participation of several different interactions. Thus neighbouring clusters may be arranged into layer-like formation *via* intercluster N–H···E or C–H···E hydrogen bonding, with such layers further combined into superstructure through van der Waals forces.<sup>131</sup>

### 1.3.3 Total Electroneutrality in Superstructures

As opposed to the local electroneutrality, *total electroneutrality* (global charge balance) refers to the overall charge density match between clusters and charge balancing species. As was discussed above, local electroneutrality generally follows the Pauling's electrostatic valence rule, making relatively straightforward calculations possible (*e.g.*, using Brown's bond valence model)<sup>132,133</sup> to explain/predict the arrangement of metal cations of different valence in particular cluster. In contrast, with total electroneutrality there are many different factors (among them, partial atomic charges on cluster core atoms and protonation ability of charge balancing species) to be taken into account simultaneously, making any attempt of its quantitative representation more difficult. Thus, an additional stabilization of superstructures assembled *via* electrostatic (Coulomb) forces can be achieved while charge-balancing species are also capable of other interactions with clusters, *e.g.*, N–H···E and C–H···E hydrogen bonding,  $\pi$ - $\pi$ , anion- $\pi$  and hydrophobic interactions. Aromatic quaternary ammonium cations and protonated organic amines are most important in this capacity. Some effects related with maintaining total electroneutrality are discussed below.

Even in solvothermally prepared covalently bonded 3D and 2D superstructures of clusters, where charge balancing species are most often highly disordered, alternating the charge balancing cations was reported to cause changes in cluster arrangement, varying from different unit cell parameters to the different packing of clusters in a superstructure. For instance, use of the larger Et<sub>4</sub>N<sup>+</sup> cation instead of Me<sub>4</sub>N<sup>+</sup> results in a change of stacking pattern for the 2D covalently bonded superstructure of T<sub>5</sub> clusters [Cu<sub>5</sub>In<sub>30</sub>S<sub>54</sub>]<sup>13-</sup> (space groups *Pm* and *C2/c*, respectively).<sup>134</sup> It was proposed that even small quaternary alkyl ammonium cations may show structure-directing effect in addition to charge compensation. Different protonated organic amines with well known structure-directing



ability may display even more remarkable effects: thus, under the same synthetic conditions the addition of dipiperidinomethane instead of 1,4-bis(3-aminopropyl)piperazine leads to the solvothermal preparation of a 3D covalent superstructure of two clusters,  $T_3$  and coreless  $T_5$  as  $[\text{In}_{10}\text{S}_{20}]^{10-}$  and  $[\text{In}_{34}\text{S}_{56}]^{10-}$ , respectively, versus that of the single  $T_4$  cluster as  $[\text{Zn}_4\text{In}_{16}\text{S}_{35}]^{14-}$  (space groups  $I4_1/a$  and  $I4_1/acd$ ).<sup>65,135</sup> It is interesting that a source of a  $M^{2+}$  *d*-block metal is present in the reaction mixtures probed with all amines, but  $M^{2+}$  only becomes incorporated into  $T_4$  clusters. The formation of superstructures with substantially different charge densities (the overall framework negative charge per metal site is -0.273 vs. -0.5 for  $T_3$ -coreless  $T_5$  and  $T_4$ , respectively) was discussed in terms of the charge densities of the incorporated protonated amine molecules, approximated by their C/N ratio (5.5 vs. 2.5 for dipiperidinomethane and 1,4-bis(3-aminopropyl)piperazine, respectively). Such an approximation is rough and cannot be generalized; for instance, the same 3D covalent superstructure of  $T_4$  clusters  $[\text{Zn}_4\text{In}_{16}\text{S}_{35}]^{14-}$  (space group  $I-42d$ ) was also reported with other protonated amine species, including 4,4'-trimethylenedipiperidine which has a C/N ratio of 6.5.<sup>135</sup>

In superstructures containing discrete clusters, additional interactions helping to stabilize negative charges are of even greater significance. Their assembly may depend to a large extent not only on the electrostatic interactions, but on hydrogen bonding as well. Though  $\text{N-H}\cdots\text{S}$  or  $\text{N-H}\cdots\text{Se}$  hydrogen bonding is weaker in comparison with  $\text{N-H}\cdots\text{O}$  that is known to direct the assembly of oxide frameworks (*e.g.*, zeolites), charge-balancing protonated organic amines in 0D superstructures of metal chalcogenide clusters are often found to be ordered and shown to play an important role in cluster formation and crystallization. A close match of charge density, geometry and additional interactions should exist between anionic clusters and cationic species in superstructures to make the formation of particular discrete clusters more favourable. The preparation of covalently bonded 3D frameworks is typically more tolerant of small variations in the size and shape of amines. For example, varying the protonation ability or steric hindrance by using similar amines (piperidine derivatives and related compounds) under the same solvothermal conditions was shown to result in the formation of different superstructures.<sup>49</sup> Thus, comparing of *o*-, *m*- and *p*-methyl piperidines with the unsubstituted one indicates that the substituent in the *p*-position gives a superstructure of

discrete  $T_4$  clusters  $[Zn_4Ga_{14}Sn_2Se_{35}]^{12-}$  with a significantly larger unit cell parameter (19.2020(3) Å vs. 18.8951(1) Å for substituted and unsubstituted piperidine, respectively; space group  $I-43m$ ). The weaker bonding in the superstructure containing protonated *p*-methyl piperidine is reflected, for instance, in the faster dissolution rate and increased solubility of the product, as well as in its band gap change. Both *o*- and *m*-methyl piperidines lead to the formation of related 3D covalently bonded  $T_4$  clusters (space group  $I4_1/acd$ ) as minor and exclusive products, respectively. It was concluded that *m*-position substitution creates the highest steric hindrance in comparison with *o*- or *p*-positions, not allowing such an arrangement of protonated amines around the discrete cluster while hydrogen bonding allows for additional stabilization.<sup>49</sup>

#### 1.4 Synthetic Approaches: Solvothermal and Ionothermal Routes

Generally, a solvothermal approach refers to conducting reactions in an appropriate solvent with the aid of suitable additives in a sealed vessel at elevated temperature and autogenous pressure. If the process is done in water, the process is differentiated as hydrothermal, and in the case of other (organic) solvents it is referred to as solvothermal. Some organic solvents widely used for the preparation of metal chalcogenide clusters are methanol, acetonitrile, DMF, and organic amines. The importance of the last (*e.g.*, N-containing aromatic heterocycles) as solvents and additives is related to the fact that organic amines can act as ligands, stabilizers and (in a protonated form) charge-balancing species for large anionic metal chalcogenide clusters. The most recently explored variation, ionothermal process, utilizes more thermally and chemically stable ionic liquids as a reaction medium. Reaction vessels may vary from sealed thick-walled glass tubes to stainless steel autoclaves with an inert lining or inner container; a combination of the sealed in glass tube with an autoclave with some liquid for counter pressure is also possible. Under solvothermal conditions a supercritical state can be achieved, when the liquid-vapour boundary disappears and the fluid achieves properties of both the liquid and the gas though for many reactions it is not necessary and rarely applied.

In a typical solvothermal or ionothermal process, the reagents are mixed with suitable additives in a chosen reaction medium, and heated to moderately-high temperature for a

period of time from several hours to several days, cooled to room temperature with a desired rate, and product(s) are isolated. Syntheses of metal chalcogenide clusters by these approaches are typically performed as small scale reactions (product weight from tens to hundreds mg). Reported yields (% based on a metal source used) may vary, although generally being higher for smaller clusters (*e.g.*, ~65% for  $P_1$ <sup>74,136</sup> or even ~90% for  $T_3$ <sup>106</sup>) and decreasing for larger systems. Optimization of reaction conditions (such as alternating metal or chalcogen source, addition of auxiliary solvents, changing reaction time or temperature)<sup>44,59</sup> helps to enhance product purity and yield, though fragmentary data available from the literature do not allow for an accurate generalization.

Although smaller metal chalcogenide clusters may be used as precursors for solvothermal or ionothermal conversion into larger ones,<sup>137,138</sup> the synthesis often starts with simple elementary forms and inorganic salts, and involves redox chemistry for cluster formation. Various clusters with different sizes and composition can be present in solution simultaneously, while upon cooling and crystallization equilibrium shifts in favour of one (or more) product(s). In comparison with a solid state chemistry approach, where performing the reactions in molten media (*e.g.*, polychalcogenide flux) requires high temperatures (> 300 °C, often 500-650 °C), the solvothermal approach offers a significant reduction in the reaction temperatures (typically  $\leq 200$  °C). The flexibility of the solvothermal approach also allows an adaption to large-scale synthesis or a combination with other techniques, *e.g.*, microwave-assisted synthesis. The combination of elevated temperature and pressure during solvothermal synthesis often allows increased solubility of precursors, promoting diffusion in reaction mixtures, improving selectivity of conversion, speeding up reactions, and facilitating crystallization of the product. Performing such synthesis in ionic liquids shares some advantages with those done in traditional organic solvents (solvothermal approach), where reaction media may simultaneously act as a structure-directing agent and as a template. In this vein, ionic liquids with voluminous quaternary ammonium and imidazolium-based cations are of particular interest.<sup>37,139</sup> At the same time, the negligible vapour pressure of ionic liquids makes the use of autoclaves (and associated equipment cost and safety measures) unnecessary. Generally, reaction pathway and outcome may be quite different under

solvothermal and ionothermal conditions, and selection of the particular synthetic approach for each system depends on multiple factors.

## 1.5 Structures of Materials Containing Metal Chalcogenide Clusters

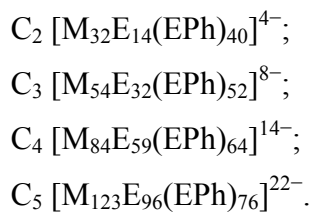
### 1.5.1 General Comments

As was described above, there are certain limitations and conditions for metal chalcogenide cluster formation related to maintaining local and total electroneutrality. Since the preparation of discrete tetrahedral metal chalcogenide clusters meets particular (different) restrictions depending on cluster composition, *i.e.*, the type of metal cations present, it is reasonable to consider solvothermal and ionothermal routes to 1) clusters with  $M^{2+}$  cations exclusively and 2) clusters with  $M^{3+}$  cations, both exclusively or doped with  $M^{4+}$ ,  $M^{2+}$ , or  $M^+$  cations, separately. Reactions where tetrahedral clusters are taken as starting reagents resulting in the preparation of new clusters are also discussed separately. As the distinct group, discrete non-tetrahedral metal chalcogenide clusters with  $M^{2+}$ ,  $M^{3+}$  and  $M^{4+}$  cations (and mixes) are described as well.

### 1.5.2 Tetrahedral Clusters with $M^{2+}$ Cations

$M^{2+}$  cations of later d-block metals have been widely used for preparing metal chalcogenide clusters. Large, discrete tetrahedral clusters made of entirely group 12 metals are known for all tetrahedral cluster series. Moreover, only  $M^{2+}$  cations have been reported to yield any  $C_n$  clusters, and the largest known solvothermally prepared cluster is  $C_3$ , containing 54 metal sites.

The adjacent tetrahedral  $M^{2+}$  sites are ideal to charge-balance the inner (tetrahedral)  $E^{2-}$ , which is essential for the formation of the core of large clusters. At the same time  $M^{2+}$  cations are not adequate for low-coordinated edge and vertex  $E^{2-}$  sites. Such sites tend to be occupied by chalcogenolate  $RE^-$  groups (most often,  $PhE^-$ ). Even with this substitution, maintaining the total electroneutrality of the clusters becomes problematic when cluster size gets larger, as the negative charge of the clusters increases considerably. This can be illustrated on  $C_n$  series clusters with  $M^{2+}$  cations,<sup>107</sup> from  $C_2$  to (theoretical)  $C_5$  showing the negative charge increase of idealized clusters from 4 to 22:



Note that  $M^{2+}$  cations in combination with a specific cluster geometry in the  $C_n$  series (*i.e.*, higher ratio between low-coordinated edge and vertex and high-coordinated inner E sites) are much more favourable for preparing large tetrahedral clusters in comparison with other cluster series, where the negative charge would increase even more dramatically. This can be seen by comparing clusters with approximately the same number of metal and chalcogenide sites in the different series, *e.g.*,  $C_2 [M_{32}E_{54}]$  and  $T_5 [M_{35}E_{56}]$ . With  $M^{2+}$  cations and all edge and vertex chalcogenide sites occupied by  $PhE^-$ , the stoichiometry of these clusters is  $[M_{32}E_{14}(EPh)_{40}]^{4-}$  and  $[M_{35}E_{28}(EPh)_{28}]^{14-}$ , respectively. The difference in negative charge (4 vs. 14) explains why there are multiple examples of  $C_2$  clusters with exclusively  $M^{2+}$  cations, while the corresponding  $T_5$  clusters are not yet known.

Thus, key synthetic strategies for large clusters with  $M^{2+}$  cations are 1) decreasing and/or 2) stabilizing the large negative charge. The first strategy can be realized by replacing four vertex negatively charged  $RE^-$  ligands with neutral ones (*e.g.*, P-, N-, or O-containing). The second requires using adequate charge-balancing species with charge density and geometry match, as well as complementary interactions (*e.g.*, hydrogen,  $\pi$ - $\pi$ , and anion- $\pi$  bonding) allowing them to perform roles of structure-directing and template agents for superlattice crystallization.

A number of  $M^{2+}$ -containing tetrahedral clusters have been originally prepared by coordination chemistry approach, and then were re-produced under solvothermal conditions. An example is the discrete neutral  $P_1$  cluster  $[Cd_8Se(SePh)_{12}Cl_2L_2]$ , where two vertexes are occupied with neutral ligands  $L = PCy_3$ , tricyclohexylphosphine, and the other two with  $Cl^-$ .<sup>140</sup> In this way, such a  $P_1$  cluster consists of a tetrahedral anti- $T_1$   $\{SeCd_4\}$  central unit capped by two tetrahedral  $\{CdSe_3L\}$  and two tetrahedral  $\{CdSe_3Cl\}$  units, with alkylphosphine or halogenide ligands replacing Se in regular  $T_1$   $\{CdSe_4\}$  unit. Using  $[Cd_4(SePh)_8]_\infty$  and  $CdCl_2$  precursors with methanol as a solvent allowed rather unusual

short reaction times and low temperatures (1 h at 130 °C, respectively) in this case; very slow cooling to room temperature (0.3 °C/min) helped product crystallization. A similar approach, based on “corner capping” with neutral ligands, was reported for the preparation of neutral discrete  $P_1$  clusters  $[Zn_8S(SPh)_{14}L_2]$  using a series of substituted pyridine ligands, *e.g.*,  $L = 3\text{-aminopyridine}$ <sup>136</sup> or fused-ring heterocyclic N-containing aromatic ligands, *e.g.*,  $L = 4,7\text{-phenanthroline}$ ,  $5\text{-aminoquinoline}$  or  $3\text{-(2-thienyl)pyridine}$  (Figure 1.12).<sup>74</sup> Varying the capping ligands was shown to influence cluster-cluster interactions (leading to crystallization in different space groups belonging to triclinic or monoclinic crystal systems) and modification of the optical properties of the clusters. For instance, in room temperature photoluminescence spectra obtained for DMSO solutions an emission band for  $[Zn_8S(SPh)_{14}L_2]$  clusters with  $L = 3\text{-(2-thienyl)pyridine}$  is substantially narrower and blue shifted in comparison with the corresponding band for the clusters with  $L = 5\text{-aminoquinoline}$  (~350 and 476 nm, respectively). In contrast, no emission was observed at room temperature for the clusters with  $L = 4,7\text{-phenanthroline}$ ,<sup>74</sup> which demonstrates that photophysical properties of such clusters are strongly effected by ligands.

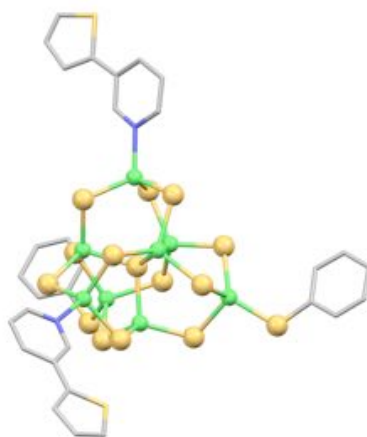


**Figure 1.12:** Neutral  $P_1$  cluster  $[Zn_8S(SPh)_{14}L_2]$ , where  $L = 3\text{-(2-thienyl)pyridine}$ . Carbon atoms of  $PhS^-$  ligands, except those on vertexes, are omitted for clarity.<sup>74</sup>

The “corner capping” with neutral ligands, occurring through the formation of  $M-O$  bonds at all four vertexes of a tetrahedral cluster, was also used to decrease the charge of even larger frameworks, resulting in the crystallization of discrete tetra-anionic  $C_3$  clusters  $[Cd_{54}S_{32}(SPh)_{48}(H_2O)_4]^{4-}$  and  $[Cd_{54}Se_{32}(SPh)_{48}(H_2O)_4]^{4-}$ .<sup>57</sup> Water ligands (replacing  $PhS^-$  sites at each vertex) arise from the use of the mixed solvent system (acetonitrile-water) for

solvothermal synthesis with  $[\text{Cd}_4(\text{SePh})_8]_\infty$  and thiourea or selenourea precursors. These large tetrahedral clusters (edge length 1.97 nm as measured between vertex metal sites) crystallize into noncentrosymmetric superlattices, either primitive or face-centered (space groups  $P23$  or  $F-43c$ , respectively) (Figure 1.13).  $[\text{Cd}_{54}\text{Se}_{32}(\text{SPh})_{48}(\text{H}_2\text{O})_4]^{4-}$  has  $\mu_3$ - and  $\mu_4$ - $\text{Se}^{2-}$  sites that were formed by replacing thiourea with selenourea, while all edge ligands are  $\mu$ - $\text{PhS}^-$ . Anionic clusters were prepared with a variety of charge-balancing alkylammonium cations, *i.e.*, tetramethylammonium,  $\text{Me}_4\text{N}^+$ ; tetraphenylphosphonium,  $\text{Ph}_4\text{P}^+$ ; and *n*-octyltrimethylammonium,  $\text{C}_{11}\text{H}_{26}\text{N}^+$ . These disordered species, along with disordered solvent molecules, occupy the large voids between  $\text{Cd}_{54}$  units.

Solvothermal preparation of various clusters belonging  $C_n$  series made convenient to follow the influence of size and composition of clusters on their optical properties. Thus, systematic blue shift of the low-energy absorption peak position (from 353 through 327 to 291 nm) was observed with cluster size decrease from  $[\text{Cd}_{54}\text{S}_{32}(\text{SPh})_{48}(\text{H}_2\text{O})_4]^{4-}$  through  $[\text{Cd}_{32}\text{S}_{14}(\text{SPh})_{40}]^{4-}$  to  $[\text{Cd}_{17}\text{S}_4(\text{SPh})_{26}(\text{H}_2\text{NCSNH}_2)_2]$ . The effect of cluster composition (for a given  $[\text{Cd}_{54}\text{E}_{32}(\text{SPh})_{48}(\text{H}_2\text{O})_4]^{4-}$  cluster size) was demonstrated by a red shift (from 353 to 393 nm) upon changing from sulfur to the heavier selenium in the cluster core.<sup>57</sup>

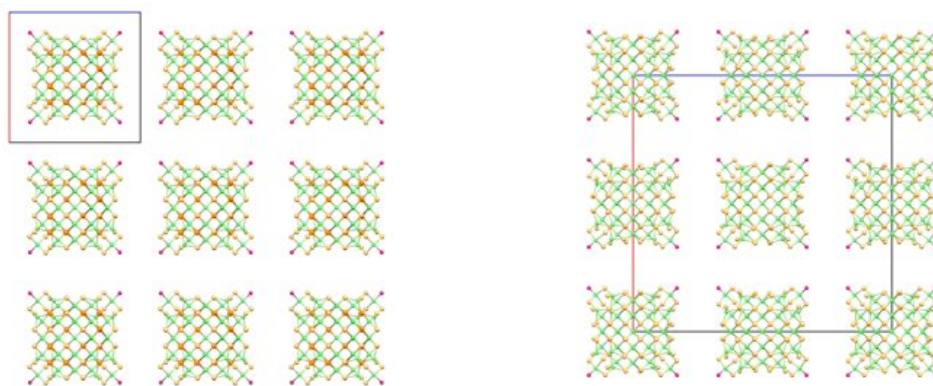


**Figure 1.13:** Fragments of cubic superlattices of  $C_3$  clusters: primitive for  $[\text{Cd}_{54}\text{Se}_{32}(\text{SPh})_{48}(\text{H}_2\text{O})_4]^{4-}$  with space group  $P23$  (left) and face-centered for  $[\text{Cd}_{54}\text{S}_{32}(\text{SPh})_{48}(\text{H}_2\text{O})_4]^{4-}$  with space group  $F-43c$  (right). Carbon atoms of  $\text{PhS}^-$  ligands, as well as disordered charge-balancing species and crystallized solvent molecules, are omitted for clarity. Viewed along the  $b$  direction; cell axis  $a$  shown red and axis  $c$  blue.<sup>57</sup>

The use of  $(\text{Me}_4\text{N})_2[\text{Cd}(\text{EPh})_4]$  as a single source precursor in DMF solvent allowed for the solvothermal preparation of the all-selenium analog  $[\text{Cd}_{54}\text{Se}_{32}(\text{SePh})_{48}(\text{dmf})_4]^{4-}$  (Figure 1.14)<sup>141</sup> and even larger CdS clusters (with the size as large as  $\text{C}_4$  and  $\text{C}_5$  mentioned above),<sup>142</sup> although orientation flexibility of the latter within the superlattice hampers single-crystal characterization. Based on series of analyses, including TEM and electron tomography, these clusters break the trend in the capped tetrahedral series and have a truncated tetrahedral shape.<sup>142,143</sup>

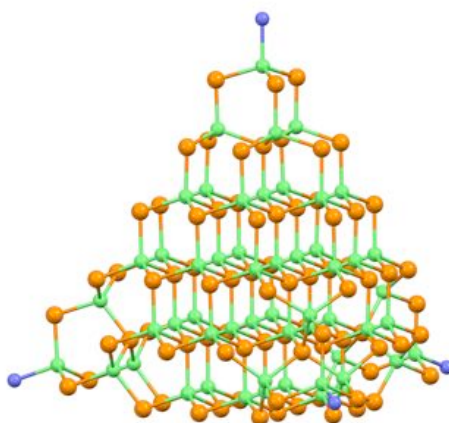


**Figure 1.14:**  $\text{Cd}_{54}\text{Se}_{80}$  structure of the anionic  $\text{C}_3$  cluster  $[\text{Cd}_{54}\text{Se}_{32}(\text{SePh})_{48}(\text{dmf})_4]^{4-}$ .<sup>141</sup>

The co-crystallization of anionic metal chalcogenide clusters with counter ions having special functions (*e.g.*, organic chromophores) enables uniform molecular-level integration of inorganic and organic components to obtain new functional materials with synergistic properties. For example, the solvothermally prepared combination of the discrete  $\text{P}_1$  anionic cluster  $[\text{Zn}_8\text{S}(\text{SPh})_{15}\text{H}_2\text{O}]^-$  with the fluorescent dye Acridine Yellow G through the formation of ion-pair charge transfer salt  $[\text{C}_{15}\text{H}_{16}\text{N}_3][\text{Zn}_8\text{S}(\text{SPh})_{15}\text{H}_2\text{O}]$  gives rise to the new crystalline material (space group  $C2/c$ ) (Figure 1.15), in which the metal chalcogenide framework serves as the electron donor and augments the colour of the fluorescent dye.<sup>23</sup> Experiments on labelling bacteria (*e.g.*, *E. coli*) using a suspension of this material show that a combination of fluorescent dye and metal chalcogenide cluster was efficient for staining under confocal microscopy conditions with minimal photo-bleaching over time, while fluorescent imaging of bacteria with Acridine Yellow G on its own was much less stable.



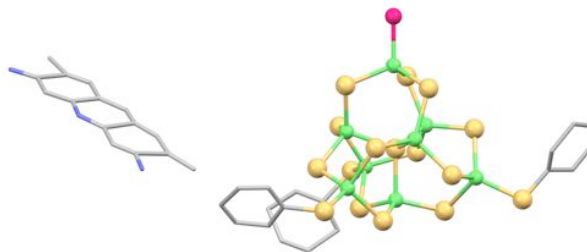


**Figure 1.15:** Ion-pair charge transfer salt  $[\text{C}_{15}\text{H}_{16}\text{N}_3][\text{Zn}_8\text{S}(\text{SPh})_{15}\text{H}_2\text{O}]$ . Carbon atoms of  $\text{PhS}^-$  ligands, except those on vertices, are omitted for clarity.<sup>23</sup>

Although the co-crystallization of metal chalcogenide clusters and optically active species can also be achieved using conventional synthesis,<sup>144–146</sup> such integration was shown to be enhanced even under mild-temperature solvothermal conditions. Moreover, an additional feature in the latter case is the possibility to realize a “one-pot synthesis”, when the assembly of large anionic clusters is combined with their co-crystallization with functional cations. When such cations represent fused-ring aromatic compounds, they can play an even more complex role, combining additional functionality, charge balancing, and superlattice stabilization (*e.g.*, through  $\pi$ - $\pi$  interactions with  $\text{PhE}^-$  ligands of clusters). This was realized, for instance, with the solvothermal preparation of the discrete  $\text{T}_3$  cluster  $[\text{Zn}_{10}\text{S}_4(\text{SPh})_{15}\text{Cl}]^{4-}$ , co-crystallized with methylviologen cation dye ( $[\text{C}_{12}\text{H}_{14}\text{N}_2]^{2+}$  or  $\text{MV}^{2+}$ ) to give ion-pair charge transfer salt  $(\text{MV})_2[\text{Zn}_{10}\text{S}_4(\text{SPh})_{15}\text{Cl}]$ .<sup>24</sup> The resulting crystalline material shows a remarkable red shift ( $> 200$  nm) of a broad absorption band in solid-state spectra in comparison with that of the individual components; such a shift was assigned to a charge-transfer from the electron-rich metal chalcogenide cluster anions to  $\text{MV}^{2+}$  cations. Similar integration with the  $\text{MV}^{2+}$  cation was achieved for discrete  $\text{C}_1$  clusters  $[\text{Cd}_{17}\text{Se}_4(\text{SPh})_{24}\text{Br}_4]^{2-}$ ;<sup>147</sup> cyclic voltammetry showed a low-potential shift of the  $\text{MV}^{2+}$  cations in this ion-pair charge transfer salt in comparison with  $\text{MVBr}_2$ , which indicates that strong cation-anion interaction preserved even upon dissolving in DMF. Examination of photocurrent responses of  $(\text{MV})[\text{Cd}_{17}\text{S}_4(\text{SPh})_{24}\text{Br}_4]$  and  $(\text{MV})[\text{Cd}_{17}\text{Se}_4(\text{SPh})_{24}\text{Br}_4]$  showed that the current intensities of the ion-pair charge transfer salts are significantly larger than those of the similar clusters  $[\text{Cd}_{17}\text{E}_4(\text{SPh})_{28}]^{2-}$  with  $(\text{Me}_4\text{N})^+$  cations; the  $\text{MV}^{2+}$  cation was found to play different roles in electron transfer under visible light or UV irradiation.<sup>147</sup>

Optically active metal-chelate dyes (e.g., complexes of  $M^{2+}$  with 1,10-phenanthroline, *phen*, or 2,2'-bipyridine, *bpy*, ligands) further extend the approach for the assembly of integrated materials through cation-anion interactions involving tetrahedral metal chalcogenide clusters. Bulky cations  $[M(\textit{phen})_3]^{2+}$  and  $[M(\textit{bpy})_3]^{2+}$ , formed *in situ* during the solvothermal process, are comparable in size with large tetrahedral clusters and can additionally play the role of space-filling (template) species. Geometry match in this case is accompanied by charge density match: compared to widely used quaternary ammonium cations and protonated organic amines, the metal-chelate dyes possess both a large size and relatively low charge density, which fits the low charge density of large anionic tetrahedral clusters belonging to the  $C_n$  series. Hydrophobic and  $\pi$ - $\pi$  interactions between fused-ring N-containing aromatic ligands of such cationic species and surface  $\text{PhE}^-$  ligands of anionic clusters also contribute to superlattice stabilization. Thus the discrete  $C_2$  anionic clusters  $[\text{Cd}_{32}\text{S}_{14}(\text{SPh})_{40}]^{4-}$  were solvothermally prepared and integrated with the metal-chelate dye cations  $[\text{Fe}(\textit{phen})_3]^{2+}$  (Figure 1.16).<sup>148</sup> The use of a bulkier ligand (namely, 3,4,7,8-tetramethyl-1,10-phenanthroline, *tmphen*) instead of *phen* as in  $[\text{Fe}(\textit{phen})_3]_2[\text{Cd}_{32}\text{S}_{14}(\text{SPh})_{40}]$  leads to crystallization of  $[\text{Fe}(\textit{tmphen})_3]_2[\text{Cd}_{32}\text{S}_{14}(\text{SPh})_{40}]$ , having different packing of the same tetrahedral clusters (space groups  $P2_1/c$  and  $P-1$ , respectively). The optical properties and photoelectrochemical performance of the composite material can be tuned by varying the cluster size, changing the type of metal centres or organic chelating ligands; for instance, the advantage of  $\text{Ru}^{2+}$  over  $\text{Fe}^{2+}$  in metal-complex dyes was demonstrated.<sup>75</sup>

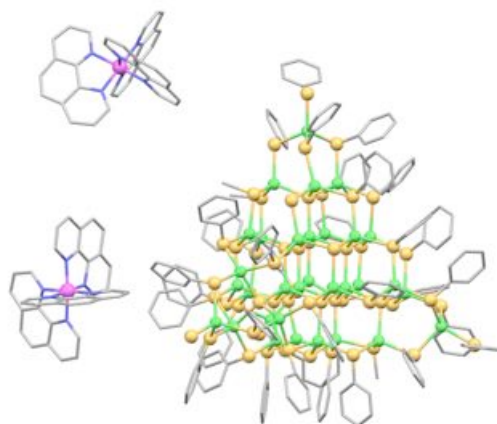


**Figure 1.16:** Ion-pair charge transfer salt  $[\text{Fe}(\textit{phen})_3]_2[\text{Cd}_{32}\text{S}_{14}(\text{SPh})_{40}]$ .<sup>148</sup>

### 1.5.3 Tetrahedral Clusters with $M^{3+}$ and Mixed Cations

In contrast to  $M^{2+}$  cations, the formation of discrete tetrahedral clusters composed entirely of trivalent metal ions is limited to relatively small species. The observation that clusters having interstitial chalcogenide atoms (*e.g.*, larger than  $T_3$ ) are unlikely to form is in accordance with Pauling's electrostatic valence rule, as the adjacent tetrahedrally coordinated  $M^{3+}$  sites would overburden the total bond valence of tetrahedrally coordinated  $E^{2-}$  sites. Therefore, access to large tetrahedral clusters with  $M^{3+}$  cations requires the presence of lower valence metals ( $M^{2+}$  or  $M^+$ ) in the inner sites to maintain the local electroneutrality. A classical example is the  $T_4$  cluster  $[Cd_4In_{16}S_{35}]^{14-}$  present in 3D covalent superstructures.<sup>149</sup> At the same time,  $M^{3+}$  cations usually provide enough bond valence to balance low-coordinate surface  $E^{2-}$  sites, which eliminates (or decreases) the need for surface ligands. That is why tetrahedral clusters with  $M^{3+}$  surface sites can exist as “naked” species, although ligands at vertexes are still useful to prevent covalent-linkage into 3D and 2D condensed frameworks. The common challenge for the preparation of large tetrahedral clusters, already addressed while discussing systems with  $M^{2+}$  cations, is related with maintaining the total electroneutrality, as the negative charge of the clusters increases with their size increase. The incorporation of lower valence metals into a  $M^{3+}$  system, unavoidable to keep the local electroneutrality in large tetrahedral clusters, simultaneously complicates maintaining the total electroneutrality by contributing to an increase in negative charge. This can be illustrated by comparison of the (hypothetical) binary and (isolated) ternary cluster compositions, *e.g.*,  $T_4 [In_{20}E_{35}]^{10-}$  vs.  $T_4 [Cd_4In_{16}E_{35}]^{14-}$ ; and  $T_5 [In_{35}E_{56}]^{7-}$  vs.  $T_5 [Cd_{13}In_{22}E_{56}]^{20-}$ .

The synthetic strategies used with mixed-metal systems based on  $M^{3+}$  cations are also related to 1) decreasing and/or 2) stabilizing the large negative charge, as was discussed above for  $M^{2+}$  systems, while the arsenal of solutions is more diverse and includes both similar routes (as “corner-capping” the cluster with neutral ligands) and those specific to mixed systems. Thus, introducing  $M^{4+}$  cations onto surface (most often, vertex) sites helps in reducing the overall cluster negative charge, also providing more flexibility to adjust charge density of the system. A general way towards large tetrahedral clusters here assumes varying the ratio between multiple metal ions in different oxidation states (*e.g.*,

$M^{4+}/M^{3+}/M^{2+}$ ,  $M^{4+}/M^{3+}/M^+$ , or even  $M^{4+}/M^{3+}/M^{2+}/M^+$ ) and meticulous selection of charge-balancing species with geometrical, charge density and mutual interactions match. The preparation of tertiary (and more complex) metal chalcogenides can often be complicated by phase separation, with  $M^{4+}$ ,  $M^{3+}$  or  $M^{2+}$  cations forming stable chalcogenides on their own. Solvothermal and ionothermal synthesis with suitable additives (charge-balancing, structure-directing and space-filling species, with possibility to blend all those functions in just one compound) provide favourable conditions to facilitate integration of different metal cations into the same cluster. Some particular cases illustrating the mentioned synthetic strategies and approaches, starting from those common between  $M^{2+}$  and  $M^{3+}$  tetrahedral clusters systems are described below.

The “corner capping” with neutral N-containing aromatic ligands in a purely  $M^{3+}$  system was achieved, for example, in the preparation of the discrete anionic  $T_3$  cluster  $[Ga_{10}S_{16}L_4]^{2-}$ , where all four vertexes are occupied by  $L = 3,5$ -dimethylpyridine, covalently attached *via* the formation of Ga–N bonds.<sup>150</sup> Each anionic cluster is charge-balanced and additionally stabilized with two monoprotonated 3,5-dimethylpyridine cations; despite the disorder of the cationic species, the orientation of the heterocyclic aromatic ring parallel to cluster faces can be distinguished (Figure 1.17).

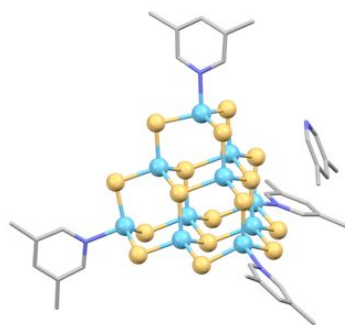


**Figure 1.17:** Anionic  $T_3$  cluster  $[Ga_{10}S_{16}L_4]^{2-}$  charge-balanced and stabilized by  $2H^+ \cdot L$ , where  $L = 3,5$ -dimethylpyridine.<sup>150</sup>

The idea of using fused-ring heterocyclic N-containing additives to corner-cap, charge-balance and stabilize large tetrahedral clusters also resulted in the solvothermal preparation of several discrete clusters with size from  $T_3$  to  $T_5$  and edge lengths reaching 1.55 nm (as measured between vertex metal sites).<sup>43</sup> Prior to this work  $T_5$  clusters were known only in

3D and 2D covalently-linked superstructures. In the discrete anionic  $T_5$  cluster  $[\text{Cd}_{13}\text{In}_{22}\text{S}_{52}\text{L}_4]^{12-}$  four vertexes are capped by  $L = 1\text{-methylimidazole (mim)}$ , ligands, and negative charge of the cluster is balanced by protonated forms of organic superbase 1,8-diazabicyclo[5.4.0]undec-7-ene (DBU) and  $\text{Li}^+$  cations. The  $\text{Cd}^{2+}$  sites in the inner fragment  $\{\text{Cd}_{13}\text{S}_4\}$ , containing four tetrahedrally coordinated  $\text{S}^{2-}$  sites, are mandated by local electroneutrality requirement, while edge and corner  $\text{In}^{3+}$  sites alleviate the otherwise low coordinate surface  $\text{S}^{2-}$  sites. The orientational disorder of *mim* ligands and charge-balancing  $\text{H}^+$ -DBU species did not allow their precise location to be determined in the superstructure of the  $T_5$  cluster (space group  $I4_1/amd$ ), although their presence was confirmed with a series of analyses. Single-crystal X-ray diffraction analysis of the smaller  $T_4$  anionic cluster  $[\text{Cd}_4\text{In}_{16}\text{S}_{31}\text{L}_4]^{6-}$ , prepared by the same “superbase route”, allowed location of the capping ligands  $L = 1,5\text{-diazabicyclo[4.3.0]non-5-ene (DBN)}$  at vertexes and charge-balancing  $\text{H}^+$ -DBN species, which create a stabilizing “cocoon” around the cluster (space group  $I4_1/a$ , see Figure 1.18).

$T_5$  cluster  $[\text{Cd}_{13}\text{In}_{22}\text{S}_{52}(\text{mim})_4]^{12-}$  exhibits distinct and broad emission in solid state at room temperature with the maximum observed at 512 nm (fwhm  $\sim 70$  nm); calculated from the diffuse reflectance UV-vis data band gap is 2.87 eV. Both absorption and emission peaks were found to be red shifted in comparison with those of smaller clusters (*e.g.*,  $T_4$   $[\text{Cd}_4\text{In}_{16}\text{S}_{31}(\text{DBN})_4]^{6-}$  with band gap 3.27 eV) as result of both size increase and composition change.<sup>43</sup>

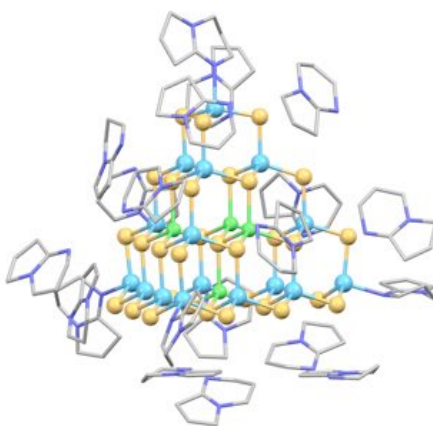


**Figure 1.18:** Anionic  $T_4$  cluster  $[\text{Cd}_4\text{In}_{16}\text{S}_{31}\text{L}_4]^{6-}$  charge-balanced and stabilized by  $\text{H}^+$ -L species, where  $L = 1,5\text{-diazabicyclo[4.3.0]non-5-ene, DBN}$  (all neighbouring DBN are shown, forming a “cocoon” around the cluster).<sup>43</sup>

Other derivatives of imidazolium salts were also useful to provide access to extra-large supertetrahedral metal chalcogenide clusters in a “corner capping” approach. Performing syntheses in the ionic liquid [Bmmim]Cl (where Bmmim = 1-butyl-2,3-dimethylimidazolium) allowed the combination of charge-decreasing (partially), charge-balancing and charge-stabilizing functions in one compound, which also served as the reaction medium. This resulted in the preparation of several discrete anionic  $T_5$  clusters, including  $(\text{Bmmim})_{12}(\text{NH}_4)[\text{Cu}_5\text{In}_{30}\text{S}_{52}(\text{SH})_2\text{Cl}_2]$  and the first Ga-based  $T_5$  cluster  $(\text{Bmmim})_8(\text{NH}_4)_3[\text{Cu}_5\text{Ga}_{30}\text{S}_{52}(\text{SH})_2(\text{Bim})_2]$ .<sup>44</sup> In the latter, the corner-capping ligand Bim (1-butyl-2-methyl-imidazole) is generated by *in situ* decomposition of the IL. The relatively unusual precursor,  $[\text{H}^+\text{-en}]_2[\text{Ga}_4\text{S}_7(\text{en})_2]$ , was separately prepared by solvothermal synthesis in ethylenediamine (en) and used as the Ga source, with  $\text{In}_2\text{S}_3$  as the In source. In  $T_5$  clusters with mixed  $M^+$  and  $M^{3+}$  cations, the central metal site, surrounded by four tetrahedrally coordinated  $\text{S}^{2-}$ , should be a  $\text{Cu}^+$  cation, and each inner tetrahedrally coordinated  $\text{S}^{2-}$  anion should be bonded with two  $\text{Cu}^+$  and two  $M^{3+}$  cations in order to maintain local electroneutrality. According to this, in each cluster one  $\text{Cu}^+$  cation occupies solely the central metal site, while four  $\text{Cu}^+$  cations are statistically distributed along with  $M^{3+}$  cations in the other twelve metal sites of the inner  $\{\text{M}_{13}\text{S}_4\}$  fragment (Figure 1.19). Most of the  $[\text{Bmmim}]^+$  cations are located between the tetrahedral faces of two  $T_5$  clusters, and the imidazolium rings of  $[\text{Bmmim}]^+$  cations are oriented such to be parallel to the nearby cluster face (Figure 1.19). The closest distances between  $\text{S}^{2-}$  on the face of the cluster and the center of imidazolium rings are such that the presence of anion- $\pi$  interaction was assumed. C-H $\cdots$ S hydrogen bonding and anion- $\pi$  interactions also help to stabilize the large anionic clusters.

Both In- and Ga-based  $T_5$  clusters show emission in solid state at room temperature, but the obtained spectra are remarkably different. Thus,  $[\text{Cu}_5\text{In}_{30}\text{S}_{52}(\text{SH})_2\text{Cl}_2]^{13-}$  shows a distinct asymmetric emission band at 540 nm (fwhm  $\sim$ 50 nm), while  $[\text{Cu}_5\text{Ga}_{30}\text{S}_{52}(\text{SH})_2(\text{Bim})_2]^{11-}$  shows an unusual broad emission band at 630 nm with fwhm of  $\sim$ 180 nm. Calculated from the diffuse reflectance UV-vis data band gaps are 2.28 and 3.68 eV for  $[\text{Cu}_5\text{In}_{30}\text{S}_{52}(\text{SH})_2\text{Cl}_2]^{13-}$  and  $[\text{Cu}_5\text{Ga}_{30}\text{S}_{52}(\text{SH})_2(\text{Bim})_2]^{11-}$ , respectively, exhibiting a blue shift compared to the bulk  $\text{CuInS}_2$  (1.53 eV) and  $\text{CuGaS}_2$  (2.40 eV).<sup>44</sup>

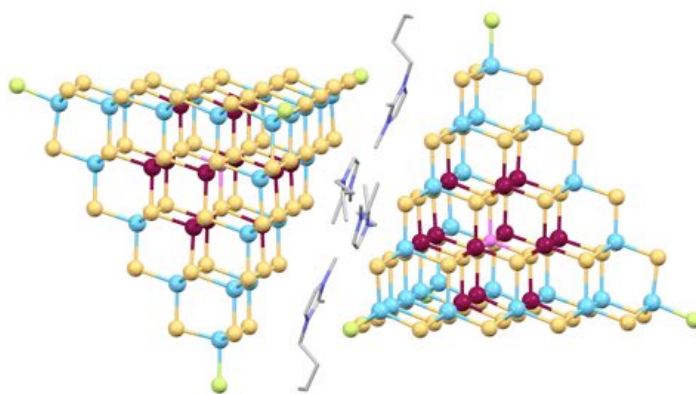


**Figure 1.19:** [Bmmim]<sup>+</sup> cations between two anionic T<sub>5</sub> clusters [Cu<sub>5</sub>In<sub>30</sub>S<sub>52</sub>(SH)<sub>2</sub>Cl<sub>2</sub>]<sup>13-</sup>: the imidazolium rings are parallel to the surfaces of neighbouring clusters and anion- $\pi$  interactions are suggested to exist. Vertex sites with partial occupancy SH/Cl are shown as lime-green in colour; metal sites Cu/Ga as maroon.<sup>44</sup>

An approach to decrease the charge of anionic clusters, complementary to the use of the “corner-capping” neutral organic ligands, was realized *via* covalent termination of the cluster vertexes with complex metal cations. In this case, instead of replacing the vertex E<sup>2-</sup> sites in tetrahedral clusters, longer E-ML<sub>n</sub> units are formed with participation of four vertex E atoms, where M is a transition metal and L = organic ligand. Thus in the discrete T<sub>3</sub> cluster [Zn<sub>2</sub>Ga<sub>4</sub>Sn<sub>4</sub>Se<sub>20</sub>]<sup>8-</sup> introducing Sn<sup>4+</sup> cations onto four vertex sites contributed to a decrease in the negative charge, while the attachment of four metal complexes [Mn(L)]<sup>2+</sup> with the polydentate organic ligand L = C<sub>8</sub>H<sub>23</sub>N<sub>5</sub>, tetraethylenepentamine (*tepa*) covalently terminates all cluster vertexes and charge balances the framework.<sup>131</sup> In the in-situ formed metal complex [Mn(*tepa*)]<sup>2+</sup>, the Mn atom is coordinated with five N sites from the organic ligand and one vertex Se site of the tetrahedral cluster, thus having a distorted octahedral environment. Hence, the distribution of Mn<sup>2+</sup> and Zn<sup>2+</sup> cations in the clusters (octahedral and tetrahedral coordination, respectively) results from the different coordination abilities of these metals. The ligand *tepa* also serves as the reaction medium in the solvothermal synthesis. The resulting neutral clusters with pendent metals, [Mn(*tepa*)]<sub>4</sub>[Zn<sub>2</sub>Ga<sub>4</sub>Sn<sub>4</sub>Se<sub>20</sub>] (Figure 1.20), assemble into a superlattice (space group *P-4b2*) with different levels of ordering provided by different intercluster forces: hydrogen bonding N-H $\cdots$ Se between *tepa* ligands on one cluster and Se sites on the face

of the adjacent cluster give a layered arrangement parallel to the (001) plane, while the layers are further packed into 3D superlattice through van der Waals interactions. Hence, the metal complexes  $[\text{Mn}(tepa)]^{2+}$  at the four cluster vertexes not only allow charge balance but also act as structure-directing agents for superstructure assembly.

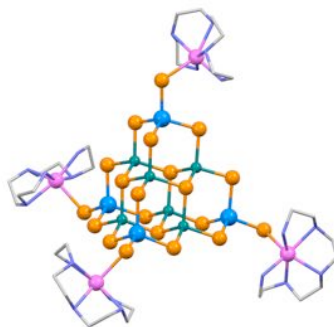


**Figure 1.20:** The neutral cluster with covalently-bonded metal complexes  $[\text{Mn}(tepa)]_4[\text{Zn}_2\text{Ga}_4\text{Sn}_4\text{Se}_{20}]$ . Metal sites with partial occupancy Zn/Ga are shown as dark cyan.<sup>131</sup>

The isostructural  $[\text{Mn}(teta)]_4[\text{Mn}_2\text{Ga}_4\text{Sn}_4\text{S}_{20}]$ , also covalently terminated with metal-complex cations  $\text{ML}_n$ , was solvothermally prepared using the shorter  $\text{C}_6\text{H}_{18}\text{N}_4$ , triethylenetetramine (*teta*) as both solvent and polydentate ligand.<sup>151</sup> Further shortening the length of the organic ligand in the metal-complex cation ( $\text{L} = \text{C}_4\text{H}_{13}\text{N}_3$ , diethylenetriamine (*dien*)) changes not only the hydrogen bonding-governed assembly of clusters into a superstructure (space group  $C2/c$ ) but the clusters composition itself, leading to formation of discrete anionic  $\text{T}_3$  clusters  $[\text{Mn}_2\text{Ga}_4\text{Sn}_4\text{S}_{20}]^{8-}$  charge-balanced and stabilized by  $[\text{Mn}(dien)_2]^{2+}$  cations (Figure 1.21) with additional hydrogen  $\text{N}-\text{H}\cdots\text{S}$  bonding (in the absence of covalent bonding) between negatively charged cluster and positively charged metal-complex. However, the use of a bidentate ligand as an extreme case of shortening ( $\text{L} = \text{C}_2\text{H}_8\text{N}_2$ , ethylenediamine (*en*)) under similar reaction conditions results in the formation of a covalently bonded 1D superstructure, where anionic clusters  $[\text{Mn}_2\text{Ga}_4\text{Sn}_4\text{S}_{20}]^{8-}$  are interlinked by two pairs of unsaturated metal complex cations  $[\text{Mn}_2(\text{en})_5]^{4+}$  via  $\text{Sn}-\text{S}-\text{Mn}$  covalent bonds.



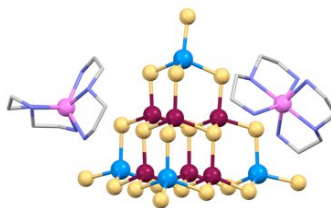


**Figure 1.21:** The anionic  $T_3$  cluster  $[\text{Mn}_2\text{Ga}_4\text{Sn}_4\text{S}_{20}]^{8-}$  with metal-complex cations  $[\text{Mn}(\text{dien})_2]^{2+}$ . Metal sites with partial occupancy Mn/Ga are shown as maroon.<sup>151</sup>

While metal-complex cations such as  $[\text{M}(\text{phen})_3]^{2+}$  and  $[\text{M}(\text{bpy})_3]^{2+}$  are used to template, charge balance, and stabilize the formation of anionic metal chalcogenide clusters, enhanced optical properties (due to cation-anion charge transfer) are also incorporated. Such integrated materials are formed to a great extent in a similar manner as was discussed above for pure  $\text{M}^{2+}$  systems (with surface  $\text{PhE}^-$  ligands) except here there are no additional  $\pi$ - $\pi$  and hydrophobic surface interactions in the case of naked  $T_n$  clusters. Some discrete anionic clusters prepared under solvothermal conditions using this approach, are the  $\text{In}^{3+}$ -containing  $T_3$  clusters  $[\text{Ni}(\text{phen})_3]_3[\text{In}_{10}\text{S}_{20}\text{H}_4]$  (Figure 1.22, left)<sup>73</sup> and  $[\text{Ni}(\text{bpy})_3]_3[\text{In}_{10}\text{S}_{20}\text{H}_4]$ ,<sup>145</sup> where *phen* and *bpy* ligands on three metal-complex cations provide steric hindrance and an aromatic environment to template and stabilize the metal chalcogenide frameworks (Figure 1.22, right). Similarly, the iron doped  $T_4$  cluster  $[\text{Fe}(\text{bpy})_3]_3[\text{Fe}_4\text{In}_{16}\text{S}_{35}\text{H}_2] \cdot 4\text{H}^+ \cdot \text{tea} \cdot 2\text{H}^+ \cdot \text{bpy}$  can be prepared, with additional charge-balance with protonated triethylamine (*tea*) and protonated bipyridine.<sup>152</sup>

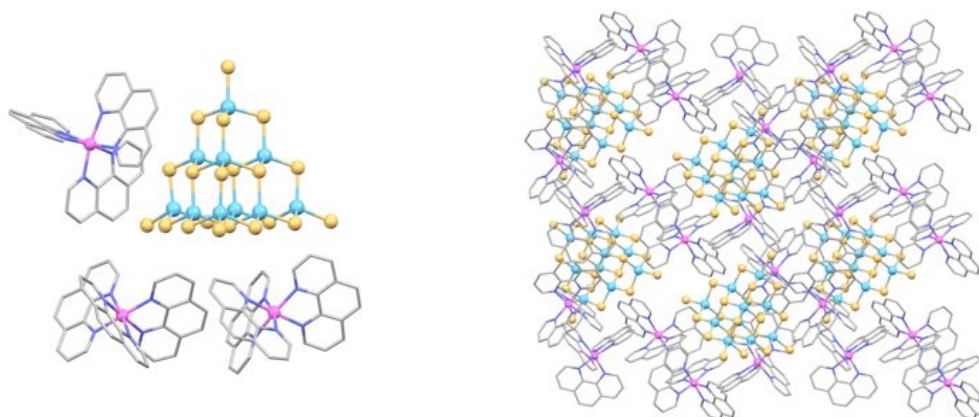


**Figure 1.22:** The anionic  $T_3$  cluster  $[\text{In}_{10}\text{S}_{20}\text{H}_4]^{6-}$  with three metal-complex cations  $[\text{Ni}(\text{phen})_3]^{2+}$  (*left*); superstructure of the clusters, charge-balanced, templated and stabilized by metal-complexes (viewed along the *b* direction) (*right*). Co-crystallized solvent molecules are omitted for clarity.<sup>73</sup>

In the examples addressed above, decreasing and balancing the charge and stabilization of large anionic clusters was achieved by 1) covalent capping/terminating of cluster vertexes by neutral and cationic groups and/or by 2) non-covalent (*e.g.*, ionic and hydrogen bonding or van der Waals forces) interactions with different species, *i.e.*, P- or N-containing organic ligands and transition metal complexes with N-containing aliphatic or aromatic chelating ligands; often several routes are realized simultaneously. A particular case where stabilization of clusters is achieved *via* non-covalent interactions with only protonated forms of organic amines can also take place. Many protonated amines provide more flexibility in templating and charge-balancing of anionic metal chalcogenide clusters, in comparison, for example, with rigid metal-complex cations with *phen* and *bpy* ligands. Thus the series of discrete anionic T<sub>4</sub> clusters [M<sub>x</sub>Ga<sub>18-x</sub>Sn<sub>2</sub>E<sub>35</sub>]<sup>12-</sup>, where x = 2 or 4; M = Mn, Cu and Zn; E = S and Se, was solvothermally prepared using piperidine (*pr*, C<sub>5</sub>H<sub>11</sub>N) as the reaction solvent.<sup>49</sup> Stabilization of the clusters is achieved, on the one hand, by varying the ratio between precursors (complex composition including M<sup>+</sup>, M<sup>2+</sup>, M<sup>3+</sup> and M<sup>4+</sup> metal sources) allowing charge tuning of the cluster, and, on the other hand, by a perfect match of charge density, geometry and mutual interactions (electrostatic and hydrogen bonding) between the highly-ordered protonated piperidine cations and the anionic clusters in the superstructure. Theoretical calculations at the DFT level show that the [Cu<sub>2</sub>Ga<sub>16</sub>Sn<sub>2</sub>Se<sub>35</sub>]<sup>12-</sup> cluster has more negative charge centers at the Se<sup>2-</sup> vertexes of the tetrahedron and at the central Se<sup>2-</sup> site of each edge. In the superstructure of such clusters (space group *I-43m*; body-centered cubic packing in unit cell) two piperidinium cations interact with Se<sup>2-</sup> at each edge center and three piperidinium cations – with each vertex Se<sup>2-</sup> with the formation of strong electrostatic interactions and additional N–H···Se hydrogen bonds, so each discrete T<sub>4</sub> cluster is surrounded by and bonded with 24 piperidinium cations (Figure 1.23). Since each piperidinium cation interacts with two adjacent metal chalcogenide clusters, it provides a total charge balance (H<sup>+</sup>-*pr*)<sub>12</sub>[Cu<sub>2</sub>Ga<sub>16</sub>Sn<sub>2</sub>Se<sub>35</sub>]<sup>12-</sup> for each cluster. The remarkable stability of such protonated amine-cluster “ion pair” was confirmed by the miniscule change of electrical conductivity upon dissolving the crystalline product in piperidine. While solvothermal synthesis was performed under similar reaction conditions but using other amines (piperidine derivatives and related compounds) possessing stronger protonation ability and/or higher steric

hindrance, only the formation of 3D covalent superstructures took place, which proves the importance of a multilateral match between the protonated amine and cluster.

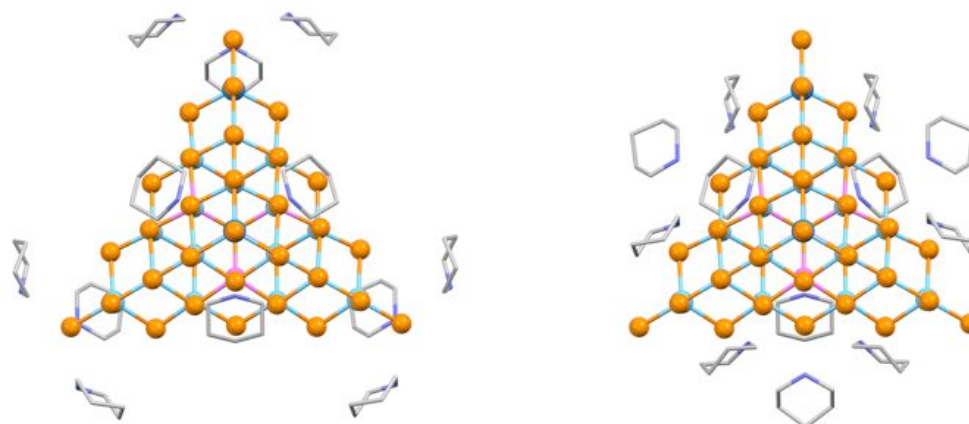


**Figure 1.23:** The anionic  $T_4$  cluster  $[\text{Cu}_2\text{Ga}_{16}\text{Sn}_2\text{Se}_{35}]^{12-}$  surrounded by 24 protonated piperidine molecules: those bonded to cluster vertexes (*left*) and the centers of edges (*right*) through  $\text{N-H}\cdots\text{Se}$  hydrogen bonding are shown separately.<sup>49</sup>

Solvothermal reactions in a mixed solvent system containing water and the organic “superbase” amine DBU allowed the preparation of very unusual large  $\text{In}^{3+}$ -containing cluster  $[\text{In}_{38}\text{S}_{65}(\text{H}_2\text{O})_6]^{16-}$  stabilized by  $\text{H}^+$ -DBU.<sup>38</sup> This cluster is covalently-bonded *via* dimeric  $[\text{In}_2\text{S}(\text{H}_2\text{O})_2]^{4+}$  units into a 2D framework (space group  $Pnma$ ). The structure of the cluster  $[\text{In}_{38}\text{S}_{65}(\text{H}_2\text{O})_6]^{16-}$  with an overall tetrahedral shape (Figure 1.24, left) is different from well known  $T_n$ ,  $P_n$  or  $C_n$  structures and can be described as a combination of an octahedral core unit  $\{\text{In}_{10}\text{S}_{13}\}$  (Figure 1.24, right) with four tetrahedral  $T_2$  corners  $\{\text{In}_4\text{S}_{10}\}$  and four hexagonal rings  $\{\text{In}_3\text{S}_3\}$  as faces. There are very few examples known for clusters containing both octahedral and tetrahedral coordination for metal sites; one example is the smaller anionic cluster  $[\text{Mn}_6\text{Ge}_4\text{Se}_{17}(\text{H}_2\text{O})_6]^{6-}$ .<sup>153</sup> In the  $[\text{In}_{38}\text{S}_{65}(\text{H}_2\text{O})_6]^{16-}$ , the core unit of the cluster  $\{\text{In}_{10}\text{S}_{13}\}$  possesses an octahedral crystalline lattice of NaCl-type and features a central  $\mu_6\text{-S}^{2-}$  site. Six  $\text{H}_2\text{O}$  molecules complete the six  $\text{In}^{3+}$  sites at the face center of the octahedral core unit. Four corner  $\{\text{In}_4\text{S}_{10}\}$   $T_2$  units are attached to the core unit  $\{\text{In}_{10}\text{S}_{13}\}$  *via* bonding between three  $\text{S}^{2-}$  sites on one face of the  $T_2$  unit and the corner  $\text{In}^{3+}$  site of the central moiety, which enables all ten  $\text{In}^{3+}$  sites within the core to have an octahedral coordination. Therefore, both  $\text{In}^{3+}$  and  $\text{S}^{2-}$  sites in this framework

have local coordination geometries that are unusual for tetrahedral metal chalcogenide clusters. A calculation of bond valence sums gives 2.078 for the central  $\mu_6\text{-S}^{2-}$  site; such a value was previously considered unlikely to be found in stable systems as local electroneutrality is not maintained. Another rare exception to Pauling's electrostatic valence rule in tetrahedral metal chalcogenide clusters is observed in the smaller covalently-bonded  $\text{P}_1$  cluster  $[\text{In}_8\text{S}_{17}\text{H}]^{9-}$  with a  $\mu_4\text{-S}^{2-}$  site (calculated bond valence sum 2.28 instead of required 3) in the central anti- $\text{T}_1$  unit  $\{\text{SIn}_4\}$ .<sup>58</sup>

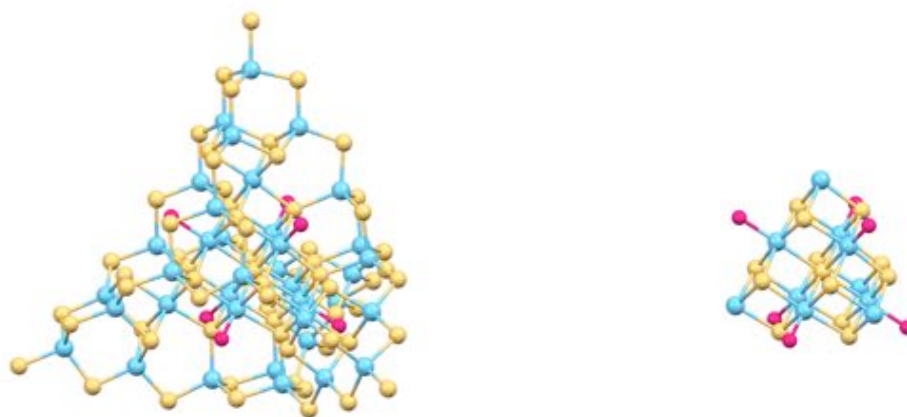


**Figure 1.24:** The anionic  $\text{TO}_2$  cluster  $[\text{In}_{38}\text{S}_{65}(\text{H}_2\text{O})_6]^{16-}$  (left); separately shown is the octahedral core unit  $\{\text{In}_{10}\text{S}_{13}\}$  in the same orientation (right).<sup>38</sup>

From the number of both metal and chalcogen sites, the 2D covalently-bonded cluster  $[\text{In}_{38}\text{S}_{65}(\text{H}_2\text{O})_6]^{16-}$  (proposed notation  $\text{TO}_2$  meant to stress the mixed tetrahedral (T) / octahedral (O) configuration of the core) exceeds the size of the discrete supertetrahedral  $\text{T}_5$  clusters (e.g.,  $[\text{Cu}_5\text{In}_{30}\text{S}_{52}(\text{SH})_4]^{13-}$ ).<sup>41</sup> Both of these tetrahedral metal chalcogenide clusters were formed due to a stabilizing “cocoon” of protonated organic “superbases”,  $\text{H}^+\text{-DBU}$  and  $\text{H}^+\text{-DBN}/\text{H}^+\text{-PR}$ , respectively.

To conclude the overview of  $\text{M}^{3+}$ -based tetrahedral metal chalcogenide clusters, it is worth mentioning the very unusual system where stabilization of a superstructure consisting of two different discrete anionic clusters is achieved with participation of protonated amines. Here, solvothermal synthesis in ethylenediamine results in the preparation of a binary superstructure, combining the tetrahedral  $\text{T}_4$   $[\text{Cu}_4\text{In}_{16}\text{S}_{35}\text{H}_4]^{14-}$  and

cubic  $[\text{Cu}_{12}\text{S}_8]^{4-}$  discrete clusters (Figure 1.25, left), with only protonated ethylenediamine species compensating the (high) charge of both anions.<sup>122</sup> It was proposed that  $[\text{Cu}_{12}\text{S}_8]^{4-}$  clusters may act as template during the formation and crystallization of  $[\text{Cu}_4\text{In}_{16}\text{S}_{35}\text{H}_4]^{14-}$ . The overall ratio between these two anionic clusters in superlattice is 1:2 and each  $[\text{Cu}_{12}\text{S}_8]^{4-}$  is located in a cavity formed by six adjacent  $[\text{Cu}_4\text{In}_{16}\text{S}_{35}\text{H}_4]^{14-}$  (Figure 1.25, right).

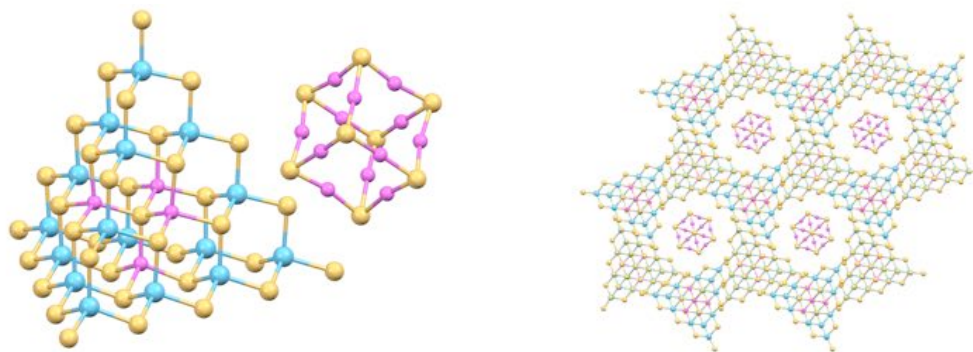


**Figure 1.25:** Tetrahedral  $T_4$   $[\text{Cu}_4\text{In}_{16}\text{S}_{35}\text{H}_4]^{14-}$  and cubic  $[\text{Cu}_{12}\text{S}_8]^{4-}$  discrete anionic clusters (*left*); fragment of packing in binary superstructure, where cubic  $[\text{Cu}_{12}\text{S}_8]^{4-}$  reside in hexagonal spaces formed by tetrahedral  $[\text{Cu}_4\text{In}_{16}\text{S}_{35}\text{H}_4]^{14-}$  clusters from different layers (viewed along the  $c$  direction) (*right*). Charge-balancing  $\text{H}^+$ -en species are mostly disordered and omitted for clarity.<sup>122</sup>

The red crystals of  $[\text{Cu}_4\text{In}_{16}\text{S}_{35}\text{H}_4]_2[\text{Cu}_{12}\text{S}_8] \cdot 32\text{H}^+$ -en (space group  $R\bar{3}$ ) are stable in their mother liquor in the sealed container, while they quickly degenerate to black product upon isolation from the solution.<sup>122</sup> The blackened crystals absorb intensely in the near-IR diapason; the absorption properties were found to be even better for the annealed product. Such remarkable near-infrared absorption properties along with photocurrent response may allow future application as a near-infrared protective material.

#### 1.5.4 Reactions of Large Tetrahedral Clusters

Recently, several cases of “solvothermal insertion” have been described, where discrete tetrahedral clusters with available cavities envelop a size-fitting metal cation, leading to the formation of a new product. Precise doping is possible due to the two-step strategy, assuming 1) solvothermal preparation and isolation of host cluster crystals, followed with

2) metal insertion into the core and crystallization of a new host-guest cluster, again enhanced under solvothermal conditions. Using soluble clusters as a host is essential, as attempts of metal cation diffusion into coreless clusters covalently bonded into rigid 3D or 2D superstructures were reported to be incomplete and inhomogeneous. Doping with a single metal ion (realizing highly ordered distribution of multiple metal components in a tetrahedral cluster) is very unlikely to be achieved in a one step preparation as multinary cluster systems often show statistical distribution of several metals over multiple possible sites to satisfy the local electroneutrality requirement. For instance, discrete  $T_5$  clusters  $[\text{Cu}_5\text{In}_{30}\text{S}_{52}(\text{SH})_4]^{13-}$  have only one central Cu site and yet twelve inner sites partially occupied by  $\text{Cu}^+$  (1/3 probability) and  $\text{In}^{3+}$  (2/3 probability). In contrast to this, monocopper doping into an  $\text{In}^{3+}$ -based  $T_5$  cluster was achieved in a two step strategy, with metal solvothermal insertion into discrete coreless  $T_5$  cluster  $[\text{Cd}_6\text{In}_{28}\text{S}_{52}(\text{SH})_4]^{12-}$  (space group  $I4_1/amd$ ) (Figure 1.26, left) realized at relatively mild temperature (150 °C) in mixed solvent (DBN, PR, and  $\text{H}_2\text{O}$ ), leading to the preparation of the discrete  $T_5$  cluster  $[\text{CuCd}_6\text{In}_{28}\text{S}_{52}(\text{H}_2\text{O})_4]^{7-}$  (crystallized in the same space group  $I4_1/amd$ ) (Figure 1.26, right).<sup>41</sup> Yield for the  $\text{Cu}^+$  insertion is ~71% based on the host cluster; the driving force for the reaction is proposed to be the reduction of the charge of anionic host. Also interesting, is that metal insertion is accompanied by four vertex  $\text{HS}^-$  sites being replaced with neutral water ligands, further decreasing the overall cluster charge. In a similar way, a single  $\text{Mn}^{2+}$  was inserted into the open  $T_5$   $[\text{Cd}_6\text{In}_{28}\text{S}_{52}(\text{SH})_4]^{12-}$  or  $[\text{Zn}_6\text{In}_{28}\text{S}_{52}(\text{SH})_4]^{12-}$  clusters, resulting in host-guest  $T_5$  cluster with drastically changed optical properties.<sup>42</sup> Thus, the  $\text{Mn}^{2+}$ -doped material shows a prominent red emission at room temperature with maximum at 630 nm, which is significantly red-shifted in comparison with both host clusters with weak green emission (~490 nm), and traditional  $\text{Mn}^{2+}$ -doped chalcogenides of group 12 metals with orange emission (~585 nm). An alkali metal cation ( $\text{Cs}^+$  or  $\text{Rb}^+$ ) was also ionothermally inserted into the central cavity of the hierarchical  $T_{2,2}$  cluster  $[\text{In}_8\text{Sn}_8\text{Se}_{34}]^{12-}$  with polyselenium  $\text{Se}_4$  chains interconnecting the clusters into a covalent 2D superstructure in a one-step process.<sup>63</sup> The larger size of the negatively-charged cavity in the host cluster (with a “missing”  $\{\text{EM}_4\}$  unit in the center in comparison with just a single M site in coreless- $T_5$  examples above) fits alkali metal cations but not alkaline earth ( $\text{Ca}^{2+}$ ,  $\text{Sr}^{2+}$ ) or transition ( $\text{Mn}^{2+}$ ,  $\text{Cu}^{2+}$ ) metals.

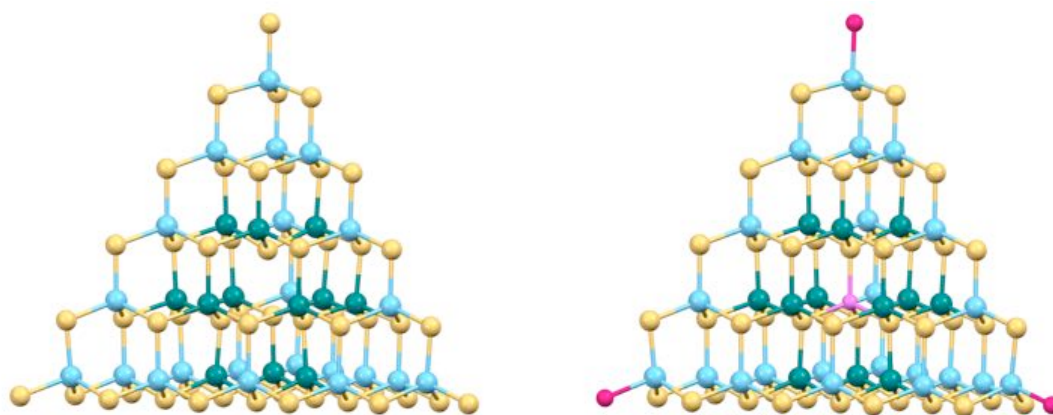


**Figure 1.26:** Discrete coreless  $T_5$   $[\text{Cd}_6\text{In}_{28}\text{S}_{52}(\text{SH})_4]^{12-}$  (left) as a host cluster and discrete  $T_5$  cluster  $[\text{CuCd}_6\text{In}_{28}\text{S}_{52}(\text{H}_2\text{O})_4]^{7-}$  (right) as a product of “solvothermal insertion” reaction. Metal sites with partial occupancy Cd/In are shown as dark cyan.<sup>41</sup>

### 1.5.5 Non-Tetrahedral Clusters with $M^{2+}$ Cations

Metal chalcogenide clusters with overall tetrahedral shape are the most common for large  $M^{2+}$  systems, especially those prepared by solvothermal approach, with only a few examples of other arrangements. One group of non-tetrahedral clusters includes relatively small, cage-like assemblies formed by group 12 metals where basic tetrahedra  $\{\text{ME}_4\}$  are linked by vertex-sharing. For instance, the discrete cubic cluster  $[\text{Cd}_8\text{L}_{14}(\text{dmf})_6(\text{NO}_3)]^+$  was prepared by a coordination chemistry approach using the fluorine-substituted ligand  $\text{L} = 3\text{-fluorophenylthiolate}$ .<sup>81</sup> In this “double four-ring” cationic cluster, eight  $\text{Cd}^{2+}$  are arranged at eight corners of a cube and bridged by twelve 3-fluorophenylthiolate ligands with S atoms being slightly out from the center of each cubic edge. Corner  $\text{Cd}^{2+}$  sites within the cube are bonded to 3-fluorophenylthiolate, *dmf* and  $\text{NO}_3^-$  ligands. The related cubic  $[\text{Cd}_8(\text{SPh})_{12}]^{4+}$  cluster (Figure 1.27) was previously prepared solvothermally as a 3D covalently bonded MOF, linked by in-situ-generated tetradentate 1,2,4,5-tetra(4-pyridyl)benzene ligands, coordinated to cube vertexes *via* the formation of Cd–N bonds.<sup>154</sup> Both cage-like cationic clusters are found to contain trapped anions ( $\text{NO}_3^-$  or  $\text{SO}_4^{2-}$ ), which come from starting reagents and may additionally play the role of template and structure-directing species. The structurally related  $[\text{Hg}_8(\mu_8\text{-S})(\text{SCH}_3)_{12}]^{2+}$  cluster has

an enclosed  $\mu_8$ -S inside its cage.<sup>155</sup> It should be mentioned that such positively charged molecular clusters (as well as 3D covalently-bonded frameworks of such clusters) are usually not accessible *via* solvothermal or ionothermal approaches. The likely reason is the difficulties with charge balancing and stabilization of the clusters and their superstructure in this case.

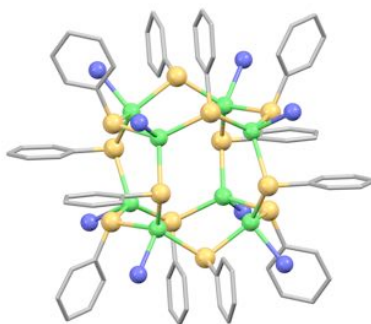


**Figure 1.27:** Cationic cubic  $[\text{Cd}_8(\text{SPh})_{12}]^{4+}$  cluster in 3D covalently bonded coordination polymer. Only N atoms from 1,2,4,5-tetra(4-pyridyl)benzene ligands are shown. A trapped anion is omitted for clarity.<sup>154</sup>

### 1.5.6 Ring- or Cage-Like Clusters with $M^{3+}$ , $M^{4+}$ and Mixed Cations

Discrete ring-shaped clusters, as well as cage-like assemblies in which metal cations are bridged by group 16 elements (oxygen or chalcogen) are relatively wide-spread for transition metals (*e.g.*, some transition metal sulfide rings, giant oxomolybdate, oxothiomolybdate, and polyoxometalate wheels or cages).<sup>156–159</sup> In contrast, such large clusters are rather unusual for group 13 and 14 metals.

Unlike the large tetrahedral metal chalcogenide clusters which represent regular fragments of related solid-state ME, ring- and cage-like clusters possess laced structures: basic tetrahedral  $\{\text{ME}_4\}$  units are combined into polymeric formations (linear and branched, respectively) *via* vertex and/or edge sharing. The higher structural flexibility of the heavier chalcogenides allows geometrical adjustment in forming arching fragments. Chalcogenide sites are generally low-coordinate (mostly  $\mu$ -, seldom  $\mu_3\text{-E}^{2-}$ ); local charge balance is maintained with high-valence metal ions. While the M : E ratio in these ring- and cage-like clusters is higher in comparison with large tetrahedral clusters ( $\sim 1 : 2.0$  vs.



$\sim 1 : 1.7$ , respectively), the presence of  $M^{3+}$  and  $M^{4+}$  cations contributes to a decrease of the negative charge. Tracery-like frameworks allow for an arrangement of a large number of charge balancing species around the anionic cluster without steric hindrance. The effect of structure-directing and templating agents on the assembly of these structures is suggested to be of a great importance. A few known examples of their solvothermal and ionothermal preparation are described below.

The previously unknown group 15 metals ring-shaped anionic cluster  $[\text{Sb}_6\text{S}_{12}]^{6-}$  (formed by six corner-sharing  $\text{SbS}_3$  pyramids) was solvothermally prepared using the multidentate amine N-(aminoethyl)-1,3-propanediamine (*aepa*) as a reaction solvent.<sup>160</sup> *In-situ* formed  $[\text{Ni}(\text{aepa})_2]^{2+}$  complexes serve to charge-balance, template and stabilize the ring-shaped clusters into a superstructure formed through hydrogen bonding and van der Waals interactions (space group  $R\bar{3}$ , featuring two crystallographically independent ring-shaped anions with slightly different geometric parameters, see Figure 1.28).

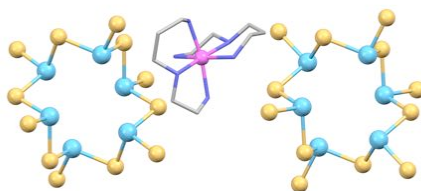


**Figure 1.28:** Ring-shaped anionic clusters  $[\text{Sb}_6\text{S}_{12}]^{6-}$  with metal-complex cation  $[\text{Ni}(\text{aepa})_2]^{2+}$ .<sup>160</sup>

The much larger and structurally-sophisticated cluster  $[\text{In}_{18}\text{Te}_{30}(\text{dach})_6]^{6-}$  was solvothermally prepared in a mixed solvent of 1,2-diaminocyclohexane (*dach*) and water.<sup>39</sup> As opposed to single-chain rings like in the  $[\text{Sb}_6\text{S}_{12}]^{6-}$  anion, this cluster has a double-decker ring or wheel topology (Figure 1.29). The structure of the highly-symmetrical  $\text{In}_{18}\text{Te}_{30}$  wheel (point group pseudo- $D_{3d}$  when ignoring the *dach* ligands) can be viewed as a combination of six  $\{\text{In}_2\text{Te}_6\}$  (representing two edge-sharing basic tetrahedra  $\text{ME}_4$ ) with six  $\{\text{InTe}_3\text{N}_2\}$  units. The latter unit is formed from the basic  $\text{ME}_4$  tetrahedron while one E site is replaced by two N from the chelating amine *dach*; it contains an unusual five-coordinated  $\text{In}^{3+}$  cation that possesses trigonal bipyramidal geometry. The organic ligand *dach* can be considered as “decorating”, in contrast with bridging ligands (*e.g.*,  $\mu$ -chalcogenolates) in some well-known<sup>161,162</sup> or recently

reported<sup>163,164</sup> metal chalcogenide rings. The  $2\text{H}^+-dach\cdot\text{H}_2\text{O}$  unit, assembled by hydrogen bonding, was found positioned as an axle with  $\text{H}_2\text{O}$  molecule located exactly at the centre of the  $\text{In}_{18}\text{Te}_{30}$  wheel. This unit is proposed to act as a template in the formation of the anionic cluster, while metal-complex cations  $[\text{Mn}(dach)_3]^{2+}$  provide additional charge-balance, templating and stabilization of the superstructure with overall composition  $[\text{Mn}(dach)_3]_2[\text{In}_{18}\text{Te}_{30}(dach)_6]\cdot 2\text{H}^+-dach\cdot\text{H}_2\text{O}$  (space group  $Pn\bar{m}$ ).

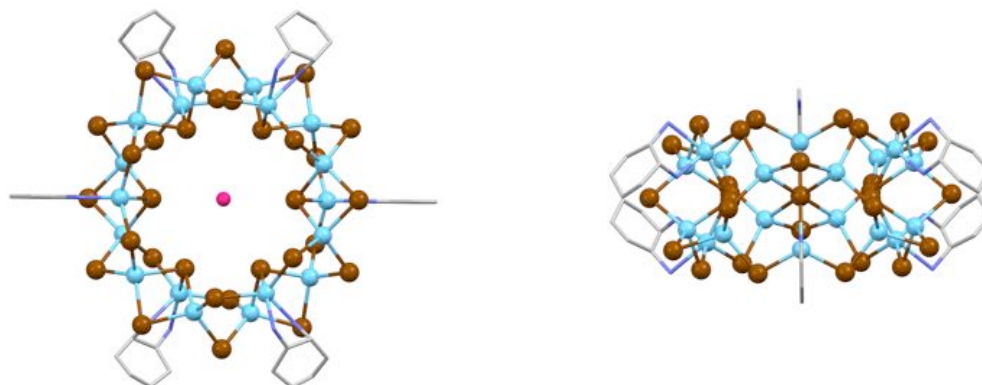


**Figure 1.29:** Two different orientations of wheel-shaped  $[\text{In}_{18}\text{Te}_{30}(dach)_6]^{6-}$  anionic cluster with  $\text{H}_2\text{O}$  molecule in the central  $2\text{H}^+-dach\cdot\text{H}_2\text{O}$  unit ( $\text{H}^+-dach$  not shown) acting as template for the wheel assembly.<sup>39</sup>

The analogous wheel-shaped cluster  $[\text{In}_{18}\text{Te}_{30}(dapn)_6]^{6-}$ , where  $dapn = 1,3$ -diaminepropane, was prepared with such metal-complex cations as  $[\text{Fe}(phen)_3]^{2+}$  or  $[\text{Ni}(phen)_3]^{2+}$  and isolated as air-stable crystals.<sup>165</sup> Unlike the  $[\text{In}_{18}\text{Te}_{30}(dach)_6]^{6-}$  anion, where  $dach$  is chelated to the  $\text{In}^{3+}$  giving  $\{\text{InTe}_3\text{N}_2\}$  units,  $dapn$  was found to react as a monodentate ligand giving  $\{\text{InTe}_3\text{N}\}$  units with tetrahedral geometry in  $[\text{In}_{18}\text{Te}_{30}(dapn)_6]^{6-}$  cluster. In the superstructures with composition  $[\text{M}(phen)_3]_2[\text{In}_{18}\text{Te}_{30}(dapn)_6]\cdot 2\text{H}^+-dapn\cdot dapn$  with  $\text{M} = \text{Fe}$  or  $\text{Ni}$  (space group  $P-1$ ) clockwise ( $\Delta$ )  $[\text{M}(phen)_3]^{2+}$  cation couples with anticlockwise ( $\Lambda$ )  $[\text{M}(phen)_3]^{2+}$  through  $\pi$ - $\pi$  interactions forming dimeric species. Such positively charged dimers are about the same size as the wheel-shaped anionic cluster  $[\text{In}_{18}\text{Te}_{30}(dapn)_6]^{6-}$  and bonded with the latter through electrostatic and additional anion- $\pi$  interactions (Figure 1.30). The solvothermal synthesis of  $[\text{In}_{18}\text{Te}_{30}(dapn)_6]^{6-}$  required substantially higher temperature and much longer reaction time in comparison with that of  $[\text{In}_{18}\text{Te}_{30}(dach)_6]^{6-}$ : the

optimized reaction conditions are 180 °C / 28-30 days and 140 °C / 4 days, respectively. This can be related to the use of elemental indium instead of  $\text{InCl}_3$  and/or different properties of *dapn* as solvent (e.g., bp 140 °C) in comparison with mixed system *dach* :  $\text{H}_2\text{O}$  = 7 : 3 (with bp of *dach* ~80 °C). *Dapn* ligands are significantly disordered, while chelating and relatively more rigid *dach* molecules were located and refined using single-crystal X-ray analysis.

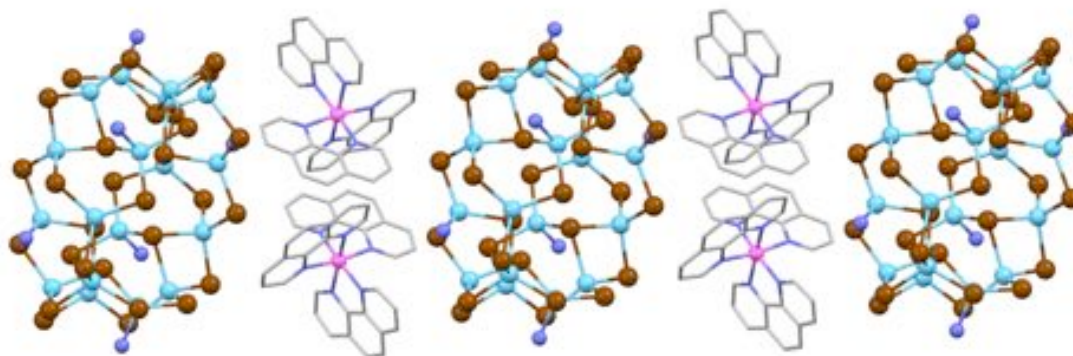


**Figure 1.30:** Fragment of packing of anionic clusters  $[\text{In}_{18}\text{Te}_{30}(\text{dapn})_6]^{6-}$  and metal-complex cations  $[\text{Ni}(\text{phen})_3]^{2+}$ , forming dimers through  $\pi$ - $\pi$  interactions. Dangling *dapn* ligand fragments, except N atoms bonded to In, are omitted for clarity.<sup>165</sup>

The combination of a mixed solvent of *dach* and  $\text{H}_2\text{O}$  with  $[\text{Bmim}]\text{Br}$  (Bmim = 1-butyl-3-methyl-imidazolium) allowed for the solvothermal preparation of the binary superstructure, combining wheel-shaped  $[\text{In}_{18}\text{Se}_{30}(\text{dach})_6]^{6-}$  with the triangular double-decker ring  $[\text{Mn}_9\text{In}_{33}\text{Se}_{60}(\text{dach})_{24}]^{3-}$  clusters in a 1 : 2 ratio (Figure 1.31, right).<sup>166</sup> While the first cluster is the Se-containing analog of  $[\text{In}_{18}\text{Te}_{30}(\text{dach})_6]^{6-}$ , the second is a novel discrete ring structure possessing a different topology and containing both  $\text{M}^{3+}$  group 13 and  $\text{M}^{2+}$  transition metal cations. The tangled structure of this triangular ring can be viewed as a complex combination of 27 basic  $\{\text{InSe}_4\}$  tetrahedral and 6  $\{\text{InSe}_3\text{N}_2\}$  trigonal bipyramidal units through either vertex- or edge-sharing (Figure 1.31, left). The outer diameter of resulting  $\text{In}_{33}\text{Se}_{60}$  ring was calculated as ~2.5 nm (while measuring between two opposite  $\text{Se}^{2-}$  sites). The  $\text{In}_{33}\text{Se}_{60}$  ring is further decorated by 9  $\{\text{Mn}(\text{dach})_2\}$  bridging units (distorted octahedral geometry for Mn), with three units on the inside, three on the outside and the other three on a same face as the ring. The discrete clusters of

$[\text{Mn}_9\text{In}_{33}\text{Se}_{60}(\text{dach})_{24}]^{3-}$  are discernable on TEM images. The charge balance in the two-anion superstructure is achieved with combination of  $[\text{Mn}(\text{dach})_3]^{2+}$ ,  $\text{Mn}^{2+}$ ,  $\text{H}^+$ -dach and  $\text{Cl}^-$ . The overall composition (deduced from both single crystal X-ray diffraction data and a set of auxiliary analyses) is  $\text{Mn}_2[\text{Mn}(\text{dach})_3]_3[\text{Mn}_9\text{In}_{33}\text{Se}_{60}(\text{dach})_{24}]_2[\text{In}_{18}\text{Se}_{30}(\text{dach})_6] \cdot (\text{H}^+ - \text{dach})_{11}\text{Cl}_9 \cdot 7\text{H}_2\text{O}$ ; space group  $R-3c$ . The assembly of the triangular double-decker ring  $[\text{Mn}_9\text{In}_{33}\text{Se}_{60}(\text{dach})_{24}]^{3-}$  is proposed to be structure-directed and templated by a  $\text{Mn}^{2+}$  cation in the center of the ring through  $\text{Mn} \cdots \text{N}$  inverse second-sphere coordination. The ionic solvent  $[\text{Bmim}]\text{Br}$  takes part in the formation of large ring-shaped anions by increasing the solubility of the products, but is not present in the final compound.

Probing the optical properties of the material containing  $[\text{Mn}_9\text{In}_{33}\text{Se}_{60}(\text{dach})_{24}]^{3-}$  and  $[\text{In}_{18}\text{Se}_{30}(\text{dach})_6]^{6-}$  clusters via UV-Vis diffuse reflectance spectroscopy showed that band gap (1.9 eV) is narrower than was expected for the nanodimensional  $\text{In}_2\text{Se}_3$ . This was attributed to a resonance effect due to a ring-like structure.

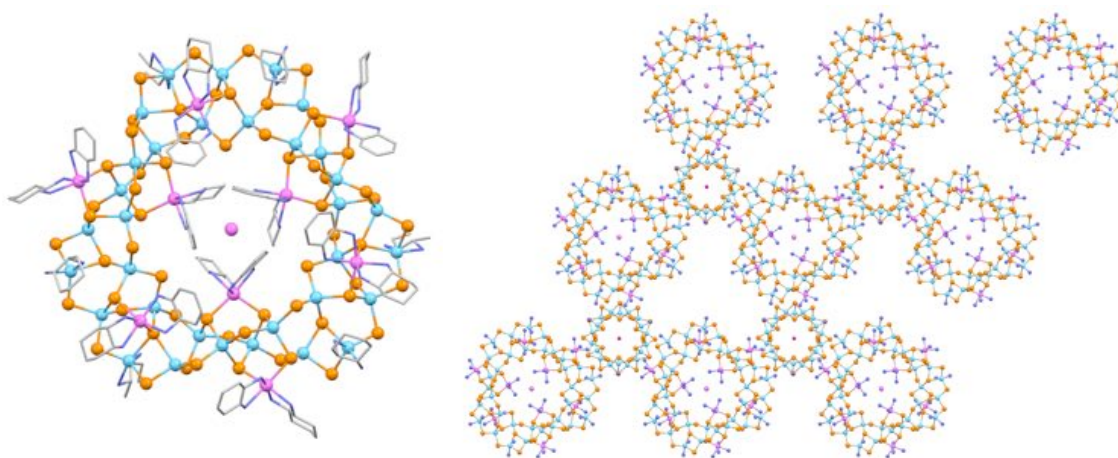


**Figure 1.31:** Triangular ring-shaped anionic cluster  $[\text{Mn}_9\text{In}_{33}\text{Se}_{60}(\text{dach})_{24}]^{3-}$  with the central  $\text{Mn}^{2+}$  cation acting as template and structure-directing agent (*left*). A fragment of packing in the binary superstructure combining larger  $[\text{Mn}_9\text{In}_{33}\text{Se}_{60}(\text{dach})_{24}]^{3-}$  and smaller  $[\text{In}_{18}\text{Se}_{30}(\text{dach})_6]^{6-}$  ring-shaped clusters; dach ligands, except N atoms, are omitted for clarity (*right*). Clusters are shown along the  $c$  direction.<sup>166</sup>

Discrete, cage-like anionic clusters of groups 13 and 14 metal-chalogenides are rare; especially those prepared under solvothermal or ionothermal conditions. For instance, the

reaction of  $[\text{K}_4(\text{H}_2\text{O})_3][\text{Ge}_4\text{Se}_{10}]$  and  $\text{SnCl}_4 \cdot 5\text{H}_2\text{O}$  in  $[\text{Bmmim}][\text{BF}_4]$  with 2,6-dimethylmorpholine as an additive under ionothermal conditions yielded the discrete cage-like cluster  $[\text{Sn}_{36}\text{Ge}_{24}\text{Se}_{132}]^{24-}$  forming ordered superstructure (space group  $P2_1/c$ ).<sup>40</sup> This cluster anion is comprised of two different types of building blocks:  $\{\text{Ge}_3\text{Se}_9\}$ , which represents a trimer of corner-sharing basic tetrahedra  $\text{GeSe}_4$  (Figure 1.32, top left), and  $\{\text{Sn}_6\text{Se}_{18}\}$ , which contains a dimer of  $\text{Sn}_3\text{Se}_4$  semicubes doubly-bridged by two Se (Figure 1.32, top right). A similar structural motif (*i.e.*,  $\{\text{M}_3\text{Se}_9\}$  unit; see Figure 1.32, top left) is also found in a smaller 72-atom supercubooctahedron cluster  $[\text{Ga}_{15}\text{Ge}_9\text{Se}_{48}]^{15-}$ , prepared by the solid state reaction in a CsCl flux.<sup>167</sup> In 192-atom cluster  $[\text{Sn}_{36}\text{Ge}_{24}\text{Se}_{132}]^{24-}$ , eight  $\{\text{Ge}_3\text{Se}_9\}$  are located at the vertexes of a cube, while six  $\{\text{Sn}_6\text{Se}_{18}\}$  occupy the vertexes of an octahedron inscribed inside of this cube; the two types of units are linked *via* the sharing of common Se sites. The resulting cluster is nearly perfectly spherical in shape, with an outer diameter of 2.83 nm (including van der Waals radii of the surface atoms), a cavity with a diameter of 1.16 nm and twelve windows with cross sections of 0.56-0.88 nm (Figure 1.32, bottom left). Similar, discrete cage-like clusters with partial metal site disorder  $[\text{Bmim}]_{24}[\text{Sn}_{32.5}\text{Ge}_{27.5}\text{Se}_{132}]$  was prepared in  $[\text{Bmim}][\text{BF}_4]$  and crystallized in the space group  $P-1$  (Figure 1.32, bottom right). In this superstructure half of the 24 charge-balancing  $[\text{Bmim}]^+$  cations is arranged at the windows, while the other half is outside of the highly charged cage-like anion. The amine additive is proposed to participate in the formation of Sn-containing units, although the mechanism is not determined yet.

Potentially, such cage-like metal chalcogenide clusters with a large confined space can be used as “molecular flasks” to host species and perform reactions, as the windows of the cluster are not blocked by covalently bonded ligands. Indeed, preliminary results show that  $[\text{Sn}_{36}\text{Ge}_{24}\text{Se}_{132}]^{24-}$  can trap  $\text{I}_2$  molecules and induce heterolytic I–I bond cleavage.

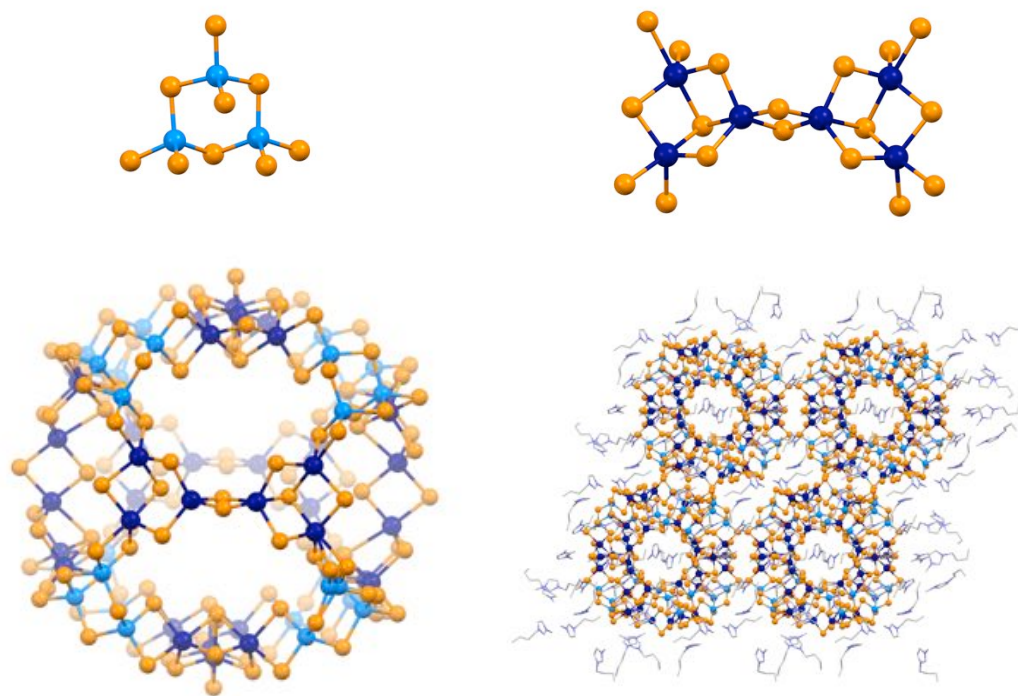


**Figure 1.32:** Building units of discrete cage-like clusters:  $\{M_3Se_9\}$  (*top left*) and  $\{M_6Se_{18}\}$  (*top right*). The discrete cage-like cluster  $[Sn_{36}Ge_{24}Se_{132}]^{24-}$  (*bottom left*), composed of eight  $\{Ge_3Se_9\}$  and six  $\{Sn_6Se_{18}\}$  units. A fragment of packing of cage-like anions and charge-balancing  $[Bmim]^+$  cations (viewed along the  $b$  direction) (*bottom right*). Ge sites are shown as blue and Sn as dark blue.<sup>40</sup>

## 1.6 Scope of the Thesis

Solvothermal and ionothermal synthetic routes, utilizing reactions in solution under increased temperature and pressure, have been proven to be efficient for the synthesis of metal chalcogenide ME clusters and their crystalline superstructures. Moreover, literature review shows that performing reactions in such conditions has a great potential for the preparation of new nanoscopic materials with unique structural features and physical properties that are inaccessible using other techniques. For group 12–16 systems (metal  $M = Zn, Cd, Hg$ ; chalcogen  $E = S, Se, Te$ ), there are now well developed routes to prepare tetrahedral clusters, stabilized by a shell of phenylchalcogenolate ligands  $PhE^-$  (*e.g.*,  $[Cd_{17}Se_4(SePh)_{28}]^{2-}$  and  $[Cd_{32}S_{14}(SPh)_{36}(dmf)_4]$ ).<sup>70,117</sup> Such monodisperse nanoscopic semiconductors have been attracting much interest due to their size-dependent electronic

and photophysical properties.<sup>19,20</sup> Self-assembly into crystalline superlattices, for which ordered array exists at a micrometer scale, helps in efficient integration of nanoscopic semiconductors into optical and electronic devices for industrial application without losing their “nano advantages”.<sup>22,26,27</sup> However, a principle limitation in size using established preparative methods still exists, and the largest isolated and characterized tetrahedral clusters for group 12–16 systems with phenylchalcogenolate ligands are the related anionic  $[\text{Cd}_{54}\text{S}_{32}(\text{SPh})_{48}(\text{H}_2\text{O})_4]^{4-}$ ,  $[\text{Cd}_{54}\text{Se}_{32}(\text{SPh})_{48}(\text{H}_2\text{O})_4]^{4-}$ , and the neutral  $[\text{Cd}_{54}\text{S}_{28}(\text{SPh})_{52}(\text{dmf})_4]$  framework,<sup>57,71</sup> each with equivalent spherical diameter of  $\sim 1.3$  nm.

This prompted us to develop a novel approach for the preparation of nanoscopic CdE materials utilizing conversion of cadmium phenylchalcogenolate precursor  $(\text{Me}_4\text{N})_2[\text{Cd}(\text{EPh})_4]$  (where E = S or Se) under solvothermal conditions. The synthetic target is superstructures of nanoscopic CdE, including both crystalline superlattices of large discrete clusters and superstructures with more complex morphology. The research objectives of this project are to reveal the parameters that govern formation of nanoscopic CdE clusters (or primary building blocks) and their subsequent self-assembly into particular arrangements. For instance, the role of halide-containing additives on the size of CdE clusters and the type of its superstructure was examined in Chapters 2, 3 and 5.

The research involves exploring the mechanism of precursor conversion (including  $^1\text{H}$  NMR analysis of intermediates and by-products in solution) (reported in Chapter 2), since the formation of large  $\text{M}_x\text{E}_y(\text{EPh})_z$  clusters from mononuclear metal chalcogenolate complex, without an additional chalcogen source, has not been previously reported. The developing synthetic approach resulted in the preparation of superstructures of nanoscopic CdS (Chapters 2 and 3) as well as CdSe (Chapter 5). In particular, 3D cubic superlattices of molecular CdS clusters of 1.9 and 2.3 nm in size were prepared and characterized by a set of techniques, including Raman spectroscopy and TGA, as described in Chapters 2 and 3.

The selection of characterization techniques for the nanoscopic materials prepared in this thesis was motivated by two main goals. First, it is to obtain structural information by methods complementary to single crystal X-ray diffraction, such as  $^{111}\text{Cd}$  SSNMR

(Chapter 4) and electron microscopy and tomography (Chapters 2, 3, and 5). Second, it is to examine their optical properties, including UV–vis absorption and photoluminescence studies under various conditions (Chapters 2 and 5). Complex analysis of the composition, structure, and optical properties of nanoscopic CdE materials in comparison with those of related compounds (*e.g.*, previous members of the same tetrahedral cluster family) was performed in order to reveal similarities with previously established trends or to explain unexpected results. An example of the latter is the distinct, room temperature emission observed both in solution and the solid state for  $[\text{Cd}_{54}\text{Se}_{32}(\text{SePh})_{48}(\text{dmf})_4]^{4-}$  (Chapter 5), while an absence of such emission was reported previously for smaller clusters. The importance of the current project lies in improving an ability to manipulate the size and organization of primary cluster building blocks into particular superstructures, and to tailor the photophysical properties of the resulting material, which enables the creation of new multifunctional systems and broadens potential area of application.

### 1.7 References

- (1) Dance, I. G. *Polyhedron* **1986**, 5 (5), 1037.
- (2) Müller, A.; Diemann, E. *Adv. Inorg. Chem.* **1987**, 31, 89.
- (3) Ansari, M.; Ibers, J. *Coord. Chem. Rev.* **1990**, 100, 223.
- (4) Krebs, B.; Henkel, G. *Angew. Chem.-Int. Ed. Engl.* **1991**, 30 (7), 769.
- (5) Roof, L.; Kolis, J. *Chem. Rev.* **1993**, 93 (3), 1037.
- (6) Dance, I.; Fisher, K. *Prog. Inorg. Chem. Vol 41* **1994**, 41, 637.
- (7) Arnold, J. In *Progress in Inorganic Chemistry, Vol 43*; Karlin, K. D., Ed.; John Wiley & Sons Inc: Hoboken, 1995; Vol. 43, pp 353–417.
- (8) Alivisatos, A. P. *Science* **1996**, 271 (5251), 933.
- (9) DeGroot, M. W.; Corrigan, J. F. In *Comprehensive Coordination Chemistry II / M. Fujita, A. Powell, C. Creutz (eds.). C.*; Amsterdam: Elsevier, 2004; Vol. 7, pp 57–123.
- (10) Corrigan, J. F.; DeGroot, M. W. In *The chemistry of nanomaterials: synthesis, properties and applications / C. N. R. Rao, A. Müller, A. K. Cheetham (eds.).*; Weinheim: Wiley-VCH; Chichester: John Wiley, 2004; Vol. 2, pp 418–451.
- (11) Corrigan, J. F.; Fuhr, O.; Fenske, D. *Adv. Mater.* **2009**, 21 (18), 1867.
- (12) Kübel, C.; Voigt, A.; Schoenmakers, R.; Otten, M.; Su, D.; Lee, T.-C.; Carlsson, A.; Bradley, J. *Microsc. Microanal.* **2005**, 11 (5), 378.
- (13) Friedrich, H.; Gomme, C. J.; Overgaag, K.; Meeldijk, J. D.; Evers, W. H.; Nijs, B. de; Boneschanscher, M. P.; de Jongh, P. E.; Verkleij, A. J.; de Jong, K. P.; van Blaaderen, A.; Vanmaekelbergh, D. *Nano Lett.* **2009**, 9 (7), 2719.
- (14) Evers, W. H.; Friedrich, H.; Filion, L.; Dijkstra, M.; Vanmaekelbergh, D. *Angew. Chem. Int. Ed.* **2009**, 48 (51), 9655.
- (15) Boneschanscher, M. P.; Evers, W. H.; Qi, W.; Meeldijk, J. D.; Dijkstra, M.; Vanmaekelbergh, D. *Nano Lett.* **2013**, 13 (3), 1312.



- (16) Alivisatos, A. P. *J. Phys. Chem.* **1996**, *100* (31), 13226.
- (17) Nirmal, M.; Brus, L. *Acc. Chem. Res.* **1999**, *32* (5), 407.
- (18) Wang, Y.; Herron, N. *Phys. Rev. B* **1990**, *42* (11), 7253.
- (19) Soloviev, V. N.; Eichhöfer, A.; Fenske, D.; Banin, U. *J. Am. Chem. Soc.* **2000**, *122* (11), 2673.
- (20) Soloviev, V. N.; Eichhöfer, A.; Fenske, D.; Banin, U. *J. Am. Chem. Soc.* **2001**, *123* (10), 2354.
- (21) Collier, C. P.; Vossmeier, T.; Heath, J. R. *Annu. Rev. Phys. Chem.* **1998**, *49*, 371.
- (22) Gao, Y.; Tang, Z. *Small* **2011**, *7* (15), 2133.
- (23) Xie, J.; Cao, S.; Good, D.; Wei, M.; Ren, X. *Inorg. Chem.* **2010**, *49* (4), 1319.
- (24) Zhang, Q.; Wu, T.; Bu, X.; Tran, T.; Feng, P. *Chem. Mater.* **2008**, *20* (13), 4170.
- (25) Yang, H.; Tao, W.; Le, W.; PingYun, F. *Sci. China-Chem.* **2013**, *56* (4), 423.
- (26) Talapin, D. V.; Lee, J.-S.; Kovalenko, M. V.; Shevchenko, E. V. *Chem. Rev.* **2010**, *110* (1), 389.
- (27) Nozik, A. J.; Beard, M. C.; Luther, J. M.; Law, M.; Ellingson, R. J.; Johnson, J. C. *Chem. Rev.* **2010**, *110* (11), 6873.
- (28) Konstantatos, G.; Sargent, E. H. *Nat. Nanotechnol.* **2010**, *5* (6), 391.
- (29) Wang, F.; Tan, W. B.; Zhang, Y.; Fan, X.; Wang, M. *Nanotechnology* **2006**, *17* (1), R1.
- (30) Bailey, R. E.; Smith, A. M.; Nie, S. *Phys. E Low-Dimens. Syst. Nanostructures* **2004**, *25* (1), 1.
- (31) Anson, C. E.; Eichhöfer, A.; Issac, I.; Fenske, D.; Fuhr, O.; Sevillano, P.; Persau, C.; Stalke, D.; Zhang, J. *Angew. Chem.-Int. Ed.* **2008**, *47* (7), 1326.
- (32) Liu, Y.; Najafabadi, B. K.; Fard, M. A.; Corrigan, J. F. *Angew. Chem.-Int. Ed.* **2015**, *54* (16), 4832.
- (33) Palchik, O.; Iyer, R. G.; Liao, J. H.; Kanatzidis, M. G. *Inorg. Chem.* **2003**, *42* (17), 5052.
- (34) Palchik, O.; Iyer, R. G.; Canlas, C. G.; Weliky, D. P.; Kanatzidis, M. G. *Z. Anorg. Allg. Chem.* **2004**, *630* (13–14), 2237.
- (35) Qian, Y. T.; Gu, Y. L.; Lu, J. In *The chemistry of nanomaterials: synthesis, properties and applications / C.N.R. Rao, A. Müller, A.K. Cheetham (eds.)*; Weinheim: Wiley-VCH; Chichester: John Wiley, 2004; Vol. 1, pp 170–207.
- (36) Xu, B.; Wang, X. *Dalton Trans.* **2012**, *41* (16), 4719.
- (37) Xiong, W.-W.; Zhang, G.; Zhang, Q. *Inorg. Chem. Front.* **2014**, *1* (4), 292.
- (38) Wu, T.; Zuo, F.; Wang, L.; Bu, X.; Zheng, S.-T.; Ma, R.; Feng, P. *J. Am. Chem. Soc.* **2011**, *133* (40), 15886.
- (39) Wang, Y.-H.; Luo, W.; Jiang, J.-B.; Bian, G.-Q.; Zhu, Q.-Y.; Dai, J. *Inorg. Chem.* **2012**, *51* (3), 1219.
- (40) Lin, Y.; Massa, W.; Dehnen, S. *J. Am. Chem. Soc.* **2012**, *134* (10), 4497.
- (41) Wu, T.; Zhang, Q.; Hou, Y.; Wang, L.; Mao, C.; Zheng, S.-T.; Bu, X.; Feng, P. *J. Am. Chem. Soc.* **2013**, *135* (28), 10250.
- (42) Lin, J.; Zhang, Q.; Wang, L.; Liu, X.; Yan, W.; Wu, T.; Bu, X.; Feng, P. *J. Am. Chem. Soc.* **2014**, *136* (12), 4769.
- (43) Wu, T.; Bu, X.; Liao, P.; Wang, L.; Zheng, S.-T.; Ma, R.; Feng, P. *J. Am. Chem. Soc.* **2012**, *134* (8), 3619.

- (44) Xiong, W.-W.; Li, J.-R.; Hu, B.; Tan, B.; Li, R.-F.; Huang, X.-Y. *Chem. Sci.* **2012**, 3 (4), 1200.
- (45) Cheetham, A. K.; Ferey, G.; Loiseau, T. *Angew. Chem.-Int. Ed.* **1999**, 38 (22), 3268.
- (46) Bu, X.; Zheng, N.; Feng, P. *Chem.-Eur. J.* **2004**, 10 (14), 3356.
- (47) Feng, P.; Bu, X.; Zheng, N. *Acc. Chem. Res.* **2005**, 38 (4), 293.
- (48) Vaqueiro, P. *Dalton Trans.* **2010**, 39 (26), 5965.
- (49) Wu, T.; Wang, L.; Bu, X.; Chau, V.; Feng, P. *J. Am. Chem. Soc.* **2010**, 132 (31), 10823.
- (50) Dehnen, S.; Eichhöfer, A.; Fenske, D. *Eur. J. Inorg. Chem.* **2002**, No. 2, 279.
- (51) Dehnen, S.; Eichhöfer, A.; Corrigan, J. F.; Fenske, D. In *Nanoparticles: From Theory to Application*. G Schmid Ed; 2004: Weinheim, Germany: Wiley-VCH; pp 107–185.
- (52) Fuhr, O.; Dehnen, S.; Fenske, D. *Chem. Soc. Rev.* **2013**, 42 (4), 1871.
- (53) Moller, A.; Amann, P.; Kataev, V.; Schittner, N. *Z. Anorg. Allg. Chem.* **2004**, 630 (6), 890.
- (54) Lin, W.-Q.; Liao, X.-F.; Jia, J.-H.; Leng, J.-D.; Liu, J.-L.; Guo, F.-S.; Tong, M.-L. *Chem.-Eur. J.* **2013**, 19 (37), 12254.
- (55) Li, H. L.; Laine, A.; O’Keeffe, M.; Yaghi, O. M. *Science* **1999**, 283 (5405), 1145.
- (56) Eichhöfer, A.; Fenske, D. *J. Chem. Soc.-Dalton Trans.* **2000**, No. 6, 941.
- (57) Zheng, N. F.; Bu, X. H.; Lu, H. W.; Zhang, Q. C.; Feng, P. Y. *J. Am. Chem. Soc.* **2005**, 127 (34), 11963.
- (58) Zhang, Q.; Bu, X.; Han, L.; Feng, P. *Inorg. Chem.* **2006**, 45 (17), 6684.
- (59) Wu, T.; Bu, X.; Zhao, X.; Khazhakyann, R.; Feng, P. *J. Am. Chem. Soc.* **2011**, 133 (24), 9616.
- (60) Wang, L.; Wu, T.; Zuo, F.; Zhao, X.; Bu, X.; Wu, J.; Feng, P. *J. Am. Chem. Soc.* **2010**, 132 (10), 3283.
- (61) Li, H.; Kim, J.; O’Keeffe, M.; Yaghi, O. M. *Angew. Chem.-Int. Ed.* **2003**, 42 (16), 1819.
- (62) Han, X.; Xu, J.; Wang, Z.; Liu, D.; Wang, C. *Chem. Commun.* **2015**, 51 (18), 3919.
- (63) Du, C.-F.; Li, J.-R.; Zhang, B.; Shen, N.-N.; Huang, X.-Y. *Inorg. Chem.* **2015**, 54 (12), 5874.
- (64) Su, W. P.; Huang, X. Y.; Li, J.; Fu, H. X. *J. Am. Chem. Soc.* **2002**, 124 (44), 12944.
- (65) Wang, C.; Bu, X. H.; Zheng, N. F.; Feng, P. Y. *J. Am. Chem. Soc.* **2002**, 124 (35), 10268.
- (66) Han, X.; Wang, Z.; Liu, D.; Xu, J.; Liu, Y.; Wang, C. *Chem. Commun.* **2014**, 50 (7), 796.
- (67) Lin, Q.; Bu, X.; Feng, P. *Chem. Commun.* **2014**, 50 (31), 4044.
- (68) Zheng, N. F.; Bu, X. H.; Feng, P. Y. *Angew. Chem.-Int. Ed.* **2004**, 43 (36), 4753.
- (69) Beecher, A. N.; Yang, X.; Palmer, J. H.; LaGrassa, A. L.; Juhas, P.; Billinge, S. J. L.; Owen, J. S. *J. Am. Chem. Soc.* **2014**, 136 (30), 10645.
- (70) Herron, N.; Calabrese, J.; Farneth, W.; Wang, Y. *Science* **1993**, 259 (5100), 1426.
- (71) Bendova, M.; Puchberger, M.; Schubert, U. *Eur. J. Inorg. Chem.* **2010**, No. 21, 3299.

- (72) Feng, M.-L.; Kong, D.-N.; Xie, Z.-L.; Huang, X.-Y. *Angew. Chem.-Int. Ed.* **2008**, *47* (45), 8623.
- (73) Lei, Z.-X.; Zhu, Q.-Y.; Zhang, X.; Luo, W.; Mu, W.-Q.; Dai, J. *Inorg. Chem.* **2010**, *49* (10), 4385.
- (74) Zeng, X.; Yao, X.; Zhang, J.; Zhang, Q.; Wu, W.; Chai, A.; Wang, J.; Zeng, Q.; Xie, J. *Inorg. Chem. Front.* **2015**, *2* (2), 164.
- (75) Liu, Y.; Lin, Q.; Zhang, Q.; Bu, X.; Feng, P. *Chem.-Eur. J.* **2014**, *20* (27), 8297.
- (76) Xie, J.; Batten, S. R.; Zou, Y.; Ren, X. *Cryst. Growth Des.* **2011**, *11* (1), 16.
- (77) Vossmeier, T.; Reck, G.; Schulz, B.; Katsikas, L.; Weller, H. *J. Am. Chem. Soc.* **1995**, *117* (51), 12881.
- (78) Voggu, R.; Biswas, K.; Govindaraj, A.; Rao, C. N. R. *J. Phys. Chem. B* **2006**, *110* (42), 20752.
- (79) Dass, A.; Guo, R.; Tracy, J. B.; Balasubramanian, R.; Douglas, A. D.; Murray, R. W. *Langmuir* **2008**, *24* (1), 310.
- (80) Pengo, P.; Pasquato, L. *J. Fluor. Chem.* **2015**, *177*, 2.
- (81) Zhang, Q.; Lin, Z.; Bu, X.; Wu, T.; Feng, P. *Chem. Mater.* **2008**, *20* (10), 3239.
- (82) Emge, T. J.; Romanelli, M. D.; Moore, B. F.; Brennan, J. G. *Inorg. Chem.* **2010**, *49* (16), 7304.
- (83) Holligan, K.; Rogler, P.; Rehe, D.; Pamula, M.; Kornienko, A. Y.; Emge, T. J.; Krogh-Jespersen, K.; Brennan, J. G. *Inorg. Chem.* **2015**, *54* (18), 8896.
- (84) Adams, R. D.; Zhang, B.; Murphy, C. J.; Yeung, L. K. *Chem. Commun.* **1999**, No. 4, 383.
- (85) Løver, T.; Bowmaker, G. A.; Seakins, J. M.; Cooney, R. P.; Henderson, W. J. *Mater. Chem.* **1997**, *7* (4), 647.
- (86) Hiratani, T.; Konishi, K. *Angew. Chem.-Int. Ed.* **2004**, *43* (44), 5943.
- (87) Nguyen, K. A.; Pachter, R.; Day, P. N.; Su, H. *J. Chem. Phys.* **2015**, *142* (23), 234305.
- (88) Lebold, T. P.; Stringle, D. L. B.; Workentin, M. S.; Corrigan, J. F. *Chem. Commun.* **2003**, No. 12, 1398.
- (89) Wallbank, A. I.; Borecki, A.; Taylor, N. J.; Corrigan, J. F. *Organometallics* **2005**, *24* (5), 788.
- (90) Ahmar, S.; MacDonald, D. G.; Vijayaratnam, N.; Battista, T. L.; Workentin, M. S.; Corrigan, J. F. *Angew. Chem.-Int. Ed.* **2010**, *49* (26), 4422.
- (91) Tsuboi, T.; Takaguchi, Y.; Tsuboi, S. *Chem. Commun.* **2008**, No. 1, 76.
- (92) Fukunaga, N.; Konishi, K. *Nanoscale* **2015**, *7* (48), 20557.
- (93) Zhou, J.; Bian, G.-Q.; Zhang, Y.; Zhu, Q.-Y.; Li, C.-Y.; Dai, J. *Inorg. Chem.* **2007**, *46* (16), 6347.
- (94) Ewing, S. J.; Romero, M. L.; Hutchinson, J.; Powell, A. V.; Vaqueiro, P. Z. *Anorg. Allg. Chem.* **2012**, *638* (15), 2526.
- (95) Ewing, S. J.; Vaqueiro, P. *Dalton Trans.* **2015**, *44* (4), 1592.
- (96) Wang, C.; Bu, X. H.; Zheng, N. F.; Feng, P. Y. *Angew. Chem.-Int. Ed.* **2002**, *41* (11), 1959.
- (97) Vaqueiro, P. *Inorg. Chem.* **2008**, *47* (1), 20.
- (98) Zheng, N. F.; Bu, X. G.; Wang, B.; Feng, P. Y. *Science* **2002**, *298* (5602), 2366.
- (99) Zheng, N. F.; Bu, X. H.; Feng, P. Y. *Nature* **2003**, *426* (6965), 428.
- (100) Vaqueiro, P.; Romero, M. L. *J. Am. Chem. Soc.* **2008**, *130* (30), 9630.

- (101) Xu, C.; Han, Y.-G.; Duan, T.; Zhang, Q.-F.; Leung, W.-H. *Inorg. Chem. Commun.* **2009**, *12* (10), 1053.
- (102) Zhang, Q.; Bu, X.; Lin, Z.; Wu, T.; Feng, P. *Inorg. Chem.* **2008**, *47* (21), 9724.
- (103) Vaqueiro, P.; Romero, M. L.; Rowan, B. C.; Richards, B. S. *Chem.-Eur. J.* **2010**, *16* (15), 4462.
- (104) Wang, Y.-H.; Zhang, M.-H.; Yan, Y.-M.; Bian, G.-Q.; Zhu, Q.-Y.; Dai, J. *Inorg. Chem.* **2010**, *49* (21), 9731.
- (105) Wang, Y.-H.; Jiang, J.-B.; Wang, P.; Sun, X.-L.; Zhu, Q.-Y.; Dai, J. *Crystengcomm* **2013**, *15* (30), 6040.
- (106) Vaqueiro, P.; Romero, M. L. *Inorg. Chem.* **2009**, *48* (3), 810.
- (107) Zheng, N.; Bu, X.; Lauda, J.; Feng, P. *Chem. Mater.* **2006**, *18* (18), 4307.
- (108) Dance, I. G.; Choy, A.; Scudder, M. L. *J. Am. Chem. Soc.* **1984**, *106* (21), 6285.
- (109) Lee, G. S. H.; Fisher, K. J.; Craig, D. C.; Scudder, M. L.; Dance, I. G. *J. Am. Chem. Soc.* **1990**, *112* (17), 6435.
- (110) Lee, G. S. H.; Craig, D. C.; Ma, I.; Scudder, M. L.; Bailey, T. D.; Dance, I. G. *J. Am. Chem. Soc.* **1988**, *110* (14), 4863.
- (111) Vossmeier, T.; Reck, G.; Katsikas, L.; Haupt, E.; Schulz, B.; Weller, H. *Science* **1995**, *267* (5203), 1476.
- (112) Gruber, F. Z. *Anorg. Allg. Chem.* **2012**, *638* (15), 2467.
- (113) Yang, X.-L.; Zhang, J.; Ren, S.-B.; Li, Y.-Z.; Du, H.-B.; You, X.-Z. *Inorg. Chem. Commun.* **2010**, *13* (4), 546.
- (114) Behrens, S.; Bettenhausen, M.; Eichhöfer, A.; Fenske, D. *Angew. Chem.-Int. Ed.* **1997**, *36* (24), 2797.
- (115) Behrens, S.; Fenske, D. *Berichte Bunsen-Ges.-Phys. Chem. Chem. Phys.* **1997**, *101* (11), 1588.
- (116) Behrens, S.; Bettenhausen, M.; Deveson, A. C.; Eichhöfer, A.; Fenske, D.; Lohde, A.; Woggon, U. *Angew. Chem.-Int. Ed. Engl.* **1996**, *35* (19), 2215.
- (117) Eichhöfer, A.; Hampe, O. *J. Clust. Sci.* **2007**, *18* (3), 494.
- (118) Lalatonne, Y.; Richardi, J.; Pileni, M. P. *Nat. Mater.* **2004**, *3* (2), 121.
- (119) Min, Y.; Akbulut, M.; Kristiansen, K.; Golan, Y.; Israelachvili, J. *Nat. Mater.* **2008**, *7* (7), 527.
- (120) Bishop, K. J. M.; Wilmer, C. E.; Soh, S.; Grzybowski, B. A. *Small* **2009**, *5* (14), 1600.
- (121) Gamez, P. *Inorg. Chem. Front.* **2014**, *1* (1), 35.
- (122) Zhao, X.-W.; Qian, L.-W.; Su, H.-C.; Mo, C.-J.; Que, C.-J.; Zhu, Q.-Y.; Dai, J. *Cryst. Growth Des.* **2015**, *15* (12), 5749.
- (123) Bag, S.; Trikalitis, P. N.; Chupas, P. J.; Armatas, G. S.; Kanatzidis, M. G. *Science* **2007**, *317* (5837), 490.
- (124) Ferey, G. *Angew. Chem.-Int. Ed.* **2003**, *42* (23), 2576.
- (125) Bu, X. H.; Zheng, N. F.; Li, Y. Q.; Feng, P. Y. *J. Am. Chem. Soc.* **2003**, *125* (20), 6024.
- (126) Wu, T.; Khazhaky, R.; Wang, L.; Bu, X.; Zheng, S.-T.; Chau, V.; Feng, P. *Angew. Chem.-Int. Ed.* **2011**, *50* (11), 2536.
- (127) Zheng, N. F.; Bu, X. H.; Feng, P. Y. *J. Am. Chem. Soc.* **2003**, *125* (5), 1138.
- (128) Wu, T.; Wang, X.; Bu, X.; Zhao, X.; Wang, L.; Feng, P. *Angew. Chem.-Int. Ed.* **2009**, *48* (39), 7204.

- (129) Wang, L.; Wu, T.; Bu, X.; Zhao, X.; Zuo, F.; Feng, P. *Inorg. Chem.* **2013**, *52* (5), 2259.
- (130) Zhang, Q.; Zheng, S.-T.; Bu, X.; Feng, P. *Z. Anorg. Allg. Chem.* **2012**, *638* (15), 2470.
- (131) Xu, G.; Guo, P.; Song, S.; Zhang, H.; Wang, C. *Inorg. Chem.* **2009**, *48* (11), 4628.
- (132) Brown, I. D.; Altermatt, D. *Acta Crystallogr. Sect. B-Struct. Sci.* **1985**, *41* (4), 244.
- (133) Brese, N. E.; O'Keeffe, M. *Acta Crystallogr. Sect. B-Struct. Sci.* **1991**, *47* (2), 192.
- (134) Zhang, C.; Liu, J.; Ji, M.; An, Y. *Inorg. Chem. Commun.* **2014**, *44*, 169.
- (135) Wang, C.; Li, Y. Q.; Bu, X. H.; Zheng, N. F.; Zivkovic, O.; Yang, C. S.; Feng, P. *Y. J. Am. Chem. Soc.* **2001**, *123* (46), 11506.
- (136) Xie, J. *Inorg. Chem.* **2008**, *47* (13), 5564.
- (137) Zheng, N. F.; Bu, X. H.; Lu, H. W.; Chen, L.; Feng, P. *Y. J. Am. Chem. Soc.* **2005**, *127* (43), 14990.
- (138) Santner, S.; Dehnen, S. *Inorg. Chem.* **2015**, *54* (4), 1188.
- (139) Freudenmann, D.; Wolf, S.; Wolff, M.; Feldmann, C. *Angew. Chem.-Int. Ed.* **2011**, *50* (47), 11050.
- (140) Stieler, R.; Bublitz, F.; Burrow, R. A.; Manzoni de Oliveira, G. N.; Villetti, M. A.; Pereira, M. B.; Piquini, P.; Lang, E. S. *J. Braz. Chem. Soc.* **2010**, *21* (11), 2146.
- (141) Levchenko, T. I.; Huang, Y.; Corrigan, J. F. Unpublished results.
- (142) Levchenko, T. I.; Kübel, C.; Huang, Y.; Corrigan, J. F. *Chem.-Eur. J.* **2011**, *17* (51), 14394.
- (143) Levchenko, T. I.; Kübel, C.; Wang, D.; Najafabadi, B. K.; Huang, Y.; Corrigan, J. F. *Chem. Mater.* **2015**, *27* (10), 3666.
- (144) Zhang, X. J.; Tian, Y. P.; Jin, F.; Wu, J. Y.; Xie, Y.; Tao, X. T.; Jiang, M. H. *Cryst. Growth Des.* **2005**, *5* (2), 565.
- (145) Jiang, J.-B.; Bian, G.-Q.; Zhang, Y.-P.; Luo, W.; Zhu, Q.-Y.; Dai, J. *Dalton Trans.* **2011**, *40* (37), 9551.
- (146) Fu, M.-L.; Adams, R. D.; Cristancho, D.; Leon-Plata, P.; Seminario, J. M. *Eur. J. Inorg. Chem.* **2011**, No. 5, 660.
- (147) Jiang, J.-B.; Huo, P.; Wang, P.; Wu, Y.-Y.; Bian, G.-Q.; Zhu, Q.-Y.; Dai, J. *J. Mater. Chem. C* **2014**, *2* (14), 2528.
- (148) Zheng, N. F.; Lu, H. W.; Bu, X. H.; Feng, P. *Y. J. Am. Chem. Soc.* **2006**, *128* (14), 4528.
- (149) Li, H. L.; Kim, J.; Groy, T. L.; O'Keeffe, M.; Yaghi, O. M. *J. Am. Chem. Soc.* **2001**, *123* (20), 4867.
- (150) Vaqueiro, P.; Romero, M. L. *Chem. Commun.* **2007**, No. 31, 3282.
- (151) Yue, C.-Y.; Lei, X.-W.; Feng, L.-J.; Wang, C.; Gong, Y.-P.; Liu, X.-Y. *Dalton Trans.* **2015**, *44* (5), 2416.
- (152) Pu, Y.-Y.; Zhang, X.; You, L.-S.; Bian, G.-Q.; Zhu, Q.-Y.; Dai, J. *Z. Anorg. Allg. Chem.* **2012**, *638* (15), 2498.
- (153) Melullis, M.; Clerac, R.; Dehnen, S. *Chem. Commun.* **2005**, No. 48, 6008.
- (154) Zheng, N. F.; Bu, X. H.; Feng, P. *Y. J. Am. Chem. Soc.* **2002**, *124* (33), 9688.
- (155) Ahamed, B. N.; Arunachalam, M.; Ghosh, P. *Inorg. Chem.* **2010**, *49* (10), 4447.

- (156) You, J.-F.; Papaefthymiou, G. C.; Holm, R. H. *J. Am. Chem. Soc.* **1992**, *114* (7), 2697.
- (157) Müller, A.; Kögerler, P.; Dress, A. W. M. *Coord. Chem. Rev.* **2001**, *222*, 193.
- (158) Kortz, U.; Müller, A.; van Slageren, J.; Schnack, J.; Dalal, N. S.; Dressel, M. *Coord. Chem. Rev.* **2009**, *253* (19–20), 2315.
- (159) Schäffer, C.; Todea, A. M.; Bögge, H.; Floquet, S.; Cadot, E.; Korenev, V. S.; Fedin, V. P.; Gouzerh, P.; Müller, A. *Dalton Trans.* **2013**, *42* (2), 330.
- (160) Seidlhofer, B.; Djamil, J.; Näther, C.; Bensch, W. *Cryst. Growth Des.* **2011**, *11* (12), 5554.
- (161) Woodward, P.; Dahl, L.; Abel, E.; Crosse, B. *J. Am. Chem. Soc.* **1965**, *87* (22), 5251.
- (162) Fenske, D.; Fischer, A. *Angew. Chem.-Int. Ed. Engl.* **1995**, *34* (3), 307.
- (163) Ivanov, S. A.; Kozee, M. A.; Merrill, W. A.; Agarwal, S.; Dahl, L. F. *J. Chem. Soc.-Dalton Trans.* **2002**, No. 22, 4105.
- (164) Yamashina, Y.; Kataoka, Y.; Ura, Y. *Inorg. Chem.* **2014**, *53* (7), 3558.
- (165) Zhang, X.; Pu, Y.-Y.; You, L.-S.; Bian, G.-Q.; Zhu, Q.-Y.; Dai, J. *Polyhedron* **2013**, *52*, 645.
- (166) Wang, Y.-H.; Wu, J.; Zhao, X.-W.; Qian, L.-W.; Zhu, Q.-Y.; Dai, J. *Chem. Commun.* **2015**, *51* (53), 10668.
- (167) Huang-Fu, S.-X.; Shen, J.-N.; Lin, H.; Chen, L.; Wu, L.-M. *Chem. – Eur. J.* **2015**, *21* (27), 9809.

## Chapter 2

### Controlled Solvothermal Routes to Hierarchical 3D Superparticles of Nanoscopic CdS <sup>β</sup>

#### 2.1 Introduction

Inorganic nanoparticles and nanoclusters, low-dimensional fragments of crystalline lattices stabilized by surface passivating ligands, represent a research focus of ever increasing interest due to the unique properties<sup>1-3</sup> and applications of quantum confined materials.<sup>4-8</sup> Being strictly uniform (same size, shape, and surface composition), metallic and semiconductor nanoclusters can themselves assemble into secondary structures or superparticles of varying morphologies.<sup>9-14</sup> In some cases, any packing order is absent (in other words, these secondary structures can be characterized as amorphous); in other cases, the presence of long-range order of such nanoclusters into superparticles creates superlattices that can reach in size up to tens of micrometers.<sup>15</sup> The assembly of such functional, nanoscale building blocks into well-defined, higher-order architectures has been identified as a key component for electronic and optoelectronic applications.<sup>16-19</sup> In this vein, the preparation and assembly of monodisperse group 12-16 semiconductor nanoclusters,<sup>20-30</sup> the largest examples of which include the structurally characterized  $[\text{Cd}_{54}\text{S}_{32}(\text{SPh})_{48}(\text{H}_2\text{O})_4]^{4-}$ ,  $[\text{Cd}_{54}\text{S}_{28}(\text{SPh})_{52}(\text{dmf})_4]$ , and  $[\text{Cd}_{84}\text{Se}_{56}(\text{O}_2\text{CPh})_{56}(\text{H}_2\text{N}^n\text{Bu})_{56}]$ ,<sup>31-33</sup> represent excellent candidates for the preparation of well-ordered (cubic) systems that can be further developed for the assembly of functional, composite lattices. Access to even larger CdS frameworks with well-defined superstructures is an attractive pursuit due to the size-dependent nature of the electronic structures.

The larger dimensions of the generated building blocks in comparison to those of atomic and molecular crystalline lattices make possible the structural characterization of many such superlattices using not only single crystal X-ray diffraction analysis but also electron

---

<sup>β</sup> A version of this work has been published in Levchenko, T. I.; Kübel, C.; Wang, D.; Khalili Najafabadi, B.; Huang, Y.; Corrigan, J. F. *Chem. Mater.* **2015**, 27 (10), 3666-3682; and has been reproduced with permission.

microscopy tools. Thus, direct imaging looking at a projection in transmission electron microscopy (TEM) provides an overview on the packing in a superlattice, whereas high-resolution (HR) TEM reveals the shape of an individual nanocluster and its internal structure. Selected area electron diffraction (SAED) identifies the local crystal structure of the nanoclusters as well as existing superstructure. Scanning electron microscopy (SEM) allows the three-dimensional morphology of superparticles to be captured and also provides, in some cases, information about the packing geometry on the surface and edge regions of a superlattice.<sup>15</sup> An extension of traditional electron microscopy, electron tomography, involves collection of a set of images at different projections that are then used to build up a three-dimensional model of the superparticles.<sup>34–38</sup>

Superlattice build up by single-component,<sup>9,24,31,39,40</sup> binary,<sup>41–45</sup> and even ternary<sup>36,46</sup> superlattices has recently been prepared and characterized, forming, in the case of single-component systems, primitive cubic,<sup>24,31,32</sup> face-centered cubic,<sup>9,31,32,47</sup> or hexagonal close-packed<sup>48</sup> superlattice cells, all of the widespread structures known for atomic solids. This structural similarity may result from similarities in the principles of formation: an assembling of nanoclusters into superlattices is suggested to follow the same fundamental laws as those for crystallization of conventional atomic and molecular solids.<sup>49</sup> Self-assembly can thus be initiated by (1) external physical parameters, *e.g.*, pressure and temperature changes,<sup>50</sup> and (2) internal physical parameters, *e.g.*, concentration change. Different types of driving forces (representing intrinsic interactions) may be involved, including (but not limited to) electrostatic (Coulomb),<sup>51,52</sup> charge–dipole and dipole–dipole interactions,<sup>53,54</sup> dispersion (London–van der Waals) forces (separately taking into consideration core–core, core–ligand, and ligand–ligand interactions),<sup>24,31,55,56</sup> and stronger ligand–ligand (*e.g.*, hydrogen bonding)<sup>25,57</sup> interparticle interactions. The synthetic routes to superparticles may include solvothermal conversion<sup>31</sup> and recrystallization methods. In the last group, techniques such as seeding,<sup>58</sup> solvent evaporation,<sup>59</sup> or diffusion of nonsolvent<sup>60</sup> have been found to be very efficient for controlled superlattice growth. Despite the remarkable progress made in this area, a clear connection between the nature of nanocluster–nanocluster interactions and the structure of resulting self-assembled superparticles has not as yet been found, and the controlling thermodynamic and kinetic factors that govern the processes of assembling



from constituents have not been fully revealed. Knowledge of the assembling mechanisms opens the door toward the manipulation of superparticle growth, tailoring its size and shape. A spherical shape of superparticles is commonly observed, fulfilling the requirement to minimize surface free energy. In many cases, self-assembly into superparticles of a particular shape was found to be strongly guided by the anisotropy of building blocks, originated either from their shape (faceting) or interaction patchiness (inhomogeneous surface coverage).<sup>61</sup> In addition, shape-controlled synthesis of superparticles that adopt different morphologies from identical constituent nanoclusters has also been reported, also illustrating that the collective properties of superparticles can be shape-dependent, too. A recent example is the substantially higher therapeutic effect of cube-shaped  $\text{Fe}_3\text{O}_4$  superparticles, in comparison to that of spherical ones, in the magnetomechanical treatment of cancer cells.<sup>62</sup>

The collective properties of nanocluster assemblies are in part inherited from their constituent nanoclusters and in part induced by the electronic, plasmonic, and/or magnetic coupling between the building blocks.<sup>63-68</sup> Obtaining better control over the formation of nanocluster superparticles will promote the successful development and implementation of electronic and optoelectronic devices utilizing the quantum-confinement-related properties.

Herein, we describe a facile route to prepare crystalline, cubic superparticles of monodisperse nanoclusters of CdS 1.9 nm in size by means of the thermally induced conversion of the readily prepared cadmium thiophenolate complex  $[\text{Me}_4\text{N}]_2[\text{Cd}(\text{SPh})_4]$ . Furthermore, we illustrate the effects that additional quaternary ammonium salts can have on the size and dispersity of the nanoclusters formed and on the nature of their self-assembly into secondary structures, with the preparation and characterization of spherical superparticles of CdS, comprised of individual nanoclusters 2.3 nm in size. Details on the formation, structural characterization (*via* powder and single crystal X-ray diffraction, HRTEM, STEM and SEM) and optical properties of these hierarchical assemblies and their constituents are described.

## 2.2 Results and Discussion

A typical procedure for the preparation of CdS nanoclusters and their self-assembly into three-dimensional superparticles involves heating a DMF solution of the mononuclear precursor  $(\text{Me}_4\text{N})_2[\text{Cd}(\text{SPh})_4]$  (in the presence/absence of an alkylammonium salt additive) in a sealed, stainless-steel reactor under solvothermal conditions (Scheme 2.1). The solvothermal treatment of  $(\text{Me}_4\text{N})_2[\text{Cd}(\text{SPh})_4]$  at 200 °C (concentration ~16 wt %) leads to the formation of pale-yellow, solid material (**1**). Examination of the morphology of the as-synthesized solid using SEM reveals perfectly faceted cubic crystals of 5–25  $\mu\text{m}$  in size (Figure 2.1).

**Scheme 2.1:** Solvothermal route to CdS superstructures.



\* Material **2** crystallizes several days after isolating **1** as a separate phase from the same mother liquor; see the main text for details.

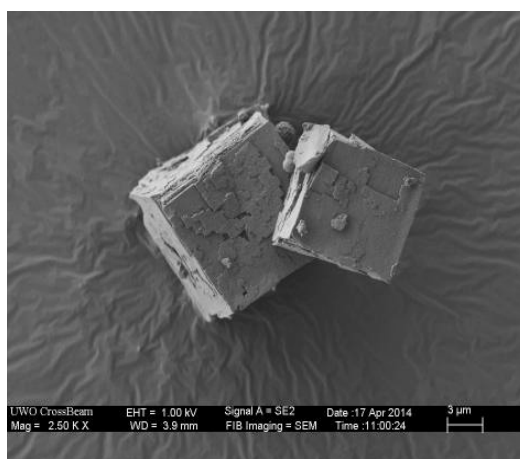


**Figure 2.1:** SEM image of cubic crystals of **1**.

The wide-angle region of the PXRD patterns for **1** (Figure 2.2) shows the presence of a crystalline CdS species. A distinction between Hawleyite (cubic) or Greenockite (hexagonal) structures is not unequivocally possible by PXRD (see Figure 2.3) because of the broad peaks that are typical for nanometer-sized systems. Calculations of the mean size

of the crystalline domains using the Scherrer equation (for the 111, 220, and 311 reflections assuming Hawleyite structure) give an average value of  $1.5 \pm 0.1$  nm. Although a precise value is not possible in such cases, the estimated value can be used for comparison to those obtained by other methods (*vide infra*). Of note is the strong, sharp reflection at  $2\theta$   $3.55^\circ$  together with a weaker and broader one at  $7.02^\circ$  (*i.e.*, at the double angle of the main diffraction peak); from the position of the first reflection, the corresponding interplanar spacing  $d$  of 2.9 nm can be calculated using Bragg's equation. Such low-angle diffraction patterns have been observed previously for crystalline superlattices of the monodisperse nanocluster systems  $[\text{Cd}_{32}\text{Se}_{14}(\text{SePh})_{36}(\text{PPh}_3)_4]$  and  $[\text{Cd}_{54}\text{S}_{32}(\text{SPh})_{48}(\text{H}_2\text{O})_4]^{4-}$ .<sup>31,69</sup> For the latter, an intense low-angle reflection at  $2\theta$   $4.24^\circ$  (Co  $K\alpha$  radiation; data in original article are given for Cu  $K\alpha$ :  $2\theta$   $3.65^\circ$ ) was reported, with the corresponding interplanar spacing  $d$  of 2.4 nm; for **1**, this is shifted to even lower angles, consistent with a markedly larger unit cell.

Despite of the evidence of the presence of long-range translational order from the PXRD patterns, several attempts of single-crystal X-ray characterization for **1** were not successful since the samples had shown mostly diffuse scattering streaks rather than clearly discernible Bragg reflections. The difficulties with characterization are most probably related to the orientation disorder of the surface thiophenolate ligands, the orientational flexibility of the large nanoclusters within the three-dimensional superlattice, and/or lattice defects.<sup>31–33,70</sup>

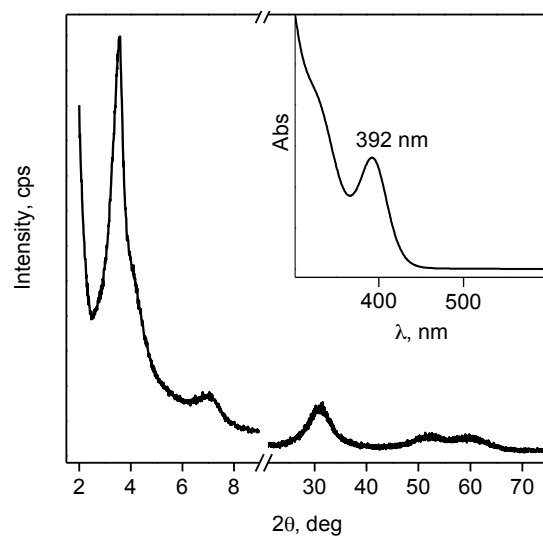


**Figure 2.2:** Powder X-ray diffraction pattern (Co  $K\alpha$  radiation) and UV–vis absorption spectrum of DMF solution (*insert*) of **1**.

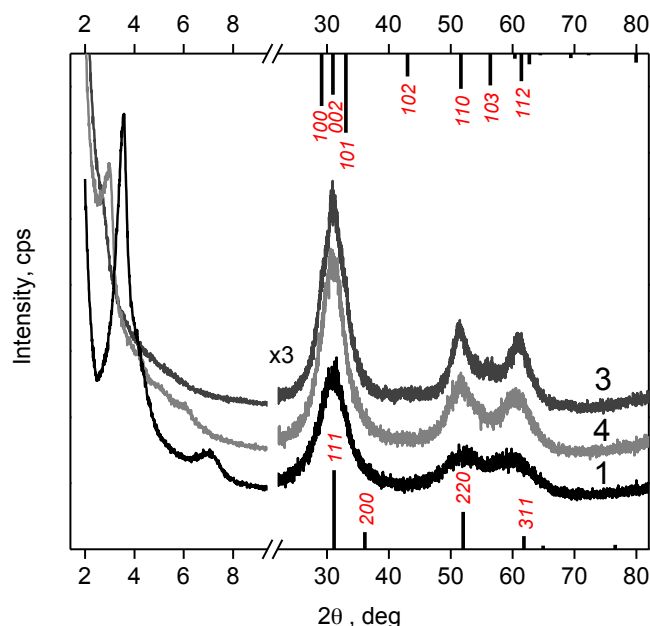


**Figure 2.3:** Powder X-ray diffraction patterns (Co K $\alpha$  radiation) of **1**, **3**, and **4** samples (Y axis offset; wide-angle region scaled x3 for all samples). Reference diffractograms are from the database of the International Centre for Diffraction Data; top: hexagonal CdS # 04-008-8223, bottom: cubic CdS # 04-008-2190.

The UV–vis absorption spectra of solutions of **1** (Figure 2.2, *insert*) clearly show the presence of sharp, narrow excitonic features at room temperature, suggesting a narrow size distribution.<sup>15</sup> The lowest absorption band is located at 392 nm, with another one, weaker and broader, at 334 nm ( $\Delta\lambda$  58 nm). The value of the Gaussian full width at half-maximum (fwhm) for the low-energy excitonic peak for **1** is found to be close to that observed for monodisperse  $[\text{Cd}_{54}\text{S}_{28}(\text{SPh})_{52}(\text{dmf})_4]$ , synthesized by a published method<sup>32</sup> (39 and 36 nm, respectively). This suggests that any peak broadening here is caused by inherent system properties (presumably, inhomogeneous distribution of surface coverage by the ligand) rather than nanocluster size polydispersity.<sup>69</sup> Due to quantum size effects, a clear connection exists between semiconductor cluster size and its lowest excited electronic state: with increasing cluster size, the low-energy absorption maximum will shift to higher wavelengths (until reaching an exciton Bohr radius; for CdS, it is about 3 nm).<sup>71</sup> For **1**, the low-energy excitonic peak position is shifted toward a longer wavelength (392 nm for **1** vs. 353 nm reported for both neutral  $[\text{Cd}_{54}\text{S}_{28}(\text{SPh})_{52}(\text{py})_{7.5}]$

and anionic  $[\text{Cd}_{54}\text{S}_{32}(\text{SPh})_{48}(\text{H}_2\text{O})_4]^{4-}$  in DMF solutions<sup>31,32</sup>), reflecting a larger cluster size in comparison with that of previously reported tetrahedral Cd<sub>54</sub> nanoclusters.<sup>72</sup>

Solutions of samples of **1** (as well as those of **3** and **4**, *vide infra*) were prepared by sonication of the respective solid in DMF solvent. This resulted in small red shifts ( $\sim 5$  nm) in the UV–vis absorption spectra (see Appendix A) when compared to that of samples that were dissolved with stirring only, presumably due to small surface changes. Smaller differences were noted in the PL or PLE spectra for samples prepared *via* these two methods. The increased concentration (and intensities) associated with samples prepared *via* sonication methods is such that these spectra are the ones reported in the Chapter 2.

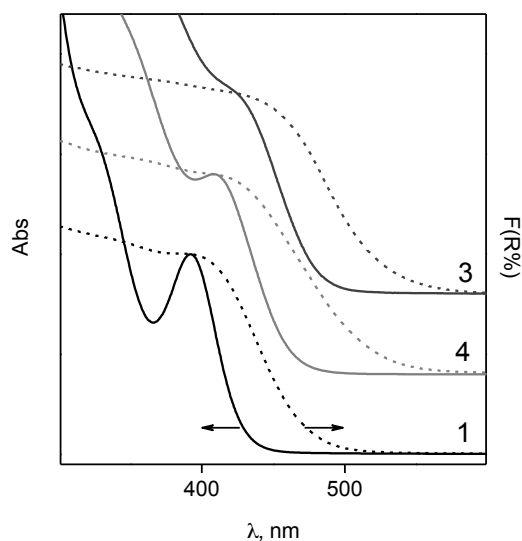


**Figure 2.4:** UV–vis absorption spectra of solutions (normalized; Y axis offset; solid lines) and diffuse reflection spectra of solid samples (processed using the Kubelka-Munk function and normalized; Y axis offset; dash lines) of **1**, **3** and **4**.

The UV–vis diffuse reflectance spectra of solid **1** are also similar to corresponding absorption spectra of the nanocluster in DMF solutions. The absorption peak of solid **1** (Figure 2.4) was found to be broader, and an onset of the peak is shifted toward a longer wavelength in comparison to the solution spectrum. A similar relation between the UV–vis absorption spectra of solid and solution samples was reported previously for smaller CdS nanoclusters and attributed to the weak cluster–cluster interaction present in the lattice.<sup>24,25</sup>

Room-temperature emission spectra of solutions of **1** show a strong broad (fwhm 140 nm) band at 587 nm (Figure 2.5); the peak position is found to be practically independent of the excitation wavelength. The excitation spectra show a strong narrow absorption band at 381 nm and a weaker one at 327 nm. On the basis of a broad line width of the emission and a significant shift to the red of the excitation (similar to that for previously reported smaller CdS nanoclusters),<sup>23,24</sup> the emission band of **1** is assumed to originate from the recombination of surface trapped charge carriers, typical for phenylchalcogenolate-stabilized nanoclusters.<sup>69,73,74</sup>

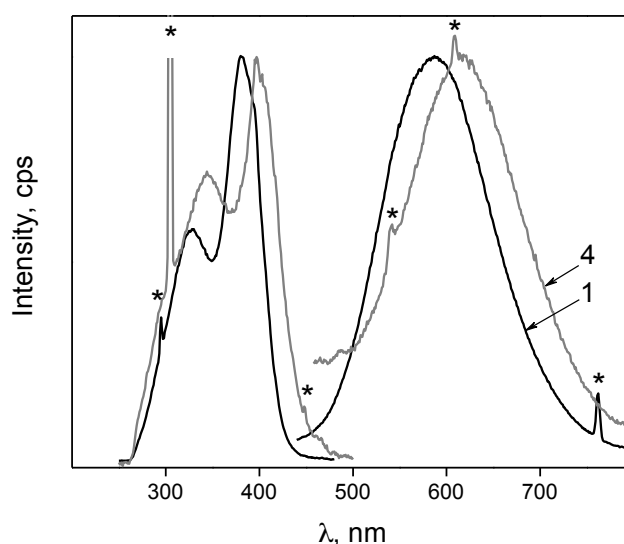


**Figure 2.5:** Normalized room temperature photoluminescence and photoluminescence excitation spectra of saturated DMF solutions of **1** (black lines) and **4** (grey lines). In the case of **1**, the excitation wavelength for the emission spectra  $\lambda_{\text{ex}}$  was 380 nm, and the monitoring wavelength for the excitation spectra  $\lambda_{\text{em}}$  was 590 nm. For **4**,  $\lambda_{\text{ex}}$  was 400 nm and  $\lambda_{\text{em}}$  was 610 nm. The asterisk \* denotes harmonic vibration and/or solvent peaks.

STEM analysis for the samples, prepared using a DMF solution of **1** (“wet” preparation) shows discrete nanoclusters  $1.9 \pm 0.4$  nm in diameter (Figure 2.6). This value characterizes the high contrast CdS core of **1**; the accuracy of measurements reflects difficulties with setting a boundary between the core and a diffuse organic shell. Only a few nanoclusters of different size, ranging from 0.8 to 3.2 nm, were identified upon the image analyses. HRTEM imaging of the discrete nanoclusters as well as their aggregates reveals

characteristic lattice distances of 3.35, 2.07, and 1.80 Å, in good agreement with the cubic crystalline structure (see Table 2.1); only traces of hexagonal structure were detected.

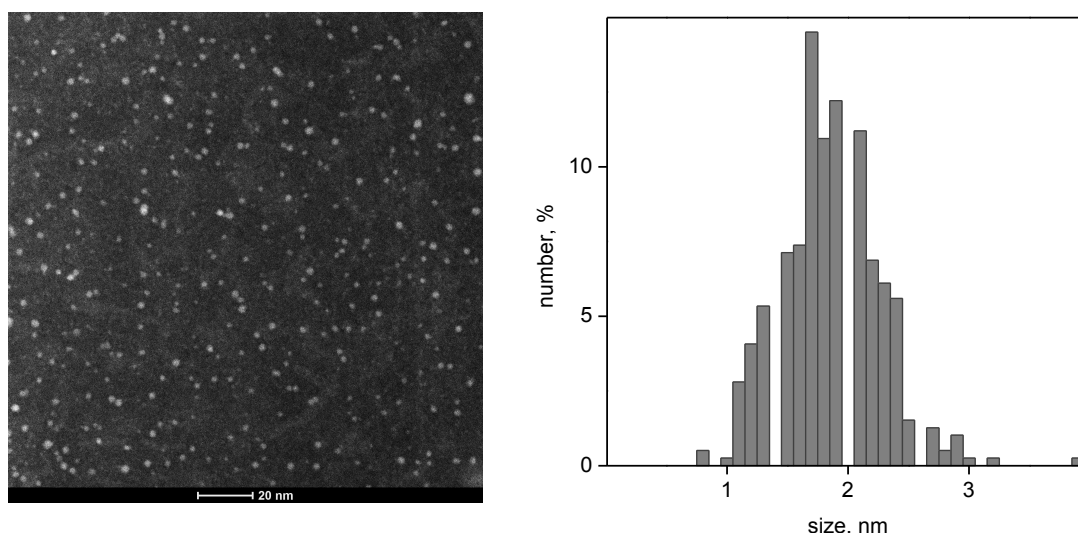


**Figure 2.6:** High angle annular dark field (HAADF) STEM image showing individual nano-clusters from DMF solution of **1** (left) and the corresponding particle size distribution (right).

**Table 2.1:** Average lattice distances measured from HR TEM of nanocluster aggregates of **1** in DMF and calculated using SAED of FIB prepared superparticle cross-sections.

$\mathbf{1}_{\text{DMF}}$	$\mathbf{1}_{\text{FIB}}$	Hawleyite		
		$d$ [Å]	hkl	Int. [%]
3.35	3.35	3.359	111	100
	2.89	2.909	200	22.8
2.07	2.05	2.057	220	55.6
1.80	1.80	1.754	113	42.9
	1.61	1.680	222	5.9
		1.455	400	8.8
	1.33	1.335	331	17.1
		1.301	420	7.0
	1.21	1.188	224	18

TEM images for the samples, prepared using suspensions of **1** in organic solvents (wet preparation), show the presence of limited domains of a well-ordered superlattice of monodisperse frameworks on the edges/surfaces of the microcrystals (Figure 2.7). Site-specific EDX spectroscopy analysis of these regions confirms the composition  $[\text{Cd}_x\text{S}_y(\text{SPh})_z]$ ; the Cd/S weight ratio was found to be 2.70 : 1 (atomic, 0.77 : 1; see

Table 2.2). The apparent square packing of nanoclusters is in agreement with a primitive cubic, three-dimensional arrangement with a lattice parameter 2.9 nm. This value shows an excellent agreement with the 2.9 nm interplanar spacing ( $d$ )<sup>75</sup> calculated from the PXRD data for **1**. Although some ordered domains are found to be detached, they are mostly present on the surface of the microcrystals. With the intense and sharp low-angle peak in the PXRD pattern for **1**, it was postulated that much larger domains of ordered superlattices should also exist inside of the cubes (which are too thick for detailed TEM analysis).

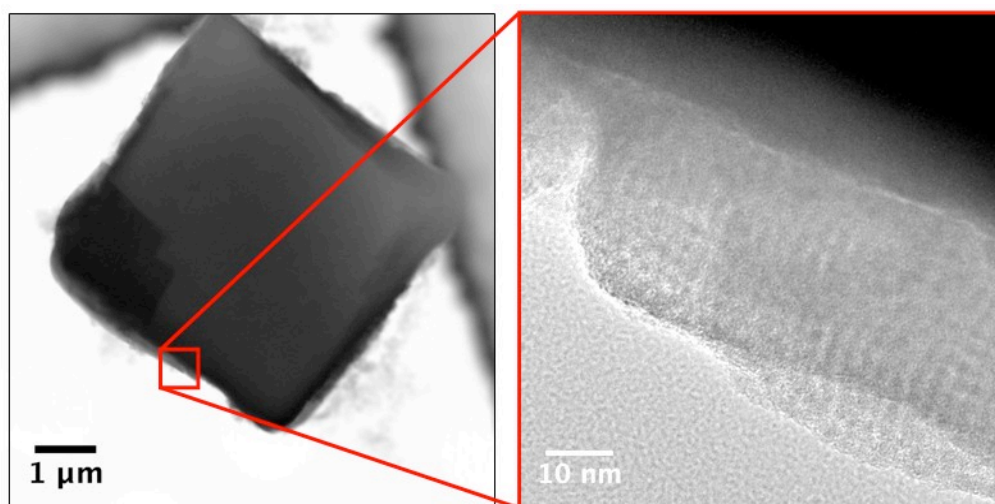


**Figure 2.7:** TEM images of **1**: aggregate of micron-sized cubes, general view (*left*); with smaller ordered domains visible at the edge of the cube, high resolution (*right*); “wet” sample preparation.

**Table 2.2:** Summary of EDX data for **1**, **3**, and **4**.

Sample		<b>1</b>	<b>3</b>	<b>4</b>
Cd/S ratio, atomic %	mean	0.77	0.91	0.83
	sd	±0.04	±0.04	±0.04
Cd/S ratio, weight %	mean	2.70	3.20	2.92
	sd	±0.13	±0.13	±0.12
Cd/Hal ratio, atomic %	mean	–	23	34
	sd	–	±6	±5
Cd/Hal ratio, weight %	mean	–	73	48
	sd	–	±19	±7

Mean values and standard deviation for each sample were calculated for set of 8-9 analyses. For **3** Hal = Cl; for **4** Hal = Br. No detectable amount of either Cl or Br was found in **1**.



To confirm this, an alternative method of sample preparation was used. It included selective material ablation from micrometer-sized cubes of **1** using a focused gallium ion beam, creating thin slices transparent for the electron beam in TEM (FIB preparation; see Appendix A).

For these samples of **1**, both TEM and STEM images clearly show the presence of continuous domains of a superlattice repeat of CdS nanoclusters (Figure 2.8); the cubic lattice parameter is very similar to those for the superlattice domains observed on the surface of the cubes themselves.

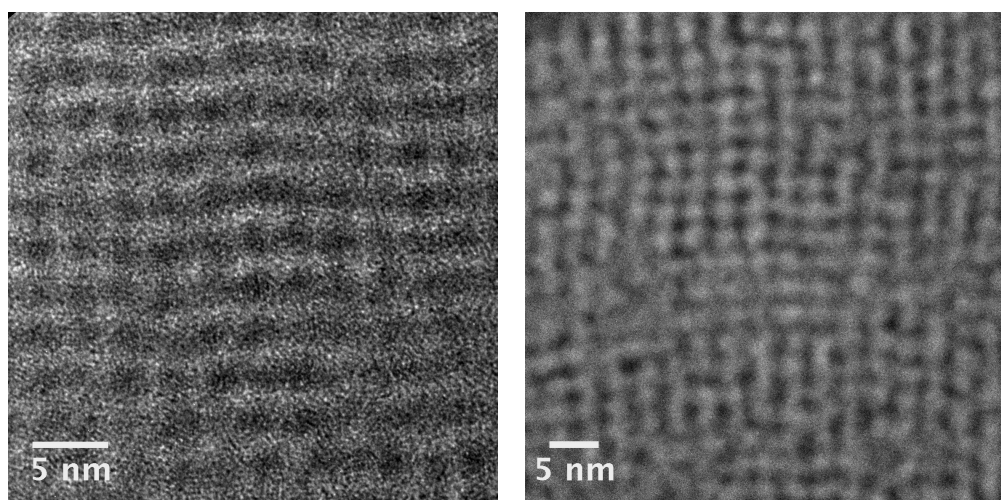


**Figure 2.8:** BF TEM (showing the CdS as dark regions and the SPh<sup>-</sup> shell as lighter spaces; *left*) and HAADF STEM (CdS: bright dots; SPh<sup>-</sup> shell: dark spaces; *right*) images of **1** with an extended nanocluster superlattice in the micron-sized cube; “FIB” sample preparation.

The low-angle electron diffraction pattern for **1** (Figure 2.9, *left*) characterizes the single crystalline superlattice of CdS nanoclusters, whereas the corresponding wide-angle electron diffraction pattern (Figure 2.9, *right*) provides information about the crystalline lattice within CdS nanoclusters. Lattice distances, obtained from the latter, are in a good agreement with Hawleyite crystalline structure (Table 2.1), providing additional information that cannot be resolved by PXRD. Moreover, the electron diffraction patterns clearly indicate that CdS nanoclusters in **1** are not all oriented in the same way: the wide angle part of the SAED pattern shows a high degree of preferential orientation of crystalline CdS nanoclusters in the superlattice and can be matched well as a superposition of three single crystalline  $\langle 110 \rangle$  Hawleyite diffraction patterns rotated  $60^\circ$  with respect to each other.

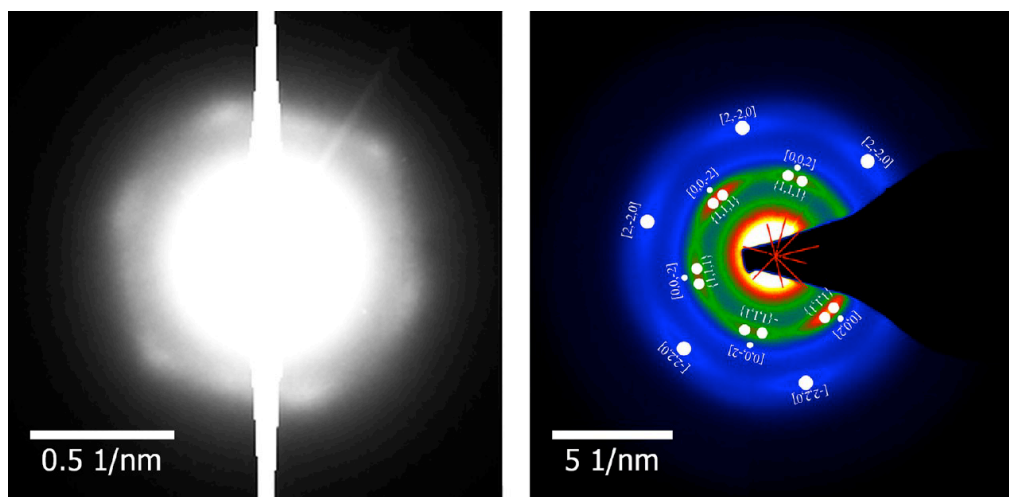


**Figure 2.9:** SAED of **1**: single crystal low-angle (*left*) and wide-angle (*right*) reflections, characterizing nanocluster superlattice and CdS crystalline lattice within nanoclusters, respectively. Overlaid on the wide-angle SAED pattern are three sets of simulated  $\langle 110 \rangle$  Hawleyite zone axis diffraction patterns with an angle of  $60^\circ$  between them.

TEM and STEM provide concrete data for both the nature of the individual nanoclusters and their secondary structures: monodisperse CdS nanoclusters **1** (with crystalline Hawleyite core) are organized into superparticles having a continuous, regular crystalline superlattice. Some defects of the superlattice, seen on both TEM and STEM images, are present; those local and continuous defects may originate from different sources. Thus, some local disorder, due to damaging of the organic shell, may be created during sample preparation for the microscopy examination or imaging itself. Long-range defects of the superlattice, such as dislocation seen in some places, are more likely to be concomitant with the crystallization solvent removal upon sample exposure to vacuum or sample deterioration upon contacting with air. In fact, superlattice degradation in both above-mentioned cases was observed experimentally by intensity decrease of low-angle PXRD reflections. Alternatively, some defects may have been present in the samples initially (*i.e.*, after the solvothermal synthesis, before the product isolation and drying), representing nonideal packing of the large nanoclusters into the superlattice. The last version is consistent with the fact that attempts at characterization of **1** using single-crystal X-ray diffraction were not successful.

After several days standing, the mother liquor of reaction solutions for isolated **1** leads to the generation of large, colorless cubic crystals (**2**). The amount of the crystals of **2** was much smaller in comparison to the amount of **1** previously isolated by centrifugation. UV–vis spectra (Figure 2.10) and elemental analysis data for **2** are in agreement with those for the previously published cadmium sulfide nanoclusters containing 54 Cd centers ( $\lambda_{\text{max}} = 355 \text{ nm}$ ).<sup>31,32</sup> UV–vis spectra for solutions of **2** show no differences for samples prepared with or without sonication. Characterization using single-crystal X-ray diffraction shows that **2** indeed has the same  $\text{Cd}_{54}\text{S}_{80}$  core (Figure 2.11) as that of previously reported  $[\text{Cd}_{54}\text{S}_{32}(\text{SPh})_{48}(\text{H}_2\text{O})_4]^{4-}$  and  $[\text{Cd}_{54}\text{S}_{28}(\text{SPh})_{52}(\text{dmf})_4]$  and crystallizes into the primitive cubic superlattice (space group P-43m) with a unit cell parameter  $23.976(8) \text{ \AA}$  (see Appendix A), very close to the one of  $[\text{Cd}_{54}\text{Se}_{32}(\text{SPh})_{48}(\text{H}_2\text{O})_4]^{4-}$  (P23 and  $24.0656(7) \text{ \AA}$ , respectively).<sup>31</sup> This observation confirms the relation of nanoclusters **1** with the known capped supertetrahedral nanocluster family (represented by previously published Cd17, Cd32, and Cd54 frameworks),<sup>22,24,31</sup> whereas the difference in solubility in DMF (**1** crystallizes much more readily than **2**) is consistent with the larger size of nanoclusters **1**.

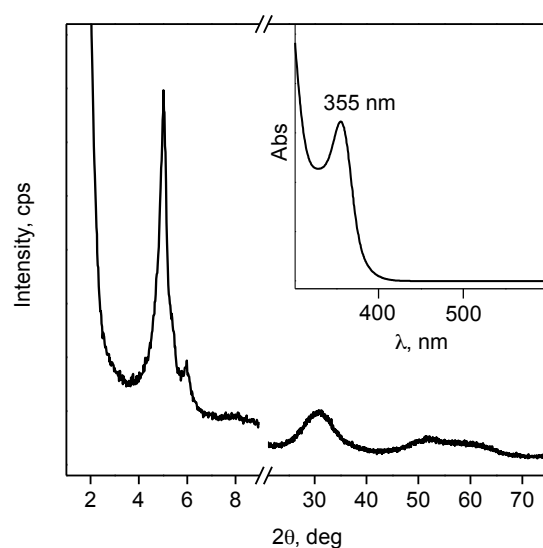


**Figure 2.10:** Powder X-ray diffraction pattern (Co  $K\alpha$  radiation) and UV–vis absorption spectrum of DMF solution (*insert*) of **2**.

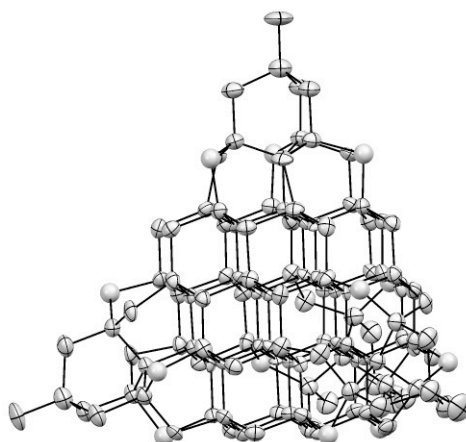


**Figure 2.11:** The  $\text{Cd}_{54}\text{S}_{80}$  core structure of **2**.

Single-crystal data for **2** show distances between clusters cores of  $\sim 1.0$  nm (calculated between the middle of tetrahedron edges) arising from the organic shell on their surfaces. The thiophenolate ligands not only serve as the passivating shell for the crystalline core but also provide the dominant cohesive interactions (mainly intercluster ligand–ligand van der Waals attraction), sustaining the superlattice and determining its parameters.<sup>10</sup> Since the TEM and STEM images for **1** also display primitive cubic packing, it is not unexpected to observe similar distances between clusters' cores in this case. With a lattice parameter 2.9 nm, one can estimate cluster size for **1** to be equal to 1.9 nm from the PXRD; this value is in an excellent agreement with the 1.9 nm nanocluster size for **1** obtained from TEM analysis. The smaller crystalline domain size calculated for **1** using the Scherrer equation from PXRD peak broadening (1.5 nm) may result from inadequate approximation used for the calculations (*e.g.*, from improperly chosen shape factor  $K$ )<sup>76</sup> or generally from the difficulties with such calculations for very small nanoclusters (due to large distortions in crystalline frameworks).<sup>77</sup>

It is important to note that for the core of nanoclusters **2** the edge length of the tetrahedron is 1.9 nm, measured from Cd to Cd (2.3 nm from O to O). However, when such a cluster is viewed along unit cell axis  $a$ , its image would appear as a square with an edge length of only 1.3–1.6 nm. Such objects are smaller than the 1.9 nm cores we observe for **1** from TEM. The projection nature of TEM and STEM is such that a definite

conclusion regarding the overall shape of clusters **1** is not possible by these methods from images of discrete nanoclusters or their arrangements into a superlattice. If clusters of **1** continue the trend for capped supertetrahedral nanoclusters family beyond Cd54, then they may correspond to those next in the size predicted to exist, namely, Cd84 or Cd123.<sup>31</sup>

Thus, we cannot preclude that what appears *via* projection (on TEM and STEM images of **1**) to be a 1.9 nm quasi-circle may, in fact, be a tetrahedrally shaped cluster with edge lengths of 2.7 nm. Bearing in mind the general trend for edge lengths for the previously known capped supertetrahedral CdS clusters (obtained from the published single-crystal X-ray diffraction data; measured from Cd to Cd: 1.1 nm for Cd17, 1.5 nm for Cd32, and 2.0 nm for Cd54),<sup>31</sup> a tetrahedrally shaped cluster with an edge of 2.7 nm could represent the next member of the capped supertetrahedral clusters family,<sup>78</sup> Cd84:  $[\text{Cd}_{84}\text{S}_{59}(\text{SPh})_{60}\text{L}_4]^{10-}$  if charged or  $[\text{Cd}_{84}\text{S}_{49}(\text{SPh})_{70}\text{L}_4]$  if neutral (where L represents a neutral ligand, *e.g.*, H<sub>2</sub>O or *dmf*).<sup>79</sup> In **1**, the Cd / S ratio found using EDX (atomic 0.77 : 1) would be consistent with having such large nanocluster frameworks, as the calculated Cd / S ratio is 0.71 : 1 for both  $[\text{Cd}_{84}\text{S}_{59}(\text{SPh})_{60}\text{L}_4]^{10-}$  and  $[\text{Cd}_{84}\text{S}_{49}(\text{SPh})_{70}\text{L}_4]$ . On the basis of the empirical formula proposed by Yu *et al.*,<sup>80</sup> the lowest-energy absorption peak at 392 nm observed for **1** would correspond to nanoclusters size of 3.1 nm, which is reasonably close to the derived edge length of a tetrahedrally shaped cluster 2.7 nm.<sup>81</sup>

Crystalline samples of **1** show ~24% weight loss between 300 and 600 °C (an abrupt step around 380 °C), as determined *via* TGA (Figure 2.12), that can be attributed to the elimination of surface thiophenolate groups<sup>82</sup> and the formation of (hexagonal) CdS. The initial gradual weight loss of ~2% observed between 25 and 300 °C in TGA for **1** can be attributed to the removal of residual lattice solvent, a loss of weakly bonded ligands, or counterions present. From the weight loss observed between 300 and 600 °C, it is possible to derive ratios between Cd / S and S<sup>2-</sup> / SPh<sup>-</sup> present in nanoclusters **1**, with the approximation that all SPh<sup>-</sup> is eliminated in the form of diphenyl sulfide (Ph-S-Ph). The calculated Cd / S ratio 0.8 : 1 was found to be close to the ratio obtained for **1** using EDX (0.77 : 1). The calculated S<sup>2-</sup> / SPh<sup>-</sup> ratio of 1.56 : 1 for **1** is markedly larger than those observed in structurally characterized smaller cadmium thiophenolate nanoclusters.<sup>83</sup> The large S<sup>2-</sup> / SPh<sup>-</sup> ratio in **1** can be explained by (1) having a much larger tetrahedral core

size than that of previously reported nanoclusters, (2) altering cluster surface chemistry (*i.e.*, ligands other than  $\text{SPh}^-$  are present in substantial quantity in nanoclusters shell) or a significant amount of lattice solvent present, and (3) adopting a core shape other than that of a regular tetrahedron (*e.g.*, truncated tetrahedron). The last is based on the idea that high-energy apexes of tetrahedron are likely to be replaced with less energetic crystal planes,<sup>84</sup> changing the core to surface atoms ratio.

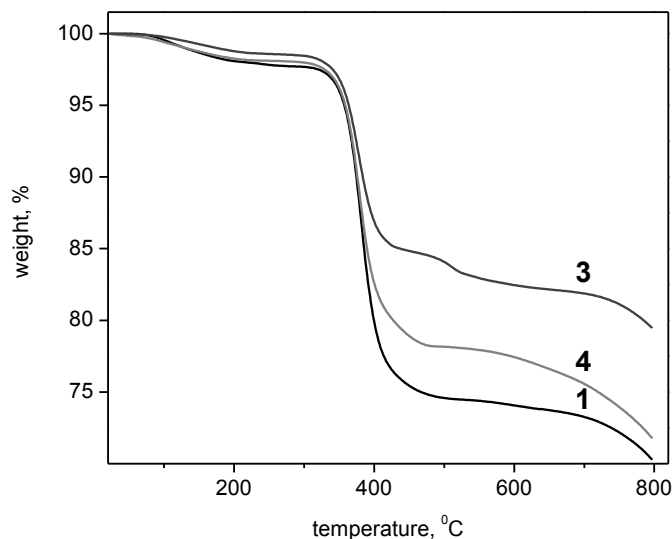


**Figure 2.12:** TGA curves for **1**, **3** and **4** samples (obtained under  $\text{N}_2$  flow).

UV–vis absorption spectra, PXRD, electron microscopy, and EDX analysis data are all consistent with a larger core size for **1** in comparison to that for previously reported nanoclusters, but this alone cannot fully explain the results of TGA, since the framework for larger tetrahedral nanoclusters would result in a larger number of surface  $\text{SPh}^-$  groups<sup>85</sup> than that observed for **1**. The Raman spectrum of **1** (Figure 2.13) contains several bands in the area characteristic of aromatic compounds (*e.g.*, at  $3056\text{ cm}^{-1}$  due to aromatic C–H stretch vibrations and  $1579\text{ cm}^{-1}$  due to aromatic C–C stretch vibrations). No band of marked intensity can be found in the area characteristic of aliphatic C–H stretching (around  $2900\text{ cm}^{-1}$ ). Aromatic Raman bands can be assigned to the phenyl rings from  $\text{SPh}^-$  groups in the stabilizing shell. Larger supertetrahedral charged  $[\text{Cd}_x\text{S}_y(\text{SPh})_z]^{n-}$  nanoclusters are expected to contain substantial amounts of counterions (in our case, most probably,  $\text{Me}_4\text{N}^+$ ). Since there are no aliphatic C–H Raman bands of high intensity present in the spectra of **1** and the nitrogen content found by the elemental

analysis is below the detection limit, it is more likely that (1) the nanoclusters **1** are neutral with no ligand other than  $\text{SPh}^-$  present in significant amounts and (2) intercluster space in the superlattice are essentially free of residual solvent molecules. Neutral  $[\text{Cd}_{84}\text{S}_{49}(\text{SPh})_{70}\text{L}_4]$  nanoclusters with  $\text{L} = \text{dmf}$  may fit these requirements, but it does not support the  $\text{S}^{2-} / \text{SPh}^-$  ratio predicted from TGA.

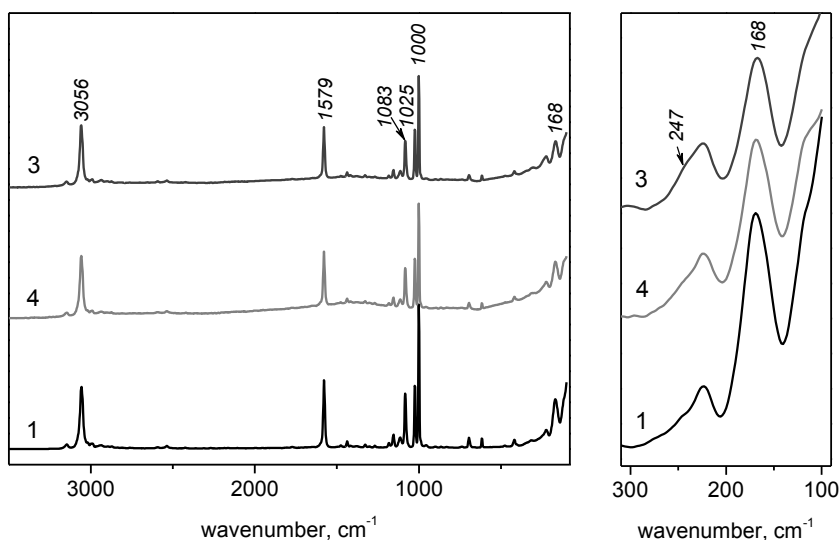


**Figure 2.13:** Raman spectra of **1**, **3** and **4** samples: general view (*left*) and low-frequency part (*right*). Spectra are normalized and shown with Y axis offset.

Slowly heating a sample of **1** within a mass spectrometer allowed for the fragments (consistent with possible surface ligands or counterion elimination) to be monitored. The total ion current profile observed was compatible with TGA curves previously obtained for **1**. After heating beyond  $\sim 270^\circ\text{C}$ , fragments at  $m/z = 110$ ,  $154$ , and  $186$  were found to be the most intense (corresponding to  $\text{PhSH}$ ,  $\text{Ph-Ph}$ , and  $\text{Ph-S-Ph}$ , respectively), which can be attributed to  $\text{Ph-S-Ph}$  elimination in the process of surface  $\text{SPh}^-$  cleavage. The lower temperature of the process initiation in comparison to the TGA experiment is attributed to the vacuum conditions (versus  $\text{N}_2$  flow) and a much faster heating rate for the mass spectrometry experiment. At a temperature below  $\sim 100^\circ\text{C}$ , a fragment at  $m/z = 218$  ( $\text{Ph-S-S-Ph}$ ) was detected, albeit with very low intensity. No fragments corresponding to DMF or  $\text{Me}_4\text{N}^+$  were detected at any temperatures, confirming the supposition that nanoclusters **1** are most probably neutral and no significant amount of lattice solvent is present.

While the cadmium thiolate clusters synthesized to date adopt a tetrahedral shape and belong to particular isomorphous families (supertetrahedral  $T_n$ , penta supertetrahedral  $P_n$ , and capped supertetrahedral  $C_n$  families according to one proposed notation),<sup>86–88</sup> structural diversity may exist for much larger clusters. Such a change in the trend, in terms of shape, upon the increase of nanocluster size is known for other metal chalcogenides. For example, in the family of copper selenide nanoclusters, there appears to be a definite transition point with the number of Cu atoms around 60: for the smaller  $\text{Cu}_{2x}\text{Se}_x$  nanoclusters, an arrangement of the  $\text{Cu}_2\text{Se}$  core can be described as spherical (or quasi-spherical) without any topological relationship with the bulk  $\text{Cu}_2\text{Se}$ .<sup>89</sup> Some examples of such nanoclusters are  $[\text{Cu}_{20}\text{Se}_{13}(\text{PET}_3)_{12}]$ ,  $[\text{Cu}_{29}\text{Se}_{15}(\text{P}^i\text{Pr}_3)_{12}]$ ,  $[\text{Cu}_{32}\text{Se}_{16}(\text{PPh}_3)_{12}]$ ,  $[\text{Cu}_{36}\text{Se}_{18}(\text{P}^i\text{Bu}_3)_{12}]$ ,  $[\text{Cu}_{52}\text{Se}_{26}(\text{PPh}_3)_{16}]$ , and  $[\text{Cu}_{59}\text{Se}_{30}(\text{PCy}_3)_{15}]$ .<sup>90–93</sup> For the larger  $\text{Cu}_{2x}\text{Se}_x$  nanoclusters, the characteristic layered arrangement of the solid in combination with an overall triangular shape are observed. Examples of such nanoclusters are  $[\text{Cu}_{70}\text{Se}_{35}(\text{PET}_3)_{21}]$  and  $[\text{Cu}_{146}\text{Se}_{73}(\text{PPh}_3)_{30}]$ .<sup>90,94,95</sup>

In the case of CdS nanoclusters, the possible existence of the transition point for cluster shape may be impelled by unfavorable high anionic charge and/or ligand bonding ( $\mu_3$  for  $\text{SPh}^-$ ) for the hypothetical very large tetrahedral nanoclusters following the trend. Wu *et al.* have proposed using the protonated forms of organic superbases (*e.g.*, 1,5-diazabicyclo[4.3.0]non-5-ene, DBN, and 1-methylimidazole, 1-MIM) to help in stabilizing the negative charge of the large hybrid supertetrahedral chalcogenide nanoclusters (*e.g.*,  $[\text{In}_{16}\text{Cd}_4\text{S}_{31}(\text{DBN})_4]^{6-}$  and  $[\text{In}_{22}\text{Cd}_{13}\text{S}_{52}(\text{1-MIM})_4]^{12-}$ ).<sup>96</sup> An overall core of a truncated tetrahedral shape better matches TGA data and elemental analysis results for **1**.

Quantum calculations performed by Zhang *et al.* showed that tetrahedral CdTe nanoparticles would possess a large dipole moment ( $\sim 40\text{--}180$  D) and preferentially form one- and two-dimensional superstructures due to anisotropic electrostatic particle–particle interactions when truncated on one, two, or three vertexes.<sup>84</sup> Proposed models are in agreement with the experimentally observed wires and sheets for CdTe nanoparticles, stabilized with thioglycolic acid or 2-(dimethylamino)-ethanethiol ligands, respectively.<sup>97</sup> Since electron microscopy examination of **1** revealed the presence of well-ordered cubic



three-dimensional superstructure, the identical truncation on all the four vertexes resulting in regular truncated tetrahedron must take place.

The shape of truncated tetrahedra of the individual nanoclusters may play an important role among the factors that determine the parameters (such as type of packing) of their superlattice in **1**. The influence of the building blocks' shape on their self-assembly into superlattice can be followed on examples of other metallic and semiconductor nanoparticles<sup>98-100</sup> (there is no precedent for CdE nanoclusters all belonging to particular tetrahedral families). For nonspherical crystalline nanoparticles, the packing arrangement is often considered by taking into account (1) entropy factors and (2) anisotropic interactions.<sup>101</sup> According to the entropy-driven approach to self-assembly, interaction potential of nanoparticles is believed to resemble that of hard spheres. Packing into densest superlattices is preferable, thus favoring face-to-face contacts of faceted nanoparticles. In contrast, specific interparticle forces leading to anisotropic bonding in a superlattice may be followed. The possible mechanism for the shape-driven anisotropic interactions was recently discussed by Talapin and co-workers for the self-assembly of CdSe nanotetrahedra with 8 and 10 nm edge lengths, capped with either oleic or stearic acid ligands.<sup>102</sup>

The larger size and shape of truncated tetrahedra (with absence of sharp vertexes) of thiophenolate-stabilized CdS nanoclusters in **1** contribute to cluster–cluster interactions in the system. These factors may cause existence of three different orientations of nanoclusters in the superlattice, whereas a single orientation was observed for smaller tetrahedral CdS nanoclusters in **2**. Potentially weaker cluster–cluster interactions may also decrease the orientational order in the superlattice, which hampers single-crystal X-ray diffraction characterization. In a similar way, the size dependence of interparticle potential, acting during the self-assembly, was reported to cause softer interactions between the larger crystalline PbS nanoparticles, resulting in a superlattice with an increased number of defects (twinning).<sup>103</sup> There are also previously described superlattices of tetrahedral Ag nanoparticles, where the packing has long-range translational order, whereas the orientational order is short-range.<sup>104</sup>

The optical properties of **1** (including UV–vis absorption and diffuse reflectance spectra, PL and PLE) show the relation of the constituent nanoclusters (1.9 nm in size) with the known families of monodisperse CdS frameworks, whereas PXRD and electron microscopy provide information on their self-assembly into cubic superparticles (5–25  $\mu\text{m}$  in size) having a crystalline superlattice. While such neutral nanoclusters forming an apparently primitive cubic cell have some similarity with superlattices of previously reported tetrahedral Cd<sub>32</sub> and Cd<sub>54</sub> nanoclusters, several structural features demonstrate the significance of **1** as a transition point from known families of smaller CdS nanoclusters to unexplored larger ones. The shape of nanoclusters in **1** is, most probably, close to truncated tetrahedral, and their surfaces are less rich in SPh<sup>-</sup>; secondary structure of **1** is more complex, with three different orientations for the constituent nanoclusters in 3D superparticles.

The mechanism of conversion of the precursor (Me<sub>4</sub>N)<sub>2</sub>[Cd(SPh)<sub>4</sub>] under solvothermal conditions was elucidated *via* a series of experiments. The solvothermal process puts the solvents under elevated temperature and pressure, allowing increasing solubility of reagents, speeding conversion to the desired product, and facilitating its crystallization.<sup>105</sup> Solutions of the precursor after solvothermal treatment at different temperatures (80–240 °C) in CH<sub>3</sub>CN-*d*<sub>3</sub> were examined. It was observed that after thermal treatment at 120–160 °C solutions of (Me<sub>4</sub>N)<sub>2</sub>[Cd(SPh)<sub>4</sub>] turn yellow and opalescent, presumably because less soluble polynuclear cadmium thiophenolates are formed. <sup>1</sup>H NMR spectroscopy of solutions isolated from solvothermal treatment at different temperatures illustrates that the growth of [Cd<sub>x</sub>S<sub>y</sub>(SPh)<sub>z</sub>] nanoclusters is accompanied by the formation of both phenyl methyl sulfide (Ph–S–Me) and diphenyl sulfide (Ph–S–Ph) as byproducts (Figure 2.14). Small amounts of diphenyl disulfide (Ph–S–S–Ph) were also detected, in agreement with mass spectrometry experiments on the thermal decomposition of solid sampled of **1**. At temperatures as low as 80 °C, signals in the <sup>1</sup>H NMR spectra are already shifted relative to those for (Me<sub>4</sub>N)<sub>2</sub>[Cd(SPh)<sub>4</sub>], indicating the formation of intermediate complexes. Starting from 120 °C, both intermediates and byproducts can be observed in the <sup>1</sup>H NMR spectra. Diphenyl sulfide is especially important as a byproduct since its formation would result in S<sup>2-</sup> release, which is necessary for [Cd<sub>x</sub>S<sub>y</sub>(SPh)<sub>z</sub>] core growth. This observation is complementary to previously explored reactions in which elemental sulfur,<sup>20</sup> Na<sub>2</sub>S<sup>22</sup> or other sulfur-releasing agents (*e.g.*, thiourea, CS<sub>2</sub> or Na<sub>2</sub>S<sub>2</sub>O<sub>3</sub>)<sup>26,31,106–108</sup>

have been added in order to prepare larger  $[\text{Cd}_x\text{S}_y(\text{SPh})_z]$  frameworks. Schubert and co-workers have proposed that mononuclear species  $[\text{Cd}(\text{SPh})_x\text{L}_y]^{(2-x)}$  ( $x \approx 3$ ) are formed upon  $[\text{Cd}_{10}\text{S}_4(\text{SPh})_{16}]^{4-}$  thiolate complex thermal transformations.<sup>109</sup> It is possible that similar intermediates are present in reaction mixtures here, too. The formation of intermediate-sized polynuclear species produced at lower temperatures in these solvothermal syntheses was confirmed by single-crystal X-ray diffraction. From the reaction solution of  $(\text{Me}_4\text{N})_2[\text{Cd}(\text{SPh})_4]$  heated at 160 °C in acetonitrile, it was possible to crystallize the previously reported  $(\text{Me}_4\text{N})_2[\text{Cd}_{17}\text{S}_4(\text{SPh})_{28}]$ .<sup>22</sup> Although they are not necessarily present in the higher-temperature reaction solutions such as in the formation of **1**, it is important evidence for the effectiveness of mononuclear cadmium thiophenolate precursor conversion leading to larger architectures. According to Herron *et al.*,<sup>24</sup> the role of DMF in the process of nanocluster growth from a precursor with lower nuclearity is closely connected with the ability of this coordinating solvent (1) to compete with thiophenolate ligands for the surface metal sites and (2) to immediately passivate dangling bonds. This ability results in individual cluster bonds breaking and different species being in rapid exchange in the solution.

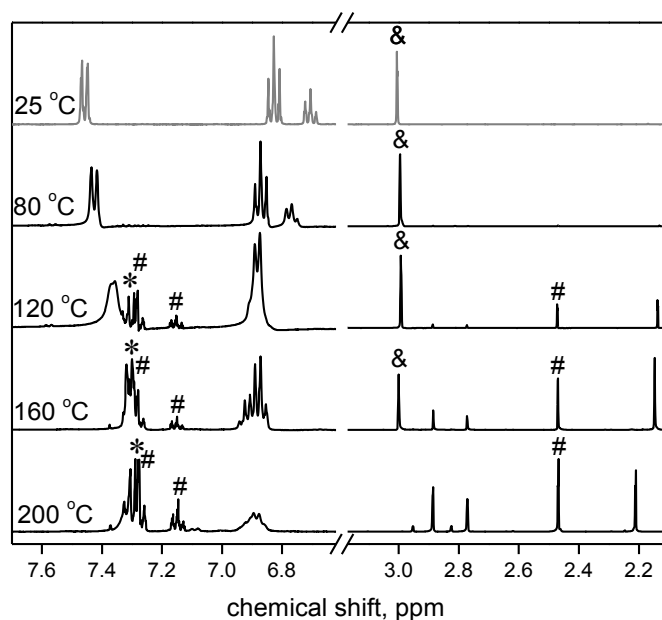


**Figure 2.14:** Room temperature <sup>1</sup>H NMR spectra for soluble species after one day solvothermal treatment of  $(\text{Me}_4\text{N})_2[\text{Cd}(\text{SPh})_4]$  in  $\text{CH}_3\text{CN}-d_3$  at different temperatures (&, # and \* refer to positions of  $\text{Me}_4\text{N}^+$ , Ph-S-Me and Ph-S-Ph signals, respectively). Spectra are normalized and scaled in order to facilitate the comparison; Y axis offset was used.

As an example of materials balance for the conversion of mononuclear cadmium thiolate precursor into larger clusters, an equation for the synthesis of  $(\text{Me}_4\text{N})_2[\text{Cd}_{17}\text{S}_4(\text{SPh})_{28}]$  can be shown as follows:



If the thermal conversion proceeded in all cases in this manner, then the larger the size of cluster grown, the larger the relative amount of S needed to build it up; therefore, more Ph-S-Ph will be found among the byproducts of conversion. Thus, for the synthesis of  $[\text{Cd}_{17}\text{S}_4(\text{SPh})_{28}]$ , a ratio Ph-S-Ph / Me-S-Ph = 1 : 8 is expected, whereas for  $[\text{Cd}_{54}\text{S}_{28}(\text{SPh})_{52}(\text{dmf})_4]$ , a ratio Ph-S-Ph / Me-S-Ph = 1 : 3.25 would be found. However, at higher reaction temperatures, additional pathways may also come into play. Konishi and co-workers have demonstrated previously that smaller  $\text{R}_4\text{N}^+$  can associate with anionic cadmium-chalcogen clusters, depending on the steric restrictions of the tetraalkylammonium ion, and  $^1\text{H}$  NMR studies indicated that the cations can be intercalated into the surface  $\text{SPh}^-$  groups.<sup>110</sup> Cao and co-workers have shown the potential of guest molecules to change the cluster-cluster interactions through an inclusion into ligands shell.<sup>111</sup> A series of experiments was performed to probe the thermal stability of tetramethylammonium chloride  $\text{Me}_4\text{NCl}$  under similar solvothermal conditions as those used for the preparation of nanomaterial **1**: solutions were examined using  $^1\text{H}$  NMR spectroscopy after solvothermal treatment at different temperatures (80–200 °C) in  $\text{CH}_3\text{CN}-d_3$ . It is observed *via*  $^1\text{H}$  NMR spectroscopy that even after heating at 200 °C the majority of  $\text{Me}_4\text{N}^+$  ions are mostly intact. This is consistent with the proposal that the disappearance of  $\text{Me}_4\text{N}^+$  from reaction mixtures after  $(\text{Me}_4\text{N})_2[\text{Cd}(\text{SPh})_4]$  conversion at 200 °C (see Figure 2.14) is not related to the simple thermal decomposition of  $\text{Me}_4\text{N}^+$  (which likely occurs to a significant extent only at much higher temperatures) but rather with a lower-energy reaction with  $\text{SPh}^-$  leading to formation of Me-S-Ph and  $\text{Me}_3\text{N}$ .

To obtain insight into the role of  $\text{Me}_4\text{N}^+$  in the process of  $(\text{Me}_4\text{N})_2[\text{Cd}(\text{SPh})_4]$  conversion, the solvothermal treatment of  $(\text{Me}_4\text{N})_2[\text{Cd}(\text{SPh})_4]$  at 200 °C was performed in the presence of additional amounts of  $\text{Me}_4\text{NCl}$  (Scheme 2.1). In this case, it is observed that

the process results in the formation of a yellow-orange solid material (**3**). Unlike **1**, SEM analysis of **3** reveals the presence of uniform spheres of 0.5–2.0  $\mu\text{m}$  in size (Figure 2.15); no faceted cubic crystals were observed. However, the higher-order colloidal spheres are themselves constructed of nanometer-sized CdS, as shown below.

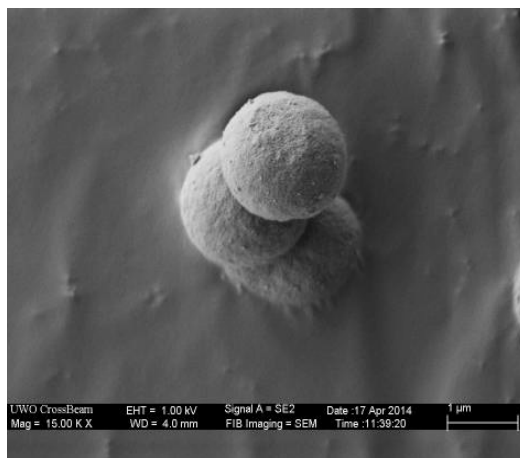


**Figure 2.15:** SEM image of spheres of **3**.

The wide-angle region of PXRD patterns for **3** (Figure 2.16) are consistent with crystalline nanometer-sized CdS. The reflections become higher and sharper in comparison with those for **1** (see Figure 2.3), which may indicate an increase in cluster size. Although peak broadening still complicates the analysis, some features characteristic of the structure of Greenockite (hexagonal) CdS can be discerned (*e.g.*, incipient 103 reflection) and are even more pronounced in SAED (*vide infra*). Calculations of the mean size of the crystalline domains using the Scherrer equation allow an average value of  $2.5 \pm 0.4$  nm to be assigned for **3**, which is substantially larger than the value found for **1** (1.5 nm). No pronounced peaks but only a weak shoulder can be observed between  $2\theta$   $2.5^\circ$  and  $3.0^\circ$  in the low-angle region of the PXRD for **3**, consistent with the fact that only a (small) part of **3** possesses a long-range order. Deconvolution revealed the presence of a weak, narrow reflection (in agreement with a limited domain of nanocluster superlattice), but its location on a steep slope complicates determining the exact position. An estimate of  $2\theta \sim 2.8^\circ$  corresponds to an interplanar spacing  $d \sim 3.7$  nm. This is consistent with the presence in **3** of nanoclusters substantially larger than in **1** (where  $d$  was calculated to be 2.9 nm).

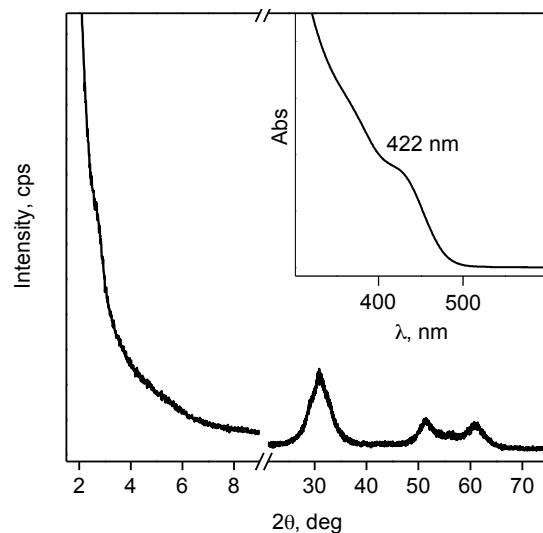


**Figure 2.16:** Powder X-ray diffraction pattern (Co K $\alpha$  radiation) and UV-vis absorption spectrum of DMF solution (*insert*) of **3** (magnification  $\times 3$ ).

In the UV-vis absorption spectra of solutions of **3** (Figure 2.16, *insert*), weak excitonic features were observed; peaks at 422 and 362 nm (fwhm for the low-energy peak 74 nm) were found upon the multipeak fitting. These excitonic peaks are shifted to higher wavelengths in comparison with **1** (where they were found at 392 and 334 nm), which is in agreement with having nanoclusters of larger size in **3**. Note that  $\Delta\lambda$  in **2** (60 nm) is very similar to that found for **1** (58 nm). The UV-vis diffuse reflectance spectra of solid **3** (Figure 2.4) are virtually featureless (the presence of extremely weak excitonic peak can be derived only from the corresponding first-derivative curve), which confirms that **3** is not composed of a homogeneous distribution of clusters of similar size. An onset of the absorption is shifted toward a longer wavelength, in comparison to the solution spectrum, in a similar way as was observed for the diffuse reflectance and solution spectra of **1**.

TGA for **3** indicated only  $\sim 16\%$  weight loss between 300 and 600  $^{\circ}\text{C}$  (Figure 2.12), markedly lower than the  $\sim 24\%$  observed for **1**. The wide-frequency part of the Raman spectra for **3** show bands very similar to those observed for **1** (Figure 2.13, *left*), in agreement with SPh $^{-}$ -covered neutral nanoclusters. The low-frequency part of the Raman spectra CdS nanoclusters provides information about core and surface structures, as the vibrational frequencies of Cd-S bonds (appearing in 50–500  $\text{cm}^{-1}$  region) were reported to be sensitive to the structure type and the connectivity of sulfur atoms.<sup>20</sup> A weak

shoulder at  $\sim 247\text{ cm}^{-1}$  (Figure 2.13, *right*) can be assigned to the  $\nu(\text{Cd-S})$  stretching frequencies of the internal Cd-S bonds of nanocluster core, whereas a strong band at  $168\text{ cm}^{-1}$  can be assigned to the ones of the bridging  $\text{Cd}_2(\mu\text{-SPh})^{112}$  and  $\text{Cd}_3(\mu_3\text{-SPh})$  ligands on the surface. Markedly larger intensity of surface *vs.* core Cd-S bands for **3** in comparison to that for **1** is consistent with a larger nanocluster size in **3**. Elemental analysis (CHNS) for **3** revealed much lower carbon content in comparison to that for **1** (13.69 *vs.* 23.93%, respectively), in agreement with fewer thiophenolate groups covering the surface of nanoclusters in **3**. The atomic Cd / S ratio found for **3** using EDX was 0.91 : 1 (Table 2.2), which is markedly larger than that found for **1** (0.77 : 1) and also consistent with a larger nanocluster size in **3**.

STEM images for (wet-prepared) samples of **3** show the presence of relatively large domains of a superlattice on the surfaces of micrometer-sized spheres (Figure 2.17). The lattice parameter for this surface arrangement is 3.4 nm (primitive cubic). Assuming a  $\sim 1.1\text{ nm}$  organic ligand shell, this corresponds to nanoclusters of 2.3 nm in diameter (while for **1**, the diameter is 1.9 nm). Despite the larger size of the nanoclusters, the ordered domains in **3** have a structural similarity with the fragments of cubic superlattice found on the surfaces of the cubes of **1**. In the case of **3**, PXRD data suggest that only limited domains of 2.3 nm nanocluster superlattice are present in the sample.

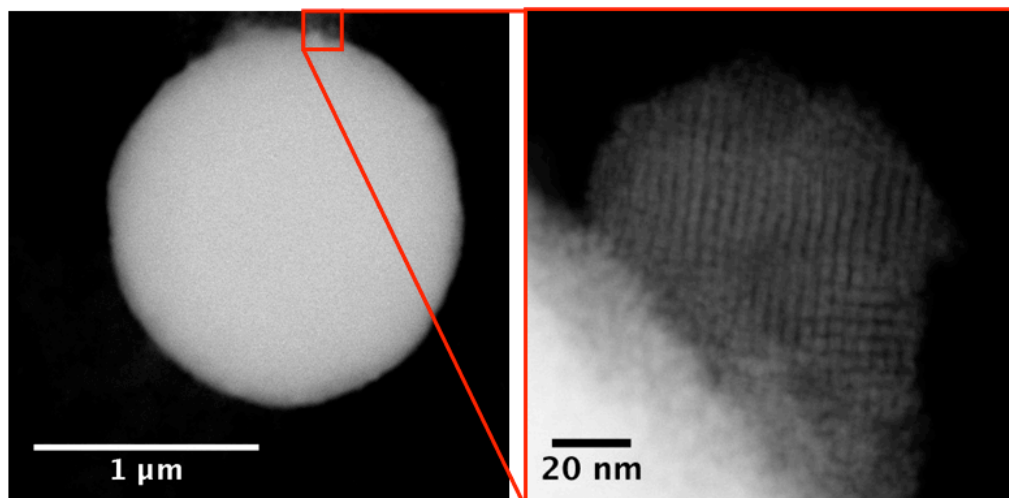


**Figure 2.17:** STEM images of **3**: sphere, general view (*left*); edge of sphere, high resolution (*right*); “wet” sample preparation.

STEM and TEM images for FIB-prepared samples of **3** (see Appendix A) provide decisive evidence that the morphology of the spheres is more complex (hierarchical) than that observed within the cubes in **1**. Some spheres (cross-section STEM image is shown in Figure 2.18) have a clearly distinguishable core-shell (CS) structure, with relatively compact outer and inner shells together with a core composed of larger components. The outer shell (~300 nm thick) consists of ~2.3 nm sized monodisperse CdS nanoclusters (composition confirmed by site-specific EDX analysis). Large domains of primitive cubic superlattice composed of the same nanoclusters can be found on the surface of such spheres (Figure 2.18, *top right*), but no sign of a continuous superlattice of nanoclusters was found in the range of the outer shell of spheres. The inner shell (~100 nm) has a gradient of CdS nanoparticles ranging in size from 2.5 to 20 nm upon going from the surface to the center of the superparticle (Figure 2.18, *bottom right*). Finally, the large core in such spheres is composed of nanoparticles ~20 nm in size, with rather uniform size and shape (Figure 2.18, *bottom left*). Thus, in **3**, the formed inorganic nanoparticles with nonuniform size distributions size-selectively segregate themselves and assemble into uniformly shaped superparticles with core-shell morphologies (core-shell or CS-spheres in **3**). Electron diffraction patterns of three areas inside the CS-spheres in **3** (at the edge, inner shell, and the center, Figure 2.19) confirm the proposed morphology, allowing the transition from nanoclusters at the edge (regular and broad diffraction patterns; dominating Hawleyite CdS structure) to large crystalline nanoparticles in the center (narrow diffraction patterns, Greenockite CdS structure can be clearly distinguished; discrete spots correspond to (a few) different large nanoparticles) to be followed. In contrast, for some spheres in **3** (Figure 2.20), no obvious size gradient of constituent units was found (homogeneous or *H*-spheres). Such spheres are formed from nearly monodisperse ~2.3 nm CdS nanoclusters but with no sign of a superlattice structure or of a preferred orientation. The 2.3 nm sized CdS nanoclusters, along with some larger nanoparticles, contribute to weight loss observed by TGA between 300 and 600 °C. The 2.5 nm size calculated using the Scherrer equation seems to be an average for the 2.3 nm nanoclusters combined with much larger nanoparticles present in the sample of **3**. Clearly, the presence of additional Me<sub>4</sub>NCl has a pronounced effect on both the size of the nanoclusters/nanoparticles as well as on the morphology of the final nanomaterial. It is interesting to note that remnants of the ordered cubic superlattice are present (similar to that of **1**, but formed by larger nanoclusters in the case of **3**), whereas the primary units in this material are not strictly monodisperse.



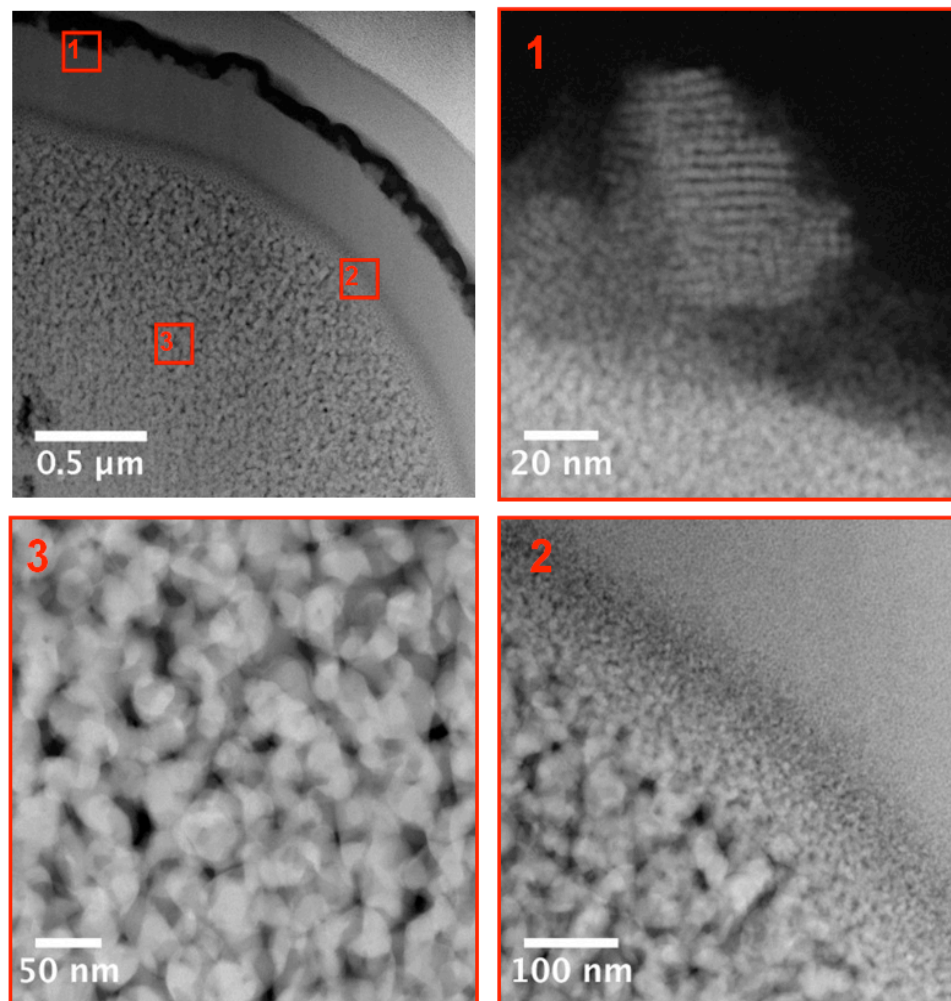


**Figure 2.18:** HAADF STEM images of **3**: CS-sphere, general view (*top left*); edge of sphere, high resolution (*top right*); core-to-shell transition, high resolution (*bottom right*); core, high resolution (*bottom left*); “FIB” sample preparation.

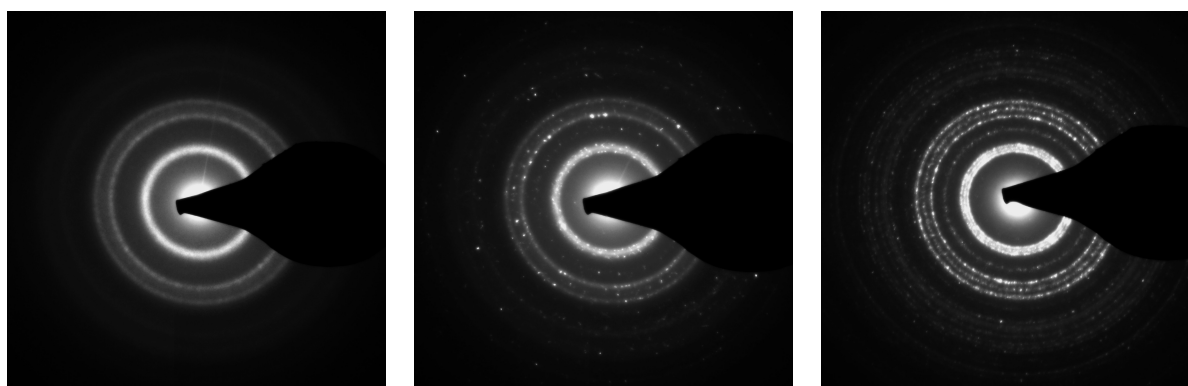


**Figure 2.19:** Wide-angle SAED of **3**, obtained from the areas at the edge (*left*), core-to-shell transition (*middle*) and core (*right*) of CS-sphere.

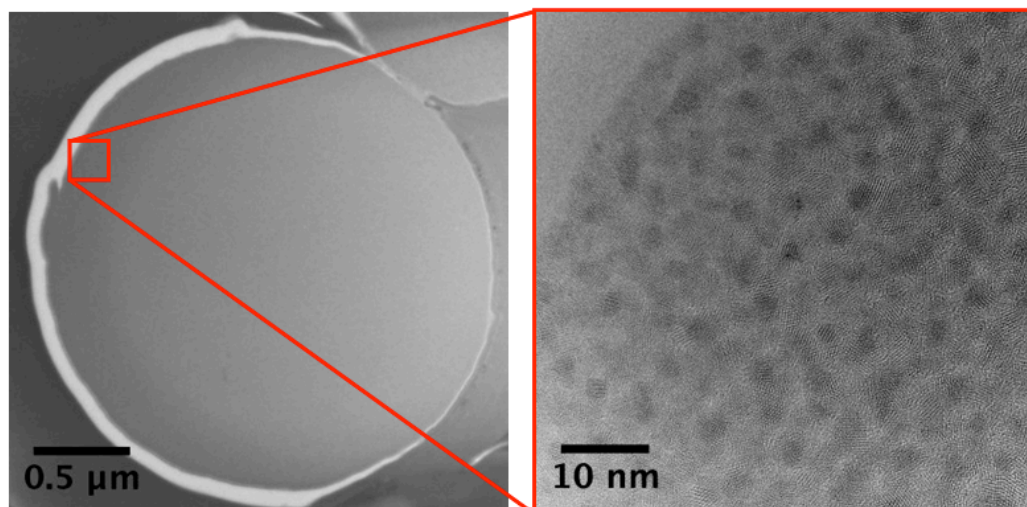


**Figure 2.20:** TEM images of **3**: *H*-sphere, general view (*left*); edge of sphere, high resolution (*right*); “FIB” sample preparation.

Although routes for the preparation of CdE secondary architectures/particles ( $E = S, Se, Te$ ) are well-established,<sup>113–115</sup> the assembly of microscopic materials from nanoscale building blocks in a hierarchical manner is an emerging area of synthesis. Uniform in size and shape, spherical CdE superparticles have been obtained using different precursors and solvents under different reaction conditions, indicating that the self-assembly of nanoparticles into monodisperse micrometer-sized secondary structures is a general phenomenon, although quantitative answers to many questions are not yet available.<sup>116</sup>

The possible mechanisms for the formation of uniform CdS spheres have been discussed by Chen and co-workers with the solvothermal reaction (140 °C for 8 h) of  $Cd(NO_3)_2$  and thiourea in ethylene glycol with the addition of poly(vinyl pyrrolidone) (PVP) as a stabilizing ligand.<sup>117</sup> According to the proposed multistep process of superparticle formation, the initial stage assumes homogeneous and slow nucleation and growth of crystalline (hexagonal structure) CdS nanoparticles of ~5 nm in diameter. These faceted nanoparticles then self-assemble to form limited domains (~23 nm after 2 h) of an ordered crystalline superlattice, as it was revealed by HR TEM imaging. At the third stage, more nanoparticles are formed in solution and randomly attached to preformed superparticles, completing uniform spheres in situ. Such surface-induced growth is fast and non-equilibrium as opposed to preceding growth of ordered core, so, essentially, an

amorphous shell is believed to be formed (although no cross-section TEM was available to confirm the structure). The size of the resulting CdS superparticles can be tuned between 80 and 500 nm by adjusting the reaction conditions, with the growth of uniform spheres most probably limited only by reagent(s) depletion. A similar growth mechanism may be realized during the formation of *H*-spheres observed in **3**, when fast (non-equilibrium) aggregation takes place and/or relatively weak and short-range van der Waals forces between stabilizing ligands of 2.3 nm CdS nanoclusters lead to self-assembly of essentially amorphous spherical superparticles.

The mechanism of the formation of uniform CdSe core-shell superspheres was recently probed by Kotov and co-workers *via* the reaction in aqueous solution (80 °C) of Cd(ClO<sub>4</sub>)<sub>2</sub> with N,N-dimethylselenourea or Na<sub>2</sub>SeSO<sub>3</sub> as a selenium source and sodium citrate as ligand.<sup>118</sup> It was found that growth and assembly of CdSe nanoparticles occurs simultaneously in this case. It is interesting that rather polydisperse CdSe nanoparticles (size distribution 20–30%) can self-assemble into core-shell secondary particles which themselves possess substantially narrower size distributions (7–9%). Such secondary particles are composed of a loosely packed core and a more densely packed outer shell, as confirmed by synchrotron small-angle X-ray scattering. A proposed mechanism for this case was a self-limiting growth governed by the balance between long-range electrostatic repulsion and short-range van der Waals attraction forces (originating from the citrate stabilizers on the surface of nanoparticles), which was stated to be aided by the polydispersity of the constituents. The strong electrostatic repulsion inside the superparticle gives rise to a loosely packed core. The different scales of particle-particle interactions together with polydispersity of CdSe nanoparticles lead to rearrangement of constituents within the superparticle so that larger nanoparticles form the core and smaller ones pack in the outer shell.

A similar morphology, namely, a core of larger loosely packed particles and an outer shell of smaller and densely packed components, is observed for CS-spheres in **3**, with the size-selective segregation upon self-assembly possibly also caused by the balance of several different particle-particle interactions. These can be electrostatic repulsion and van der Waals attraction, too, but there are no data supporting the conjecture that nanoparticles in CS-spheres in **3** carry a charge. Alternatively, a size-selective sorting

effect, previously reported for polydisperse nanoparticles self-assembly driven with van der Waals forces only,<sup>119</sup> may be operating. In this case, nanoparticle segregation is based on size-dependent interaction strength (scaling as  $\sim a$  at short distances and as  $\sim a^6$  at long distances, where  $a$  represents particle size): for a localized superstructure, the overall potential energy of the system reaches a minimum when the largest particles (interacting strongly) are in the center and the smallest particles (interacting weakly) are at the edge of assembly.<sup>119</sup> Size-selective segregation driven by van der Waals forces has been reported for metallic nanoparticles;<sup>120–122</sup> for semiconductor ones, interparticle van der Waals interactions are much weaker<sup>119,123</sup> and may not lead to the same effect in the formation of *CS*-spheres in **3**.

The optical properties, PXRD, and electron microscopy data for **3** revealed that the constituents (CdS nanoclusters 2.3 nm in size and even larger nanoparticles) self-assemble into a uniform in size and shape superspheres of at least two distinct morphological types (namely, *H*-spheres and *CS*-spheres) with different distributions of the primary particles. No direct information is available on the abundance of each observed morphology of the superspheres, but according to calculations based on TGA and the wide-angle PXRD peaks broadening, *CS*-spheres with large CdS nanoparticles can hardly be the dominant species in **3**. Only a few reports of the size-selective segregation of CdS nanoparticles into spherical superparticles have been published. The formation of such secondary particles occurs under the influence of complex factors, where a balance of van der Waals interactions and other force(s) takes place. It is clear that the presence of additional Me<sub>4</sub>NCl benefits the formation of larger CdS nanoclusters upon solvothermal conversion of the cadmium thiophenolate precursor. Further investigation is needed to reveal the mechanism of growth of larger nanoclusters in the presence of other tetraalkylammonium salts and the influence that the halogen counterion may play.

Treatment of (Me<sub>4</sub>N)<sub>2</sub>[Cd(SPh)<sub>4</sub>] in the presence of Me<sub>4</sub>NBr yields a bright yellow solid material (**4**) (Scheme 2.1). SEM examination of the morphology of **4** shows that neither cubes (as for **1**) nor spheres (as for **3**) are present as the main morphological features in this case. Only a limited amount of detached spheres is present, along with the complex aggregates formed by intergrowing cubes and spheres (Figure 2.21).

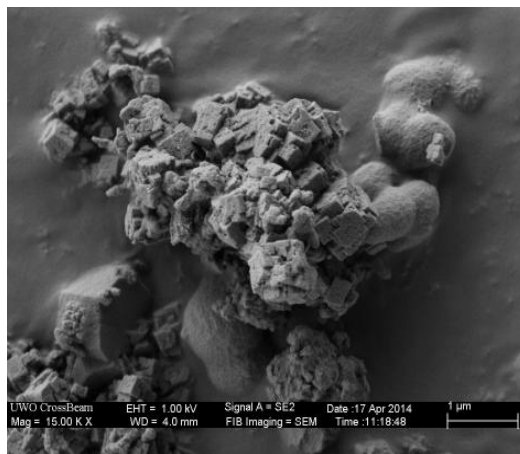


**Figure 2.21:** SEM image of mixed species of **4**.

In the wide-angle region of the PXRD patterns for **4** (Figure 2.3), reflections consistent with crystalline CdS species were found to be sharper in comparison to those in the patterns for **1**, but they are still not that differentiated as they are for **3**. Calculations of the mean size of the crystalline domains give a value of  $1.9 \pm 0.1$  nm, compared to the 1.5 nm calculated for **1** and 2.5 nm for **3** (illustrating the size trend within the limitations of the method). A strong, sharp reflection in the low-angle PXRD patterns for **4** (Figure 2.22) was found at  $2\theta$   $3.00^\circ$ , shifted toward the lower values due to a larger unit cell in comparison to that for **1**. Thus, the interplanar spacing  $d$  for **4** is 3.4 nm, whereas for **1** it was only 2.9 nm.

A superlattice with exactly the same cubic lattice parameter<sup>75</sup> of 2.3 nm CdS nanoclusters with a distance between clusters' cores of  $\sim 1.1$  nm was also prepared by solvothermal conversion of  $(\text{Me}_4\text{N})_2[\text{Cd}(\text{SPh})_4]$  in the presence of CTAB additive (see Chapter 3) as continuous domains, whereas in the presence of  $\text{Me}_4\text{NCl}$  additive, it was observed only as limited fragments in **3**. It must be noted that despite the larger size (2.3 vs. 1.9 nm) HR TEM images obtained for the discrete crystalline nanoclusters in this system still do not allow a definite conclusion about its shape to be made.

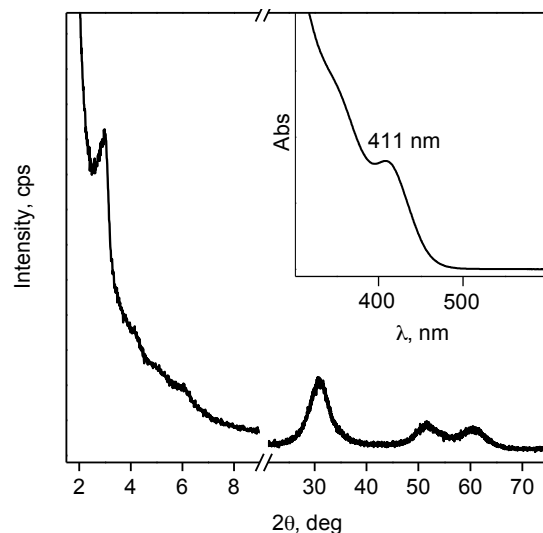


**Figure 2.22:** Powder X-ray diffraction pattern (Co K $\alpha$  radiation) and UV–vis absorption spectrum of DMF solution (*insert*) of **4**.

In the UV–vis absorption spectrum of **4** (Figure 2.22, *insert*), peak positions are found to be shifted toward longer wavelengths in comparison to those for **1** (for low-energy excitonic peak 411 and 392 nm for **4** and **1**, respectively), which reflects the size increase of the nanoclusters in comparison to **1**. The fwhm value for the low-energy excitonic peak for **4** is 53 nm, consistent with monodisperse nanoclusters. With the prominent low-energy excitonic peak at 411 nm and an additional feature at 351 nm, the  $\Delta\lambda$  of **4** (60 nm) is very similar to those observed for **1** and **3** (*i.e.*, 58 and 60 nm, respectively). The UV–vis absorption bands of **3** are virtually identical to those reported for the 2.3 nm CdS nanoclusters prepared with the addition of CTAB (see Chapter 3).

The UV–vis diffuse reflectance spectra of solid **4** generally resemble the corresponding absorption spectra in DMF solutions (Figure 2.4), although in the solid state the peaks are broader and red-shifted in comparison to the solution spectra (in the same way as was observed for **1**). The similarity between the DMF solution and solid-state spectra (assuming relatively weak cluster–cluster interactions exist in the crystalline superlattice) indicates homogeneity of the solid samples **4**.

DMF solutions of **4** (much more diluted because of the limited solubility in comparison to those of **1**) were found to emit at ~615 nm (Figure 2.5) when excited at 410 nm. The emission peak is less symmetrical, broader (fwhm 155 nm), and shifted to higher wavelengths in comparison to that for **1** (with maximum at 587 nm). The corresponding excitation spectra of **4** show sharp absorption bands at 397 and 344 nm, similar to those observed for **1** (at 381 and 327 nm) except that they are shifted to longer wavelengths. The observed PL and PLE spectra are in agreement with deep trap type of emission for nanoclusters in **4**.

The TGA for **4** revealed ~20% weight loss between 300 and 600 °C (Figure 2.12); the calculated  $S^{2-} / SPh^{-}$  ratio of 1.93 : 1 is larger than 1.56 : 1 for **1**, in agreement with the presence of larger 2.3 nm CdS nanoclusters with their shape changed further from that of a regular tetrahedron. Elemental analysis data (carbon content 18.23 vs. 23.93 for **4** and **1**, respectively) and EDX data (Cd/S atomic ratio 0.83 : 1 vs. 0.77 : 1 for **4** and **1**, respectively; see Table 2.2) support the formulation of a larger nanocluster size. In the Raman spectra of **4** (Figure 2.13), the absence of any intense bands in the area characteristic of aliphatic C–H stretching (as observed for **1** and **3**) is again consistent with an absence of charge on the nanoclusters; the surface to core Cd–S band intensity ratio for **4** is larger than that for **1**, whereas it is smaller than that for **3**. The results of analyses are complementary to the observed optical properties and PXRD data, confirming the preparation of CdS nanoclusters.

The formation of 2.3 nm CdS nanoclusters and their self-assembly into a similar superlattice upon solvothermal conversion of  $(Me_4N)_2[Cd(SPh)_4]$  with addition of either  $Me_4NBr$  or CTAB (see Chapter 3) implies that for nanocluster growth and superstructure formation the nature of the anion plays a decisive role while the size of cation of alkylammonium salt additive is less important. Halides are known to bind strongly with Cd; halide-substituted nanoclusters  $[Cd_{10}S_4X_4(SR)_{12}]^{4-}$ , where R = Ph, X = I; R = p-MeC<sub>6</sub>H<sub>4</sub>, X = I or Br, with four halide anions coordinated to the apex cadmium atoms have been reported previously.<sup>124</sup> In materials **3** and **4**, both EDX and Rutherford backscattering spectroscopy (RBS) analyses revealed that only trace amounts of halogens may be incorporated (Table 2.2 and Figure 2.23). Thus, although halides may play a role in the

molecule-to-material conversion process, they are not present in the final product in a significant amount (as ligands on the surface of nanoclusters or as a separate  $\text{CdCl}_2$  /  $\text{CdBr}_2$  phase). Neither Cl nor Br was found in a detectable amount by both EDX and RBS analyses in **1** (prepared without alkylammonium additives; see Table 2.2 and Figure 2.23).

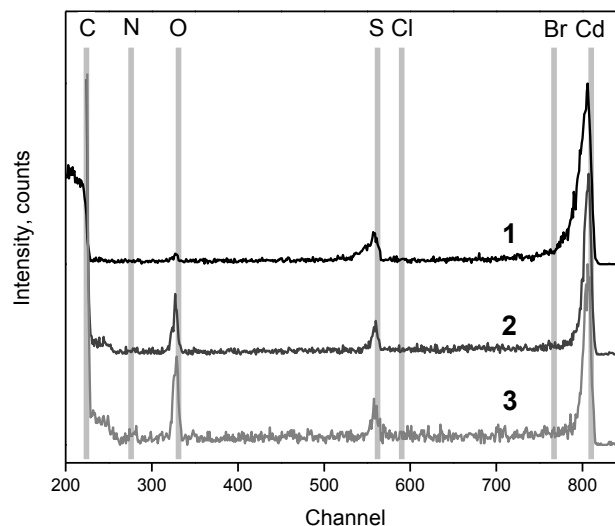


**Figure 2.23:** Rutherford backscattering spectra for **1**, **3** and **4** samples. No detectable amount of either Cl or Br was found in any of analyzed samples (see the main text).

The presence of particular ions in reaction mixtures has been recognized as an important factor influencing both the size and shape of nanoparticles<sup>125,126</sup> as well as the morphology of their self-assembled superstructures.<sup>127–129</sup> One of the proposed mechanisms for this is the strong interaction with the specific facets of crystalline nanoparticles. For instance, Xiong *et al.* have recently discussed the role of  $\text{Cl}^-$  ions in the growth and self-assembly of  $\text{Cu}_2\text{S}$  nanowires *vs.* nanoparticles *via* the solventless thermolysis at 200 °C of copper salts in the presence of 11-mercaptoundecanoic acid (MUA) and lauric acid as stabilizing ligands.<sup>128</sup> It was shown that at the early stage of the reaction  $\text{Cl}^-$  ions may preferentially adsorb on the (110) facets of the hexagonal  $\text{Cu}_2\text{S}$  crystallites, whereas the (001) and (100) facets are covered with laurate or MUA ligands. Because  $\text{Cl}^-$  ions are so much smaller than other ligands, such adsorption strongly reduces steric hindrance between the (110) facets of neighboring crystallites, by which their close contacts and fusion are promoted. Since the subsequent growth occurs mostly along the [110] direction, nanowire arrays are obtained. EDX analysis demonstrates that



in the solid phase the Cu / Cl ratio is gradually increased upon increasing the reaction time; only a trace amount of  $\text{Cl}^-$  was detected in the final product, which was explained by its presence in trapping defects in  $\text{Cu}_2\text{S}$  nanowires. On the contrary, in the absence of  $\text{Cl}^-$ , MUA ligands are homogeneously adsorbed on the whole surface of the growing  $\text{Cu}_2\text{S}$  crystallites and thus isotropic nanoparticle superlattices are achieved.

We propose that in our system halides added to the reaction mixture may participate in the solvothermal conversion of the precursor through the formation of halide-containing intermediates. The presence of halide ligands in lower-nuclearity-clusters may facilitate their fusion into larger clusters by decreasing steric hindrance in comparison to that for much bulkier  $\text{PhS}^-$  ligands. This explains the formation of monodisperse 2.3 nm CdS nanoclusters in the presence of  $\text{Me}_4\text{NBr}$  additives in contrast to 1.9 nm CdS nanoclusters when solvothermal conversion of the  $(\text{Me}_4\text{N})_2[\text{Cd}(\text{SPh})_4]$  precursor was performed without any additives. Because of the smaller van der Waals radius of  $\text{Cl}^-$  in comparison to that of  $\text{Br}^-$ , the fusion of chloride-containing intermediates occurs relatively easier than that for those containing bromide, so the larger CdS particles grow when  $\text{Me}_4\text{NCl}$  is added. Since neither Br nor Cl is present in a remarkable quantity in the final frameworks, such a catalysis-like fusion process may be related to the catassembly concept suggested by Tian and co-workers.<sup>130</sup> Alternatively, halides may simply alter the mechanism of  $(\text{Me}_4\text{N})_2[\text{Cd}(\text{SPh})_4]$  precursor conversion by participating in Ph-S- ligands cleavage through the formation of the highly reactive electrophile Ph-S-Hal. In this case, the different reactivity of different sulfenyl derivatives (with benzenesulfenyl chloride being more reactive and thus mediating the growth of larger CdS particles than benzenesulfenyl bromide) can be used to explain the formation of 2.3 nm CdS nanoclusters vs. larger nanoparticles.

### 2.3 Conclusions

The results show that the simple, thermally induced conversion of the readily prepared cadmium thiophenolate complex  $(\text{Me}_4\text{N})_2[\text{Cd}(\text{SPh})_4]$  provides a convenient route to prepare monodisperse CdS nanoclusters of tuned diameter with their subsequent self-assembly into micrometer-sized superparticles of different morphology. Thus, monodisperse 1.9 nm CdS nanoclusters are prepared by this route and are self-assembled into a crystalline cubic

superlattice, forming three-dimensional cubic crystals reaching 5–25  $\mu\text{m}$  in size. The optical properties of the constituents (*via* UV–vis absorption, diffuse reflectance, and PL/PLE spectroscopy) demonstrate their relation to known families of tetrahedral cadmium thiolate nanoclusters, whereas further detailed examination (including SAED and TGA) revealed their unusual structural properties, both on the level of individual nanoclusters and of the crystalline superlattices. In contrast to the preparation of 1.9 nm CdS nanoclusters by the thermolysis of  $(\text{Me}_4\text{N})_2[\text{Cd}(\text{SPh})_4]$  only, the addition to the reaction mixture of  $\text{Me}_4\text{NBr}$  results in the formation of a cubic superlattice of monodisperse 2.3 nm CdS nanoclusters. Based on close similarity of the materials, obtained with addition of either  $\text{Me}_4\text{NBr}$  or CTAB (see Chapter 3), it was supposed that the presence of halide rather than the nature of  $\text{R}_4\text{N}^+$  governs the growth of a larger cluster core. The role of the halide thus may lie in facilitating the fusion of lower-nuclearity-intermediates during the solvothermal process by replacing much bulkier  $\text{PhS}^-$  ligands. Alternatively, the halide may participate in  $\text{PhS}^-$  ligand cleavage by formation of  $\text{Ph-S-Hal}$ , altering the mechanism of  $(\text{Me}_4\text{N})_2[\text{Cd}(\text{SPh})_4]$  precursor conversion. In the presence of  $\text{Me}_4\text{NCl}$  additive, 2.3 nm CdS nanoclusters are formed along with larger nanoparticles and are self-assembled into spherical superparticles 0.5–2.0  $\mu\text{m}$  in size. The size-selective segregation upon self-assembly results in the formation of either homogeneous (*H*-spheres, composed of randomly attached 2.3 nm CdS nanoparticles) or core–shell superparticles (*CS*-spheres, having a gradient of CdS nanoparticles ranging in size from 2.5 nm at the surface to 20 nm in the center). The formation of such secondary particles occurs under the influence of complex factors where a balance of van der Waals interactions and other force(s) takes place. A proposed route to larger monodisperse CdS nanoclusters promises a broader potential area of application due to an improved ability to tailor their photophysical properties. Work will be continued to extend the developing route to CdSe phenylchalcogenolate system to expand the emission across the visible part of the spectrum for these materials.

## 2.4 Experimental Section

### 2.4.1 Syntheses

All synthetic and handling procedures were carried out under an atmosphere of high-purity dried nitrogen using standard double manifold Schlenk line techniques and a MBraun

Labmaster 130 glovebox. Solvents, if not specified below, were purchased from Caledon. Oxygen was removed from the solvents (*i.e.*, acetonitrile, *n*-propanol, methanol, and *N,N'*-dimethylformamide (DMF)) and liquid reagents (*i.e.*, tributylamine) using Schlenk and cannula techniques and sparging with nitrogen. Thiophenol, tributylamine, and tetramethylammonium chloride,  $\text{Me}_4\text{NCl}$ , were purchased from Aldrich; tetramethylammonium bromide,  $\text{Me}_4\text{NBr}$ , was obtained from Kodak; cadmium nitrate tetrahydrate,  $\text{Cd}(\text{NO}_3)_2 \cdot 4\text{H}_2\text{O}$ , was from Alfa Aesar. All solid reagents were reagent grade ( $\geq 98\%$ ) and were not further purified.

$(\text{Me}_4\text{N})_2[\text{Cd}(\text{SPh})_4]$  was synthesized by a slight modification of the published procedure<sup>20</sup> from  $\text{Cd}(\text{NO}_3)_2 \cdot 4\text{H}_2\text{O}$  and thiophenol deprotonated by tributylamine: the synthesis was done on a larger scale, and the amount of methanol used to dissolve  $\text{Me}_4\text{NCl}$  was 2 times smaller in order to facilitate product crystallization. Product purification was achieved by recrystallization from a saturated solution in boiling acetonitrile.

Syntheses of  $[\text{Cd}_x\text{S}_y(\text{SPh})_z]$  nanoclusters were performed in a sealed reactor at controlled temperature and increased pressure using polar organic solvents (solvothermal conditions).

Preparation of 1.  $(\text{Me}_4\text{N})_2[\text{Cd}(\text{SPh})_4]$  (1.791 g; 2.57 mmol) was combined with DMF (10 mL) in a 35 mL glass bottle and mixed thoroughly until a clear solution was obtained. The bottle was sealed in a stainless steel autoclave and placed into preheated oven at 200 °C for 48 h. The oven was then opened, and the sealed autoclave was allowed to cool naturally to ambient temperature. The autoclave was opened under the inert atmosphere, and the solid material was collected by centrifugation at 4000 rpm for 20 min, washed several times with DMF and finally with methanol, and dried under vacuum for 4–6 h. Mass yield, ~0.3 g.

After isolation of **1**, the mother liquor was filtered and allowed to stay undisturbed; after several days, a small amount of transparent cubic crystals (**2**) appeared. Solid material was isolated as described for **1**.

Preparation of 3. The procedure for the preparation of **3** was similar to that used for **1**, but  $\text{Me}_4\text{NCl}$  (0.141 g; 1.28 mmol) was added to a clear solution of  $(\text{Me}_4\text{N})_2[\text{Cd}(\text{SPh})_4]$

(2.57 mmol) in DMF and the suspension obtained was stirred for an additional 15 min prior to heating. Mass yield, ~0.2 g.

Preparation of 4. The procedure for the preparation of **4** was similar to that used for **3**, but Me<sub>4</sub>NBr (0.198 g; 1.28 mmol) was used instead of Me<sub>4</sub>NCl. Mass yield, ~0.2 g.

#### 2.4.2 Characterization

Elemental analysis (CHNS) was performed by Laboratoire d'Analyse Élémentaire de l'Université de Montréal (Quebec, Canada). The values of nitrogen found for all samples except **2** were less than the minimum detection limit (0.3%). Results are reported as an average of 2 to 3 measurements.

Found for **1**: C 23.93, H 1.58, S 20.07, N 0.22 %.

Calcd. for Cd<sub>54</sub>S<sub>80</sub>C<sub>316</sub>H<sub>316</sub>N<sub>8</sub>O<sub>4</sub> ((Me<sub>4</sub>N)<sub>4</sub>[Cd<sub>54</sub>S<sub>32</sub>(SPh)<sub>48</sub>(dmf)<sub>4</sub>):

C 29.36, H 2.46, S 19.85, N 0.87 %;

Found for **2**: C 30.89, H 2.29, S 20.18, N 0.58 %.

Found for **3**: C 13.69, H 0.87, S 20.17, N 0.20 %.

Found for **4**: C 18.23, H 1.19, S 19.86, N 0.20 %.

Solution UV–vis absorption spectra were acquired using a Varian Cary 50 Bio UV–vis spectrometer at 25 °C in 1 cm quartz cells against pure solvent (DMF). To obtain a saturated solution, a small portion (2–5 mg) of solid sample was sonicated with DMF (15–20 mL) for 6–12 h; then, the suspension was filtered through a syringe filter (0.22 μm, PTFE 100/pk membrane, Dikma Technologies Inc. and/or 0.02 μm, Anotop, Whatman GmbH) and diluted, if necessary, by pure DMF. The multipeak fitting of the spectra was carried out with Gaussian function,<sup>131</sup> using OriginPro 9.1 software.

UV–vis diffuse reflectance spectra of the solid samples were recorded using a Shimadzu UV–vis–NIR spectrophotometer UV-3600 with an integrating sphere attachment ISR-3100. Barium sulfate was used as reflectance standard and as the diluting matrix for the finely ground samples. To compare with absorption spectra, diffuse reflectance spectra were converted to the Kubelka–Munk function and normalized.

Room-temperature photoluminescence (PL) and photoluminescence excitation (PLE) spectra of DMF solutions (prepared using sonication as described above for UV–vis absorption spectroscopy) were acquired using a Photon Technologies International Inc. Quanta Master 7 fluorescence spectrofluorometer equipped with a xenon lamp. PLE were recorded using an excitation energy at the observed PL maximum of the individual samples.

Powder X-ray diffraction (PXRD) patterns of the samples were obtained using a Rigaku Rotaflex RU-200 BVH rotating-anode X-ray diffractometer with a Co K $\alpha$  ( $\lambda = 1.79026 \text{ \AA}$ ) radiation. X-ray generator (Rigaku Rotaflex RTP 300 RC) was operated at 45 kV and 160 mA, with monochromation being achieved using a curved crystal, diffracted beam, and graphite monochromator. The normal scan rate of  $10^\circ 2\theta/\text{min}$  for the instrument is equivalent to  $0.5^\circ$  on conventional diffractometers. X-rays were collimated using  $1^\circ$  divergent and scatter slits and a 0.15 mm receiving slit. The samples (in the form of a fine powder) were placed on a standard glass holder and measured from  $2$  to  $82^\circ 2\theta$  with a scan rate of  $2^\circ 2\theta/\text{min}$  and a sampling interval of  $0.02^\circ$ ; low-angle parts (from  $2$  to  $12^\circ 2\theta$ ) were additionally measured with the a scan rate of  $0.5^\circ 2\theta/\text{min}$  and a sampling interval of  $0.01^\circ$ .

TEM analyses were performed using an image aberration corrected Titan 80-300 (FEI) operated at an acceleration voltage of 300 kV and equipped with an S-UTW EDX detector (EDAX) and a US1000 CCD camera (Gatan). STEM images were acquired using a high-angle annular dark field (HAADF) detector with a nominal spot size of 0.14 nm. Imaging was mostly performed in bright-field transmission electron microscopy (BF TEM) and HAADF-STEM modes; the electron beam current/exposure time used for analysis was limited to minimize morphological changes in the samples.

Two different procedures, (1) wet and (2) FIB, were applied to prepare solid samples for morphological and compositional characterization by electron microscopy.

In the wet preparation method, suspensions and solutions of the material under study in organic solvents were used. In a typical procedure for a suspension, a small amount of solid material was sonicated with 5–10 mL of EtOH for 15 min. One drop of such a suspension was placed on a holey carbon copper TEM grid coated with an additional 2 nm carbon film

(Quantifoil) and allowed to stand for 1 to 2 min; then, the liquid was carefully removed by filter paper, followed by thorough drying of the grid. To prepare a solution, a small amount of solid material was sonicated with 5–10 mL of DMF for several hours, and the suspension was filtered through a 0.22  $\mu\text{m}$  PTFE syringe filter. The solution was dropped on the TEM grid and allowed to stand for 1–2 min; then, the liquid was carefully removed by filter paper, and the grid was washed three times by EtOH and thoroughly dried.

In the FIB preparation method, thin slices (lamellae) of the material under study were prepared: a Strata 400s DualBeam FIB (FEI) was used for in situ lift-out in a focused ion beam (FIB) system with parallel SEM imaging. The solid material was first covered with a protective carbon coating. A platinum protective coating was added (thick layer) at the target location, and the lamella was lifted after applying FIB milling and attached to a lift-out microscopy grid (Omicron). The lamella was further thinned to a thickness of 50–100 nm. The initial cutting was performed using 30 kV  $\text{Ga}^+$  ions with final polishing at 5 kV.

SEM imaging and energy-dispersive X-ray (EDX) spectroscopy analysis were performed using a LEO (Zeiss) 1540XB FIB/SEM system. Prior to imaging, a thin film of amorphous osmium metal was deposited on the samples using a Filgen osmium plasma coater OPC80T to prevent charging and reduce damage from the electron beam during imaging.

Solution  $^1\text{H}$  NMR spectra were obtained on a Varian Mercury 400 ( $^1\text{H}$  at 400.088 MHz) spectrometer using standard settings. Spectra were referenced internally to  $\text{SiMe}_4$  using the residual proton signal of deuterated solvents.

Thermal gravimetric analyses (TGA) were conducted on a Q600 SDT TA instrument: samples of about 10 mg were placed in an alumina crucible with a lid and heated at a rate of 1  $^\circ\text{C}/\text{min}$  from room temperature to 800  $^\circ\text{C}$  under nitrogen flow (100 mL/min).

FT Raman spectra were recorded on a Bruker RFS 100/S FT Raman spectrometer equipped with a  $\text{Nd}^{3+}/\text{YAG}$  laser operating at a wavelength of 1064 nm and a liquid nitrogen-cooled Ge detector. Typical laser powers ranged from 20 to 50 mW at the sample (fine powder in a glass capillary). 1024 spectra were averaged for each sample; the resolution used was 2  $\text{cm}^{-1}$ .

Rutherford backscattering spectroscopy (RBS) analyses were performed using  $^4\text{He}^{2+}$  ions produced by a 1.7 MV Tandem high-current accelerator facility, Western University. The incident beam angle was  $0^\circ$ , with incident energy of 2.5 MeV. Cumulative dose was varied from 1.25 to 20  $\mu\text{C}$ . A Si solid barrier detector mounted at a  $170^\circ$  angle was used for detection. An Sb-implanted amorphous silicon sample with a known total Sb content of  $4.82 \times 10^{15}$  atoms/ $\text{cm}^2$  was used to calibrate the detector solid angle. To prepare samples for the analysis, a small amount of solid material was sonicated with 5 mL of EtOH for 5–10 min. Resulting suspension was dropped on the carbon-coated substrate and allowed to stand until the solvent evaporated; then, the substrate was washed by EtOH and thoroughly dried.

#### ***2.4.3 Single-Crystal X-ray Diffraction***

Crystals suitable for single-crystal X-ray diffraction were taken directly from the reaction solutions, selected under Paratone N oil, and mounted on a Mitegen polyimide micromount. All X-ray measurements were made on a Bruker Kappa Axis Apex2 diffractometer in a nitrogen stream at 110 K. Graphite-monochromated Mo  $K\alpha$  radiation ( $\lambda = 0.71073 \text{ \AA}$ ) was used for the measurements. The unit cell dimensions were determined from a symmetry constrained fit of 9369 reflections with  $5.1^\circ < 2\theta < 45.82^\circ$ . The data collection strategy was a number of  $\omega$  and  $\phi$  scans, which collected data up to  $46.036^\circ$  ( $2\theta$ ). The frame integration was performed using the SAINT program (Bruker AXS Inc., version 2013.8). The resulting raw data was scaled and absorption corrected using a multiscan averaging of symmetry equivalent data using the SADABS program (Bruker AXS Inc., version 2012.1). The structure of **2** was solved by using a dual space methodology using the SHELXT program (Bruker AXS Inc., version 2014). All non-hydrogen atoms were obtained from the initial solution. The structural model was fit to the data using full matrix least-squares based on  $|F_2|$ . The structure was refined using the SHELXL-2014 program package from the SHELXTL suite of crystallographic software.<sup>132</sup> All of the Cd, S, and O atoms were refined anisotropically, whereas C atoms of the found phenyl groups were treated isotropically and as rigid hexagon rings. Hydrogen atoms were not added to the phenyl rings. The apex ligands (probably, DMF) could not be found in the residual electron density except for the Cd-bonded O atom. No

C atoms belonging to phenyl rings were distinguished near any of S atoms of four corner hexagonal cages. The difficulties in locating organic ligands, counterions, and cocrystallized small molecules due to their substantial disorder are typical for single-crystal structures based on monodisperse CdS or CdSe nanoclusters.<sup>31–33</sup> The residual electron density was treated as a diffused contribution without specific atomic positions using the program package PLATON (Squeeze).<sup>133</sup> For this structure, PLATON calculates a void volume of 6638 Å<sup>3</sup> containing 2889 electrons.

## 2.5 References and Notes

- (1) Murray, C.; Norris, D.; Bawendi, M. *J. Am. Chem. Soc.* **1993**, *115* (19), 8706.
- (2) Alivisatos, A. P. *J. Phys. Chem.* **1996**, *100* (31), 13226.
- (3) Soloviev, V. N.; Eichhöfer, A.; Fenske, D.; Banin, U. *J. Am. Chem. Soc.* **2000**, *122* (11), 2673.
- (4) Nozik, A. J. *Phys. E Low-Dimens. Syst. Nanostructures* **2002**, *14* (1–2), 115.
- (5) Bailey, R. E.; Smith, A. M.; Nie, S. *Phys. E Low-Dimens. Syst. Nanostructures* **2004**, *25* (1), 1.
- (6) Wang, F.; Tan, W. B.; Zhang, Y.; Fan, X.; Wang, M. *Nanotechnology* **2006**, *17* (1), R1.
- (7) Sapra, S.; Mayilo, S.; Klar, T. A.; Rogach, A. L.; Feldmann, J. *Adv. Mater.* **2007**, *19* (4), 569.
- (8) Konstantatos, G.; Sargent, E. H. *Nat. Nanotechnol.* **2010**, *5* (6), 391.
- (9) Murray, C. B.; Kagan, C. R.; Bawendi, M. G. *Science* **1995**, *270* (5240), 1335.
- (10) Collier, C. P.; Vossmeier, T.; Heath, J. R. *Annu. Rev. Phys. Chem.* **1998**, *49*, 371.
- (11) Whetten, R. L.; Shafiqullin, M. N.; Khoury, J. T.; Schaaff, T. G.; Vezmar, I.; Alvarez, M. M.; Wilkinson, A. *Acc. Chem. Res.* **1999**, *32* (5), 397.
- (12) Sun, S. H.; Murray, C. B.; Weller, D.; Folks, L.; Moser, A. *Science* **2000**, *287* (5460), 1989.
- (13) Corrigan, J. F.; DeGroot, M. W. In *The chemistry of nanomaterials: synthesis, properties and applications* / C. N. R. Rao, A. Müller, A. K. Cheetham (eds.); Weinheim: Wiley-VCH; Chichester: John Wiley, 2004; Vol. 2, pp 418–451.
- (14) Zheng, N.; Fan, J.; Stucky, G. D. *J. Am. Chem. Soc.* **2006**, *128* (20), 6550.
- (15) Murray, C. B.; Kagan, C. R.; Bawendi, M. G. *Annu. Rev. Mater. Sci.* **2000**, *30* (1), 545.
- (16) Talapin, D. V.; Lee, J.-S.; Kovalenko, M. V.; Shevchenko, E. V. *Chem. Rev.* **2010**, *110* (1), 389.
- (17) Nozik, A. J.; Beard, M. C.; Luther, J. M.; Law, M.; Ellingson, R. J.; Johnson, J. C. *Chem. Rev.* **2010**, *110* (11), 6873.
- (18) Gao, Y.; Tang, Z. *Small* **2011**, *7* (15), 2133.
- (19) Xu, L.; Ma, W.; Wang, L.; Xu, C.; Kuang, H.; Kotov, N. A. *Chem. Soc. Rev.* **2013**, *42* (7), 3114.
- (20) Dance, I. G.; Choy, A.; Scudder, M. L. *J. Am. Chem. Soc.* **1984**, *106* (21), 6285.



- (21) Lee, G. S. H.; Fisher, K. J.; Craig, D. C.; Scudder, M. L.; Dance, I. G. *J. Am. Chem. Soc.* **1990**, *112* (17), 6435.
- (22) Lee, G. S. H.; Craig, D. C.; Ma, I.; Scudder, M. L.; Bailey, T. D.; Dance, I. G. *J. Am. Chem. Soc.* **1988**, *110* (14), 4863.
- (23) Vossmeier, T.; Reck, G.; Katsikas, L.; Haupt, E.; Schulz, B.; Weller, H. *Science* **1995**, *267* (5203), 1476.
- (24) Herron, N.; Calabrese, J.; Farneth, W.; Wang, Y. *Science* **1993**, *259* (5100), 1426.
- (25) Vossmeier, T.; Reck, G.; Schulz, B.; Katsikas, L.; Weller, H. *J. Am. Chem. Soc.* **1995**, *117* (51), 12881.
- (26) Yang, X.-L.; Zhang, J.; Ren, S.-B.; Li, Y.-Z.; Du, H.-B.; You, X.-Z. *Inorg. Chem. Commun.* **2010**, *13* (4), 546.
- (27) Behrens, S.; Bettenhausen, M.; Eichhöfer, A.; Fenske, D. *Angew. Chem.-Int. Ed.* **1997**, *36* (24), 2797.
- (28) Behrens, S.; Fenske, D. *Berichte Bunsen-Ges.-Phys. Chem. Chem. Phys.* **1997**, *101* (11), 1588.
- (29) Behrens, S.; Bettenhausen, M.; Deveson, A. C.; Eichhöfer, A.; Fenske, D.; Lohde, A.; Woggon, U. *Angew. Chem.-Int. Ed. Engl.* **1996**, *35* (19), 2215.
- (30) Eichhöfer, A.; Hampe, O. *J. Clust. Sci.* **2007**, *18* (3), 494.
- (31) Zheng, N. F.; Bu, X. H.; Lu, H. W.; Zhang, Q. C.; Feng, P. Y. *J. Am. Chem. Soc.* **2005**, *127* (34), 11963.
- (32) Bendova, M.; Puchberger, M.; Schubert, U. *Eur. J. Inorg. Chem.* **2010**, No. 21, 3299.
- (33) Beecher, A. N.; Yang, X.; Palmer, J. H.; LaGrassa, A. L.; Juhas, P.; Billinge, S. J. L.; Owen, J. S. *J. Am. Chem. Soc.* **2014**, *136* (30), 10645.
- (34) Midgley, P. A.; Weyland, M.; Thomas, J. M.; Johnson, B. F. G. *Chem. Commun.* **2001**, No. 10, 907.
- (35) Kübel, C.; Voigt, A.; Schoenmakers, R.; Otten, M.; Su, D.; Lee, T.-C.; Carlsson, A.; Bradley, J. *Microsc. Microanal.* **2005**, *11* (5), 378.
- (36) Evers, W. H.; Friedrich, H.; Filion, L.; Dijkstra, M.; Vanmaekelbergh, D. *Angew. Chem. Int. Ed.* **2009**, *48* (51), 9655.
- (37) Friedrich, H.; Gommers, C. J.; Overgaag, K.; Meeldijk, J. D.; Evers, W. H.; Nijs, B. de; Boneschanscher, M. P.; de Jongh, P. E.; Verkleij, A. J.; de Jong, K. P.; van Blaaderen, A.; Vanmaekelbergh, D. *Nano Lett.* **2009**, *9* (7), 2719.
- (38) Boneschanscher, M. P.; Evers, W. H.; Qi, W.; Meeldijk, J. D.; Dijkstra, M.; Vanmaekelbergh, D. *Nano Lett.* **2013**, *13* (3), 1312.
- (39) Puentes, V. F.; Krishnan, K. M.; Alivisatos, A. P. *Science* **2001**, *291* (5511), 2115.
- (40) Nagel, M.; Hickey, S. G.; Froemsdorf, A.; Kornowski, A.; Weller, H. *Z. Phys. Chem.-Int. J. Res.* **2007**, *221* (3), 427.
- (41) Redl, F. X.; Cho, K. S.; Murray, C. B.; O'Brien, S. *Nature* **2003**, *423* (6943), 968.
- (42) Shevchenko, E. V.; Talapin, D. V.; Kotov, N. A.; O'Brien, S.; Murray, C. B. *Nature* **2006**, *439* (7072), 55.
- (43) Chen, Z.; Moore, J.; Radtke, G.; Siringhaus, H.; O'Brien, S. *J. Am. Chem. Soc.* **2007**, *129* (50), 15702.
- (44) Chen, Z.; O'Brien, S. *ACS Nano* **2008**, *2* (6), 1219.

- (45) Chen, J.; Ye, X.; Murray, C. B. *Acs Nano* **2010**, *4* (4), 2374.
- (46) Dong, A.; Ye, X.; Chen, J.; Murray, C. B. *Nano Lett.* **2011**, *11* (4), 1804.
- (47) Lisiecki, I.; Albouy, P. A.; Pileni, M. P. *Adv. Mater.* **2003**, *15* (9), 712.
- (48) Stoeva, S. I.; Prasad, B. L. V.; Uma, S.; Stoimenov, P. K.; Zaikovski, V.; Sorensen, C. M.; Klabunde, K. J. *J. Phys. Chem. B* **2003**, *107* (30), 7441.
- (49) Hanrath, T. *J. Vac. Sci. Technol. A* **2012**, *30* (3), 30802.
- (50) Bodnarchuk, M. I.; Kovalenko, M. V.; Heiss, W.; Talapin, D. V. *J. Am. Chem. Soc.* **2010**, *132* (34), 11967.
- (51) Kolny, J.; Kornowski, A.; Weller, H. *Nano Lett.* **2002**, *2* (4), 361.
- (52) Kalsin, A. M.; Fialkowski, M.; Paszewski, M.; Smoukov, S. K.; Bishop, K. J. M.; Grzybowski, B. A. *Science* **2006**, *312* (5772), 420.
- (53) Talapin, D. V.; Shevchenko, E. V.; Murray, C. B.; Titov, A. V.; Kral, P. *Nano Lett.* **2007**, *7* (5), 1213.
- (54) Lalatonne, Y.; Richardi, J.; Pileni, M. P. *Nat. Mater.* **2004**, *3* (2), 121.
- (55) Landman, U.; Luedtke, W. D. *Faraday Discuss.* **2004**, *125*, 1.
- (56) Shevchenko, E. V.; Talapin, D. V.; Murray, C. B.; O'Brien, S. *J. Am. Chem. Soc.* **2006**, *128* (11), 3620.
- (57) Han, L.; Luo, J.; Kariuki, N. N.; Maye, M. M.; Jones, V. W.; Zhong, C. J. *Chem. Mater.* **2003**, *15* (1), 29.
- (58) Kim, J. Y.; Chang, J.-B.; Ross, C. A.; Stellacci, F. *Rsc Adv.* **2013**, *3* (27), 10628.
- (59) Courty, A.; Richardi, J.; Albouy, P.-A.; Pileni, M.-P. *Chem. Mater.* **2011**, *23* (18), 4186.
- (60) Talapin, D. V.; Shevchenko, E. V.; Kornowski, A.; Gaponik, N.; Haase, M.; Rogach, A. L.; Weller, H. *Adv. Mater.* **2001**, *13* (24), 1868.
- (61) Glotzer, S. C.; Solomon, M. J. *Nat. Mater.* **2007**, *6* (8), 557.
- (62) Wang, T.; Wang, X.; LaMontagne, D.; Wang, Z.; Wang, Z.; Cao, Y. C. *J. Am. Chem. Soc.* **2012**, *134* (44), 18225.
- (63) Pileni, M. P. *Surf. Sci.* **2009**, *603* (10–12), 1498.
- (64) Heath, J. R. *Nature* **2007**, *445* (7127), 492.
- (65) Liz-Marzan, L. M. *Langmuir* **2006**, *22* (1), 32.
- (66) Wang, R. Y.; Feser, J. P.; Lee, J.-S.; Talapin, D. V.; Segalman, R.; Majumdar, A. *Nano Lett.* **2008**, *8* (8), 2283.
- (67) Mueggenburg, K. E.; Lin, X.-M.; Goldsmith, R. H.; Jaeger, H. M. *Nat. Mater.* **2007**, *6* (9), 656.
- (68) Urban, J. J.; Talapin, D. V.; Shevchenko, E. V.; Kagan, C. R.; Murray, C. B. *Nat. Mater.* **2007**, *6* (2), 115.
- (69) Soloviev, V. N.; Eichhöfer, A.; Fenske, D.; Banin, U. *J. Am. Chem. Soc.* **2001**, *123* (10), 2354.
- (70) Wu, T.; Zhang, Q.; Hou, Y.; Wang, L.; Mao, C.; Zheng, S.-T.; Bu, X.; Feng, P. *J. Am. Chem. Soc.* **2013**, *135* (28), 10250.
- (71) Wang, Y.; Herron, N. *Phys. Rev. B* **1990**, *42* (11), 7253.
- (72) As all known CdS nanoclusters belong to particular tetrahedral cluster families where each member has particular stoichiometry, it is convenient to identify such nanoclusters by the number of Cd atoms. This notation is used throughout the Chapter 2 along with molecular formulae.

- (73) Eychmüller, A.; Hässelbarth, A.; Katsikas, L.; Weller, H. *J. Lumin.* **1991**, 48–9, 745.
- (74) Eychmüller, A.; Hässelbarth, A.; Katsikas, L.; Weller, H. *Berichte Bunsen-Ges.-Phys. Chem. Chem. Phys.* **1991**, 95 (1), 79.
- (75) For primitive cubic packing, the unit cell length  $a$  would also correspond to the interplanar spacing  $d$ .
- (76) Shape factor  $K = 0.9$ , widely used for spherical nanoparticles with cubic cages, may not be fully applicable to tetrahedrally shaped nanoclusters built by the fusion of cubic and hexagonal cages *via* edge-sharing interactions, as nanoclusters of capped supertetrahedral family are.
- (77) Langford, J.; Wilson, A. *J. Appl. Crystallogr.* **1978**, 11 (APR), 102.
- (78) Feng, P.; Bu, X.; Zheng, N. *Acc. Chem. Res.* **2005**, 38 (4), 293.
- (79) The stoichiometry of nanoclusters in the capped supertetrahedral  $C_n$  family, assuming all surface ligands are phenylthiolates, by Feng *et al.*,<sup>78</sup> can be expressed as  $M_xE_y$ , where  $x = [n(n+1)(n+2)]/6 + [4(n+1)(n+2)]/2 + 4$ ;  $y = [(n+1)(n+2)(n+3)]/6 + [4(n+2)(n+3)]/2 + 4$ , and  $n$  corresponds to the order of the member in the homological series. Thus, for the first member  $C1$ , the above-mentioned formulae yield  $M_{17}E_{32}$ , represented by  $[Cd_{17}S_4(SPh)_{28}]^{2-}$ . According to this, the fourth member,  $C4$ , would have a composition  $M_{84}E_{123}$ . The chemical formula of the neutral  $Cd_{84}$  nanocluster can be made by analogy with the neutral  $Cd_{54}$  nanoclusters, described by Schubert and co-workers.<sup>32</sup> These possess a larger number of  $\mu_3$ - versus  $\mu_2$ -SPh moieties, resulting in an overall neutral CdS framework.
- (80) Yu, W. W.; Qu, L. H.; Guo, W. Z.; Peng, X. G. *Chem. Mater.* **2003**, 15 (14), 2854.
- (81) Although Yu's formula may not necessarily give adequate sizes ( $D$ ) for all supertetrahedral CdS nanoclusters with thiophenolate surface ligands, the results of similar calculations using the reported absorption peak positions ( $\lambda_{max}$ ) for DMF solutions of the smaller family members are in good agreement with the their edge lengths,  $l$ , obtained from the published single-crystal X-ray diffraction data.<sup>31</sup> Thus, for the  $Cd_{17}$ ,  $Cd_{32}$ , and  $Cd_{54}$  ( $\lambda_{max}$  equal to 290, 327, and 353 nm, respectively),<sup>31</sup> using Yu's empirical formula,  $D$  values are 1.3, 1.7, and 2.1 nm, respectively, and average  $l$  values are 1.1 / 1.6, 1.5 / 1.9, and 2.0 / 2.3 nm, respectively (measured from Cd to Cd / from S to S or O to O).
- (82) Farneth, W. E.; Herron, N.; Wang, Y. *Chem. Mater.* **1992**, 4 (4), 916.
- (83) For example,  $S^{2-} / SPh^-$  ratios are 0.35 : 1 and 0.67 : 1 for tetrahedral anionic  $[Cd_{32}S_{14}(SPh)_{40}]^{4-}$  and  $[Cd_{54}S_{32}(SPh)_{48}(H_2O)_4]^{4-}$ , respectively, and are even lower if nanoclusters are neutral, *e.g.*, 0.54 : 1 for  $[Cd_{54}S_{28}(SPh)_{52}(dmf)_4]$ .
- (84) Zhang, Z.; Tang, Z.; Kotov, N. A.; Glotzer, S. C. *Nano Lett.* **2007**, 7 (6), 1670.
- (85) For the predicted anionic, tetrahedral  $[Cd_{84}S_{59}(SPh)_{60}L_4]^{10-}$  and  $[Cd_{123}S_{96}(SPh)_{72}L_4]^{18-}$  frameworks (where L represents a neutral ligand, *e.g.*,  $H_2O$  or *dmf*) a  $S^{2-} / SPh^-$  ratio of 0.98 : 1 and 1.33 : 1 can be calculated, respectively; for neutral  $[Cd_{84}S_{49}(SPh)_{70}L_4]$  and  $[Cd_{123}S_{78}(SPh)_{90}L_4]$ , this ratio becomes 0.70 : 1 and 0.87 : 1, respectively.
- (86) Bu, X.; Zheng, N.; Feng, P. *Chem.-Eur. J.* **2004**, 10 (14), 3356.

- (87) Li, H. L.; Laine, A.; O'Keeffe, M.; Yaghi, O. M. *Science* **1999**, 283 (5405), 1145.
- (88) Vaqueiro, P. *Dalton Trans.* **2010**, 39 (26), 5965.
- (89) Dehnen, S.; Eichhöfer, A.; Fenske, D. *Eur. J. Inorg. Chem.* **2002**, No. 2, 279.
- (90) Fenske, D.; Krautscheid, H. *Angew. Chem.-Int. Ed. Engl.* **1990**, 29 (12), 1452.
- (91) Fenske, D.; Krautscheid, H.; Balter, S. *Angew. Chem.-Int. Ed. Engl.* **1990**, 29 (7), 796.
- (92) Eichhöfer, A.; Fenske, D. *J. Chem. Soc.-Dalton Trans.* **1998**, No. 18, 2969.
- (93) Deveson, A.; Dehnen, S.; Fenske, D. *J. Chem. Soc.-Dalton Trans.* **1997**, No. 23, 4491.
- (94) Crawford, N. R. M.; Hee, A. G.; Long, J. R. *J. Am. Chem. Soc.* **2002**, 124 (50), 14842.
- (95) Krautscheid, H.; Fenske, D.; Baum, G.; Semmelmann, M. *Angew. Chem.-Int. Ed. Engl.* **1993**, 32 (9), 1303.
- (96) Wu, T.; Bu, X.; Liao, P.; Wang, L.; Zheng, S.-T.; Ma, R.; Feng, P. *J. Am. Chem. Soc.* **2012**, 134 (8), 3619.
- (97) Tang, Z.; Zhang, Z.; Wang, Y.; Glotzer, S. C.; Kotov, N. A. *Science* **2006**, 314 (5797), 274.
- (98) Tao, A. R.; Ceperley, D. P.; Sinsersuksakul, P.; Neureuther, A. R.; Yang, P. *Nano Lett.* **2008**, 8 (11), 4033.
- (99) Henzie, J.; Grünwald, M.; Widmer-Cooper, A.; Geissler, P. L.; Yang, P. *Nat. Mater.* **2012**, 11 (2), 131.
- (100) Liao, C.-W.; Lin, Y.-S.; Chanda, K.; Song, Y.-F.; Huang, M. H. *J. Am. Chem. Soc.* **2013**, 135 (7), 2684.
- (101) Quan, Z.; Fang, J. *Nano Today* **2010**, 5 (5), 390.
- (102) Boles, M. A.; Talapin, D. V. *J. Am. Chem. Soc.* **2014**, 136 (16), 5868.
- (103) Rupich, S. M.; Shevchenko, E. V.; Bodnarchuk, M. I.; Lee, B.; Talapin, D. V. *J. Am. Chem. Soc.* **2010**, 132 (1), 289.
- (104) Wang, Z. L.; Harfenist, S. A.; Vezmar, I.; Whetten, R. L.; Bentley, J.; Evans, N. D.; Alexander, K. B. *Adv. Mater.* **1998**, 10 (10), 808.
- (105) Xu, B.; Wang, X. *Dalton Trans.* **2012**, 41 (16), 4719.
- (106) Jin, X.; Tang, K.; Jia, S.; Tang, Y. *Polyhedron* **1996**, 15 (15), 2617.
- (107) Zheng, N. F.; Bu, X. H.; Lu, H. W.; Chen, L.; Feng, P. Y. *J. Am. Chem. Soc.* **2005**, 127 (43), 14990.
- (108) Zhang, Q.; Bu, X.; Lin, Z.; Wu, T.; Feng, P. *Inorg. Chem.* **2008**, 47 (21), 9724.
- (109) Bendova, M.; Puchberger, M.; Pabisch, S.; Peterlik, H.; Schubert, U. *Eur. J. Inorg. Chem.* **2010**, No. 15, 2266.
- (110) Hiratani, T.; Konishi, K. *Angew. Chem.-Int. Ed.* **2004**, 43 (44), 5943.
- (111) Nagaoka, Y.; Chen, O.; Wang, Z.; Cao, Y. C. *J. Am. Chem. Soc.* **2012**, 134 (6), 2868.
- (112) Løver, T.; Bowmaker, G. A.; Seakins, J. M.; Cooney, R. P. *Chem. Mater.* **1997**, 9 (4), 967.
- (113) Matijevic, E.; Wilhelmy, D. *J. Colloid Interface Sci.* **1982**, 86 (2), 476.
- (114) Ramsden, J. J. *Surf. Sci.* **1985**, 156, 1027.
- (115) Ramsden, J. *Proc. R. Soc. Lond. Ser. -Math. Phys. Eng. Sci.* **1987**, 413 (1845), 407.

- (116) Xia, Y.; Tang, Z. *Chem. Commun.* **2012**, 48 (51), 6320.
- (117) Li, X.-H.; Li, J.-X.; Li, G.-D.; Liu, D.-P.; Chen, J.-S. *Chem.- Eur. J.* **2007**, 13 (31), 8754.
- (118) Xia, Y.; Nguyen, T. D.; Yang, M.; Lee, B.; Santos, A.; Podsiadlo, P.; Tang, Z.; Glotzer, S. C.; Kotov, N. A. *Nat. Nanotechnol.* **2011**, 6 (9), 580.
- (119) Bishop, K. J. M.; Wilmer, C. E.; Soh, S.; Grzybowski, B. A. *Small* **2009**, 5 (14), 1600.
- (120) Ohara, P.; Leff, D.; Heath, J.; Gelbart, W. *Phys. Rev. Lett.* **1995**, 75 (19), 3466.
- (121) Murthy, S.; Wang, Z. L.; Whetten, R. L. *Philos. Mag. Lett.* **1997**, 75 (5), 321.
- (122) Lin, X. M.; Sorensen, C. M.; Klabunde, K. J. *J. Nanoparticle Res.* **2000**, 2 (2), 157.
- (123) Min, Y.; Akbulut, M.; Kristiansen, K.; Golan, Y.; Israelachvili, J. *Nat. Mater.* **2008**, 7 (7), 527.
- (124) Adams, R. D.; Zhang, B.; Murphy, C. J.; Yeung, L. K. *Chem. Commun.* **1999**, No. 4, 383.
- (125) Grzelczak, M.; Perez-Juste, J.; Mulvaney, P.; Liz-Marzan, L. M. *Chem. Soc. Rev.* **2008**, 37 (9), 1783.
- (126) Chen, M.; Wu, B.; Yang, J.; Zheng, N. *Adv. Mater.* **2012**, 24 (7), 862.
- (127) Houtepen, A. J.; Koole, R.; Vanmaekelbergh, D.; Meeldijk, J.; Hickey, S. G. *J. Am. Chem. Soc.* **2006**, 128 (21), 6792.
- (128) Xiong, Y.; Deng, K.; Jia, Y.; He, L.; Chang, L.; Zhi, L.; Tang, Z. *Small* **2014**, 10 (8), 1523.
- (129) Distaso, M.; Taylor, R. N. K.; Taccardi, N.; Wasserscheid, P.; Peukert, W. *Chem.- Eur. J.* **2011**, 17 (10), 2923.
- (130) Wang, Y.; Lin, H.-X.; Chen, L.; Ding, S.-Y.; Lei, Z.-C.; Liu, D.-Y.; Cao, X.-Y.; Liang, H.-J.; Jiang, Y.-B.; Tian, Z.-Q. *Chem. Soc. Rev.* **2014**, 43 (1), 399.
- (131) Maric, D.; Burrows, J. P. *J. Phys. Chem.* **1996**, 100 (21), 8645.
- (132) Sheldrick, G. M. *Acta Crystallogr. Sect. A* **2008**, 64, 112.
- (133) Spek, A. L. *J. Appl. Crystallogr.* **2003**, 36 (1), 7.

## Chapter 3

# From Molecule to Materials: Crystalline Superlattices of Nanoscopic CdS Clusters<sup>†</sup>

### 3.1 Introduction

Low-dimensional semiconductor structures continue to be the focus of attention due to the great potential for their application in optics, electronics and biological labeling.<sup>1–8</sup> A key problem that hampers the optimal development of technologies based on nanosized semiconductors is the variation of size and shape (polydispersity) of synthesized nanoparticles, as these strongly affect their electronic and photophysical properties.<sup>9–13</sup> Any polydispersity in size therefore substantially diminishes the advantages of these materials regarding well defined electronic structure. One route to circumvent polydispersity may lie in the synthesis of nanoclusters.<sup>14–16</sup> The synthesis of nanoclusters allows creation of particles with exactly the same size, shape, and surface chemistry. There has been much success in this area for the preparation of group 11–16 nanoclusters, most notably for silver-sulfide systems (*e.g.*, [Ag<sub>70</sub>S<sub>16</sub>(SPh)<sub>34</sub>(PhCO<sub>2</sub>)<sub>4</sub>(*triphos*)<sub>4</sub>] and [Ag<sub>188</sub>S<sub>94</sub>(PR<sub>3</sub>)<sub>30</sub>], [Ag<sub>262</sub>S<sub>100</sub>(S'Bu)<sub>62</sub>(dppb)<sub>6</sub>], [Ag<sub>344</sub>S<sub>124</sub>(S'Bu)<sub>96</sub>], and [Ag<sub>490</sub>S<sub>188</sub>(S'C<sub>5</sub>H<sub>11</sub>)<sub>114</sub>]).<sup>17–20</sup> Herein we describe the facile preparation of a crystalline, three dimensional superlattice of 2.3 nm molecular nanoclusters of CdS **5** with a formula approximating [Cd<sub>130</sub>S<sub>103</sub>(SPh)<sub>54</sub>] *via* the thermally induced conversion of the readily prepared cadmium thiophenolate precursor (Me<sub>4</sub>N)<sub>2</sub>[Cd(SPh)<sub>4</sub>].

### 3.2 Results and Discussion

For group 12–16 materials, previously synthesized and characterized large tetrahedral cadmium thiophenolate nanoclusters include [Cd<sub>17</sub>S<sub>4</sub>(SPh)<sub>28</sub>]<sup>2–</sup> and [Cd<sub>32</sub>S<sub>14</sub>(SPh)<sub>40</sub>]<sup>4–</sup>.<sup>21–23</sup> Well defined crystalline tetrahedral CdS cores of such nanoclusters are encapsulated and stabilized by a shell of chalcogen based ligands (*i.e.*, SPh<sup>–</sup>). The dimensions of such large nanoclusters cores overlap with those for some colloidal systems.<sup>24</sup> Due to their size

<sup>†</sup> A version of this work has been published as communication in Levchenko, T. I.; Kübel, C.; Huang, Y.; Corrigan, J. F. *Chem.-Eur. J.* **2011**, *17* (51), 14394–14398; and has been reproduced with permission.

monodispersity the nanoclusters can be crystallized into superlattices and isolated as single crystals.<sup>25</sup> A route to larger monodisperse cadmium thiophenolate nanoclusters promises a broader potential area of application because of an improved ability to tailor the photophysical properties. A typical procedure for the preparation of **5** involves heating the mononuclear precursor  $(\text{Me}_4\text{N})_2[\text{Cd}(\text{SPh})_4]$ <sup>26</sup> and an alkylammonium salt solution in sealed stainless steel reactor under solvothermal conditions. The solvothermal process uses the solvents under elevated temperature and pressure, allowing increasing solubility of reagents, speeding up the conversion to desired product and facilitating its crystallization. Carrying out the reaction under solvothermal conditions is widely used in advanced materials synthesis,<sup>27–29</sup> including preparation of polynuclear metal chalcogenide nanoclusters and their assemblies.<sup>30–32</sup> Solvothermal synthesis has recently been exploited for CdS nanocluster preparation and has been used for the synthesis of the 1.9 nm nanoclusters  $[\text{Cd}_{54}\text{S}_{32}(\text{SPh})_{48}(\text{H}_2\text{O})_4]^{4-}$  (with  $[\text{Cd}_4(\text{SPh})_8]_{\infty}$  and thiourea as precursors).<sup>25</sup> Neutral nanoclusters  $[\text{Cd}_{54}\text{S}_{28}(\text{SPh})_{52}(\text{dmf})_4]$  ( $\text{dmf} = \text{N,N}'\text{-dimethylformamide}$ ) with the same tetrahedral Cd<sub>54</sub> metal-chalcogenide core have also been isolated in an alternative two-step process.<sup>33</sup>

After thermal treatment at 120–160 °C, solutions of  $(\text{Me}_4\text{N})_2[\text{Cd}(\text{SPh})_4]$  turn yellow and opalescent, as the precursor conversion progresses, and polynuclear cadmium thiophenolates are formed. Increasing the temperature to 200 °C results in obtaining **5** as a bright yellow-orange solid, which was characterized by Raman and UV–vis absorption spectroscopy, thermogravimetric analysis (TGA), elemental analysis, powder X-ray diffractions (PXRD) and electron microscopy.

UV–vis absorption spectra of as-synthesized samples of **5** (Figure 3.1, *insert*) provide a qualitative indication of nanocluster size and monodispersity: the presence of excitonic features in spectra recorded at room temperature suggests a narrow size distribution for semiconductor nanoclusters.<sup>11</sup> The value of the Gaussian full widths at half-maximum for the low-energy excitonic peak for **5** was found to be close to that observed for  $[\text{Cd}_{54}\text{S}_{28}(\text{SPh})_{52}(\text{dmf})_4]$ , synthesized by published method<sup>33</sup> (39 and 36 nm, respectively), which suggests that any peak broadening is caused by inherent system properties rather than nanocluster size polydispersity.<sup>13</sup> The shift of the peak position toward a longer

wavelength (413 nm for **5** vs. 353 nm for  $[\text{Cd}_{54}\text{S}_{32}(\text{SPh})_{48}(\text{H}_2\text{O})_4]^{4-}$ <sup>25</sup>) reflects the size increase in comparison with previously reported frameworks. Such a band gap energy (3.01 eV) for **5** is consistent with core sizes of 2.3 nm.<sup>34</sup>

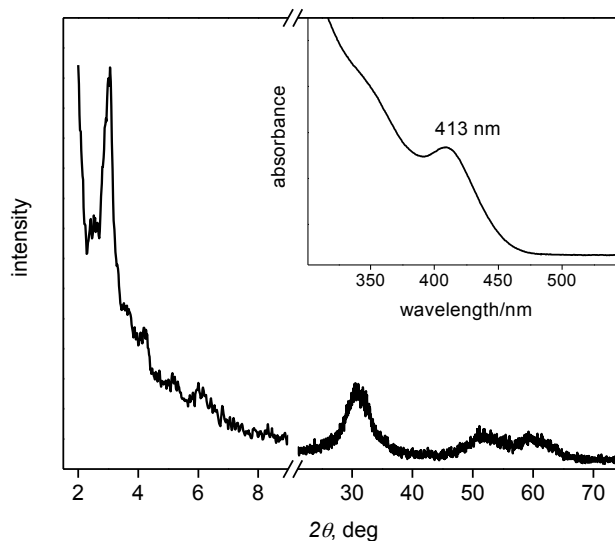


**Figure 3.1:** Powder X-ray diffraction patterns (Co K $\alpha$  radiation) and UV–vis absorption spectrum (*insert*) of **5**.

PXRD permits an examination of the structure of both crystalline core of individual nanoclusters (wide-angle region) and their assembly into a superlattice (low-angle region) over the large volume of the sample.<sup>35</sup> The wide-angle region of the PXRD patterns for **5** (Figure 3.1) shows the presence of crystalline CdS species. A distinction between Hawleyite (cubic) or Greenockite (hexagonal) structures is not unequivocally possible by PXRD because of the broad peaks, which is typical for nanometer-sized systems.<sup>11</sup> Low-angle region of PXRD patterns of **5** (Figure 3.1) show a strong, sharp reflection at  $2\theta$  2.98° from which the corresponding interplanar spacing  $d$  of 3.5 nm can be calculated using Bragg's equation. Such low-angle diffraction patterns have been observed previously for crystalline superlattices of Cd<sub>32</sub> and Cd<sub>54</sub> nanoclusters.<sup>25</sup> For **5**, these are shifted to a lower angle, consistent with a much larger unit cell.

The HAADF-STEM (Figures 3.2, 3.3b) and the HRTEM images (Figure 3.3a) of **5** clearly show the near perfect crystalline arrangement of monodisperse  $[\text{Cd}_x\text{S}_y(\text{SPh})_z]$  clusters 2.3 nm in size. An approximate number of 130 Cd metal centers per cluster can be calculated using



the density of CdS.<sup>36</sup> The shell of surface thiophenolate ligands maintains a constant 1.1 nm spacing between the nanoclusters, in agreement with the SPh<sup>-</sup> rich surfaces. Internal lattice imaging shows a projection of Cd and S atoms along the <110> direction in Hawleyite as can be deduced from the Fourier transform (FT) of the HRTEM image (Figure 3.3a, *inset*). Furthermore, the rectangular packing and the corresponding low-angle reflections in the fast FT suggest a cubic packing of the nanoclusters. A limited number of nanoparticles, substantially larger than 2.3 nm, are also present in samples of **5**. An HAADF-STEM electron tomographic reconstruction<sup>37-39</sup> of the nanocluster packing in 3D reveals a simple cubic packing of nanoclusters with lattice parameters of  $3.40 \pm 0.05$  nm;  $90^\circ \pm 3^\circ$ . The first value is in good agreement with  $d$  value calculated from the PXRD data, since for simple cubic packing the unit cell length would also correspond to the inter-planar spacing. The volume rendering (Figure 3.4) shows a visualization of the reconstructed 3D volume along the <100> direction together with 3 digital slices through the reconstructed volume corresponding to the [100], [110] and [010] planes. Superlattices have been documented for well-defined CdSe nanoparticles (size polydispersity less than 5 % and strictly uniform shape), prepared by colloidal routes with subsequent narrowing of the size distribution by size-selective precipitation.<sup>35,40</sup> The self-assembly of nanoclusters and nearly monodisperse nanoparticles into crystalline superlattices, for which ordered arrays exist on the micrometer scale, helps in the integration of nanosized semiconductors into optical and electronic devices.<sup>41,42</sup>

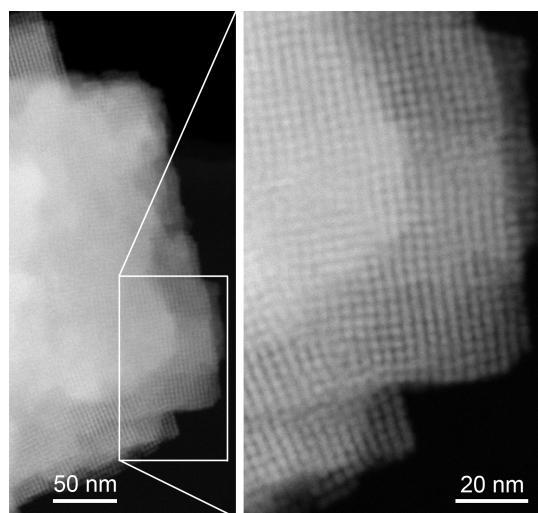


**Figure 3.2:** HAADF-STEM images of **5** and their packing into 3D crystalline superlattice (showing the CdS as bright dots and the SPh<sup>-</sup> shell as dark spaces around each nanocluster).

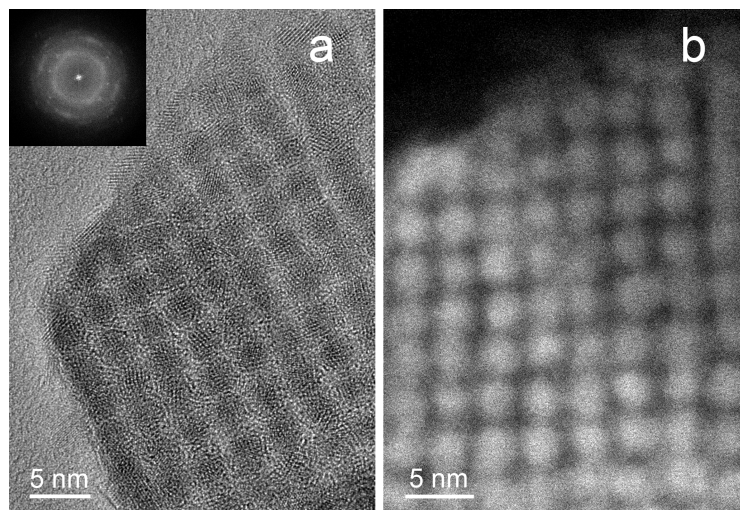


**Figure 3.3:** HRTEM (**a**, showing the CdS as dark regions and the SPh<sup>-</sup> shell as lighter spaces) and HAADF-STEM (**b**, CdS – bright dots, SPh<sup>-</sup> shell – dark spaces) images of **5** and nanoclusters superlattice. Inset: Fourier transform of the HRTEM image showing reflections due to the ordered Hawleyite (cubic) CdS structure and the cubic superlattice packing.

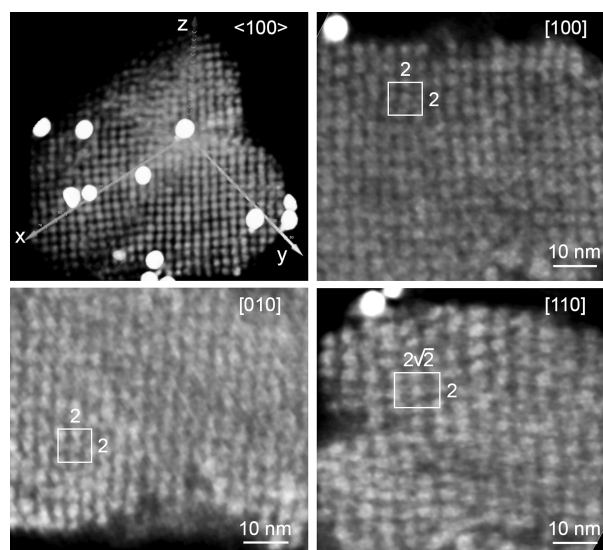


**Figure 3.4:** Volume rendering showing the 3D packing of the CdS nanoclusters along  $\langle 100 \rangle$  orientation (larger and brighter particles are 5 nm gold labels used for tomographic alignment) together with digital slices along the [100], [110] and [010] plane of the superlattice with the unit cell indicated in the slices.

Samples of **5** show ~ 21 % weight loss between 300 and 600 °C as determined *via* TGA (Figure 3.5) that can be attributed to the elimination of the surface thiophenolate groups and the formation of hexagonal CdS. From the observed weight loss it is possible to derive a ratio between  $S^{2-} / SPh^{-}$  present in the nanoclusters **5**, with the approximation that all  $SPh^{-}$  is eliminated in the form of  $SPh_2$ . The calculated 1.9 : 1 ratio for **5** is markedly larger than those of previously reported cadmium thiophenolate nanoclusters (0.39 : 1 and 0.54 : 1 for neutral  $[Cd_{32}S_{14}(SPh)_{36}(dmf)_4]$  and  $[Cd_{54}S_{28}(SPh)_{52}(dmf)_4]$ , respectively), consistent with a much larger core size in **5**. Taking into account the number of Cd atoms per nanocluster (calculated using electron microscopy data), the TGA results allow an approximate formula of  $[Cd_{130}S_{103}(SPh)_{54}] \cdot 10DMF$  for **5** to be proposed. Elemental analyses (%C, H, N, S) and atomic absorption spectrometry for Cd are in reasonable agreement with such a formulation; the presence of some larger CdS nanoparticles in **5** (as observed by HRTEM) and residual lattice solvent or coordinated *dmf* cause some uncertainty.

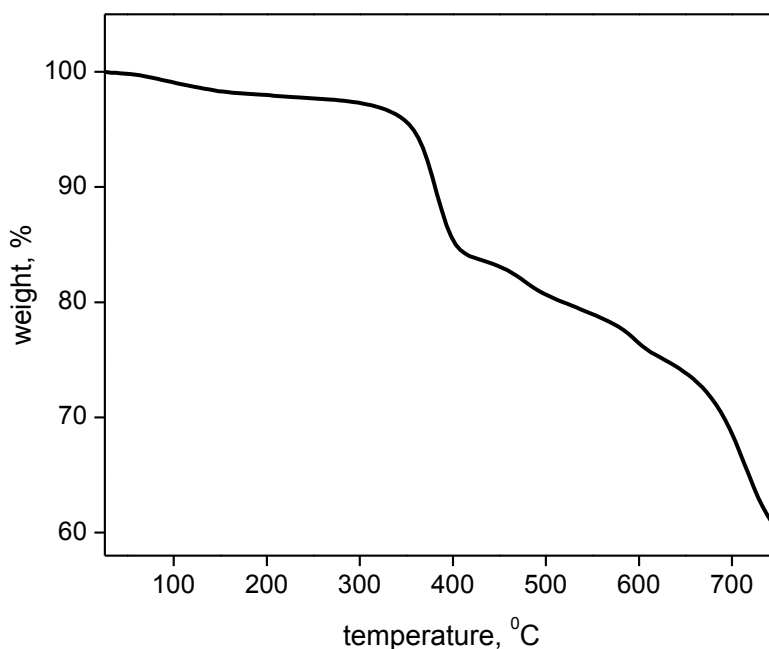


**Figure 3.5:** TGA curve for **5**, obtained under  $N_2$  flow during 1 °C/min ramp

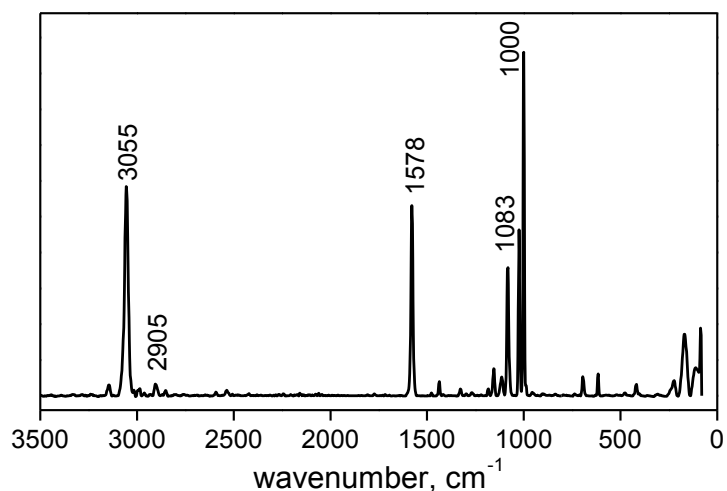


**Figure 3.6:** Raman spectrum of **5**.

The Raman spectrum of **5** (Figure 3.6) contains several characteristic aromatic bands (e.g., at  $3055\text{ cm}^{-1}$  due to aromatic C–H stretch vibrations and  $1578\text{ cm}^{-1}$  due to aromatic C–C stretch vibrations). Only a weak band (at  $2905\text{ cm}^{-1}$ ) can be found in the area characteristic for aliphatic C–H stretching. Aromatic Raman bands can be assigned to phenyl rings from  $\text{SPh}^-$  groups in the stabilizing shell of nanoclusters **5**. The weak aliphatic signal may originate from residual lattice solvent (DMF) or coordinated *dmf* in the stabilizing shell of nanoclusters **5** by analogy with  $[\text{Cd}_{54}\text{S}_{28}(\text{SPh})_{52}(\text{dmf})_4]$ .<sup>33</sup> Alternatively, charge-balancing species may be present in crystalline nanocluster packing. Larger supertetrahedral charged  $[\text{Cd}_x\text{S}_y(\text{SPh})_z]^{n-}$  nanoclusters are expected to contain substantial amounts of cations (in our case  $\text{Me}_4\text{N}^+$ ) to balance the charge.<sup>43</sup> However, the TGA results for **5** suggest that the nanoclusters adopt a shape other than the regular tetrahedral as the framework of larger tetrahedral nanoclusters would have a markedly larger weight percent assigned to surface  $\text{SPh}^-$  groups.<sup>44</sup> Since there are no aliphatic C–H Raman bands of high intensity present in the spectra of **5**, it is more likely that the nanoclusters **5** are neutral and that their shape is close to truncated tetrahedra.

### 3.3 Conclusions

These results illustrate the successful synthesis of monodisperse CdS nanoclusters 2.3 nm in size and their assembly into a crystalline superlattice. Although single crystals of these

remain at present elusive, HRTEM and STEM tomography provide concrete data for the nature of the nanoclusters and their crystallographic repeat. Moreover, our preliminary results show that the synthetic method using solvothermal conversion of  $(\text{Me}_4\text{N})_2[\text{Cd}(\text{SPh})_4]$  precursor can potentially be extended on the preparation of superlattices of nanoclusters of other group 12-16 semiconductor materials. Thus, solvothermal treatments of  $(\text{Me}_4\text{N})_2[\text{Cd}(\text{SePh})_4]$  was shown to occur with formation of Me–Se–Ph and Ph–Se–Ph by-products, providing the source of  $\text{Se}^{2-}$  for the growth of the core of large frameworks, similar as it was discussed for  $(\text{Me}_4\text{N})_2[\text{Cd}(\text{SPh})_4]$  (see Chapter 2). Further systematic work will be done to optimize the conditions for the preparation of ordered superlattices of monodisperse CdS and CdSe nanoclusters.

### 3.4 Experimental Section

#### 3.4.1 Syntheses

All synthetic and handling procedures were carried out under an atmosphere of high purity dried nitrogen using standard double manifold Schlenk line techniques and a MBraun Labmaster 130 glovebox.

$(\text{Me}_4\text{N})_2[\text{Cd}(\text{SPh})_4]$  was synthesized by slight modification of the published procedure<sup>26</sup> from cadmium nitrate and thiophenol deprotonated by tributylamine: the amount of methanol used to dissolve tetramethylammonium chloride was two times smaller in order to facilitate product crystallization. The product purification was achieved by recrystallization from boiling acetonitrile.

Syntheses of  $[\text{Cd}_x\text{S}_y(\text{SPh})_z]$  nanoclusters are performed in a sealed reactor at controlled temperature and increased pressure using polar organic solvents (solvothermal conditions). A typical procedure for the preparation of **5** was the following: an appropriate amount of the  $(\text{Me}_4\text{N})_2[\text{Cd}(\text{SPh})_4]$  (usually 0.5–3.5 g) was combined with DMF (10–20 mL) in a 60 mL Teflon bottle and mixed thoroughly until a clear solution was obtained. Cetyltrimethylammonium bromide was then added and suspension was stirred for an extra 15 min. The bottle was sealed in a stainless steel autoclave and heated in an oven for several days at 200 °C. After cooling to room temperature, the solid

material was collected by centrifugation at 4000 rpm for 20 min, washed several times with DMF and finally with methanol, then dried under vacuum for 4–6 h.

Elemental analysis (C, H, N, S) was performed by Laboratoire d'Analyse Élémentaire de l'Université de Montréal (Quebec, Canada). Calcd (%) for  $\text{Cd}_{130}\text{S}_{157}\text{C}_{354}\text{H}_{340}\text{N}_{10}\text{O}_{10}$  ( $[\text{Cd}_{130}\text{S}_{103}(\text{SPh})_{54}] \cdot 10\text{DMF}$ ): C 17.32, H 1.40, S 20.51, N 0.57; found: C 17.81, H 1.18, S 20.31, N, 0.35.

To determine the amount of Cd, portions of samples (5–50 mg) were dissolved by concentrated nitric acid solution (1 ml) and then diluted to be in the concentration interval 0.1–5 ppm of Cd in 1 % nitric acid solution. The Cd content in as-prepared solutions was determined by atomic absorption spectrometry using Varian 240 AAS, calibrated using the standard Cd solutions. Calcd (%) for  $\text{Cd}_{130}\text{S}_{157}\text{C}_{354}\text{H}_{340}\text{N}_{10}\text{O}_{10}$ : 59.54; found:  $57.52 \pm 2.32$ .

### 3.4.2 Characterization

Solution UV–vis absorption spectra were acquired using a Varian Cary 100 Bio UV–vis spectrometer at 25 °C in 1 cm quartz cells against air; spectra of the pure solvent (DMF) were subtracted. To prepare solutions, a small portion (0.02–0.05 g) of sample was sonicated with DMF (15–20 mL) for 8–12 h, and then the suspension was filtered through a syringe filter (0.22  $\mu\text{m}$ , PTFE membrane, Dikma Technologies Inc).

Powder X-ray diffraction patterns were obtained using a Rigaku diffractometer with a Co K $\alpha$  radiation source ( $\lambda = 1.79926 \text{ \AA}$ ). The samples were placed on a standard holder and measured with sampling interval 0.02° and scan speed 10 °/min.

Transmission electron microscopy (TEM) analyses were performed using an image corrected FEI Titan 80-300 electron microscope operated at 300 kV and equipped with a Gatan US1000 CCD camera for TEM imaging. Scanning transmission electron microscopy (STEM) images were acquired using a HAADF (High Angle Annular Dark Field) detector with a nominal spot size of 0.14 nm. TEM samples were prepared by dropping dilute THF suspensions of the material onto carbon coated Cu grids (Quantifoil holey carbon grids coated with 2 nm carbon) and excess solvent was allowed to evaporate.

Electron tomographic analysis was performed using HAADF-STEM tilt-series consisting of 75 images acquired over a tilt-range of  $\pm 75^\circ$ . The tilt-series were aligned with IMOD Version 4.1 using gold labels deposited on the carbon grid. The 3D reconstruction was performed using the SIRT algorithm implemented in Inspect3D Version 3.0. The 3D visualization was performed using Amira Version 5.2.

Solution  $^1\text{H}$  NMR spectra were obtained on a Varian Mercury 400 ( $^1\text{H}$  at 400.088 MHz) spectrometer using standard settings. Spectra were referenced internally to  $\text{SiMe}_4$  using the residual proton signal of deuterated solvents.

Thermogravimetric analyses were conducted under nitrogen flow using a Mettler Toledo TGA/SDTA 851 $^\circ$  instrument (heating rate 1  $^\circ\text{C}/\text{min}$  between 25–750  $^\circ\text{C}$ ).

FT-Raman spectra were collected using a Bruker RFS 100/S spectrometer, with a resolution of 4  $\text{cm}^{-1}$ .

### 3.5 References

- (1) Sapra, S.; Mayilo, S.; Klar, T. A.; Rogach, A. L.; Feldmann, J. *Adv. Mater.* **2007**, *19* (4), 569.
- (2) Konstantatos, G.; Sargent, E. H. *Nat. Nanotechnol.* **2010**, *5* (6), 391.
- (3) Nozik, A. J. *Phys. E Low-Dimens. Syst. Nanostructures* **2002**, *14* (1–2), 115.
- (4) Tang, J.; Wang, X.; Brzozowski, L.; Barkhouse, D. A. R.; Debnath, R.; Levina, L.; Sargent, E. H. *Adv. Mater.* **2010**, *22* (12), 1398.
- (5) Rühle, S.; Shalom, M.; Zaban, A. *ChemPhysChem* **2010**, *11* (11), 2290.
- (6) Wang, F.; Tan, W. B.; Zhang, Y.; Fan, X.; Wang, M. *Nanotechnology* **2006**, *17* (1), R1.
- (7) Bailey, R. E.; Smith, A. M.; Nie, S. *Phys. E Low-Dimens. Syst. Nanostructures* **2004**, *25* (1), 1.
- (8) Fang, Z.; Soleymani, L.; Pampalakis, G.; Yoshimoto, M.; Squire, J. A.; Sargent, E. H.; Kelley, S. O. *Acs Nano* **2009**, *3* (10), 3207.
- (9) Alivisatos, A. P. *J. Phys. Chem.* **1996**, *100* (31), 13226.
- (10) Nirmal, M.; Brus, L. *Acc. Chem. Res.* **1999**, *32* (5), 407.
- (11) Murray, C. B.; Kagan, C. R.; Bawendi, M. G. *Annu. Rev. Mater. Sci.* **2000**, *30* (1), 545.
- (12) Soloviev, V. N.; Eichhöfer, A.; Fenske, D.; Banin, U. *J. Am. Chem. Soc.* **2000**, *122* (11), 2673.
- (13) Soloviev, V. N.; Eichhöfer, A.; Fenske, D.; Banin, U. *J. Am. Chem. Soc.* **2001**, *123* (10), 2354.
- (14) Bu, X.; Zheng, N.; Feng, P. *Chem.-Eur. J.* **2004**, *10* (14), 3356.

- (15) Corrigan, J. F.; DeGroot, M. W. In *The chemistry of nanomaterials: synthesis, properties and applications* / C. N. R. Rao, A. Müller, A. K. Cheetham (eds.); Weinheim: Wiley-VCH; Chichester: John Wiley, 2004; Vol. 2, pp 418–451.
- (16) Corrigan, J. F.; Fuhr, O.; Fenske, D. *Adv. Mater.* **2009**, *21* (18), 1867.
- (17) Wang, X. J.; Langetepe, T.; Persau, C.; Kang, B. S.; Sheldrick, G. M.; Fenske, D. *Angew. Chem.-Int. Ed.* **2002**, *41* (20), 3818.
- (18) Fenske, D.; Persau, C.; Dehnen, S.; Anson, C. E. *Angew. Chem.-Int. Ed.* **2004**, *43* (3), 305.
- (19) Fenske, D.; Anson, C. E.; Eichhofer, A.; Fuhr, O.; Ingendoh, A.; Persau, C.; Richert, C. *Angew. Chem.-Int. Ed.* **2005**, *44* (33), 5242.
- (20) Anson, C. E.; Eichhöfer, A.; Issac, I.; Fenske, D.; Fuhr, O.; Sevillano, P.; Persau, C.; Stalke, D.; Zhang, J. *Angew. Chem.-Int. Ed.* **2008**, *47* (7), 1326.
- (21) Lee, G. S. H.; Craig, D. C.; Ma, I.; Scudder, M. L.; Bailey, T. D.; Dance, I. G. *J. Am. Chem. Soc.* **1988**, *110* (14), 4863.
- (22) Herron, N.; Calabrese, J.; Farneth, W.; Wang, Y. *Science* **1993**, *259* (5100), 1426.
- (23) Vossmeier, T.; Reck, G.; Schulz, B.; Katsikas, L.; Weller, H. *J. Am. Chem. Soc.* **1995**, *117* (51), 12881.
- (24) Müller, A.; Fenske, D.; Kögerler, P. *Curr. Opin. Solid State Mater. Sci.* **1999**, *4* (2), 141.
- (25) Zheng, N. F.; Bu, X. H.; Lu, H. W.; Zhang, Q. C.; Feng, P. Y. *J. Am. Chem. Soc.* **2005**, *127* (34), 11963.
- (26) Dance, I. G.; Choy, A.; Scudder, M. L. *J. Am. Chem. Soc.* **1984**, *106* (21), 6285.
- (27) Rowsell, J. L. C.; Yaghi, O. M. *Microporous Mesoporous Mater.* **2004**, *73* (1–2), 3.
- (28) Rao, C. N. R.; Govindaraj, A. *Adv. Mater.* **2009**, *21* (42), 4208.
- (29) Yu, J.; Xu, R. *Acc. Chem. Res.* **2010**, *43* (9), 1195.
- (30) Lang, E. S.; Burrow, R. A.; Stieler, R.; Villetti, M. A. *J. Organomet. Chem.* **2009**, *694* (18), 3039.
- (31) Zhang, Q.; Chung, I.; Jang, J. I.; Ketterson, J. B.; Kanatzidis, M. G. *Chem. Mater.* **2009**, *21* (1), 12.
- (32) Vaqueiro, P. *Dalton Trans.* **2010**, *39* (26), 5965.
- (33) Bendova, M.; Puchberger, M.; Schubert, U. *Eur. J. Inorg. Chem.* **2010**, No. 21, 3299.
- (34) Wang, Y.; Herron, N. *Phys. Rev. B* **1990**, *42* (11), 7253.
- (35) Murray, C. B.; Kagan, C. R.; Bawendi, M. G. *Science* **1995**, *270* (5240), 1335.
- (36) Fregnaux, M.; Arl, D.; Dalmasso, S.; Gaumet, J.-J.; Laurenti, L.-P. *J. Phys. Chem. C* **2010**, *114* (41), 17318.
- (37) Kübel, C.; Voigt, A.; Schoenmakers, R.; Otten, M.; Su, D.; Lee, T.-C.; Carlsson, A.; Bradley, J. *Microsc. Microanal.* **2005**, *11* (5), 378.
- (38) Midgley, P. A.; Weyland, M.; Thomas, J. M.; Johnson, B. F. G. *Chem. Commun.* **2001**, No. 10, 907.
- (39) Evers, W. H.; Friedrich, H.; Filion, L.; Dijkstra, M.; Vanmaekelbergh, D. *Angew. Chem. Int. Ed.* **2009**, *48* (51), 9655.
- (40) Talapin, D. V.; Shevchenko, E. V.; Kornowski, A.; Gaponik, N.; Haase, M.; Rogach, A. L.; Weller, H. *Adv. Mater.* **2001**, *13* (24), 1868.
- (41) Nozik, A. J.; Beard, M. C.; Luther, J. M.; Law, M.; Ellingson, R. J.; Johnson, J. C. *Chem. Rev.* **2010**, *110* (11), 6873.



- (42) Gao, Y.; Tang, Z. *Small* **2011**, 7 (15), 2133.  
(43) Zheng, N.; Bu, X.; Lauda, J.; Feng, P. *Chem. Mater.* **2006**, 18 (18), 4307.  
(44) Feng, P.; Bu, X.; Zheng, N. *Acc. Chem. Res.* **2005**, 38 (4), 293.

## Chapter 4

### Crystalline Superlattices of Nanoscopic CdS Molecular Crystals: an X-ray Crystallography and $^{111}\text{Cd}$ SSNMR Spectroscopy Study\*

#### 4.1 Introduction

Polynuclear metal chalcogenide ME nanoclusters (where M = metal, E = group 16 element heavier than oxygen) continue to be the focus of attention within inorganic chemistry, material science and nanoscience because of their size-dependent electronic and optical properties due to quantum confinement effects.<sup>1-4</sup> Since many such ME nanoclusters can be prepared and isolated as single crystals (ordered superlattices),<sup>5</sup> it is possible to probe their structural features at the atomic level by X-ray crystallography and to correlate structure-property relationships.<sup>4,6</sup> Molecular metal chalcogenide nanoclusters of well-defined size, chemical composition and structure can contain tens to hundreds of metal core atoms, reaching several nanometers in size.<sup>7-10</sup> This means that dimensions of large ME nanoclusters overlap with those of some colloidal nanoparticles.<sup>11</sup> In the case of nanoclusters, polydispersity and structure ambiguity – often inherent to colloidal nanoparticles – are absent.

In many metal chalcogenide nanoclusters metal sites have tetrahedral or distorted tetrahedral coordination.<sup>12-15</sup> Moreover, for metal chalcogenide nanoclusters created by metals that belong to group 12 (*i.e.*, Zn, Cd, Hg) some frameworks have an overall tetrahedral shape, being regular fragments of ME crystalline lattices.<sup>14,16</sup> Such fragments contain tetrahedrally coordinated atoms in cubic or hexagonal cages – two structures well known for bulk crystalline metal chalcogenides (*i.e.*, the minerals zinc blende and wurtzite, respectively).

Considering an idealized ME framework (*i.e.*, containing regularly arranged tetrahedral units  $\text{ME}_4$  with all bonds of equal length and all angles of  $109.5^\circ$ ), all tetrahedral ME nanoclusters belong to a particular series depending on the connectivity of cubic and hexagonal cages.<sup>17,18</sup> Thus, in a basic supertetrahedral series (denoted  $T_n$ , where  $n$

---

\* In the Chapter 4 the materials **1** and **2** are denoted as **CdS-1.9 nm** and **Cd54**, respectively, in the interest of consistency with notations for smaller clusters characterized here.

identifies the member's number), each molecular nanocluster consists of a regular tetrahedral-shaped fragment of the cubic lattice; larger nanoclusters in this series are formed by fusion of cubic cages only. Nanoclusters belonging to related capped supertetrahedral series (denoted  $C_n$ ) consist of a core, which is a regular fragment of the cubic lattice, and four hexagonal cages capping the vertices. The cubic lattice is confined in such a way that an open cleft runs along each of the tetrahedral edges – the structural feature of nanoclusters belonging to capped supertetrahedral series. In nanoclusters in both series the adjacent tetrahedral  $M^{2+}$  sites are not adequate to charge-balance low-coordinated edge and vertex  $E^{2-}$  sites, so such sites tend to be occupied by chalcogenolate  $RE^-$  groups (in particular, phenyl chalcogenolates  $PhE^-$ ), bridging and terminal, respectively. In this way inorganic ME frameworks of supertetrahedral nanoclusters are encapsulated and stabilized by organic groups, forming a ligand shell. The faces of large nanoclusters are usually bounded by triply-bridging  $\mu_3-S$  sites. In accordance with the geometry of the inorganic framework, a single row of ligands is present at the edges of  $T_n$  nanoclusters, while a double row is found at the edges of  $C_n$  nanoclusters. For the latter series the double row of  $RE^-$  ligands allows for relatively lower charge density and creates a different coordination environment for the edge-related metal sites in comparison with those in the  $T_n$  series. Some examples of  $T_n$  metal chalcogenolates complexes and nanoclusters are  $[Cd(SPh)_4]^{2-}$ ,  $[Cd_4(SePh)_{10}]^{2-}$  and  $[Zn_4(SePh)_{10}]^{2-}$ ,  $[Zn_{10}S_4(SPh)_{16}]^{4-}$  and  $[Cd_{10}Se_4(SPh)_{16}]^{4-}$ , while  $C_n$  nanoclusters are represented by  $[Cd_{17}S_4(SPh)_{28}]^{2-}$  and  $[Cd_{32}S_{14}(SPh)_{40}]^{4-}$ .<sup>19–23</sup>

In contrast to idealized structures, distortions from ideal tetrahedral geometry for metal and chalcogenide sites occur primarily because of chemically different functionalities. For instance, different chalcogenide sites (*i.e.*,  $\{\mu_4-S^{2-}\}$ ,  $\{\mu_3-S^{2-}\}$ , bridging  $\{\mu-SR^-\}$  and terminal  $\{SR^-\}$ ) have different Cd–S bond lengths and Cd–S–Cd angles, which affects the geometry of the inorganic framework. The sources of further variations in metrical parameters (and thus of crystallographic inequivalence) for chemically equivalent sites are generally related with isomerism present in nanoclusters.

Isomerism and conformation diversity of tetrahedral ME nanoclusters may occur on several levels, including variations in the: 1) nanocluster core; 2) nanocluster surface; and 3)

organic ligand shell. Particular configurations and conformations of substituents in  $RE^-$  ligands may be associated with distortions from tetrahedral coordination of metal and chalcogen sites and reflected in the overall shape of the inorganic framework (*vide infra*).

Structural isomerism in the nanocluster core assumes a difference in constitution of the inorganic framework. Thus, in the capped supertetrahedral series, each hexagonal cage (more precisely, a  $M_4E_5$  unit) at one of four vertices of the nanocluster can also be independently rotated by  $60^\circ$  around the threefold axis of the (idealized) tetrahedron. Considering the nanoclusters with fully open cleft as “unchanged”, the rotation of hexagonal cages interrupts the cleft near vertices and shifts the interface between the cubic core and the hexagonal vertex by one atomic layer toward the center of the nanocluster.<sup>23</sup> In the first member of the  $C_n$  series, containing 17 metal sites (*e.g.*,  $[Cd_{17}S_4(SPh)_{28}]^{2-}$ ), only one hexagonal cage at a vertex can be possibly rotated,<sup>23</sup> while for larger members potentially five structural isomers can exist due to rotation of all four vertices. In addition to altering the inorganic framework, some structural isomers may have different disposition of ligands, and are thus also different in terms of intramolecular ligand-ligand interactions. Ligand-ligand interactions (both intra- and intermolecular) for phenyl chalcogenolate-capped nanoclusters may include, for instance, dispersion (van der Waals) forces and  $\pi$ - $\pi$  interactions.

Configurational isomerism on a nanocluster surface occurs in  $\mu$ -ER due to the different disposition of the lone electron pair and substituent R upon the chalcogen atom.<sup>24</sup> Two possible positions of each substituent create different micro-configurations; the number of theoretically possible configurational isomers increases quickly with an increase of the total number of  $\mu$ -ER. For instance, in the T3 nanocluster  $[Cd_{10}S_4(SPh)_{16}]^{4-}$  (whose formula can be alternatively written as  $[Cd_{10}(\mu_3-S)_4(\mu-SPh)_{12}(SPh)_4]^{4-}$  to distinguish the different types of thiophenolate ligands) can potentially have 186 configurational isomers (resulting from  $2^{12} = 4096$  micro-configurations).<sup>21,25</sup> Different configurational isomers may have different point groups of symmetry, taking into consideration an idealized inorganic framework and only the configurations of  $\mu$ -ER ligands. For example,  $[Cd_4(SePh)_{10}]^{2-}$  has two configurational isomers belonging to the  $C_1$  point group and two isomers belonging to  $C_3$ .<sup>20</sup> Configurational isomers of the next member of the  $T_n$  series,  $[Cd_{10}S_4(SPh)_{16}]^{4-}$ , are much more diverse, with point groups of symmetry for nanocluster anion varying from numerous

possibilities belonging to  $C_1$ ,  $C_2$  and  $C_3$  to just a few examples belonging to  $S_4$ ,  $D_2$  and  $T$ .<sup>21</sup> Nanoclusters representing configurational isomers may also crystallize in different space groups (for example,  $I-4$  and  $I-42m$  for two different  $[\text{Cd}_{10}\text{S}_4(\text{SPh})_{16}]^{4-}$  with achiral point group of symmetry  $S_4$ )<sup>21</sup>. Many configurational isomers are chiral; as corresponding compounds typically crystallize in centrosymmetric space groups, both enantiomers are present in ordered superlattice as racemic mixture.<sup>20,24</sup>

The substituent groups R on framework edges can be positioned either axially or equatorially with respect to a nanocluster's face (which is equivalent to or derived from a  $\text{M}_3(\mu\text{-E})_3$  ring in a chair conformation). Two vicinal substituents (*i.e.*, those bonded to neighbouring sulfur atoms  $(\mu\text{-S})\text{Cd}(\mu\text{-S})$ ) experience the strongest (typically, repulsive) interaction when they both have the same disposition, such as “*ax,ax* pair”.<sup>20,24</sup> Taking this into account, it is possible to characterize different configurational isomers by the number of interacting pairs (*e.g.*, number of *ax,ax* pairs per face or per nanocluster in total). Interaction of contiguous substituents in the ligand shell may contribute considerably to the degree of distortion from tetrahedral geometry on metal and chalcogen sites in inorganic framework, especially in relatively small nanoclusters.<sup>21</sup> For example, the configurational isomer of  $[\text{Cd}_4(\text{SePh})_{10}]^{2-}$  belonging to asymmetric  $C_1$  point group can be described as having substituent disposition (aae, aae, aee, aee), thus it contains one *ax,ax* pair in two out of four faces, resulting in two such pairs in total. In this way such isomer has the lowest possible number of interacting ligands between four existing configurational isomers of the tetranuclear cluster, which are also different in the degree of distortion of the  $\text{M}_4\text{E}_{10}$  framework from the idealized adamantane-like geometry.<sup>20</sup>

Variations at the periphery of the nanocluster may include ligand-ligand interactions related with a particular conformation of substituents. An arrangement of phenyl rings in phenylchalcogenolato ligands arise from rotations about the  $\text{M-EPh}$  and the  $(\mu\text{-E})\text{-C}$  bonds and appears as various dihedral angles between the planes of the phenyl rings and the plane containing an  $\text{E-M-E'}$  bond in a cubic or hexagonal cage at the nanocluster surface.<sup>20,21</sup> The conformation of substituents is energetically subordinate to the configuration of bridging ligands, but it also contributes to intramolecular ligand-ligand interactions and to distortions from tetrahedral bond lengths and angles on metal sites

associated with such interactions. Another source of inequivalence for metal sites with the same coordination environment is hydrogen bonding in a ligand shell, *e.g.*, in the anionic nanocluster  $[\text{Cd}_{10}\text{S}_4(\text{SPh})_{16}]^{4-}$  it is N–H $\cdots$ S hydrogen bond between  $\text{PhS}^-$  ligands and alkylammonium cations  $\text{Et}_3\text{NH}^+$ .<sup>26</sup> It should be noted, that *intermolecular* ligand-ligand interactions (*i.e.*, between organic shells of different nanoclusters) are significant as well and thus should be taken into account, though it is virtually impossible to trace the influence of such interactions on the local environments in the inorganic framework.<sup>26</sup>

Solid-state NMR (SSNMR) spectroscopy is a powerful tool to probe the local environment of metal and chalcogenide sites in objects varying from inorganic semiconductors to proteins.<sup>27,28</sup> For cadmium, there are two NMR-active isotopes with spin ( $I$ ) =  $\frac{1}{2}$  that are feasible targets for such experiments:  $^{111}\text{Cd}$  (natural abundance 12.80% and relative receptivity  $D^p$   $1.24 \cdot 10^{-3}$ ) and  $^{113}\text{Cd}$  (12.22% and  $1.35 \cdot 10^{-3}$ , respectively).<sup>29</sup> Both isotopes can be examined; usually the  $^{113}\text{Cd}$  isotope is preferred, hence its wide usage in the literature. In this work  $^{111}\text{Cd}$  was chosen as the target nucleus because the  $^{113}\text{Cd}$  Larmor frequency at 9.4 T is approximately 89.3 MHz, which strongly overlaps with a local FM radio band and gives rise to NMR spectra of poor quality. Results obtained on both NMR-active cadmium isotopes can be directly compared on the same chemical shift scale.<sup>30</sup> Resonances of cadmium in different compounds span a wide range of > 900 ppm on the chemical shift ( $\delta$ ) scale. The large chemical shift range makes SSNMR spectra of cadmium compounds very sensitive to even the smallest variations in metrical parameters (*i.e.*, bond lengths and angles) about the metal sites, since any minor change in coordination environment can be reflected in a significant difference of chemical shift parameters.<sup>27</sup>

For instance, decanuclear cadmium complexes with bidentate 2-mercaptoethanol ligands  $[\text{Cd}_{10}(\text{SCH}_2\text{CH}_2\text{OH})_{16}]^{4+}$  were extensively studied using a combination of X-ray crystallography and  $^{113}\text{Cd}$  SSNMR,<sup>31,32</sup> since such compounds serve as potential models of cadmium(II)-cysteinate aggregates in mammalian metallothionein proteins. Generally,  $[\text{Cd}_{10}(\text{SCH}_2\text{CH}_2\text{OH})_{16}]^{4+}$  complexes contain three distinct types of metal sites (*i.e.*, a distorted *fac*-octahedral  $\{\text{S}_3\text{CdO}_3\}$  at vertices, a trigonal-bipyramidal  $\{\text{S}_4\text{CdO}\}$  and a distorted tetrahedral  $\{\text{S}_4\text{Cd}\}$  on edges). The inorganic frameworks of  $[\text{Cd}_{10}\text{S}_4(\text{SPh})_{16}]^{4-}$  and

$[\text{Cd}_{10}(\text{SCH}_2\text{CH}_2\text{OH})_{16}]^{4+}$  are similar, but the latter is modified by coordination of hydroxyl groups of 2-mercaptoethanol ligands to all the vertex cadmium atoms (thus the appearance of four  $\{\text{S}_3\text{CdO}_3\}$  sites) and to four out of six edge cadmium atoms (thus the  $\{\text{S}_4\text{CdO}\}$  sites).<sup>33</sup> In  $^{113}\text{Cd}$  SSNMR spectra of the complexes, the difference between chemical shifts of the most deshielded  $\{\text{S}_4\text{Cd}\}$  sites and the most shielded  $\{\text{S}_3\text{CdO}_3\}$  sites reaches  $\sim 300$  ppm. Further splitting of resonances for three coordination environments of up to 82 ppm was found in some complexes; such splitting was attributed to crystallographic inequivalence of the sites due to small differences in bond length and angles. From the comparison of differences in metrical parameters for the cadmium sites with the value of splitting of resonances, it was suggested that  $^{113}\text{Cd}$  SSNMR chemical shifts for these complexes are influenced less by variations in E–Cd–E angles, being more sensitive to differences in Cd–E bond lengths.<sup>32</sup>

SSNMR studies of semiconductor nanoparticles were previously aimed at 1) finding suitable NMR parameter(s) to correlate with average nanoparticle sizes, and 2) characterizing the local environment of the surface sites.<sup>34</sup> Large, monodisperse, semiconductor nanoclusters with known formula and crystal structure (e.g.,  $[\text{Cd}_{54}\text{S}_{32}(\text{SPh})_{48}(\text{dmf})_4]^{4-}$ ) are an attractive model to address both objectives. However, to consider the applicability of CdS nanoclusters as standards with known sizes and surface chemistry, it should be possible to correlate their crystal structure (obtained for fresh, often solvated, materials) with SSNMR data (obtained for dried materials). Powder X-ray diffraction data for the dried materials can be used as a mediator for such a comparison.

In this work, systematic  $^{111}\text{Cd}$  SSNMR experiments were performed in order to correlate X-ray crystallographic data from literature sources with SSNMR parameters of different  $\text{Cd}_x\text{S}_y(\text{SPh})_z$  molecular compounds. A combination of X-ray crystallography and  $^{113}\text{Cd}$  SSNMR spectroscopy was previously used to study  $[\text{Cd}_{10}\text{S}_4(\text{SPh})_{16}]^{4-}$ , including analysis of different configurational isomers.<sup>26</sup> Here, the range of compounds under study is much broader, varying from relatively small complexes  $[\text{Cd}(\text{SPh})_4]^{2-}$  and  $[\text{Cd}_4(\text{SPh})_{10}]^{2-}$  to the largest structurally characterized nanocluster  $[\text{Cd}_{54}\text{S}_{32}(\text{SPh})_{48}(\text{dmf})_4]^{4-}$ . In addition, generalized information was also used for the interpretation of  $^{111}\text{Cd}$  SSNMR data for an even larger nanocluster for which crystal structure analysis remains inaccessible.

## 4.2 Results and Discussion

### 4.2.1 Short-Range and Long-Range Structures

As all known tetrahedral  $\text{Cd}_x\text{S}_y(\text{SPh})_z$  nanoclusters belong to a particular series where each member has a defined stoichiometry,<sup>16–18</sup> it is convenient to identify such nanoclusters by the number of metal atoms  $x$ , *i.e.*,  $\text{Cdx}$ . This notation is used throughout this chapter along with molecular formulae, which are necessary to stress nanocluster composition and, for example, to distinguish between neutral and charged nanoclusters having the same composition of inorganic frameworks. When considering the local environment in the nanocluster framework, it is also important to distinguish between multiple variants (isomers) of nanoclusters having the same stoichiometry. To avoid any ambiguity, the notation  $\text{Cdx}$  here refers not only to the particular member of supertetrahedral or capped supertetrahedral series, but also to the particular structural and configurational isomer. Also, in this chapter  $\text{Cd}_x\text{S}_y(\text{SPh})_z$  nanoclusters larger than **Cd54**, for which a crystal structure is not yet available,<sup>35</sup> are denoted **CdS-1.9 nm** to stress the size (from TEM) of the inorganic framework. The relevant crystal data are tabulated in Table 4.1; structures are shown in Figure 4.1. An alternative view for two configurational isomers of  $(\text{Me}_4\text{N})_4[\text{Cd}_{10}\text{S}_4(\text{SPh})_{16}]$ , **Cd10** and **Cd10(I-4)**, is shown separately to illustrate the configuration of  $\mu$ -SPh ligands (Figure 4.2). Notation **Cd10(I-4)** is used to stress that this isomer crystallizes in the different space group in contrast with that of **Cd10** (*i.e.*,  $I-42m$ ).

From the literature crystal data it can be seen, for instance, that crystals of cadmium thiophenolate complexes **Cd1** and **Cd4** are monoclinic; and for tetrahedral nanoclusters the symmetry of their crystalline lattice increases upon nanocluster size increase. Thus, the crystal system for **Cd17** is orthorhombic, while for **Cd32** and **Cd54** it is cubic.



**Table 4.1:** Selected crystal data for molecular cadmium thiophenolate complexes and tetrahedral nanoclusters with thiophenolate ligand shell  $\text{Cd}_x\text{S}_y(\text{SPh})_z$ .

compound		crystal system; space group	dimensions, Å	angles, °	Z	reference; CCDC # <sup>a</sup>
<b>Cd1</b>	$(\text{Me}_4\text{N})_2[\text{Cd}(\text{SPh})_4]$	<i>monoclinic</i> ; $P2_1$ (No. 4)	<i>a</i> 12.053(2) <i>b</i> 14.570(2) <i>c</i> 9.827(5)	$\alpha$ 90 $\beta$ 90.89(2) $\gamma$ 90	2	[19]; 1163267
<b>Cd4</b>	$(\text{Me}_4\text{N})_2[\text{Cd}_4(\text{SePh})_{10}]^b$	<i>monoclinic</i> ; $P2_1/c$ (No. 14)	<i>a</i> 20.830(2) <i>b</i> 14.282(1) <i>c</i> 25.872(1)	$\alpha$ 90 $\beta$ 99.626(6) $\gamma$ 90	4	[20]; 1201264
<b>Cd10</b>	$(\text{Me}_4\text{N})_4[\text{Cd}_{10}\text{S}_4(\text{SPh})_{16}]$	<i>tetragonal</i> ; $I-42m$ (No. 121)	<i>a</i> 20.140(2) <i>b</i> 20.140(2) <i>c</i> 16.896(1)	$\alpha$ 90.00 $\beta$ 90.00 $\gamma$ 90.00	2	[21]; 1112093
<b>Cd17</b>	$(\text{Me}_4\text{N})_2[\text{Cd}_{17}\text{S}_4(\text{SPh})_{28}]$	<i>orthorhombic</i> ; $Ccca$ (No. 68)	<i>a</i> 30.930(5) <i>b</i> 32.772(5) <i>c</i> 19.997(2)	$\alpha$ 90.00 $\beta$ 90.00 $\gamma$ 90.00	4	[22]; 1166964
<b>Cd32</b>	$[\text{Cd}_{32}\text{S}_{14}(\text{SPh})_{36}(\text{dmf})_4]$	<i>cubic</i> ; $P23$ (No. 195)	<i>a</i> 21.856(2) <i>b</i> 21.856(2) <i>c</i> 21.856(2)	$\alpha$ 90.00 $\beta$ 90.00 $\gamma$ 90.00	1	[36]; 1191309
<b>Cd54</b>	$(\text{Me}_4\text{N})_4[\text{Cd}_{54}\text{S}_{32}(\text{SPh})_{48}(\text{dmf})_4]$	<i>cubic</i> ; $P-43m$ (No. 215)	<i>a</i> 23.976(8) <i>b</i> 23.976(8) <i>c</i> 23.976(8)	$\alpha$ 90.00 $\beta$ 90.00 $\gamma$ 90.00	1	[35]; 1440110

<sup>a</sup> References are given to the original publications containing structural information, as well as to CCDC numbers of deposited crystal structures.

<sup>b</sup> The data shown are for the phenylselenolate analog  $(\text{Me}_4\text{N})_2[\text{Cd}_4(\text{SePh})_{10}]$ , which is expected to be crystallography isomorphous and have relatively small difference in metrical parameters from  $(\text{Me}_4\text{N})_2[\text{Cd}_4(\text{SPh})_{10}]$ .

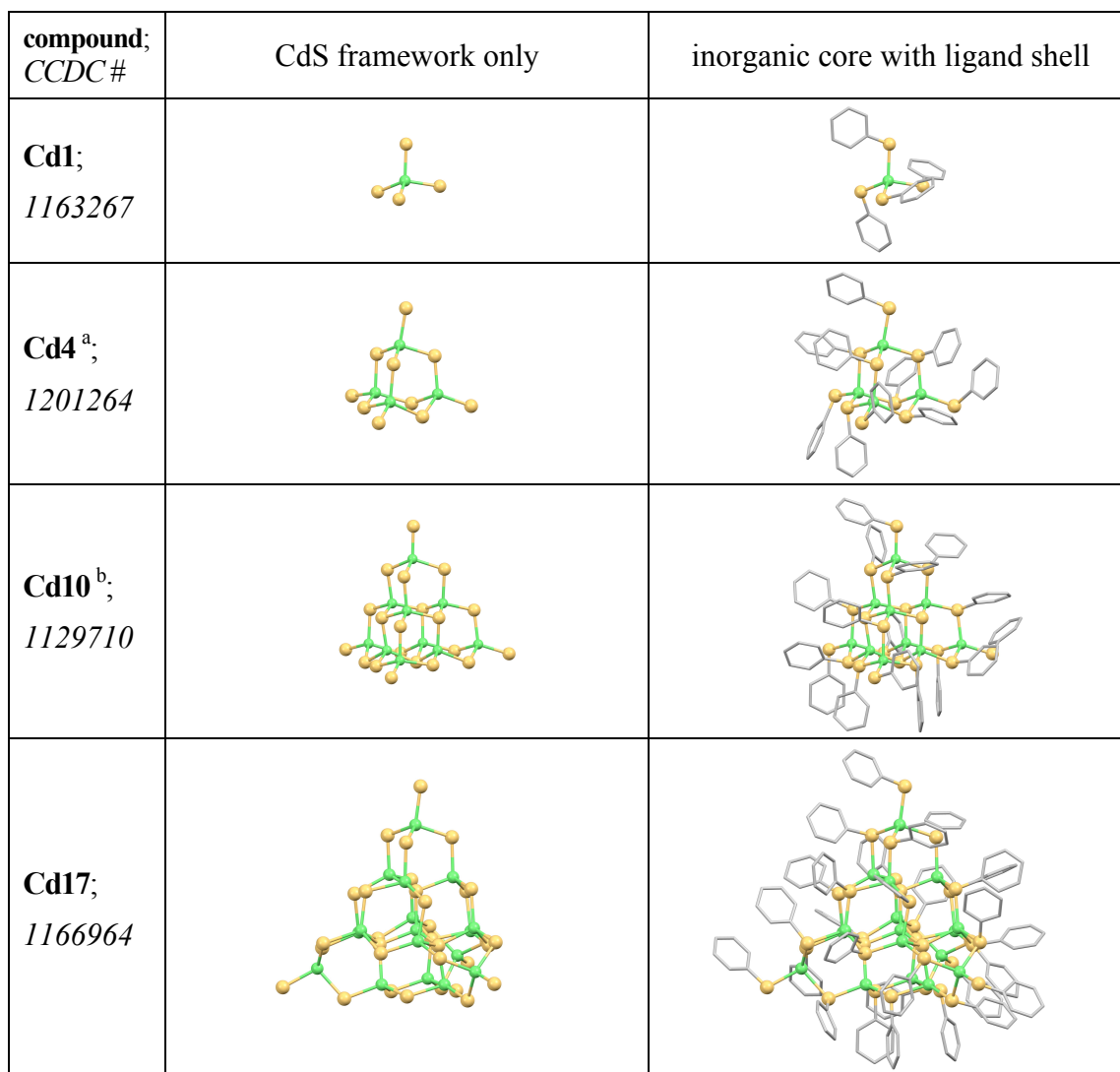


**Figure 4.1:** Structures of molecular cadmium thiophenolate complexes and tetrahedral nanoclusters with thiophenolate ligand shell  $\text{Cd}_x\text{S}_y(\text{SPh})_z$ : inorganic frameworks only (left) and complete nanocluster structures with organic ligands (right) are shown. The counterions and crystallization solvent molecules are not included.  $\text{M}^{2+}$  sites are shown as green;  $\text{E}^{2-}$ , yellow-orange; C, light grey; O or N, pink. Atoms and bonds in the nanocluster core are shown as spheres and sticks, respectively, while in ligands the atoms and bonds are shown as capped sticks.

<sup>a</sup> The structure shown is for (presumably) crystallographically isomorphous phenylselenolate analog  $(\text{Me}_4\text{N})_2[\text{Cd}_4(\text{SePh})_{10}]$ , expected to have only some metrical differences from  $(\text{Me}_4\text{N})_2[\text{Cd}_4(\text{SPh})_{10}]$  due to the different chalcogen atoms.

<sup>b</sup> The structure shown is for crystallography isomorphous zinc-containing analog,  $(\text{Me}_4\text{N})_4[\text{Zn}_{10}\text{S}_4(\text{SPh})_{16}]$ , which crystallizes in the related space group  $P-42_1c$  (No. 114); other than the metrical differences due to different metal it has no substantial crystallographic differences with  $(\text{Me}_4\text{N})_4[\text{Cd}_{10}\text{S}_4(\text{SPh})_{16}]$  (space group  $I-42m$ ).

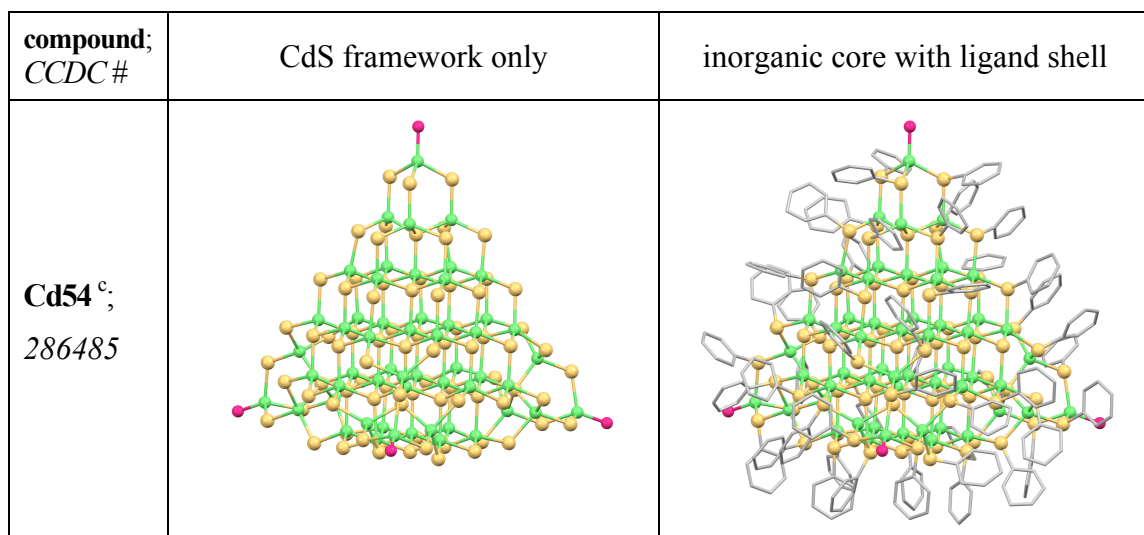


**Figure 4.1 (continued):** Structures of molecular cadmium thiophenolate complexes and tetrahedral nanoclusters with thiophenolate ligand shell  $Cd_xS_y(SPh)_z$ : inorganic frameworks only (left) and complete nanocluster structures with organic ligands (right) are shown. The counterions and crystallization solvent molecules are not included.  $M^{2+}$  sites are shown as green;  $E^{2-}$ , yellow-orange; C, light grey; O or N, pink. Atoms and bonds in the nanocluster core are shown as spheres and sticks, respectively, while in ligands the atoms and bonds are shown as capped sticks.

<sup>c</sup> The structure shown is for closely related analog with aqua ligands instead of *dmf* at four vertices  $(Me_4N)_4[Cd_{54}S_{32}(SPh)_{48}(H_2O)_4]$ , which crystallizes in related space group  $F-43m$  (No. 219) and has better resolved  $\mu$ -SPh ligands in comparison with  $(Me_4N)_4[Cd_{54}S_{32}(SPh)_{48}(dmf)_4]$  (space group  $P-43m$ ).

The metal thiophenolate complexes and small thiophenolate-capped tetrahedral  $Cd_xS_y(SPh)_z$  nanoclusters were prepared by a coordination chemistry approach using literature methods.<sup>21,22</sup> Their purity was confirmed using solution  $^1H$  and  $^{13}C$  NMR spectra (neither included nor discussed here). The large nanoclusters were obtained by solvothermal synthesis as described elsewhere.<sup>35</sup> The identity and the purity of all compounds were confirmed using powder X-ray diffraction (PXRD) by comparing the measured patterns (either for dried or fresh materials) with those simulated using single crystal X-ray data from the Cambridge Crystallographic Data Centre (CCDC).

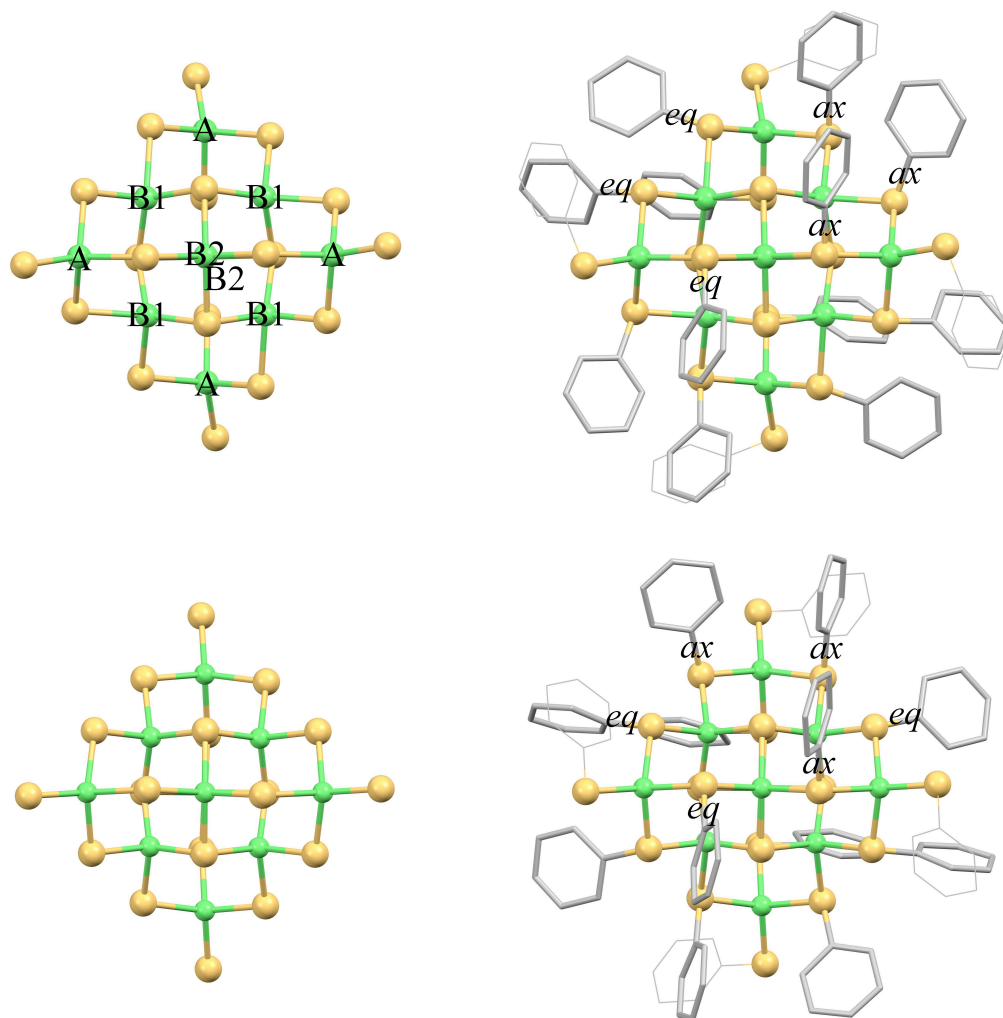


**Figure 4.2:** Configuration of substituents on the bridging ( $\mu$ -SPh) thiophenolate ligands in two configurational isomers of  $(\text{Me}_4\text{N})_4[\text{Cd}_{10}\text{S}_4(\text{SPh})_{16}]$ , **Cd10(I-4)** and **Cd10**, that crystallize in space groups  $I-4$  (upper figures) and  $I-42m$  (lower figures) (CCDC-1129708 and 1129710 structures, respectively). The inorganic framework only (left) is viewed along the symmetry axis  $S_4$  of the idealized nanocluster core; complete nanocluster structure (right) shown in the same orientation. Different cadmium sites are labeled on the upper left structure: vertex (A) and two crystallographically inequivalent edge sites (B1, B2). Axial (*ax*) or equatorial (*eq*) configurations of  $\mu$ -SPh ligands, which belong to the edges bounding one triangular face, are additionally labeled on both right structures. Cd and S atoms and bonds between them are shown as balls and sticks; C atoms and bonds in phenyl rings in  $\mu$ -SPh ligands are shown as capped sticks; while C atoms and bonds in phenyl rings in terminal SPh ligands are shown as wireframes.

### 4.2.2 PXRD Data

PXRD patterns for **Cd1**, **Cd4**, **Cd10**, and **Cd17** in both the low-angle and wide-angle regions are in good agreement with the literature data (Figures 4.3-4.6); a comparison of measured and simulated low-angle reflection positions shows only small discrepancies (Tables 4.2-4.5). Measured PXRD patterns for **Cd10** also allowed confirmation of the preparation of a particular configurational isomer (that crystallizes in space group  $I-42m$ ; see Figure 4.2), since the other known isomer **Cd10(I-4)** would give considerably different PXRD patterns.<sup>21</sup> Greater than expected intensity of some measured reflections (for instance,  $(020)$  for **Cd1**, see Figure 4.3) may result from the presence of preferential orientation in the crystalline sample.

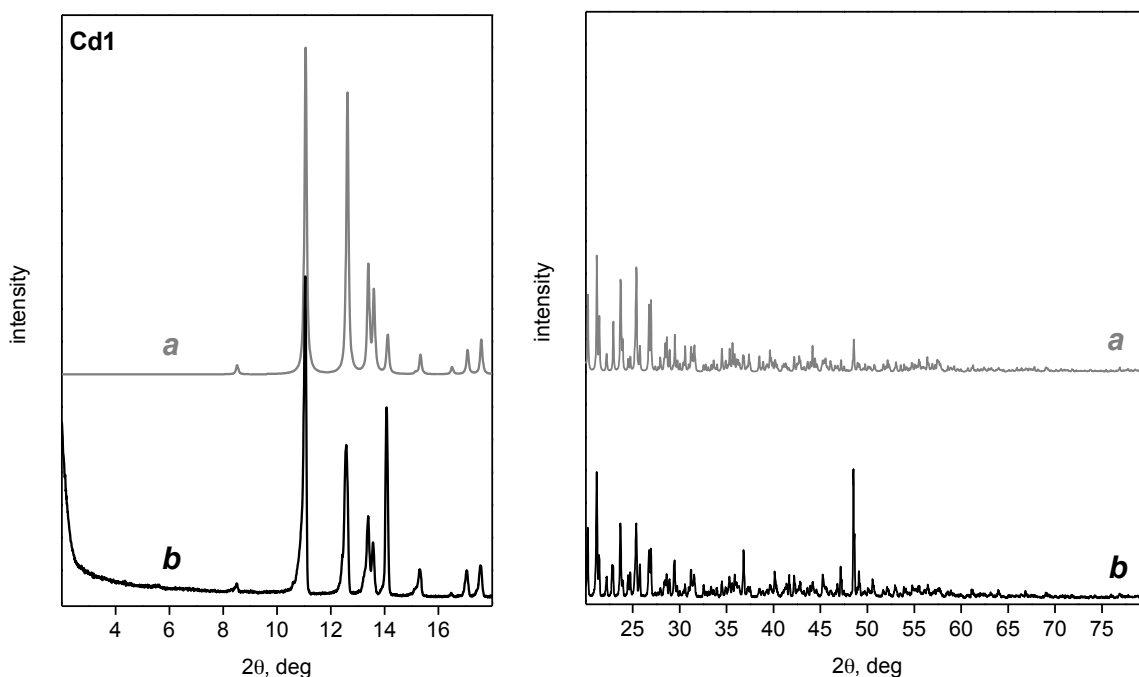


**Figure 4.3:** Measured (dried material, *b*) and simulated (*a*) PXRD patterns (Co  $K\alpha$  radiation) for **Cd1**: low-angle region, left; wide-angle region, right. The simulation was performed using structure *CCDC-1163267*. The data are shown with Y-axis offset for clarity.

**Table 4.2:** Measured (dried material) and simulated low-angle reflections (selected,  $2\theta$  from 2 to  $18^\circ$ ) for **Cd1**.

indexing, $hkl$	100	110	011	10-1	101	020	111	120	200	021
simulated, $d^a$	12.05	9.29	8.15	7.67	7.56	7.29	6.71	6.23	6.03	5.85
simulated, $2\theta^b$	8.52	11.06	12.62	13.40	13.60	14.12	15.33	16.51	17.09	17.60
measured, $2\theta^\circ$	8.52	11.05	12.57	13.39	13.57	14.08	15.32	16.48	17.05	17.57

<sup>a</sup> The simulation was performed using structure *CCDC-1163267* for  $(Me_4N)_2[Cd(SPh)_4]$ .

<sup>b</sup> Calculated from simulated  $d$  values using  $\lambda = 1.79026 \text{ \AA}$  (which corresponds to Co  $K\alpha$  radiation).

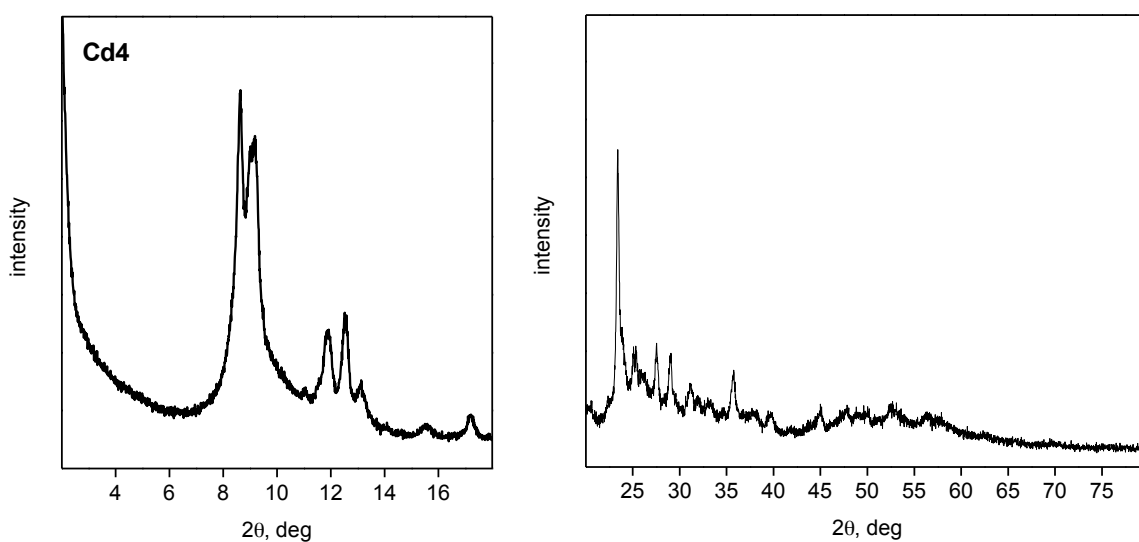


**Figure 4.4:** PXR D patterns (Co  $K\alpha$  radiation) measured for dried **Cd4**: low-angle region, left; wide-angle region, right.

**Table 4.3:** Measured in this work (dried material) and previously reported low-angle reflections (selected,  $2\theta$  from 2 to  $18^\circ$ ) for **Cd4**.

measured lit., $d^a$	11.91	11.05	9.36	8.19	7.89	6.54	6.01
measured lit., $2\theta^b$	8.62	9.29	10.98	12.55	13.04	15.74	17.14
measured in this work, $2\theta$	8.62	9.19	11.02	12.55	13.13	15.59	17.22

<sup>a</sup> Reported for  $(Me_4N)_2[Cd_4(SPh)_{10}]$  in ref. 21.

<sup>b</sup> Calculated from measured lit.  $d$  values using  $\lambda = 1.79026 \text{ \AA}$  (which corresponds to Co  $K\alpha$  radiation).

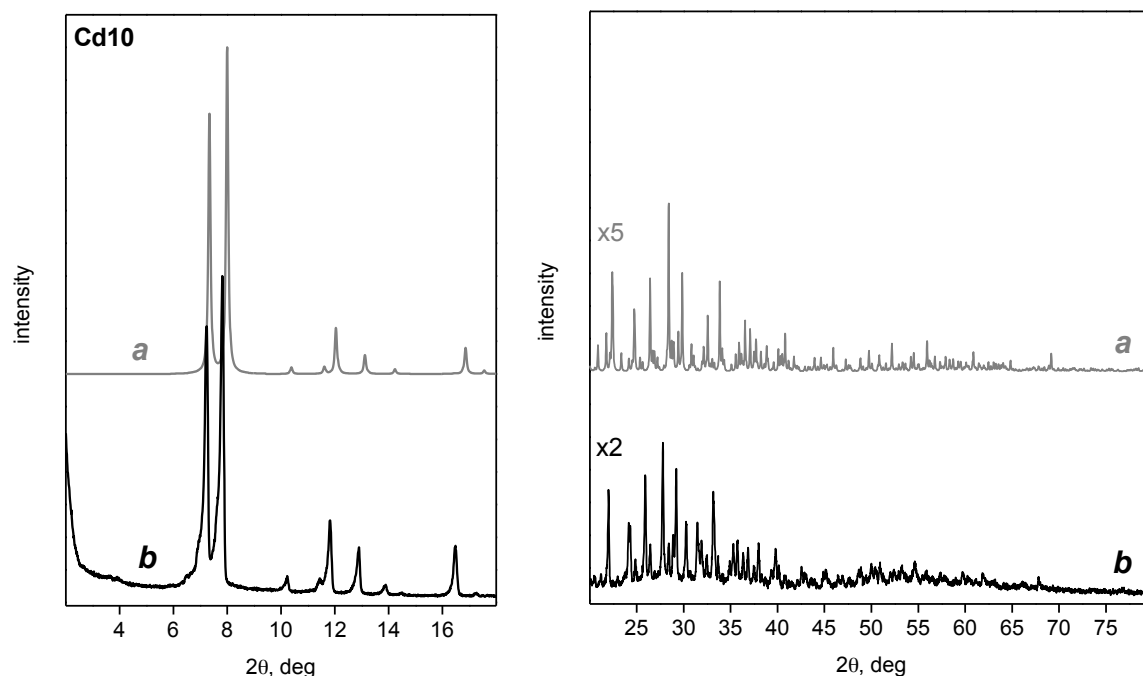


**Figure 4.5:** Measured (dried material, *b*) and simulated (*a*) PXRD patterns (Co K $\alpha$  radiation) for **Cd10**: low-angle region, left; wide-angle region, right. The simulation was performed using structure *CCDC-1129710*. The wide-angle region is scaled  $\times 2$  for pattern *b*, and  $\times 5$  for pattern *a*; the data are shown with Y-axis offset for clarity.

**Table 4.4:** Measured (dried material) and simulated low-angle reflections (selected,  $2\theta$  from 2 to 18 $^\circ$ ) for **Cd10**.

indexing, <i>hkl</i>	<i>110</i>	<i>101</i>	<i>200</i>	<i>210</i>	<i>201</i>	<i>211</i>	<i>112</i>	<i>212</i>	<i>311</i>
measured lit., $d^a$	13.83	12.85	9.89	8.85	8.51	7.82	7.23	6.12	5.87
simulated, $d^b$	13.99	12.84	9.89	8.85	8.53	7.84	7.22	6.11	5.87
simulated, $2\theta^c$	7.34	8.00	10.38	11.61	12.04	13.12	14.24	16.86	17.56
measured lit., $2\theta^d$	7.42	7.99	10.38	11.62	12.08	13.14	14.23	16.82	17.55
measured in this work, $2\theta$	7.23	7.82	10.23	11.44	11.83	12.90	13.89	16.49	17.27

<sup>a</sup> Reported for  $(\text{Me}_4\text{N})_4[\text{Cd}_{10}\text{S}_4(\text{SPh})_{16}]$  in ref. 21.

<sup>b</sup> Simulation was performed using structure *CCDC-1129710* for  $(\text{Me}_4\text{N})_4[\text{Zn}_{10}\text{S}_4(\text{SPh})_{16}]$ .

<sup>c</sup> Calculated from simulated  $d$  values using  $\lambda = 1.79026 \text{ \AA}$  (which corresponds to Co K $\alpha$  radiation).

<sup>d</sup> Calculated from measured lit.  $d$  values using  $\lambda = 1.79026 \text{ \AA}$  (which corresponds to Co K $\alpha$  radiation).

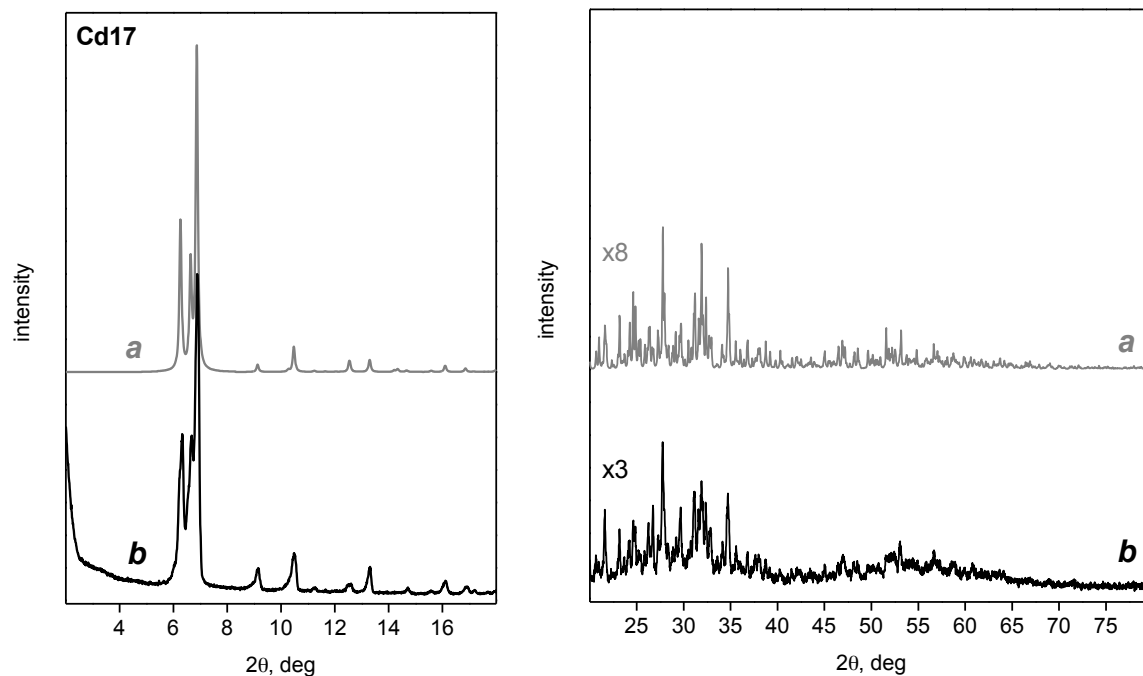


**Figure 4.6:** Measured (dried material, *b*) and simulated (*a*) PXRD patterns (Co K $\alpha$  radiation) for **Cd17**: low-angle region, left; wide-angle region, right. The simulation was performed using structure *CCDC-166964*. The wide-angle region is scaled  $\times 3$  for pattern *b*, and  $\times 8$  for pattern *a*; the data are shown with Y-axis offset for clarity.

**Table 4.5:** Measured (dried material) and simulated low-angle reflections (selected,  $2\theta$  from 2 to  $18^\circ$ ) for **Cd17**.

indexing, <i>hkl</i>	020	200	111	220	221	112	040	400	420	113	151
simulated, $d^a$	16.39	15.47	14.95	11.25	9.80	9.14	8.19	7.73	6.99	6.39	6.11
simulated, $2\theta^b$	6.26	6.64	6.87	9.13	10.48	11.24	12.54	13.30	14.71	16.10	16.86
measured, $2\theta^\circ$	6.33	6.68	6.88	9.16	10.50	11.27	12.60	13.31	14.72	16.11	16.89

<sup>a</sup> Simulation was performed using structure *CCDC-166964* for  $(\text{Me}_4\text{N})_2[\text{Cd}_{17}\text{S}_4(\text{SPh})_4]$ .

<sup>b</sup> Calculated from simulated  $d$  values using  $\lambda = 1.79026 \text{ \AA}$  (which corresponds to Co K $\alpha$  radiation).



In addition to the identification and purity confirmation, PXRD patterns for the large tetrahedral nanocluster **Cd54** revealed an interesting superstructure re-arrangement that was not observed for the smaller frameworks. While PXRD patterns of **Cd1-Cd17** measured for the dried materials match very well with the corresponding simulated patterns (Figures 4.3-4.6), this is not the case for **Cd54**. Thus, **Cd54** was found to crystallize in the space group  $P-43m$ ,<sup>35</sup> simulated PXRD pattern for this structure features a strong, sharp reflection at  $2\theta$   $4.28^\circ$  in the low-angle region together with several weaker reflections, equally spaced from each other (Figure 4.7, left, *a*). These reflections appear in accordance with systematic absences for primitive cubic superlattice; they are indexed as  $(100)$ ,  $(110)$ ,  $(111)$ ,  $(200)$ , and  $(210)$  (Table 4.6). In the wide-angle region, sharp reflections are displayed that characterize the short-range structure in the inorganic framework of the nanocluster and in its ligand shell (Figure 4.7, right, *a*). In contrast, the low-angle PXRD pattern for dried **Cd54** contains only a strong broad reflection at  $2\theta$   $5.02^\circ$ . No other reflections can be clearly discerned, though the presence of three very broad and weak ones can be proposed around  $\sim 6$ ,  $8$ , and  $9^\circ$  (Figure 4.7, left, *c*). From the position of the low-angle reflection, a corresponding interplanar spacing  $d$  of 2.04 nm was calculated using the Bragg equation. The wide-angle region of the PXRD pattern for dried **Cd54** contains three very broad reflections (Figure 4.7, right, *c*). The position of the observed peaks is in agreement with the presence of a crystalline CdS species, but drawing a distinction between cubic or hexagonal structures is not possible. Note that such broad and unresolved peaks in wide-angle PXRD patterns are typical for very small CdE nanoparticles, while narrower and easily discernable characteristic reflections for larger nanoparticles usually enable identification of the crystal structure.<sup>37</sup>

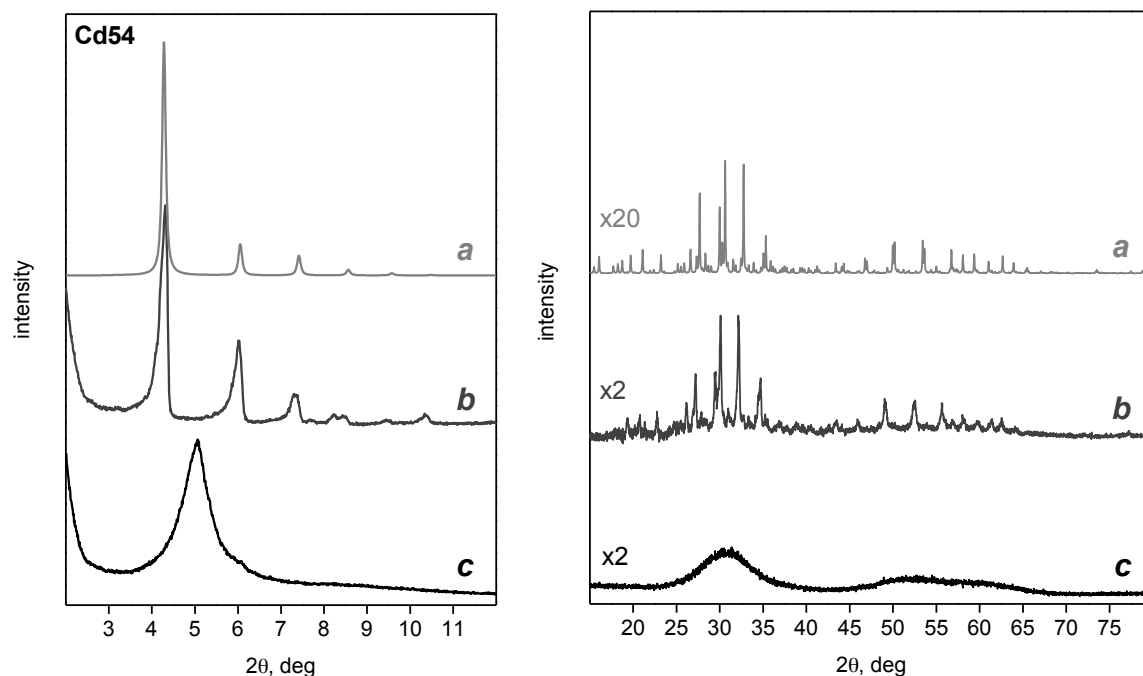


**Figure 4.7:** Measured (fresh material in paraffin oil, *b*; dried material, *c*) and simulated (*a*) PXR D patterns (Co  $K\alpha$  radiation) for **Cd54**: low-angle region, left; wide-angle region, right. The simulation was performed using structure *CCDC-1440110*. Pattern *b* was corrected for paraffin oil background. The wide-angle region is scaled  $\times 2$  for patterns *b* and *c*, and  $\times 20$  for pattern *a*; the data are shown with Y-axis offset for clarity.

**Table 4.6:** Measured (fresh material) and simulated low-angle reflections (selected,  $2\theta$  from 2 to  $12^\circ$ ) for **Cd54**.

indexing, <i>hkl</i>	100	110	111	200	210	211
simulated, $d^a$	23.98	16.95	13.84	11.99	10.72	9.79
simulated, $2\theta^\circ{}^b$	4.28	6.05	7.42	8.56	9.58	10.49
measured, $2\theta^\circ$	4.31	6.02	7.38	8.43	9.44	10.34

<sup>a</sup> Simulation was performed using structure *CCDC-1440110* for  $(\text{Me}_4\text{N})_4[\text{Cd}_{54}\text{S}_{32}(\text{SPh})_{48}(\text{dmf})_4]$ .

<sup>b</sup> Calculated from simulated  $d$  values using  $\lambda = 1.79026 \text{ \AA}$  (which corresponds to Co  $K\alpha$  radiation).

The substantial difference between simulated and measured (using the dried material) PXR D patterns for **Cd54** reflects some changes in the superlattice, most probably due to

removal of the lattice solvent. For the dried **Cd54**, elemental analysis data are consistent with the formula  $(\text{Me}_4\text{N})_4[\text{Cd}_{54}\text{S}_{32}(\text{SPh})_{48}(\text{dmf})_4]$ ; the position of the lowest absorption band in UV–vis spectrum ( $\lambda_{\text{max}} = 355 \text{ nm}$  in DMF) is in agreement with those for the previously published cadmium sulfide nanoclusters containing 54 metal atoms.<sup>23,35,38</sup> These facts argue in favour of the successful preparation and crystallization of **Cd54** with subsequent structure re-arrangement of the superlattice as a result of desolvation. To confirm that re-arrangement occurs upon drying, PXRD patterns for **Cd54** were also obtained using freshly prepared crystals ground under paraffin oil with some mother liquor. It was revealed that PXRD patterns for fresh **Cd54** match the corresponding simulated patterns: similar, equally spaced reflections were found in the low-angle region, while sharp and rather intense reflections dominate in the wide-angle region, being accompanied by some broad and unresolved ones (Figure 4.7, *b*). A small shift towards low angles of the reflections for measured PXRD patterns for fresh material versus calculated ones was observed previously (see, for example, ref. 39) and can be explained by the effect of thermal expansion. In particular, PXRD patterns for **Cd54** were obtained at room temperature, while single crystal data for **Cd54** were collected at 110 K. From the position of the first low-angle reflection at  $2\theta$   $4.31^\circ$ , a corresponding interplanar spacing  $d$  of 2.38 nm was calculated.

Quantitative comparison of the peak intensities for fresh *vs.* dried samples of **Cd54** is complicated, as different sample preparation techniques were used for collecting the diffraction patterns. However, the intensity of low-angle peaks for dried **Cd54** is noticeably lower and the peaks themselves are less sharp, reflecting a decrease of order upon superlattice re-arrangement. The absence of sharp reflections in the wide-angle region of PXRD patterns for dried **Cd54** is also consistent with the superlattice rearrangement with a decrease in its long range order. This re-arrangement may occur in such way that tetrahedrally-shaped crystalline frameworks are no longer oriented strictly in the same way and the translational order from cluster to cluster is gone. Nonetheless, nanoclusters as a whole (*i.e.*, viewed as pseudo-atoms) continue to occupy ordered positions in a superlattice.

The broad and low intensity nature of nearly all low-angle reflections for dried **Cd54** makes proper indexing impossible. If the primitive cubic superlattice persists after drying, the first low-angle reflection at  $2\theta$   $5.02^\circ$  can be indexed as  $(100)$ , with a calculated  $d$  spacing of 2.04 nm corresponding to the unit cell length  $a$ . Consequently, the cell dimensions for dried **Cd54** are considerably smaller than those for fresh **Cd54** (Table 4.1).

In this way, parameters of the ordered superlattice in **Cd54** upon isolation and drying are found to be different from those of the fresh material: rearrangement occurs with a unit cell length decrease of  $\sim 14\%$ , probably due to removal of crystallization solvent. Such significant structure re-arrangement (instead of crystalline lattice collapse) is unusual for metal chalcogenide nanoclusters. The re-arrangement is expected to be the distinctive feature of the superlattices of large thiophenolate-capped nanoclusters, with high (cubic) symmetry and spacious intercluster voids. It also has consequences for assigning  $^{111}\text{Cd}$  SSNMR resonances in the spectra of **Cd54**, as discussed below.

Several attempts at single-crystal X-ray characterization of **CdS-1.9 nm** were unsuccessful, as samples showed mostly diffuse scattering streaks rather than clearly discernible Bragg reflections. The difficulties with characterization may be related with the orientational flexibility of the large nanoclusters within a three-dimensional superlattice and/or superlattice defects of a different nature.<sup>23,38,40</sup> Thus, co-crystallization of the nanoclusters having different conformations of Ph groups or even different configurations of  $\mu$ -SPh ligands as “defects” would prevent resolving any atomic positions in the ligand shell by X-ray crystallography. Analysis of PXRD patterns of fresh **CdS-1.9 nm** provides some arguments in favour of the suppositions made. In particular, relatively strong and sharp reflections are found in the low-angle region (Figure 4.8, left, *a*) in agreement with the presence of a nanocluster superlattice. The first low-angle reflection is observed at  $2\theta$   $3.48^\circ$  (calculated  $d$  spacing is 2.95 nm), with additional reflections of lower intensity located at  $4.34$ ,  $4.86$ ,  $5.87$ ,  $6.78$ ,  $\sim 7.6$ , and  $\sim 8.3^\circ$ . An attempt of indexing the low-angle reflections for fresh **CdS-1.9 nm** showed no match with expected patterns for any cubic (*i.e.*, primitive, body-centered or face-centered) superlattices. The wide-angle region for fresh **CdS-1.9 nm** contains broad peaks (Figure 4.8, right, *a*), indicating non-uniform orientation of nanoclusters in the

superlattice. In this way, the wide-angle PXRD patterns of fresh **CdS-1.9 nm** are different from those of fresh **Cd54** (where both sharp and broad reflections were found), becoming similar to the PXRD pattern of dried **Cd54**. The most intense reflection at  $2\theta$   $3.48^\circ$  in the low-angle region of PXRD patterns for fresh **CdS-1.9 nm** is shifted considerably to lower angles in comparison with the corresponding reflection at  $2\theta$   $4.31^\circ$  for fresh **Cd54**. This is consistent with **CdS-1.9 nm** nanoclusters being larger than **Cd54**, hence a larger  $d$  spacing characterizing its superlattice. Based on results of the set of analyses,<sup>35</sup> **CdS-1.9 nm** nanoclusters were previously proposed to be close in size and composition to the predicted **Cd84**, but adopting a modified shape (*i.e.*, truncated tetrahedral).

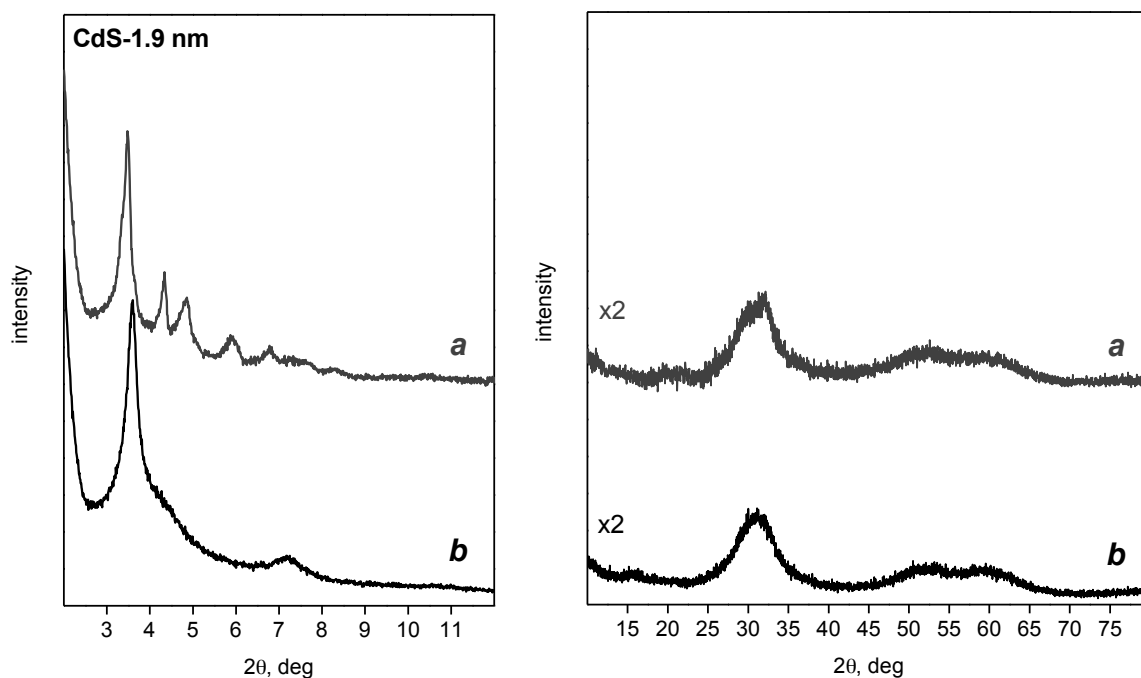


**Figure 4.8:** Measured (fresh material in paraffin oil, *a*; dried material, *b*) PXRD patterns (Co  $K\alpha$  radiation) for **CdS-1.9 nm**: low-angle region, left; wide-angle region, right. Pattern *a* was corrected for paraffin oil background. The wide-angle region is scaled  $\times 2$  for both patterns; the data are shown with Y-axis offset for clarity.

PXRD patterns for dried **CdS-1.9 nm** show that some structure re-arrangement occurs for this nanocluster superlattice upon drying, as was also found for **Cd54**. The low-angle

region contains a strong, sharp reflection at  $2\theta$   $3.55^\circ$ , together with a weaker and broader one at  $7.1^\circ$  (Figure 4.8, left, *b*). From the position of the first reflection, the corresponding *d* spacing of 2.89 nm was calculated. This implies that there are some changes in the superlattice upon sample drying but unlike for **Cd54**, a decrease of superlattice order for **CdS-1.9 nm** is accompanied by a less significant unit cell length decrease, from 2.95 to 2.89 nm. This may suggest smaller intercluster voids exist in **CdS-1.9 nm**, which can be related to the modified shape of these nanoclusters. When comparing the wide-angle regions of PXRD patterns for the dried samples, peaks are narrower for **CdS-1.9 nm** (Figure 4.8, right, *b*) than for **Cd54** (Figure 4.7, right, *c*), which is also in agreement with **CdS-1.9 nm** being larger in size than **Cd54**. TEM images for dried **CdS-1.9 nm** show apparent square packing of the nanoclusters with a lattice parameter of 2.9 nm, which is in agreement with a primitive cubic 3D arrangement.<sup>35</sup> Selected area electron diffraction (SAED) for dried **CdS-1.9 nm** allowed for confirming and detailing of the conclusions based on PXRD data. Thus, the low-angle part of the SAED pattern also showed the presence of an ordered superlattice. Lattice distances obtained from the wide-angle SAED reflections suggest a cubic crystalline structure for the inorganic framework of **CdS-1.9 nm**. Moreover, it was confirmed that nanoclusters in the superlattice of dried **CdS-1.9 nm** are not all oriented in the same way and exhibit a complex pattern for the orientations. In particular, the observed reflections can be matched with those for a model assuming a superposition of three distinct types of nanocluster orientation rotated  $60^\circ$  with respect to each other.<sup>35</sup>

#### **4.2.3 Local Environment**

For **Cd1**, **Cd4**, **Cd10**, **Cd17** and **Cd54**, as well as some related nanoclusters, the number of tetrahedral cadmium sites having a particular coordination environment (Table 4.7) was derived from the analysis of reported crystal structures or, in the case of predicted structures, by approximation using general bonding principles for the corresponding tetrahedral nanocluster series. Such analysis also allowed for some general trends to be found.

**Table 4.7:** Composition of molecular cadmium thiophenolate complexes and tetrahedral nanoclusters with thiophenolate ligand shell  $Cd_xS_y(SPh)_z$ .

		number of chemically (and crystallographically) different metal sites <sup>a</sup>
compound		“isolated” $\{(SPh)_4Cd\}$
<b>Cd1</b>	$[Cd(SPh)_4]^{2-}$	1

compound		vertex $\{(\mu-SPh)_3Cd(SPh)\}$	–	edge $\{(\mu_3-S)_2Cd(\mu-SPh)_2\}$	face $\{(\mu_4-S)Cd(\mu_3-S)_3\}$	inner $\{(\mu_4-S)_4Cd\}$
<b>Cd4</b>	$[Cd_4(SPh)_{10}]^{2-}$	4 (1+1+1+1)	–	–	–	–
<b>Cd10</b>	$[Cd_{10}S_4(SPh)_{16}]^{4-}$	4	–	6 (4+2)	–	–
predicted structure						
<b>Cd20</b>	$[Cd_{20}S_{13}(SPh)_{22}]^{8-}$	4	–	12	4	–
<b>Cd35</b>	$[Cd_{35}S_{28}(SPh)_{28}]^{14-}$	4	–	18	12	1
<b>Cd56</b>	$[Cd_{56}S_{50}(SPh)_{34}]^{22-}$	4	–	24	24	4

compound		vertex $\{(\mu-SPh)_3Cd(SPh)\}$ or $\{(\mu-SPh)_3CdL\}$ <sup>b</sup>	edge-near-vertex $\{(\mu_4-S)Cd(\mu-SPh)_3\}$	edge-central $\{(\mu_4-S)(\mu_3-S)Cd(\mu-SPh)_2\}$	face $\{(\mu_4-S)Cd(\mu_3-S)_3\}$	inner $\{(\mu_4-S)_4Cd\}$
<b>Cd17</b>	$[Cd_{17}S_4(SPh)_{28}]^{2-}$	4	12 (4+4+4)	–	–	1
<b>Cd32</b>	$[Cd_{32}S_{14}(SPh)_{36}L_4]$	4	12	12	–	4
<b>Cd54</b>	$[Cd_{54}S_{32}(SPh)_{48}L_4]^{4-}$	4	12	24	4	10 (6+4)
predicted structure						
<b>Cd84</b>	$[Cd_{84}S_{59}(SPh)_{60}L_4]^{10-}$	4	12	36	12	20
<b>Cd123</b>	$[Cd_{123}S_{96}(SPh)_{72}L_4]^{18-}$	4	12	48	24	35

<sup>a</sup> When applicable, numbers in round brackets reflect crystallographic inequivalence of the metal sites having the same coordination environment. Different summation terms represent groups of crystallographically inequivalent metal sites. The value of a given term shows the number of equivalent metal sites in a group.

<sup>b</sup> L = neutral ligands, e.g., *dmf* (coordinated to cadmium *via* O) or H<sub>2</sub>O (coordinated *via* O).

In particular, it can be seen that the coordination environment of cadmium sites along the edges is not the same between different nanocluster series. For example, it is  $\{(\mu_3\text{-S})_2\text{Cd}(\mu\text{-SPh})_2\}$  in basic supertetrahedral nanoclusters (for instance, in **Cd10**) and  $\{(\mu_4\text{-S})(\mu_3\text{-S})\text{Cd}(\mu\text{-SPh})_2\}$  and/or  $\{(\mu_4\text{-S})\text{Cd}(\mu\text{-SPh})_3\}$  in capped supertetrahedral nanoclusters (for instance, in **Cd54**) (Table 4.7). Such differences are connected with the structural features of the capped supertetrahedral nanoclusters series, *i.e.*, hexagonal cage capping each of four vertices and the open cleft that runs along each of the tetrahedral edges in inorganic framework. Some sites (*e.g.*, edge-central or face cadmium,  $\{(\mu_4\text{-S})(\mu_3\text{-S})\text{Cd}(\mu\text{-SPh})_2\}$  or  $\{(\mu_4\text{-S})\text{Cd}(\mu_3\text{-S})_3\}$ , respectively) appear only in the largest nanoclusters belonging to the  $C_n$  series (**Cd32** and larger; **Cd54** and larger, respectively; see Table 4.7). Note that inner  $\{(\mu_4\text{-S})_4\text{Cd}\}$  sites, found in the core of the largest synthesized and characterized nanoclusters of the  $C_n$  series, would appear only in predicted nanoclusters of the  $T_n$  series, but have no analogs in known frameworks. With nanocluster size increase, the ratio between different cadmium sites naturally changes in such a way that the fraction of sites associated with the surface decreases; the fraction of sites where cadmium is bonded to SPh or (at vertices) to other ligands decreases even faster.

It should be noted that the classification of metal sites by their coordination environment based on chemical functionality only. For the sites with particular coordination environment some parameters, such as corresponding bond lengths and angles, effective charges on particular atoms *etc.*, may not be the same 1) in one framework, and 2) in frameworks of different size; thus such metal sites can be crystallographically and magnetically inequivalent. An example of crystallographic inequivalence of cadmium atoms within a single nanocluster is the edge sites of **Cd10**, where there are two groups of crystallographically inequivalent Cd atoms composed of two and four sites, respectively (Table 4.7).

#### 4.2.4 SSNMR Data

$^1\text{H}\text{-}^{111}\text{Cd}$  variable amplitude cross polarization with magic angle spinning (VACP/MAS) and  $^1\text{H}\text{-}^{111}\text{Cd}$  VACP/MAS echo SSNMR spectra were obtained and analyzed alongside X-ray crystallographic data in order to find a correlation between chemical shifts of



observed resonances and particular coordination environments for cadmium sites, taking into account the structural features of complexes and nanoclusters under study.

The mononuclear cadmium thiophenolate complex **Cd1** (Table 4.1, Figure 4.1) can be viewed as the smallest member of the basic supertetrahedral nanocluster series. While containing a single type of cadmium coordination environment  $\{(SPh)_4Cd\}$  (see Table 4.7), this simple compound can be used to illustrate distortions from idealized tetrahedral stereochemistry at metal site related to the particular conformation of SPh ligands. According to the crystal structure, the Cd–SPh bond lengths of the four thiophenolate ligands varies from 2.531(3) to 2.556(3) Å; the angles S–Cd–S also vary from 98.9(1) to 116.6(1)°.<sup>19</sup> The  $^1H$ - $^{111}Cd$  VACP/MAS SSNMR spectrum of **Cd1** features a single, narrow resonance at 645 ppm (Figure 4.9, lower trace).

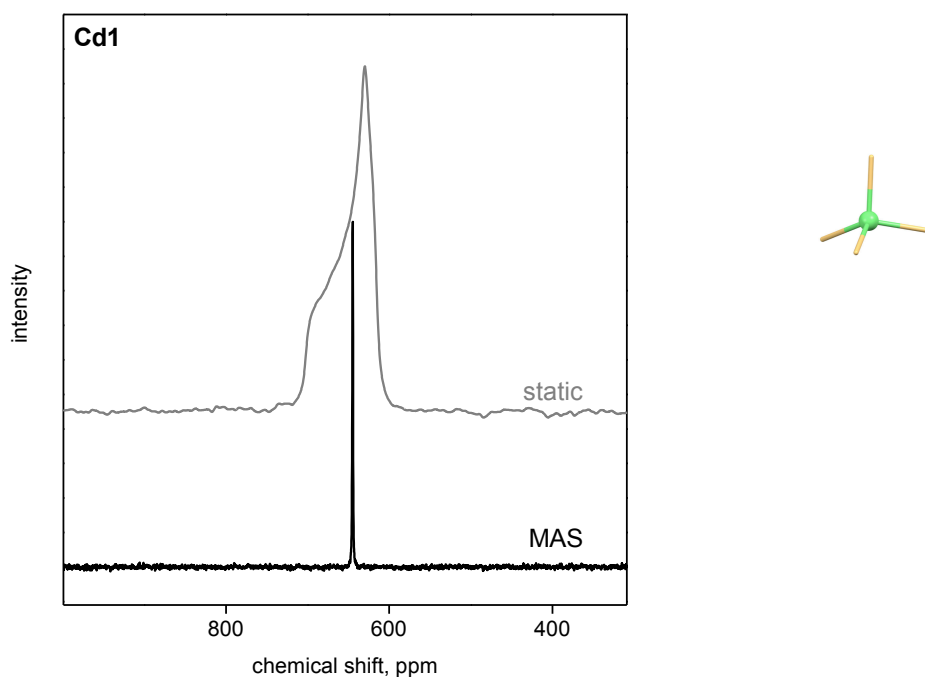


**Figure 4.9:**  $^1H$ - $^{111}Cd$  VACP/MAS SSNMR spectrum of **Cd1** (left, lower trace, black), acquired at a spinning frequency of 15.5 kHz; along with the static  $^1H$ - $^{111}Cd$  VACP echo SSNMR spectrum of **Cd1** (left, upper trace, grey). Both spectra were processed using 500 Hz of line broadening and normalized. The spectra are shown with Y-axis offset. The inorganic framework of **Cd1** (right): Cd atom and bonds are shown as green ball and sticks, S atoms and bonds are shown as yellow-orange capped sticks.

The local distortions in cadmium coordination environment become obvious in the static  $^1\text{H}$ - $^{111}\text{Cd}$  VACP SSNMR spectrum of **Cd1**, where chemical shift anisotropy (CSA) is reflected in the line shape and width (Figure 4.9, upper trace). The lineshape of the static spectrum of **Cd1** suggests the presence of a  $C_3$  axis for the cadmium coordination environment. Although, from the crystallographic data, the distribution of Cd–S bond lengths supports such a description, the variations of angles S–Cd–S do not reinforce this model.

In the case of **Cd4** the influence of structural features (*i.e.*, geometrical variations in distorted tetrahedral coordination of the four cadmium sites) on  $^{111}\text{Cd}$  chemical shifts can be clearly followed in SSNMR spectra. For **Cd4** the formula  $[\text{Cd}_4(\text{SPh})_{10}]^{2-}$  can also be written as  $[(\mu\text{-SPh})_6(\text{CdSPh})_4]^{2-}$  to distinguish the different types of thiophenolate ligands. An idealized inorganic framework of **Cd4** resembles an adamantane cage (Figure 4.1), though considerable difference in metrical parameters of Cd–S bonds in the actual **Cd4** core makes its point symmetry stray from the  $T_d$  symmetry of adamantane. Moreover, the symmetry of the **Cd4** complex is additionally lowered to point group  $C_1$  by the thiophenolate ligand substituents. In **Cd4** four metal sites form a (non bonded) distorted tetrahedron with thiophenolate ligands bridging the six edges, thus the  $\{(\mu\text{-SPh})_3\text{Cd}(\text{SPh})\}$  coordination environment with terminal Cd–SPh bonding here can be classified as “vertex”. While there is a single type of coordination environment for the metal sites in **Cd4** (Table 4.7), all four vertex sites are crystallographically inequivalent. Substantial deviations from local  $C_{3v}$  symmetry at the vertices are apparent from the large variations in  $(\mu\text{-SPh})\text{-Cd}\text{-(}\mu\text{-SPh)}$  and  $(\mu\text{-SPh})\text{-Cd}\text{-(SPh)}$  angles and all Cd–S bond lengths at each metal site.<sup>41</sup> The crystallographic inequivalence of the four  $\{(\mu\text{-SPh})_3\text{Cd}(\text{SPh})\}$  sites thus originates from these bond length and angle variations, which in turn can be traced to intramolecular interactions between the contiguous phenyl substituents. The magnitude of such an interaction can be related with the configuration of substituents on  $\mu\text{-SPh}$  (axial or equatorial) and their conformation in terminal SPh. The most influential is an interaction between *ax,ax* pairs of vicinal substituents. An assumption is made that configuration and conformation of substituents on EPh in **Cd4** is the same as observed in  $(\text{Me}_4\text{N})_2[\text{Cd}_4(\text{SePh})_{10}]$  (CCDC-1201264)<sup>20</sup> (Table 4.1, Figure 4.1) and  $(\text{Et}_4\text{N})(\text{Et}_3\text{NH})[\text{Cd}_4(\text{SPh})_{10}]$  (CCDC-1310452).<sup>41</sup> This particular configurational isomer has the smallest possible number of *ax,ax* phenyl substituents on the bridging ligands (two *ax,ax* pairs per nanocluster) and occurs very often in

adamantane-type M4 frameworks.<sup>20</sup> For the  $\{(\mu\text{-SPh})_3\text{Cd}(\text{SPh})\}$  sites the more substantial distortions can be related at the first level of approximation with interactions of phenyl rings in *ax,ax* ( $\mu\text{-SPh}$ ) pairs. Thus, in  $(\text{Et}_4\text{N})(\text{Et}_3\text{NH})[\text{Cd}_4(\text{SPh})_{10}]$  angles ( $\mu\text{-SPh}_{ax}$ )–Cd–( $\mu\text{-SPh}_{ax}$ ) are significantly larger in comparison with ( $\mu\text{-SPh}_{ax}$ )–Cd–( $\mu\text{-SPh}_{eq}$ ) and ( $\mu\text{-SPh}_{eq}$ )–Cd–( $\mu\text{-SPh}_{eq}$ ); the mean values for the angles are 116.6, 107.0 and 92.5°, respectively.<sup>41</sup>

In agreement with X-ray crystallographic data, the  $^1\text{H}\text{-}^{111}\text{Cd}$  VACP/MAS spectrum of **Cd4** features a relatively broad asymmetric resonance ( $\sim 608$  ppm) with hints of further resonance splitting or multiple overlapping resonances (Figure 4.10).

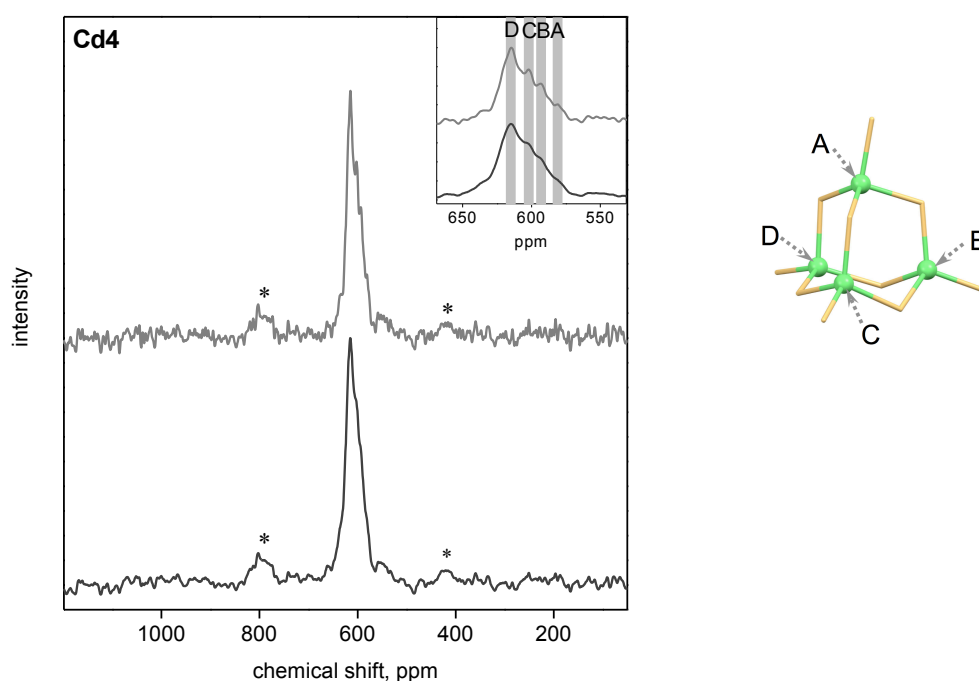


**Figure 4.10:**  $^1\text{H}\text{-}^{111}\text{Cd}$  VACP/MAS SSNMR spectra of **Cd4** (left), acquired at a spinning frequency of 15.5 kHz. The spectra represent the same data set processed using 200 and 500 Hz of line broadening (upper trace, grey, and lower trace, dark grey, respectively); normalized and shown with Y-axis offset. The insets show enlarged spectral regions along with the proposed labelling of the resonances. The inorganic framework of **Cd4** (right): Cd atoms and bonds are shown as green balls and sticks, S atoms and bonds are shown as yellow-orange capped sticks, along with the assignment of the resonances to four crystallographically inequivalent vertex sites (see text for details).

Indeed, processing the spectrum with less line broadening (thus being able to resolve more details at the cost of lower signal-to-noise ratio, S/N) indicates that this spectral

region is actually composed of four individual resonances located at approximately 581, 594, 602 and 615 ppm (labelled A-D on Figure 4.10). These four individual resonances, Cd4(A)-Cd4(D), can be correlated with the four crystallographically inequivalent  $\{(\mu\text{-SPh})_3\text{Cd}(\text{SPh})\}$  sites. Note that the chemical shift of the most deshielded vertex metal site Cd4(D) in **Cd4** is close to the chemical shift of the vertex metal sites Cd10(A) in the larger **Cd10** nanocluster, which can be used for the assignment of the resonances Cd4(A)-Cd4(D) to the particular cadmium sites (*vide infra*).

The distortions from idealized tetrahedral coordination for all four crystallographically inequivalent cadmium sites in **Cd4** are reflected in the static  $^1\text{H}\text{-}^{111}\text{Cd}$  VACP echo SSNMR spectrum of this cadmium thiophenolate complex, where the  $^{111}\text{Cd}$  resonance exhibits a broad width of  $\sim 400$  ppm and a complex lineshape (Figure 4.11). Any reliable modeling of contributions from each cadmium site and fitting the parameters of individual resonances based on the static spectrum of **Cd4** is virtually impossible due to the distribution of relatively close chemical shifts and (presumably) CSAs for the four cadmium atoms.

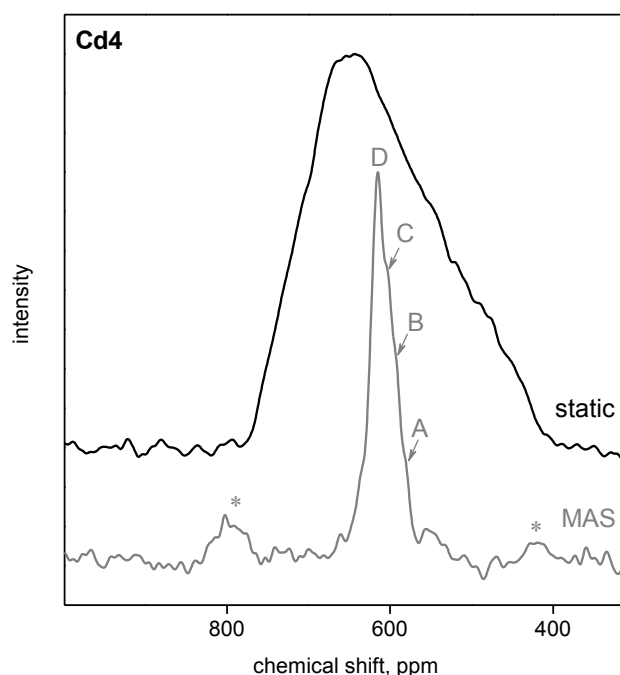


**Figure 4.11:** Static  $^1\text{H}\text{-}^{111}\text{Cd}$  VACP echo SSNMR spectrum of **Cd4**. The spectrum was processed using 1000 Hz of line broadening and normalized. The corresponding  $^1\text{H}\text{-}^{111}\text{Cd}$  VACP/MAS echo SSNMR spectrum of **Cd4** is shown with Y-axis offset for comparison.

Generally, in decanuclear thiophenolate complexes  $[\text{Cd}_{10}\text{S}_4(\text{SPh})_{16}]^{4-}$  two types of coordination environment for the metal are possible, *i.e.*, vertex  $\{(\mu\text{-SPh})_3\text{Cd}(\text{SPh})\}$  and edge  $\{(\mu_3\text{-S})_2\text{Cd}(\mu\text{-SPh})_2\}$  sites (see Table 4.7). Additional crystallographic inequivalence of the edge cadmium sites  $\{(\mu_3\text{-S})_2\text{Cd}(\mu\text{-SPh})_2\}$  in  $[\text{Cd}_{10}\text{S}_4(\text{SPh})_{16}]^{4-}$  is related to 1) primary inorganic framework distortions due to differences in Cd–( $\mu_3\text{-S}$ ), Cd–( $\mu\text{-SPh}$ ), and Cd–(SPh) distances; 2) further distortions due to *intramolecular* interactions between the contiguous phenyl substituents; as well as 3) more difficult-to-trace distortions due to *intermolecular* ligand-cation hydrogen bonding and *intermolecular* ligand-ligand interactions.<sup>26</sup> Thus, the splitting of six edge cadmium sites into two crystallographically and magnetically inequivalent groups was previously found in **Cd10(I-4)** (CCDC-1129708; see Figure 4.2, upper). From X-ray crystallographic data, the nanocluster anion of this isomer belongs to the  $S_4$  point group,<sup>21</sup> there are two *ax,ax* pairs of phenyl substituents per face. The configuration of phenyl substituents on the bridging ( $\mu\text{-SPh}$ ) ligands at edge metal sites is either *ax,ax* or *ax,eq*,<sup>42</sup> thus yielding the local configuration  $\{(\mu_3\text{-S})_2\text{Cd}(\mu\text{-SPh}_{ax})(\mu\text{-SPh}_{ax})\}$  or  $\{(\mu_3\text{-S})_2\text{Cd}(\mu\text{-SPh}_{ax})(\mu\text{-SPh}_{eq})\}$  for two edge coordination environments, respectively. The inequivalence of these two local configurations for the edge sites can be illustrated by the differences of the ( $\mu\text{-SPh}_{ax}$ )–Cd–( $\mu\text{-SPh}_{ax}$ ) and ( $\mu\text{-SPh}_{ax}$ )–Cd–( $\mu\text{-SPh}_{eq}$ ) angles, 104.6(1) and 98.2(1)°, respectively.<sup>21</sup> Consequently, together with vertex sites, there are three crystallographically inequivalent metal sites in **Cd10(I-4)**; in the  $^1\text{H}$ - $^{113}\text{Cd}$  CP/MAS spectrum three resonances were observed.<sup>26</sup> The chemical shift for edge sites with the local configuration  $\{(\mu_3\text{-S})_2\text{Cd}(\mu\text{-SPh}_{ax})(\mu\text{-SPh}_{eq})\}$  is the largest; it is separated by 36 ppm from the one for edge sites with the local configuration  $\{(\mu_3\text{-S})_2\text{Cd}(\mu\text{-SPh}_{ax})(\mu\text{-SPh}_{ax})\}$ , and by 106 ppm from the chemical shift for vertex sites  $\{(\mu\text{-SPh})_3\text{Cd}(\text{SPh})\}$ .<sup>26</sup>

In **Cd10** (space group  $I-42m$ ), where the anionic nanocluster also belongs to the  $S_4$  point group, there is only one *ax,ax* pair per each of the four nanocluster faces.<sup>21</sup> The configuration of phenyl substituents on the bridging ligands at all edge cadmium sites is *ax,eq* (Figure 4.2, lower), thus the local configuration can be denoted as  $\{(\mu_3\text{-S})_2\text{Cd}(\mu\text{-SPh}_{ax})(\mu\text{-SPh}_{eq})\}$ . Though the edge metal sites in **Cd10** are crystallographically inequivalent (six sites form two groups containing four and two sites) (Table 4.7), the difference in bond lengths and angles is less significant than in the isomer discussed above. For instance, the angles ( $\mu\text{-SPh}_{ax}$ )–Cd–( $\mu\text{-SPh}_{eq}$ ) for two crystallographically inequivalent

edge metal sites are 101.7(2) and 102.1(3) $^{\circ}$ .<sup>21</sup> In this way, there are three crystallographically inequivalent metal sites in **Cd10**, but only two separate resonances (at 620 and 712 ppm for vertex and edge sites, respectively) were observed previously in its  $^1\text{H}$ - $^{113}\text{Cd}$  CP/MAS spectrum, since the two signals for different edge metal sites are not resolved (*i.e.*,  $\Delta < 3$  ppm for these signals).<sup>26</sup> In agreement with previously reported results, the  $^1\text{H}$ - $^{111}\text{Cd}$  VACP/MAS echo spectrum of **Cd10** features two sharp resonances, Cd10(A) at 615 ppm and Cd10(B) at 705 ppm (Figure 4.12), which are assigned to the vertex and edge metal sites, respectively. The static  $^1\text{H}$ - $^{111}\text{Cd}$  VACP echo SSNMR spectrum of **Cd10** (Figure 4.12) closely resembles the one reported and analysed previously.<sup>26</sup>

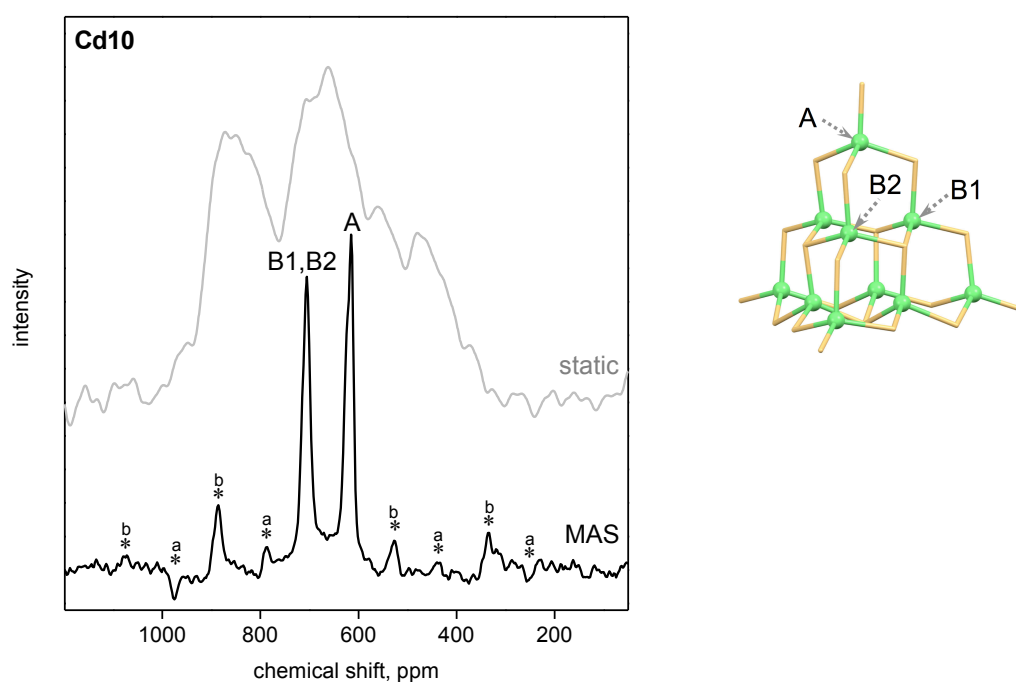


**Figure 4.12:**  $^1\text{H}$ - $^{111}\text{Cd}$  VACP/MAS echo SSNMR spectrum of **Cd10** (left, lower trace, black), acquired at a spinning frequency of 15.5 kHz and processed using 500 Hz of line broadening. The two resonances corresponding to the different isotropic chemical shifts of **Cd10** are labelled with capital letters, while spinning sidebands (SSBs) are marked with asterisks (\*) and corresponding lowercase letters on spectra. In some instances, one or several SSBs were impossible to phase and appear as negative intensity from the baseline. Static  $^1\text{H}$ - $^{111}\text{Cd}$  VACP echo SSNMR spectrum of **Cd10** (left, upper trace, grey), processed using 2000 Hz of line broadening. The spectra are normalized and shown with Y-axis offset. The inorganic framework of **Cd10** (right): Cd atoms and bonds are shown as green balls and sticks, S atoms and bonds are shown as yellow-orange capped sticks. Two crystallographically inequivalent edge sites are labeled B1 and B2, while the vertex site is labeled A.

The relatively straightforward interpretation of SSNMR data for **Cd10** makes spectra of this compound convenient for comparison with spectra for both smaller and larger  $\text{Cd}_x\text{S}_y(\text{SPh})_z$  nanoclusters. We assume that the chemical shifts for cadmium sites with particular coordination environment in two different nanoclusters can be related with the level of distortion from idealized tetrahedral geometry for such sites. Thus for two configurational isomers of  $(\text{Me}_4\text{N})_4[\text{Cd}_{10}\text{S}_4(\text{SPh})_{16}]$  the chemical shift for the vertex sites of **Cd10(I-4)** was reported to be smaller in comparison with chemical shift for the vertex sites of **Cd10** (604 and 620 ppm, respectively).<sup>26</sup> According to X-ray crystallographic data,<sup>21</sup> vertex sites of **Cd10(I-4)** generally have lower local symmetry in comparison with the vertex sites of **Cd10**. Structural data also correlate with CSA values from analysis of the intensities of the combs of spinning side bands obtained at various MAS spinning speeds, using Herzfeld-Berger analysis, and refined by fitting to the absorption envelopes in the static spectra.<sup>26</sup> In particular, the maximum chemical shift anisotropies ( $\delta_{33} - \delta_{11}$ ) were calculated as 280 and 270 ppm for the vertex sites of **Cd10(I-4)** and of **Cd10**, respectively.<sup>26</sup> Thus, a smaller chemical shift for the cadmium sites with particular coordination environment can be associated with the larger local distortions. Based on this, it is possible to assign the four resonances in the spectrum of **Cd4** to the four crystallographically inequivalent metal sites, which have different metrical parameters. As was mentioned above, the chemical shift for vertex sites in the spectrum of **Cd10** (*i.e.*, 615 ppm) is close to the chemical shift for one of the four vertex sites in the spectrum of **Cd4**, which can be related with comparable level of distortions for the sites in both cases. Since the chemical shifts of the other three vertex sites of **Cd4** are smaller (602, 584, and 581 ppm), these sites are supposed to have the higher level of distortions. Thus, the two resonances with lower frequencies Cd4(A) and Cd4(B) may be assigned to the two vertex sites in **Cd4** that contain *ax,ax* ( $\mu$ -SPh) pair each and deviate the most from the ideal tetrahedral geometry. The other two resonances Cd4(C) and Cd4(D) thus would originate from the two vertex sites in **Cd4** with less substantial distortions. The resonances and resonance groups for different cadmium thiophenolate complexes and tetrahedral nanoclusters along with the proposed assignment to the cadmium sites with particular coordination environments are summarized in Table 4.8.

**Table 4.8:** Chemical shifts and proposed assignment for different resonances and/or groups of resonances of **Cd1**, **Cd4**, **Cd10** and **Cd17** (referenced to 0.1 M aqueous solution of  $\text{Cd}(\text{ClO}_4)_2$ ).

compound		“isolated” $\{(\text{SPh})_4\text{Cd}\}$ sites		
<b>Cd1</b>	$[\text{Cd}(\text{SPh})_4]^{2-}$	645		
compound		vertex $\{(\mu\text{-SPh})_3\text{Cd}(\text{SPh})\}$ sites	edge $\{(\mu_3\text{-S})_2\text{Cd}(\mu\text{-SPh})_2\}$ sites	inner sites $\{(\mu_4\text{-S})_4\text{Cd}\}$
<b>Cd4</b>	$[\text{Cd}_4(\text{SPh})_{10}]^{2-}$	Cd4(A), Cd4(B), Cd4(C), Cd4(D) 581, 594, 602, 615	–	–
<b>Cd10</b>	$[\text{Cd}_{10}\text{S}_4(\text{SPh})_{16}]^{4-}$	Cd10(A) 615	Cd10(B) 705	–
compound		vertex $\{(\mu\text{-SPh})_3\text{Cd}(\text{SPh})\}$ sites	edge-near-vertex $\{(\mu_4\text{-S})\text{Cd}(\mu\text{-SPh})_3\}$ sites	inner sites $\{(\mu_4\text{-S})_4\text{Cd}\}$
<b>Cd17</b>	$[\text{Cd}_{17}\text{S}_4(\text{SPh})_{28}]^{2-}$	Cd17(A) 553	Cd17(B), Cd17(C), Cd17(D) 569, 598, 615	Cd17(E) 641



When considering the idealized core of **Cd17** (Table 4.1, Figure 4.1), the first member of the capped supertetrahedral nanocluster series, there are three types of cadmium coordination environments: vertex, edge-near-vertex, and inner sites (see Table 4.7). The name “edge-near-vertex” is chosen for  $\{(\mu_4\text{-S})\text{Cd}(\mu\text{-SPh})_3\}$  sites to distinguish them from other edge-related metal sites with different coordination environments, such as 1) “edge”  $\{(\mu_3\text{-S})_2\text{Cd}(\mu\text{-SPh})_2\}$  sites in nanoclusters belonging to the  $T_n$  series; and 2) “edge-central”  $\{(\mu_4\text{-S})(\mu_3\text{-S})\text{Cd}(\mu\text{-SPh})_2\}$  sites in large nanoclusters belonging to the same  $C_n$  series (Table 4.7). The inner  $\{(\mu_4\text{-S})_4\text{Cd}\}$  metal site, not present in smaller frameworks, appears for the first time in **Cd17**.

The actual structure of **Cd17** contains distortions on several levels, from the distorted tetrahedral coordination environment for metal sites to the somewhat twisted shape of the anionic framework on the whole, which is reflected in its  $D_2$  point group of symmetry.<sup>22</sup> Such distortions chiefly originate from differentiation of Cd–( $\mu_4\text{-S}$ ) and Cd–( $\mu\text{-SPh}$ ) distances, and from intramolecular ligand interactions. As for the latter, each nanocluster face contains a  $\text{Cd}_3(\mu\text{-SPh}_{ax})_3$  ring in a chair conformation; in other words, there are three  $ax,ax$  pairs of interacting substituents on face. Considering the structural isomerism of supertetrahedral nanoclusters, the inorganic framework of **Cd17** has fully open clefts running without interruption along the full length of each edge.

According to X-ray crystallographic data, there are five symmetrically independent cadmium atoms in each **Cd17** nanocluster. Crystallographic inequivalence of three edge-near-vertex  $\{(\mu_4\text{-S})\text{Cd}(\mu\text{-SPh})_3\}$  sites at each of four vertices is induced by variations of Cd–S distances as well as S–Cd–S angles. Thus, the Cd–( $\mu_4\text{-S}$ ) bond lengths at the three different edge-near-vertex  $\{(\mu_4\text{-S})\text{Cd}(\mu\text{-SPh})_3\}$  sites are 2.513(5), 2.537(5) and 2.550(5) Å; the corresponding angles related with those bonds ( $\mu_4\text{-S}$ )–Cd–( $\mu\text{-SPh}_{eq}$ ) are 110.1(2), 110.8(2), and 107.9(2)°, respectively.<sup>22</sup> The local configuration of  $\mu\text{-SPh}$  ligands bonded to all three edge-near-vertex metal sites is identical (as each contains one  $ax,ax$  pair), thus a more detailed description of the metal sites is  $\{(\mu_4\text{-S})\text{Cd}(\mu\text{-SPh}_{eq})(\mu\text{-SPh}_{ax})_2\}$ . Considerable interaction of Ph substituents in  $ax,ax$  pair is reflected, for instance, in distortions from ideal tetrahedral angles at edge-near-vertex metal sites: ( $\mu\text{-$

$\text{SPh}_{ax}$ –Cd–( $\mu$ - $\text{SPh}_{ax}$ ) angles at these sites in **Cd17** are all large (116.0(2), 117.3(2), and 118.3(2) $^\circ$ ).<sup>22</sup>

In agreement with the X-ray crystallographic data, the  $^1\text{H}$ - $^{111}\text{Cd}$  VACP/MAS echo spectrum of **Cd17** shows five groups of resonances (labelled A-E on Figure 4.13); within some of these Cd17(A)-Cd17(E) groups, further resonance splitting and/or multiple resonances can also be discerned. The splitting of asymmetric resonances in groups Cd17(B), Cd17(C) and Cd17(D) becomes more pronounced when less line broadening is used for processing the spectrum, at the cost of lower S/N (Figure 4.13, upper vs. lower traces).

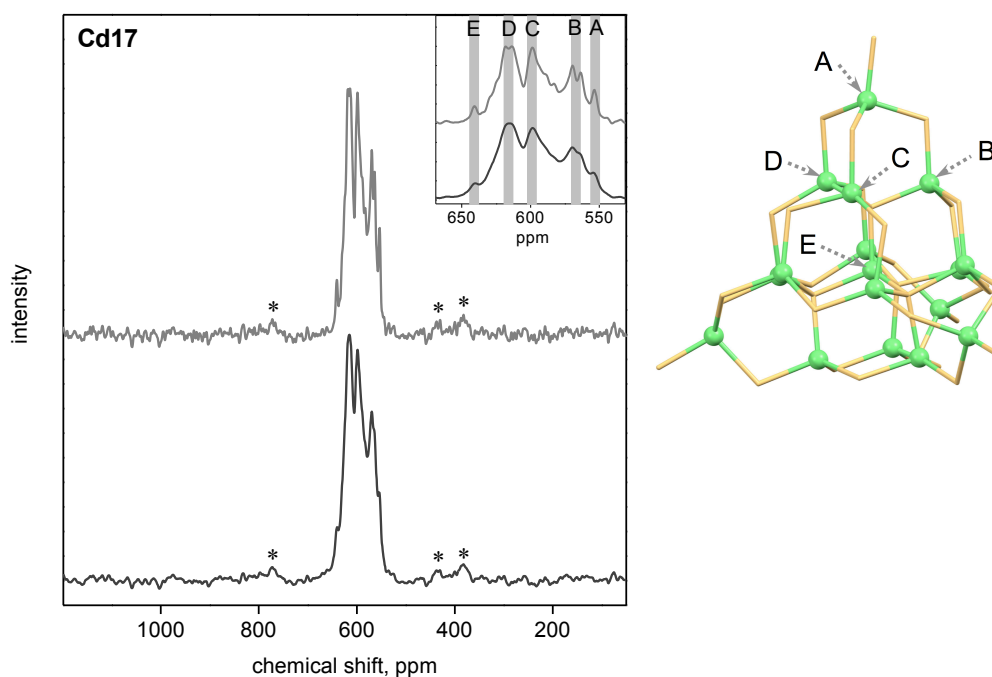


**Figure 4.13:**  $^1\text{H}$ - $^{111}\text{Cd}$  VACP/MAS echo SSNMR spectra **Cd17** (left), acquired at a spinning frequency of 15.5 kHz. The spectra represent the same data set processed using 200 and 500 Hz of line broadening (upper trace, grey, and lower trace, dark grey, respectively); normalized and shown with Y-axis offset. The insets show enlarged fragments of spectra along with proposed groups of resonances for **Cd17** (see text for details). The inorganic framework of **Cd17** (right): Cd atoms and bonds are shown as green balls and sticks, S atoms and bonds are shown as yellow-orange capped sticks, along with the proposed assignment of the resonances to five metal sites (see text for details).

Chemical shifts for the different resonances and resonance groups of **Cd17** along with the assignment to the cadmium sites with particular coordination environments are shown in Table 4.8. The resonance Cd17(A) at 553 ppm is assigned to  $\{(\mu\text{-SPh})_3\text{Cd}(\text{SPh})\}$  sites at the four vertices of the tetrahedral nanocluster. The resonance from these sites in **Cd17** is remarkably shifted to lower frequencies in comparison with the resonance arising from corresponding sites in **Cd10** (553 vs. 615 ppm, respectively), which can be explained with different local geometry in the capping hexagonal vs. cubic cages. It was previously found that the differences in bond distances and angles of  $\leq 0.03 \text{ \AA}$  and  $\leq 10^\circ$  for particular metal sites are sufficient to induce cadmium chemical shift differences up to 82 ppm.<sup>32</sup> While comparing the metrical parameters of the vertex sites in **Cd17** vs. **Cd10**, Cd–(SPh) distances are longer (2.482(6) vs. 2.459(8) Å, respectively), average Cd–( $\mu$ -SPh) distances are shorter (2.556 vs. 2.566 Å, respectively); ( $\mu$ -SPh)–Cd–(SPh) angles vary more (from 102.8(2) to 115.6(2)° vs. 109.6(2) to 113.2(3)°, respectively), while ( $\mu$ -SPh)–Cd–( $\mu$ -SPh) angles vary less (from 108.3(2) to 111.0(2)° vs. 101.4(3) to 115.6(2)°, respectively).<sup>22,26</sup> The latter can be related with the difference in configuration of Ph substituents and associated interactions between the substituents in ( $\mu$ -SPh)–Cd–( $\mu$ -SPh) fragments of the vertex sites  $\{(\mu\text{-SPh})_3\text{Cd}(\text{SPh})\}$  in **Cd17** and **Cd10**. Indeed, for **Cd17** all three fragments have the same configuration, ( $\mu\text{-SPh}_{ax}$ )–Cd–( $\mu\text{-SPh}_{eq}$ ), and the angle values are relatively close. For **Cd10** the corresponding fragments are different, ( $\mu\text{-SPh}_{eq}$ )–Cd–( $\mu\text{-SPh}_{eq}$ ), ( $\mu\text{-SPh}_{ax}$ )–Cd–( $\mu\text{-SPh}_{eq}$ ) and ( $\mu\text{-SPh}_{ax}$ )–Cd–( $\mu\text{-SPh}_{ax}$ ), which is reflected in considerable difference of three ( $\mu$ -SPh)–Cd–( $\mu$ -SPh) angles. Another possible reason for the markedly different chemical shifts ( $\Delta = 62$  ppm) for  $\{(\mu\text{-SPh})_3\text{Cd}(\text{SPh})\}$  sites in **Cd17** vs. **Cd10** may be different effective charges on particular atoms in the *Cn* series vs. the *Tn* series.

The resonance Cd17(E) at 641 ppm is assigned to the single inner  $\{(\mu_4\text{-S})_4\text{Cd}\}$  site. At this site, the Cd–S bond distance is smaller in comparison with the Cd–S bond distance in bulk CdS (2.497(5) vs. 2.519 Å, respectively); S–Cd–S angles are slightly different from the tetrahedral angle, varying from 108.2(2) to 110.6(2)°.<sup>22</sup> These discrepancies can explain the shift to lower frequencies of the Cd17(E) resonance with respect to the one for cadmium in bulk CdS, 641 vs. 706 ppm,<sup>43</sup> respectively (see Table 4.9).

**Table 4.9:** Literature data on the chemical shifts for selected cadmium compounds, crystalline bulk materials, referenced to 0.1 M aqueous solution of  $\text{Cd}(\text{ClO}_4)_2$ .

	$\text{CdS}_{(s)}$	$\text{CdSe}_{(s)}$	$\text{CdO}_{(s)}$	$\text{CdTe}_{(s)}$	$\text{CdCl}_{2(s)}$	references value / conv. <sup>a</sup>
$\delta$ , ppm	687	–	394	–	–	[31] <sup>b</sup>
	687	545	414	278	206	[44]/[45]
	685	–	–	–	–	[46]/[47]
	706	558	–	295	–	[43]/[48]

<sup>a</sup> References are shown for particular compound chemical shift data and for the data used for chemical shift scale conversion (see Table 4.15 in Experimental Section 4.4).

<sup>b</sup> Chemical shift of 0.5 M aqueous  $\text{Cd}(\text{ClO}_4)_2$  was measured in the same work; scale conversion was done by setting it as 0 and reversing the signs of chemical shifts quoted.

The three groups of resonances Cd17(B), Cd17(C) and Cd17(D) at 569, 598 and 615 ppm, respectively, are assigned to three symmetrically inequivalent edge-near-vertex metal sites  $\{(\mu_4\text{-S})\text{Cd}(\mu\text{-SPh})_3\}$ . In this instance, further splitting of the resonance groups is unusual, and reasons for such splitting should be discussed separately. A possible reason for resonance splitting or the appearance of “extra” resonances is sample contamination. It was found previously based on results of mass spectrometry that even re-crystallized samples of **Cd17** may include a chlorine-containing impurity and actually represent a mixture of  $[\text{Me}_4\text{N}]_2[\text{S}_4\text{Cd}_{17}(\text{SPh})_{28}]$ ,  $[\text{Me}_4\text{N}]_2[\text{S}_4\text{Cd}_{17}\text{Cl}(\text{SPh})_{27}]$ , and  $[\text{Me}_4\text{N}]_2[\text{S}_4\text{Cd}_{17}\text{Cl}_2(\text{SPh})_{26}]$  in the ratio 100 : 31 : 3.<sup>49</sup> Nonetheless, such contamination seems unlikely to have occurred, since the presence of Cd–Cl bond in any cadmium sites should shift its resonance position substantially to lower frequencies (as the difference between chemical shifts of CdS and  $\text{CdCl}_2$  is  $\sim 500$  ppm,<sup>44</sup> see Table 4.9), which was never observed for our samples of **Cd17**. Any additional splitting of resonances within the group is highly unlikely due to  $J$  coupling: since  $^1\text{H}$ - $^{111}\text{Cd}$  VACP/MAS echo spectra are proton decoupled, no  $^{111}\text{Cd}$ - $^1\text{H}$   $J$  coupling is observed, and at the natural abundances of  $^{111}\text{Cd}$  and  $^{113}\text{Cd}$  (12.80 and 12.22%, respectively),<sup>29</sup> the probability of adjacent  $^{111}\text{Cd}$ - $^{111}\text{Cd}$  and  $^{111}\text{Cd}$ - $^{113}\text{Cd}$   $J$  coupling is too low to significantly influence spectral appearance.

It should be noted that a similar splitting of particular cadmium resonance by  $\sim 5$  ppm was observed previously for  $[\text{Cd}_{10}(\text{SCH}_2\text{CH}_2\text{OH})_{16}](\text{ClO}_4)_4$ ,<sup>31</sup> though lacunas in crystal

structure data for this compound (*e.g.*, inability to resolve perchlorate anions) did not allow correlation of Cd SSNMR resonance splitting to the details of the nanocluster packing into a superlattice. Further work, including additional X-ray crystallographic data for the structure of  $[\text{Cd}_{10}(\text{SCH}_2\text{CH}_2\text{OH})_{16}](\text{ClO}_4)_4 \cdot 8\text{H}_2\text{O}$  revealed a crystallographic inequivalence of the metal sites, correlated with hydrogen bonding involving the counterion  $\text{ClO}_4^-$ , co-crystallized solvent  $\text{H}_2\text{O}$  and hydroxyl groups of 2-mercaptoethanol ligands.<sup>32</sup>

In the case of **Cd17**, further splitting of resonances for each of three crystallographically inequivalent edge-near-vertex metal sites  $\{(\mu_4\text{-S})\text{Cd}(\mu\text{-SPh})_3\}$  (doublet for Cd17(B) with  $\Delta = 5$  ppm; quadruplet for both Cd17(C) and Cd17(D)) may also be related with some (weak) intermolecular interactions that act to remove crystallographic equivalence of the corresponding metal sites at the four vertices of the distorted tetrahedron (that is the inorganic framework of **Cd17**). A more detailed determination of the crystal structure of **Cd17** would be necessary to confirm this.

Using the number of metal sites having particular coordination environments from crystal structure data (see Table 4.7), it is possible to predict the idealized ratio between integrated intensities of different groups of resonances Cd17(A) : Cd17(B) : Cd17(C) : Cd17(D) : Cd17(E) as 4 : 4 : 4 : 4 : 1. Due to the very complex lineshape of  $^1\text{H}\text{-}^{111}\text{Cd}$  VACP/MAS echo SSNMR spectra of **Cd17**, multiple peak fitting cannot reliably deconvolute the separate resonances, thus quantitative integrated intensities remain elusive. The variations in the ratio of experimental versus expected intensities, such as the apparently inflated relative intensities for the Cd17(B), Cd17(C) and Cd17(D) groups of resonances, is likely related to the different efficiency of  $^1\text{H}\text{-}^{111}\text{Cd}$  cross polarization for metal sites with different coordination environment and different metal-proton proximities. This particularly applies to resonances Cd17(E) assigned to the inner  $\{(\mu_4\text{-S})_4\text{Cd}\}$  site, as that cadmium site has no protons in close proximity and thus will appear artificially weak in cross polarization spectra in comparison with resonances arising from any metal sites with a more proton-rich coordination environment. Another possible source of variation from the idealized intensity ratios may be related to the fact that for

nanoclusters  $\text{Cd}_x\text{S}_y(\text{SPh})_z$  the proton relaxation time ( $^1\text{H } T_1$ ) values are large<sup>26</sup> and spectra were acquired under conditions of incomplete relaxation.

As expected, based on the large number of chemically and crystallographically different cadmium sites in **Cd17** and the ensuing distribution of local environments about Cd, the static  $^1\text{H}$ - $^{111}\text{Cd}$  VACP echo SSNMR spectrum of **Cd17** reveals a broad resonance with a rather featureless lineshape (Figure 4.14).

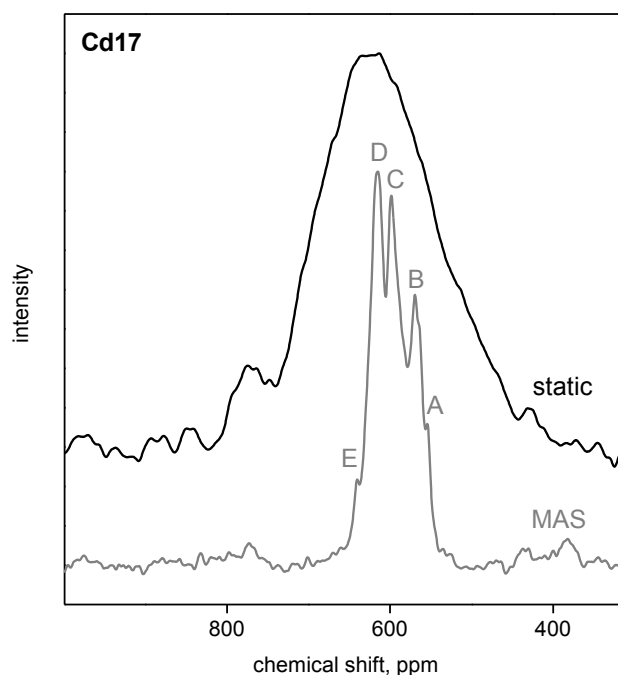


**Figure 4.14:** Static  $^1\text{H}$ - $^{111}\text{Cd}$  VACP echo SSNMR spectrum of **Cd17**. The spectrum was processed using 1000 Hz of line broadening and normalized. The corresponding  $^1\text{H}$ - $^{111}\text{Cd}$  VACP/MAS echo SSNMR spectrum of **Cd17** along with the proposed labeling of different groups of resonances is shown with Y-axis offset for comparison.

In larger members of the  $C_n$  nanocluster series, new types of cadmium coordination environments appear. An example is metal sites with  $\{(\mu_4\text{-S})(\mu_3\text{-S})\text{Cd}(\mu\text{-SPh})_2\}$  coordination that are found at the centre of edges, and are thus denoted “edge-central” sites (Table 4.7). These metal sites first appear in Cd32-type nanoclusters, represented, for instance, by neutral  $[\text{Cd}_{32}\text{S}_{14}(\text{SPh})_{36}(\text{dmf})_4]$  (selected crystal data are shown in Table 4.1)<sup>36</sup> and anionic  $[\text{Cd}_{32}\text{S}_{14}(\text{SPh})_{40}]^{4-}$  nanoclusters (CCDC-286488).<sup>23</sup> In the following series members, **Cd54** (Table 4.1) and predicted **Cd84**, the edge-central

coordination environment is the most commonly occurring one among all other types of metal environment (Table 4.7). Considering the other nanocluster series, the cadmium coordination environment in the edge-central sites  $\{(\mu_4\text{-S})(\mu_3\text{-S})\text{Cd}(\mu\text{-SPh})_2\}$  resembles the environment in the edge sites  $\{(\mu_3\text{-S})_2\text{Cd}(\mu\text{-SPh})_2\}$  in larger members of the  $T_n$  nanocluster series (*i.e.*, in **Cd10**).

Another type of cadmium coordination environment, face sites  $\{(\mu_4\text{-S})\text{Cd}(\mu_3\text{-S})_3\}$  (Table 4.7), also appears in large frameworks exclusively. The anionic nanocluster **Cd54** has such sites in the middle of each face.<sup>35</sup> Despite being surface sites – and thus more easily subjected to distortions of various origins – cadmium atoms with  $\{(\mu_4\text{-S})\text{Cd}(\mu_3\text{-S})_3\}$  coordination environments have no protons in close proximity and are expected to have similar CP efficiencies as the inner metal sites  $\{(\mu_4\text{-S})_4\text{Cd}\}$  in  $^1\text{H}\text{-}^{111}\text{Cd}$  CP experiments. Peculiarly, in some nanoclusters with 54 cadmium atoms, the coordination environment of the metal sites in the middle of the face can differ and in neutral  $[\text{Cd}_{54}\text{S}_{28}(\text{SPh})_{52}(\text{dmf})_4]$  (CCDC-767709) it is  $\{(\mu_4\text{-S})(\mu_3\text{-S})_2\text{Cd}(\mu_3\text{-SPh})\}$ .<sup>38</sup> Such sites contain triply bridging thiophenolate ( $\mu_3\text{-SPh}$ ) ligands in place of one sulfide ion ( $\mu_3\text{-S}$ ). The presence of such an unusual sulfur coordination mode ( $\mu_3\text{-SPh}$ ) at four faces decreases negative charge of the nanocluster, which resolves one of the problems that hampers the preparation of larger  $\text{M}_x\text{E}_y(\text{ER})_z$  frameworks – local and total charge balance. The overall negative charge of anionic supertetrahedral nanoclusters quickly increases with nanocluster size, making it increasingly difficult to achieve total charge balance and accomplish a successful crystallization. Another strategy to decrease negative charge includes replacing the four charged vertex  $\text{PhS}^-$  ligands with neutral ones. This results in the appearance of  $\{(\mu\text{-SPh})_3\text{CdL}\}$  vertex sites, where neutral ligand L can be  $\text{H}_2\text{O}$  or *dmf* molecules, such as in  $(\text{Me}_4\text{N})_4[\text{Cd}_{54}\text{S}_{32}(\text{SPh})_{48}(\text{H}_2\text{O})_4]$  (CCDC-286485) and **Cd54** (*i.e.*,  $(\text{Me}_4\text{N})_4[\text{Cd}_{54}\text{S}_{32}(\text{SPh})_{48}(\text{dmf})_4]$ ).<sup>23,35</sup>

Considering the structural isomerism of supertetrahedral nanoclusters, **Cd54**, as well as  $(\text{Me}_4\text{N})_4[\text{Cd}_{54}\text{S}_{32}(\text{SPh})_{48}(\text{H}_2\text{O})_4]$  and  $[\text{Cd}_{54}\text{S}_{28}(\text{SPh})_{52}(\text{dmf})_4]$ , is a  $C3,4$  isomer, *i.e.*, the hexagonal cages are rotated at all four vertexes. This contrasts with **Cd17**, which is a  $C1,0$  isomer, *i.e.*, none of hexagonal cages is rotated. In **Cd54** an open cleft is interrupted near vertices by cadmium atoms belonging to edge-near-vertex sites. This is the case

when structural isomerism changes the disposition of ( $\mu$ -SPh) ligands, in this way influencing ligand-ligand interactions and related distortions. Large nanoclusters like **Cd54** potentially have a huge number of configurational isomers (since the number of possible microstates for ( $\mu$ -SPh) is  $2^{48} \approx 2.8 \cdot 10^{14}$ ). In practice, even when prepared by different synthetic routes and crystallized from different solvents,  $[\text{Cd}_{54}\text{S}_{32}(\text{SPh})_{48}(\text{H}_2\text{O})_4]^{4-}$  and  $[\text{Cd}_{54}\text{S}_{28}(\text{SPh})_{52}(\text{dmf})_4]^{23,38}$  have an identical configuration of all 48 ( $\mu$ -SPh). In the solved structure of **Cd54** (*CCDC-1440110*), the ligand shell was found substantially disordered and thus only partially resolved. Meanwhile, the configuration of all distinguishable ( $\mu$ -SPh) ligands coincides with the configuration of corresponding ligands in  $[\text{Cd}_{54}\text{S}_{32}(\text{SPh})_{48}(\text{H}_2\text{O})_4]^{4-}$  and  $[\text{Cd}_{54}\text{S}_{28}(\text{SPh})_{52}(\text{dmf})_4]$ . Note that in this configurational isomer the distortions from tetrahedral coordination of metal atoms can be associated specifically with interaction of pairs of vicinal phenyl substituents in edge-near-vertex sites  $\{(\mu_4\text{-S})\text{Cd}(\mu\text{-SPh})_3\}$ .

In total there are five types of metal coordination environments in **Cd54**: vertex, edge-near-vertex, edge-central, face, and inner (Table 4.7). Note that predicted members of *C<sub>n</sub>* nanocluster series will contain the same five types of metal sites (assuming that the same trend for nanocluster stoichiometry persists); only the ratio between sites in each particular coordination environment would change.

According to X-ray crystallographic data, there are seven symmetrically independent cadmium atoms in both the  $(\text{Me}_4\text{N})_4[\text{Cd}_{54}\text{S}_{32}(\text{SPh})_{48}(\text{H}_2\text{O})_4]$  and  $[\text{Cd}_{54}\text{S}_{28}(\text{SPh})_{52}(\text{dmf})_4]$  (*CCDC-286485* and *767709*, respectively), with two crystallographically inequivalent groups of edge-central sites  $\{(\mu_4\text{-S})(\mu_3\text{-S})\text{Cd}(\mu\text{-SPh})_2\}$  (two and two per each cleft) and two groups of inner sites  $\{(\mu_4\text{-S})_4\text{Cd}\}$  (four and six per nanocluster). In **Cd54** there is no differentiation of edge-central sites, while two crystallographically inequivalent groups of inner sites are still present (*CCDC-1440110*). In this way, there are six symmetrically independent cadmium atoms in **Cd54**. Both groups of inner sites  $\{(\mu_4\text{-S})_4\text{Cd}\}$  have similar metrical parameters about cadmium, and these parameters are also relatively close to the distances and angles for face sites  $\{(\mu_4\text{-S})\text{Cd}(\mu_3\text{-S})_3\}$ . Thus, angles S–Cd–S vary from 107.85(17) to 111.04(16)° and from 108.1(3) to 110.8(4)° for two groups of inner sites, while these angles range from 108.4(3) to 110.5(2)° for face sites.



It should be noted that assigning different  $^{111}\text{Cd}$  SSNMR resonances in spectra of **Cd54** to the metal sites with particular coordination environment relying on X-ray crystallographic data (*i.e.*, bond lengths and angles) involves a greater degree of uncertainty in comparison to assigning resonances in spectra of **Cd1-Cd17**. This is related to the re-arrangement of the superstructure of **Cd54** upon drying. For **Cd1-Cd17**, the dried samples retain both the long- and short-range order inherent to freshly prepared crystals, as confirmed by the similarity of simulated and measured PXRD patterns for the dried material. However, the removal of the crystallization solvent upon drying **Cd54** is accompanied by a substantial change in the long range order (*i.e.*, superlattice re-arrangement and decrease of its order), as evidenced by the difference of measured PXRD patterns for the fresh and dried material in both the low- and wide-angle regions. The short-range order is also expected to change to some extent. In particular, different mutual positions of the nanoclusters in the superlattice assume the different *inter*- and *intra*-molecular ligand-ligand interactions. Considering the metal coordination environment, such a difference in ligand-ligand interactions is related to changes of bond lengths and angles (and thus the level of distortion from idealized tetrahedral coordination), and the sites where cadmium is bonded with  $\text{SPh}^-$  ligands are most affected.

The following conjecture is used to assign the  $^{111}\text{Cd}$  SSNMR resonances in spectra of **Cd54**: the level of distortion from idealized tetrahedral coordination remains close in the fresh material and in the dried one. As a consequence, if site X was more distorted than site Y in the fresh material, then X will remain more distorted than Y upon drying.

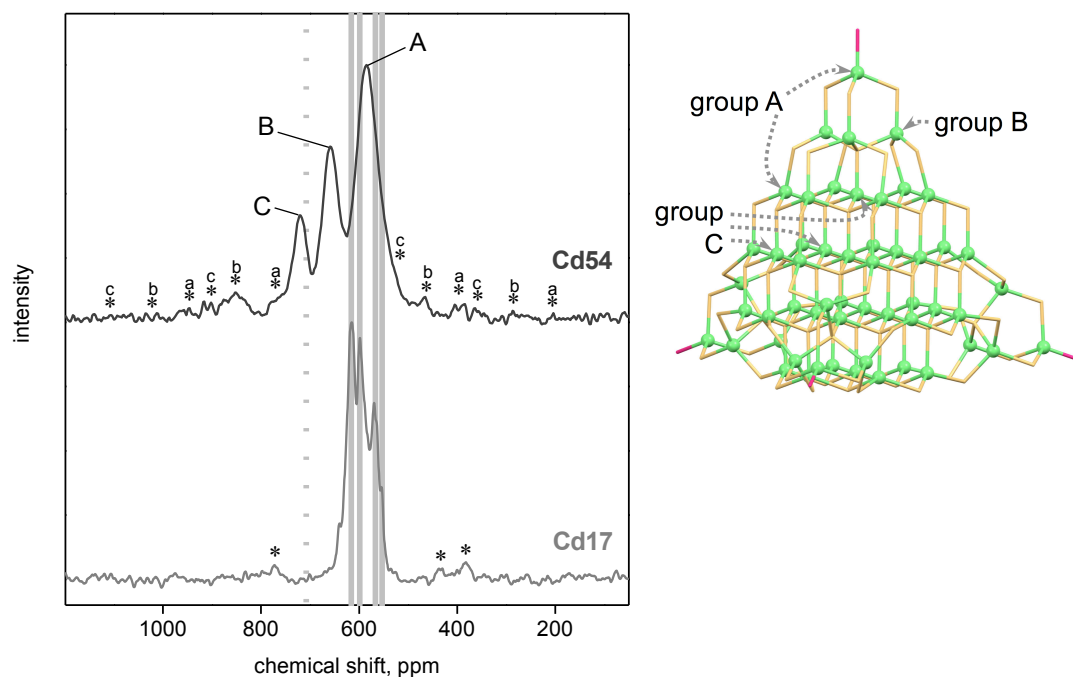


**Figure 4.15:**  $^1\text{H}$ - $^{111}\text{Cd}$  VACP/MAS echo SSNMR spectra of **Cd17** and **Cd54** (left), acquired at a spinning frequency of 15.5 kHz. The proposed groups of resonances from vertex and edge metal sites in **Cd17** are highlighted in solid light grey. The reported resonance position of bulk CdS at 706 ppm<sup>43</sup> is denoted with a dotted grey line. The spectra were processed using 500 Hz of line broadening. The spectra are normalized and shown with the Y-axis offset. The inorganic framework of **Cd54** (right): Cd atoms and bonds are shown as green balls and sticks, S atoms and bonds are shown as capped yellow-orange sticks, along with the proposed assignment of the groups of resonances (see text for details).

The  $^1\text{H}$ - $^{111}\text{Cd}$  VACP/MAS echo SSNMR spectrum of **Cd54** features three broad resonances or close groups of resonances, labelled A-C in the upper trace of Figure 4.15. Unlike smaller nanoclusters, *e.g.*, **Cd17**, no fine structure for the resonance groups Cd54(A)-Cd54(C) could be found, despite comparable line broadening used in processing the spectra. The presence of a small number of broad resonance groups in the spectrum of **Cd54** resembles those of some CdE nanoparticles.<sup>50–53</sup> Thus, two groups of resonances, assigned to “core” and “surface” cadmium sites, were observed for CdS and CdSe nanoparticles with hexagonal and cubic crystalline lattices, respectively, with oleate ligands on the surface. In both cases the average diameter of nanoparticles is  $\sim 4$  nm

according to electron microscopy.<sup>50,53</sup> The structure of many CdE nanoparticles can be described using the widely-accepted model  $\text{CdE}_{\text{core}}(\text{CdX}_2)_{\text{surface}}$ , where the crystalline CdE core is covered with a  $\text{CdX}_2$  shell, which is a labile layer of surface cadmium atoms bond to anionic ligands X (such as carboxylates).<sup>54</sup> The two close groups of cadmium resonances (*i.e.*, core and surface) fit this model well. For **Cd54**, it is possible that the observed groups of resonances also contain signals from cadmium sites with a different coordination environment. In contrast to the previously reported spectra of CdE nanoparticles, assigning the three groups of cadmium resonances in **Cd54** nanocluster spectra requires that details of metal coordination environments are taken into account. Resonances groups Cd54(A)-Cd54(C) were deconvoluted; <sup>111</sup>Cd chemical shifts and width based on fits using Gaussian lineshape are summarized in Table 4.10. Note that shown standard errors characterize fitting rather than experimental uncertainty bounds for the measured resonance positions and widths.

**Table 4.10:** Chemical shifts and proposed assignment for different groups of resonances of **Cd54** and **CdS-1.9 nm** (referenced to 0.1 M aqueous solution of  $\text{Cd}(\text{ClO}_4)_2$ ).

Compound	group A			group B			group C		
	$\delta$ , ppm <sup>a</sup>	FWHM, ppm <sup>a</sup>	Int. <sup>b</sup>	$\delta$ , ppm <sup>a</sup>	FWHM, ppm <sup>a</sup>	Int. <sup>b</sup>	$\delta$ , ppm <sup>a</sup>	FWHM, ppm <sup>a</sup>	Int. <sup>b</sup>
	vertex $\{(\mu\text{-SPh})_3\text{CdOR}\}$ and edge-central sites $\{(\mu_4\text{-S})(\mu_3\text{-S})\text{Cd}(\mu\text{-SPh})_2\}$			edge-near-vertex $\{(\mu_4\text{-S})\text{Cd}(\mu\text{-SPh})_3\}$ sites			inner $\{(\mu_4\text{-S})_4\text{Cd}\}$ and face $\{(\mu_4\text{-S})\text{Cd}(\mu_3\text{-S})_3\}$ sites		
<b>Cd54</b>	583.2±0.3	58.6±0.7	1.00	658.8±0.3	37.8±0.8	0.44	720.0±0.5	34.2±1.3	0.22
<b>CdS-1.9nm</b>	587.4±0.2	47.8±0.6	1.00	656.3±0.3	43.9±1.0	0.64	712.3±0.2	33.5±0.6	0.58

<sup>a</sup> Shifts and widths based on multiple peak Gauss fitting.

<sup>b</sup> Relative integrated intensity, based on multiple peak Gauss fitting.

The broad, low-frequency resonance Cd54(A) with the maximum at ~583 ppm lies fairly close to the median (~590 ppm) of the area where resonances of all surface-related (*i.e.*, vertex and edge-near-vertex) sites of the smaller nanocluster **Cd17** were found (Figure 4.15). For thiolate-stabilized CdS nanoparticles with the calculated average diameter 2.0-3.5 nm based on PXRD data, a resonance assigned to surface cadmium sites was observed at 565 ppm.<sup>46</sup>

It can be suggested that resonances group A for **Cd54** also originates from some surface-related cadmium atoms, namely, vertex and edge-central sites (Table 4.7). Including vertex sites in this resonance group can be justified by the following reasoning. From X-ray crystallographic data, it can be seen that vertex sites in **Cd54** have local  $C_{3v}$  symmetry, which is relatively higher than the  $C_1$  symmetry of vertex sites in **Cd17**.<sup>22,35</sup> Consequently, the resonance of vertex sites in **Cd54** is expected to have larger chemical shift in comparison with the resonance of vertex sites in **Cd17** – in the similar way as it was discussed above for **Cd4** and **Cd10**. Simultaneously, vertex sites in **Cd54** reside in the coordination environment  $\{(\mu\text{-SPh})_3\text{CdOR}\}$  (where OR stands for  $\text{HCONMe}_2$  to stress the coordination of *dmf* ligand to metal *via* O). The influence of the nature of bonded atom on cadmium chemical shift can be followed on example of bulk crystalline CdS and CdO (Table 4.9): for the latter chemical shift is smaller by  $\sim 300$  ppm.<sup>31,44</sup> According to this, the presence of the Cd–O bond (along with three Cd–S) should result in smaller chemical shift for the vertex sites  $\{(\mu\text{-SPh})_3\text{CdOR}\}$  in **Cd54** in comparison with the vertex sites  $\{(\mu\text{-SPh})_3\text{Cd(SPh)}\}$  in **Cd17**, where cadmium is bonded with four sulfur atoms. Taking into account both circumstances, it is likely that the resonance of **Cd54** vertex sites appears in the 550-620 ppm region, thus contributing to Cd54(A). Then, coordination environment of the edge-central sites  $\{(\mu_4\text{-S})(\mu_3\text{-S})\text{Cd}(\mu\text{-SPh})_2\}$  in **Cd54** is similar to that of the edge sites  $\{(\mu_3\text{-S})_2\text{Cd}(\mu\text{-SPh})_2\}$  in **Cd10**. Since the edge-central sites in **Cd54** are relatively more distorted in comparison with the edge sites in **Cd10**,<sup>21,35</sup> the chemical shift of the edge-central sites in **Cd54** is expected to be smaller than 705 ppm, which is the value of chemical shift of the edge sites in **Cd10**. An additional argument for shifting the resonance of the edge-central sites in **Cd54** to lower frequencies may be that there are different effective charges on particular atoms in the  $C_n$  series nanoclusters vs. those in the  $T_n$  series. Finally, the resonance of edge-near-vertex sites of **Cd54** is related with group Cd54(B) rather than Cd54(A) (as is discussed below).

For CdE nanoparticles, the NMR signal of the surface cadmium atoms was often found to give rise to multiple prominent spinning sidebands, which reflects generally lower symmetry about surface sites and often higher magnitude of CSA associated with such sites.<sup>50,53</sup> A similar effect for nanoclusters can be illustrated by **Cd10**: the broader range of bonding distances and angles for edge sites, in comparison with vertex ones, is

reflected in higher magnitude of the CSAs for edge sites<sup>26</sup> and in more intense SSBs for resonance Cd10(B) in comparison with those for Cd10(A) (Figure 4.12). For **Cd54**, the intensity of the majority of SSBs is not significant and they are not easily distinguished from the background; an exception is some SSBs from Cd54(B) (Figure 4.15). According to X-ray crystallographic data, the edge-near-vertex sites of **Cd54** have the highest level of distortion from the idealized tetrahedral environment of cadmium atoms in comparison with any other metal sites in this nanocluster. Based on this, the resonances in the broad group B with the maximum at ~659 ppm can be assigned to the edge-near-vertex sites  $\{(\mu_4\text{-S})\text{Cd}(\mu\text{-SPh})_3\}$  of **Cd54**.

The broad high-frequency resonance Cd54(C) with maximum at ~720 ppm is suggested to originate from the cadmium atoms bonded with  $\text{S}^{2-}$  only. Such an assignment is consistent with cadmium resonance for bulk (hexagonal) CdS at 706 ppm<sup>43</sup> (Figure 4.15). Note that chemical shift for cadmium in bulk CdS was also reported by different authors as 687 ppm<sup>31,44</sup> and 685 ppm<sup>46</sup> (Table 4.9). The discrepancy between reported values is, most probably, due to the usage of different references and different resources for the conversion between different chemical shift scales for cadmium (see Table 4.15 in Experimental Section 4.4). For CdS nanoparticles, the broad resonance assigned to core cadmium sites was observed in different experiments at 703 ppm<sup>46</sup> or at 692 ppm<sup>50</sup> (Table 4.11). Note that position of cadmium resonances in nanoparticles was suggested to be size-dependent (see below). In Cd SSNMR spectra of CdS nanoparticles the observed peak width (50-60 ppm) was explained by the presence of a distribution of metal sites with slightly different coordination environments or/and by the presence of the distribution in particle size.<sup>46,50</sup> Unlike for CdS nanoparticles, two particular types of cadmium coordination environment, where a metal has four sulfide neighbours, are known in **Cd54**, viz. the inner  $\{(\mu_4\text{-S})_4\text{Cd}\}$  and the face  $\{(\mu_4\text{-S})\text{Cd}(\mu_3\text{-S})_3\}$  sites (Table 4.7). The two groups of crystallographically inequivalent inner sites and face sites in **Cd54** have relatively close metrical parameters; consequently, all three can contribute to the resonances group C. Low intensity of SSBs for group C of **Cd54** is consistent with a relatively more symmetric environment expected for these sites.

**Table 4.11:** Literature data on the chemical shifts for resonances from different cadmium sites in CdS nanoparticles; assignment of resonances to surface (s) or core (c) sites is shown in round brackets (if available). Referenced to 0.1 M aqueous solution of Cd(ClO<sub>4</sub>)<sub>2</sub>.

size; surface ligands	$\delta$ , ppm				references value / conv. <sup>a</sup>
N/A; thiophenolate	477	572	643	719	[38]/[45]
2.0-3.5 nm from PXRD; thiophenolate	–	565 (s)	~640	703 (c)	[46]/[47]
~2.7 nm from UV-Vis; (~4 nm from TEM) oleate	–	371 (s)	–	692 (c)	[50]/[48]
~2.9 nm from UV-Vis; oleate	–	~350- 370 (s)	–	708 (c)	[50]/[48]

<sup>a</sup> References are shown for particular compound chemical shift data and for the data used for chemical shift scale conversion (see Table 4.15 in Experimental Section 4.4).

It was reported previously that for some CdE nanoparticles the resonance assigned to core cadmium sites shows < 25 ppm discrepancy with the cadmium resonance for bulk crystalline CdE.<sup>43,46,50</sup> Typically, the resonance for nanoparticles was found shifted to higher frequencies with respect to that for corresponding bulk material.<sup>43,46</sup> A similar effect was also observed for **Cd54**, where the chemical shift of resonance group C (with maximum at ~720 ppm from the peak fitting) is larger than any reported chemical shift for bulk CdS (Table 4.9). It should be noted that available literature values for chemical shifts of bulk CdS characterize the hexagonal crystalline lattice,<sup>31,43,44,46</sup> while the environment of the inner  $\{(\mu_4\text{-S})_4\text{Cd}\}$  and the face  $\{(\mu_4\text{-S})\text{Cd}(\mu_3\text{-S})_3\}$  sites in **Cd54** corresponds to the cubic crystalline lattice. No literature data of chemical shift values for bulk cubic CdS were found. A single communication on <sup>113</sup>Cd SSNMR measurements for different phases of crystalline CdS,<sup>55</sup> where equal chemical shifts were reported for cadmium resonances in hexagonal and cubic CdS structures, contains no details, which puts under question the reliability of the conclusions made. Considering the related bulk crystalline lattices in ZnS, the chemical shift of <sup>67</sup>Zn in the cubic structure is greater than in hexagonal (381.9 and 364.5 ppm, respectively).<sup>56</sup> By analogy, it is possible that the resonance for cubic CdS also lies at higher frequencies (*i.e.*, 715-720 ppm) than the

resonance for hexagonal CdS, although chemical shift comparisons between such significantly different nuclei (*i.e.*, spin 5/2 vs. 1/2 for  $^{67}\text{Zn}$  vs. both  $^{111}\text{Cd}$  and  $^{113}\text{Cd}$ , respectively) should be treated with an abundance of caution. Additional Cd SSNMR experiments will be necessary to confirm that the chemical shift of inner and core sites in **Cd54** is equal or close to the chemical shift of bulk cubic CdS.

The chemical shift for inner cadmium sites in nanocluster **Cd17** (641 ppm) is smaller in comparison with **Cd54** (~720 ppm), which is consistent with the supposition about the cadmium resonance shift to lower frequencies for smaller thiophenolate-capped CdS nanoparticles due to quantum size effect.<sup>46</sup> A similar effect was observed for oleate-capped CdS nanoparticles, where chemical shifts of 692 and 708 ppm were found for core cadmium sites in particles having average diameter ~2.7 and ~2.9 nm, respectively, based on calculations using UV-vis spectroscopy data.<sup>50</sup>

For **Cd54**, an experimental ratio between the integrated intensities of deconvoluted groups of resonances Cd54(A) : Cd54(B) : Cd54(C) is found to be 1 : 0.44 : 0.22 (Table 4.10). Corresponding SSBs were not taken into account in the integrated intensities of deconvoluted signals. The proposed assignment of cadmium sites to the three groups assumes that Cd54(A) contains contributions from 4 vertex and 24 edge-central sites; Cd54(B) – from 12 edge near vertex sites, and Cd54(C) – from 4 face and 10 inner sites. According to this, the theoretical ratio between integrated intensities is expected to be 1 : 0.43 : 0.5. Taking into account the different efficiency of  $^1\text{H}$ - $^{111}\text{Cd}$  cross polarization for different cadmium sites, the experimental and theoretical ratios are in good agreement.

Observation of the three distinct groups of resonances for **Cd54** is unusual, since either one or two broad cadmium resonances were typically found in SSNMR spectra of CdE nanoparticles (Table 4.11). Scarce examples of the spectra with more than two cadmium resonances include the report of Herron *at el.*, where two moderately broad resonances were accompanied by another extremely broad and low-intense resonance in the spectra of thiolate-stabilized CdS nanoparticles, having the calculated average diameter 2.0-3.5 nm based on PXRD data.<sup>46</sup> While the two distinct resonances (at 703 and 565 ppm)

were assigned to core and surface cadmium sites, the broad central resonance ( $\sim 640$  ppm from rough estimation) was proposed to originate 1) from the cadmium sites having mixed  $\text{SPh}^-/\text{S}^{2-}$  coordination (*i.e.*, surface sites), and/or 2) from the core sites  $\{(\mu_4\text{-S})_4\text{Cd}\}$  belonging to very small nanoparticles. The three resonances at 565,  $\sim 640$  and 703 ppm in Herron's work<sup>46</sup> are close to resonance groups A, B, and C (at 583, 659, and 720 ppm) for **Cd54**; unlike in Herron's work, all three resonances for **Cd54** are distinct and well resolved. Then, four broad overlapping resonances at 477, 572, 643, and 719 ppm were observed for the material " $\text{Cd}_{10}\text{S}_4(\text{SPh})_{12}$ ", obtained by thermolysis of **Cd10**.<sup>38</sup> This material was shown to represent a mixture of different  $\text{Cd}_x\text{S}_y(\text{SPh})_z$  nanoclusters and/or nanoparticles; from solutions of " $\text{Cd}_{10}\text{S}_4(\text{SPh})_{12}$ " in a strongly coordinating solvent neutral nanoclusters  $[\text{Cd}_{54}\text{S}_{28}(\text{SPh})_{52}(\text{L})_4]$  ( $\text{L} = \text{pyridine}$  or *dmf*) were crystallized (CCDC-767708, 767709). In Bendova's work<sup>38</sup> the resonance with the smallest chemical shift has no analogy in our work, while other three resonances are very close to groups A, B, and C for **Cd54**.

In the  $^1\text{H}$ - $^{111}\text{Cd}$  VACP/MAS echo SSNMR spectrum of **CdS-1.9 nm** three groups of resonances were also found (Figure 4.16). Changing the spinning frequency caused only shifts of SSBs (Figure 4.16, upper vs. lower traces). It can be seen that at lower spinning frequency, 11.0 kHz, the high and low-frequency isotropic signals contain contribution from each other's SSBs, which slightly broadens the line. Besides this, the position and width of resonances groups for **CdS-1.9 nm** remains virtually the same, which argues in favour that the lineshape of each resonances group is mainly determined by the contribution of cadmium sites with slightly different coordination environments but not by the parameters of the experiment.



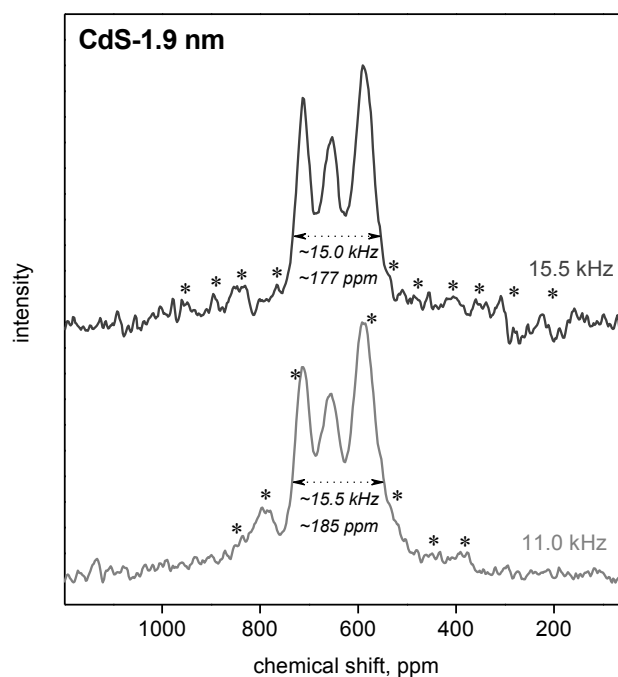


**Figure 4.16:**  $^1\text{H}$ - $^{111}\text{Cd}$  VACP/MAS echo SSNMR spectra of **CdS-1.9 nm** acquired at spinning frequencies 15.5 kHz (upper trace, dark grey) and 11.0 kHz (lower trace, grey). Spectra were processed using 500 Hz of line broadening, normalized and shown with Y-axis offset.

The three groups of resonances for **CdS-1.9 nm** are very similar to the three groups for **Cd54** (Figure 4.17, upper vs. lower traces). Signal deconvolution confirmed that the chemical shifts of the three resonance groups in **Cd54** and **CdS-1.9 nm** are also close, while the relative intensities of the signals are remarkably different (Table 4.10). Thus, an experimental ratio between integrated intensities of deconvoluted groups of resonances CdS-1.9 nm(A) : CdS-1.9 nm(B) : CdS-1.9 nm(C) was found to be 1 : 0.64 : 0.58 (Table 4.10).

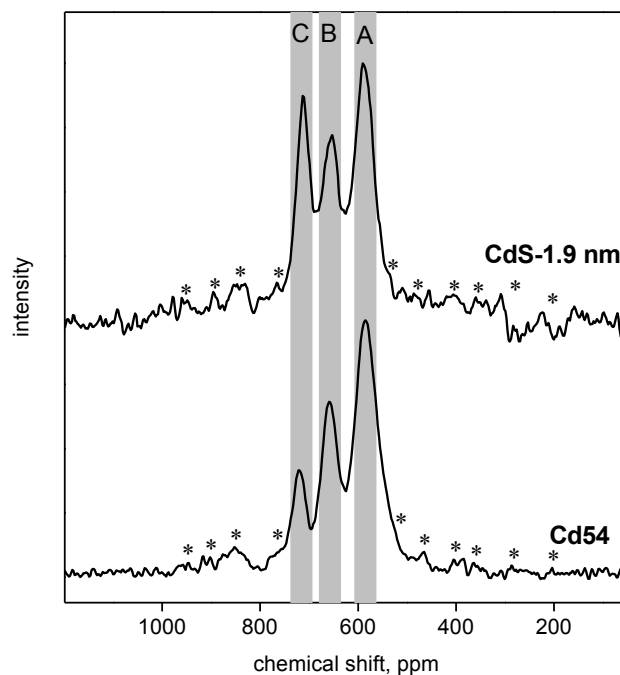


**Figure 4.17:**  $^1\text{H}$ - $^{111}\text{Cd}$  VACP/MAS echo SSNMR spectra of large nanoclusters **Cd54** and **CdS-1.9 nm** acquired at a spinning frequency of 15.5 kHz. The proposed groups of resonances are highlighted in light grey (see text for details). Spectra were processed using 500 Hz of line broadening. The spectra are normalized and shown with Y-axis offset.

Similarity in chemical shifts of the resonances groups for **Cd54** and **CdS-1.9 nm** can be related with the similarity of the cadmium sites in these two nanoclusters. Peculiarly, the most intense SSBs originate from the resonances group B in **CdS-1.9 nm** as well as in **Cd54**. Using similar reasoning as in the case of **Cd54**, the resonances group B in **CdS-1.9 nm** can be related with the most distorted cadmium coordination environment (probably, some analog of the edge-near-vertex sites). Since **CdS-1.9 nm** was proposed to be close in size and composition to the next  $C_n$  series member – the predicted nanocluster **Cd84** (Table 4.7) – the same types of metal sites are expected to contribute to groups A-C in the spectrum of **CdS-1.9 nm** (Table 4.10). The observed difference ( $\leq 8$  ppm) between the fitted Gaussian maximum positions of deconvoluted groups A-C in **Cd54** and **CdS-1.9 nm** (Table 4.10) can be rationalized based on the fact that the fraction of particular cadmium sites among all cadmium sites changes with the nanocluster size

(Table 4.7). For instance, in **Cd54** there are 4 face and 10 inner sites contributing to group C; while in **Cd84** there expected to be 12 face and 20 inner sites.

Using the expected numbers of metal sites (having particular coordination environment) for **Cd84** (Table 4.7), theoretical ratio between integrated intensities is calculated as  $40 : 12 : 32 = 1 : 0.3 : 0.8$ . The larger discrepancy with the experimental ratio in comparison with **Cd54** can be explained by the larger fraction of the sites where cadmium bonded with  $S^{2-}$  only (*i.e.*, has no protons in close proximity), thus having smaller CP efficiency in  $^1H-^{111}Cd$  CP experiments, in **CdS-1.9 nm** vs. **Cd54**.

Inspection of  $^1H-^{111}Cd$  VACP/MAS echo SSNMR spectra of **Cd54** and **CdS-1.9 nm**, acquired at different contact times, reveals that the relative intensity of resonances group C decreases relatively more in comparison to the other groups when shorter CP contact times were used (Figure 4.18). This effect is more obvious in the case of **CdS-1.9 nm**, while for **Cd54** it is partially masked by noise. For **CdS-1.9 nm** it is also apparent that the relative intensity of the groups A and B changes in such a way that the intensity decay for the group A is larger than for the group B. If we assume the distance to protons and the number of protons in close proximity are the only two factors influencing the CP efficiency of different cadmium sites, then the degree of intensity decay when shorter CP contact times are used for cadmium sites in **Cd84** and **Cd54** is expected to change in the following order: vertex  $\{(\mu-SPh)_3CdL\}$  sites < edge-near-vertex  $\{(\mu_4-S)Cd(\mu-SPh)_3\}$  sites < edge-central  $\{(\mu_4-S)(\mu_3-S)Cd(\mu-SPh)_2\}$  sites < inner  $\{(\mu_4-S)_4Cd\}$  and face  $\{(\mu_4-S)Cd(\mu_3-S)_3\}$  sites. This corresponds very well with the experimental order of the relative intensity decrease observed for **CdS-1.9 nm** (and partially **Cd54**): group B < group A < group C. For group A, the observed decrease of the relative intensity can be explained by the fact that the sites that mainly contribute to this group are the most abundant edge-central sites.

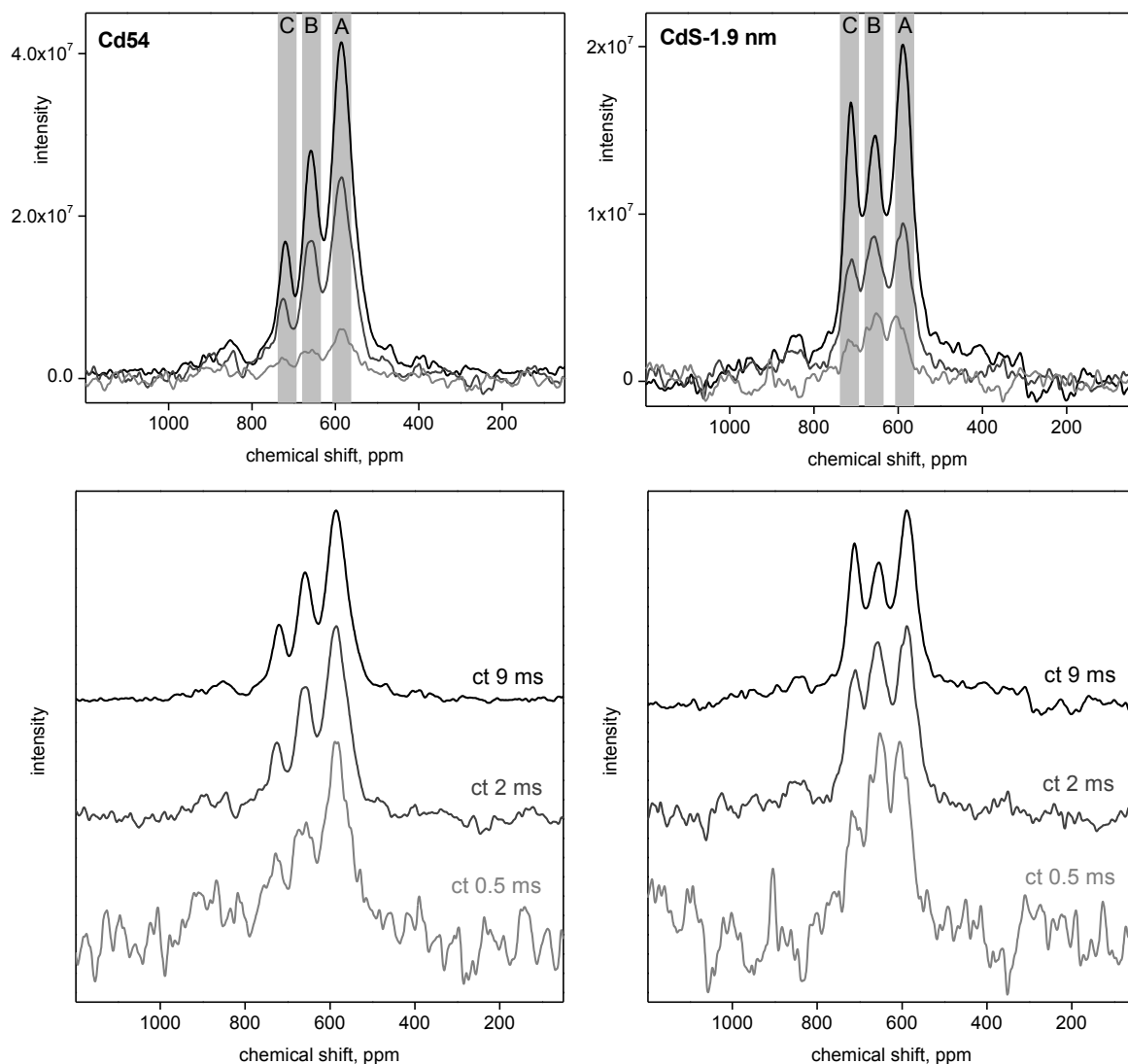


**Figure 4.18:**  $^1\text{H}$ - $^{111}\text{Cd}$  VACP/MAS echo SSNMR spectra of **Cd54** (left) and **CdS-1.9 nm** (right) acquired at a spinning frequency of 15.5 kHz and  $^1\text{H}$ - $^{111}\text{Cd}$  CP contact times of 9, 2, and 0.5 ms (black, dark grey, and grey traces, respectively). The spectra are superimposed in the two upper figures; normalized and Y-axis offset spectra are shown at the lower figures for convenient comparison. All spectra were processed using 1000 Hz of line broadening to increase the S/N ratio. In the upper right graph, the spectrum for **CdS-1.9 nm** at a contact time 9 ms, obtained with a much larger number of scans ( $\sim 50,000$  vs.  $\sim 15,000$ ), was scaled with a coefficient 0.5.

Static  $^1\text{H}$ - $^{111}\text{Cd}$  VACP echo SSNMR spectra of **Cd54** and **CdS-1.9 nm** show that both nanoclusters give rise to a signal of comparable width, while the lineshape is quite

different (Figure 4.19). The obtained spectra may be interpreted in such a way that the cadmium sites with the similar parameters contribute to the static spectra, but the ratio between such sites is different for **Cd54** and **CdS-1.9 nm**. Quantitative analysis of the static spectra is virtually impossible due to the large number of different cadmium sites presumably having a distribution of very different CSA values.

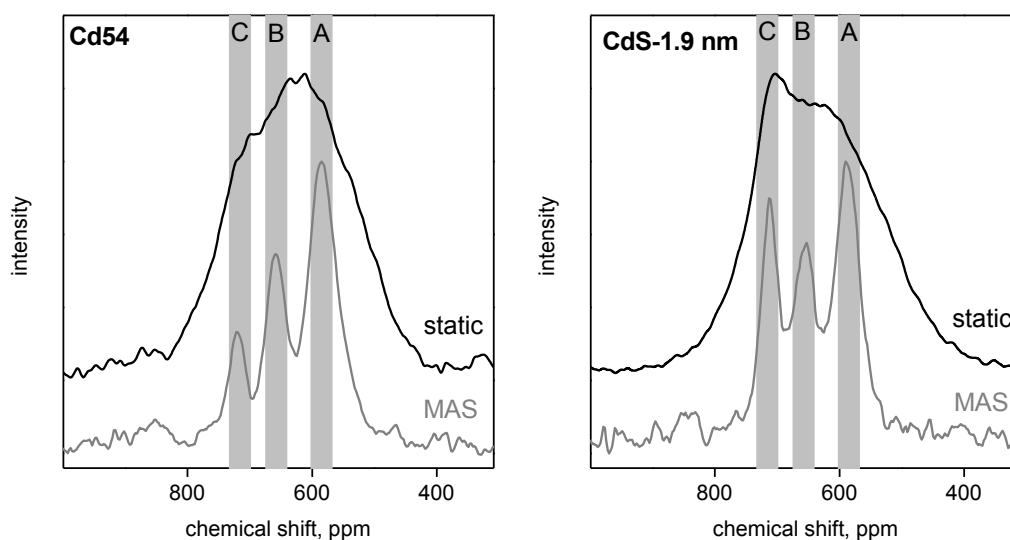


**Figure 4.19:** Static  $^1\text{H}$ - $^{111}\text{Cd}$  VACP echo SSNMR spectra of **Cd54** (left) and **CdS-1.9 nm** (right). Spectra were processed using 1000 Hz of line broadening and normalized. Corresponding  $^1\text{H}$ - $^{111}\text{Cd}$  VACP/MAS echo SSNMR spectra of **Cd54** and **CdS-1.9 nm** are shown with Y-axis offset for comparison. Isotropic chemical shift regions for the proposed groups of resonances for **Cd54** and **CdS-1.9 nm** are highlighted in light grey.

### 4.3 Conclusions

Analysis of  $^{111}\text{Cd}$  SSNMR spectra of the series of molecular cadmium thiophenolate complexes and tetrahedral nanoclusters with thiophenolate ligand shell in conjunction with X-ray crystallographic data allowed for assigning individual resonances or resonance groups to particular types of cadmium sites, having chemically and/or crystallographically different coordination environments.

For large frameworks, such as  $[\text{Cd}_{54}\text{S}_{32}(\text{SPh})_{48}(\text{dmf})_4]^{4-}$ , cadmium resonances were found to form three groups. This result is unusual, since for related systems with size polydispersity and composition variations, such as CdS or CdSe nanoparticles protected with an organic

ligand shell, typically only two groups of resonances were observed. For nanoparticles, these two groups of resonances were assigned to “core” and “surface” types of cadmium sites. In contrast, in order to assign all three of the resonance groups for  $[\text{Cd}_{54}\text{S}_{32}(\text{SPh})_{48}(\text{dmf})_4]^{4-}$  details of the metal coordination environment have to be taken into account instead of a simple core or surface assignment.

In addition, consideration of the degree of distortion from the idealized tetrahedral coordination was found to be very useful for assigning resonances in  $^{111}\text{Cd}$  SSNMR spectra of the examined cadmium thiophenolate complexes and nanoclusters. For large frameworks, correlating SSNMR and X-ray data requires additional suppositions to be made, because substantial structure re-arrangement upon drying was found for  $[\text{Cd}_{54}\text{S}_{32}(\text{SPh})_{48}(\text{dmf})_4]^{4-}$ . Results for  $[\text{Cd}_{54}\text{S}_{32}(\text{SPh})_{48}(\text{dmf})_4]^{4-}$  provide referencing data for the interpretation of the spectra of similar nanoclusters and nanoparticles, having comparable or larger size.

## 4.4 Experimental Section

### 4.4.1 Syntheses

All synthetic and handling procedures were carried out under an atmosphere of high-purity dried nitrogen using standard double manifold Schlenk line techniques and a MBraun Labmaster 130 glovebox.

**Cd1** was synthesized by a slight modification of the published procedure:<sup>21</sup> the synthesis was done on a larger scale, and the amount of methanol used to dissolve  $\text{Me}_4\text{NCl}$  was two times smaller in order to facilitate product crystallization. Product purification was achieved by recrystallization from a saturated solution in boiling acetonitrile; the isolated products were dried under vacuum for at least 2 h before being used for any characterization method.

**Cd4**, **Cd10**, **Cd17** were synthesized according to published procedures<sup>21,22</sup> but in larger scale; all isolated products were dried under vacuum for at least 2 h before being used for any characterization method.

**Cd54** and **CdS-1.9 nm** were synthesized as described in Chapter 2 (denoted there as materials **2** and **1**, respectively); products were either isolated and dried under vacuum for at least 2 h or used as freshly-prepared crystals (for PXRD, see below).

#### 4.4.2 Characterization

Powder X-ray diffraction (PXRD) patterns of the samples were obtained using a Rigaku Rotaflex RU-200 BVH rotating-anode X-ray diffractometer with a Co K $\alpha$  ( $\lambda = 1.79026$  Å) radiation. The X-ray generator (Rigaku Rotaflex RTP 300 RC) was operated at 45 kV and 160 mA, with monochromation being achieved using a curved crystal, diffracted beam, and graphite monochromator. The normal scan rate of  $10^\circ$   $2\theta$ /min for the instrument is equivalent to  $0.5^\circ$  on conventional diffractometers. X-rays were collimated using  $1^\circ$  divergent and scatter slits and a 0.15 mm receiving slit. The samples were placed on a standard glass holder and measured from  $2$  to  $82^\circ$   $2\theta$  with a scan rate of  $2^\circ$   $2\theta$ /min and a sampling interval of  $0.02^\circ$ . Low-angle parts (from  $2$  to  $12$ - $18^\circ$   $2\theta$ ) were additionally measured with a scan rate of  $0.5^\circ$   $2\theta$ /min and a sampling interval of  $0.01^\circ$ .

Two different sample preparation procedures were applied while obtaining PXRD patterns of 1) dried and 2) fresh materials. Dried samples were ground with a mortar and pestle to fine powders, then were pressed to pack in the holder with a workstation ionizer on to diminish the influence of static electricity. For fresh sample preparation (performed under a nitrogen atmosphere in a glovebox), crystals with a small portion of the mother liquor were collected, combined with Paratone N oil and ground with a mortar and pestle to a very thick homogeneous suspension. A measured portion of such a suspension was placed into the holder and left to spread for at least 30 min to ensure proper levelling. Measured PXRD patterns for fresh materials were corrected for any oil contribution by subtracting a smoothed pattern (very broad low-intense peak at  $2\theta \sim 20^\circ$ ) obtained for the holder with oil only.

Simulated powder patterns (wavelength  $\lambda = 1.79026$  Å) were produced using the Mercury 3.7 (build RC1) program suite using single crystal X-ray data from Cambridge Crystallographic Data Centre.<sup>57-59</sup> Selected details of simulation are as follows: all reflections were assumed to have a symmetric pseudo-Voigt peak shape with a full

width half maximum of 0.1 degree  $2\theta$ ; no absorption is simulated; no background is included; no preferred orientation is included.

All SSNMR experiments were carried out on a Varian Infinity Plus wide-bore spectrometer operating at a magnetic field of 9.4 T. Samples were ground with a mortar and pestle, obtained fine powders were packed into 4 mm outer diameter zirconia rotors. A 4 mm HXY Varian/Chemagnetics triple-resonance MAS probe was doubly tuned to  $^1\text{H}$  ( $\nu_0 = 399.7$  MHz) and  $^{111}\text{Cd}$  ( $\nu_0 = 85.2$  MHz). Both static and magic angle spinning (MAS)  $^{111}\text{Cd}$  SSNMR experiments were conducted, and a spinning frequency of 15.5 kHz was used for MAS experiments if not stated otherwise. The SSNMR experimental conditions are summarized in Tables 4.12-4.14. In general, the variable amplitude cross polarization (VACP)<sup>60</sup> pulse sequence with two pulse phase modulated (TPPM)  $^1\text{H}$  decoupling was used for MAS acquisition of the metal thiophenolate complexes (**Cd1** and **Cd4**), while a VACP echo (or more simply, CP echo) pulse sequence with regular continuous-wave  $^1\text{H}$  decoupling was used for MAS acquisition of thiophenolate-capped clusters (**Cd10** and larger) due to rapid signal decay.  $^{111}\text{Cd}$  VACP echo experiments used an echo pulse sequence of the form  $\pi/2(^1\text{H})$  - contact time -  $\tau_1$  -  $\pi(^{111}\text{Cd})$  -  $\tau_2$ , typically with contact times of 9-10 ms, a  $^1\text{H}$   $90^\circ$  ( $\pi/2$ ) pulse length of 3.8  $\mu\text{s}$ , a  $^{111}\text{Cd}$   $180^\circ$  ( $\pi$ ) pulse length of 4.0  $\mu\text{s}$ , and rotor-synchronized interpulse delays of 64.62  $\mu\text{s}$  for  $\tau_1$  and 24.52  $\mu\text{s}$  for  $\tau_2$ . The number of scans acquired typically varied from  $\sim 5,000$  to  $\sim 50,000$  in order to achieve a satisfactory signal-to-noise ratio. The exception was **Cd1** spectra, which typically demanded much smaller acquisition numbers (Table 4.12) due to high sample crystallinity and narrow powder patterns. In a separate series of  $^1\text{H}$ - $^{111}\text{Cd}$  VACP/MAS echo experiments, the contact time for **Cd54** and **CdS-1.9 nm** was varied from 0.5 to 9.0 ms. Static experiments for all compounds were performed using the  $^1\text{H}$ - $^{111}\text{Cd}$  VACP echo pulse sequence with regular  $^1\text{H}$  decoupling. In both MAS and static experiments, a spectral width of 100 kHz was employed, along with a recycle delay (or pulse delay) of typically 5.0 s. All spectra were obtained at room temperature, and  $^{111}\text{Cd}$  chemical shifts were referenced to a 0.1 M aqueous solution of  $\text{Cd}(\text{ClO}_4)_2$  ( $\delta_{\text{iso}} = 0$  ppm) or powdered  $\text{Cd}(\text{NO}_3)_2 \cdot 4\text{H}_2\text{O}$  as a secondary reference ( $\delta_{\text{iso}} = -100$  ppm under MAS).<sup>48</sup> All NMR data were processed using the Nuts software by Acorn NMR, Inc.; line broadening of 200-1000 Hz (an exponential multiplication factor) was typically incorporated to enhance S/N. The least squares multiple



peak fitting of the spectra was carried out with area version of the Gaussian function using the Levenberg–Marquardt algorithm in OriginPro 9.1 software.

**Table 4.12:** Summary of conditions and parameters for  $^1\text{H}$ - $^{111}\text{Cd}$  VACP/MAS SSNMR experiments.\*

compound	Cd1	Cd4	Cd10	Cd17	Cd54	CdS- 1.9 nm	CdS- 1.9 nm
spinning speed, kHz	15.5	15.5	15.5	15.5	15.5	15.5	11.0
pulse sequence	VACP TPPM	VACP TPPM	VACP echo	VACP echo	VACP echo	VACP echo	VACP echo
number of scans	328	4914	16276	6792	14005	49658	12946
pl $90^\circ$ $^1\text{H}$ , $\mu\text{s}$	3.80	3.80	3.80	3.80	3.80	4.43	3.80
$\tau_1$ , $\mu\text{s}$	–	–	64.52	64.52	64.52	64.52	90.91
pl $180^\circ$ $^{111}\text{Cd}$ , $\mu\text{s}$	–	–	4.0	4.0	4.0	4.5	4.0
$\tau_2$ , $\mu\text{s}$	–	–	24.52	24.52	14.62	24.52	20.91
ct, ms	9	9	10	10	9	9	9
sw, kHz	100	100	100	100	100	100	100
rd, s	5.0	5.0	5.0	3.0	5.0	5.0	5.0

\*Abbreviations used in this and following tables: VACP, *variable amplitude cross polarization*; TPPM, *two pulse phase modulated decoupling*; pl, *pulse length*; ct,  $^1\text{H}$ - $^{111}\text{Cd}$  *cross-polarization contact time*; sw, *spectral width*; rd, *recycling delay between scans, calibrated for each sample*.

**Table 4.13:** Summary of conditions and parameters for static  $^1\text{H}$ - $^{111}\text{Cd}$  VACP echo SSNMR experiments.

compound	<b>Cd1</b>	<b>Cd4</b>	<b>Cd10</b>	<b>Cd17</b>	<b>Cd54</b>	<b>CdS-1.9 nm</b>
pulse sequence	VACP echo	VACP echo	VACP echo	VACP echo	VACP echo	VACP echo
number of scans	844	12120	18836	22310	15682	12108
pl $90^\circ$ $^1\text{H}$ , $\mu\text{s}$	3.80	3.80	3.80	3.80	4.43	3.80
$\tau_1$ , $\mu\text{s}$	40	40	40	40	40	40
pl $180^\circ$ $^{111}\text{Cd}$ , $\mu\text{s}$	4.0	4.0	4.0	4.0	4.0	4.0
$\tau_2$ , $\mu\text{s}$	20	20	20	20	20	20
ct, ms	9	9	9	10	9	9
sw, kHz	100	100	100	100	100	100
rd, s	5.0	5.0	5.0	3.0	5.0	5.0

**Table 4.14:** Summary of conditions and parameters for  $^1\text{H}$ - $^{111}\text{Cd}$  VACP/MAS echo NMR experiments performed at a spinning frequency of 15.5 kHz using short contact times.

compound	<b>Cd54</b>	<b>Cd54</b>	<b>CdS-1.9 nm</b>	<b>CdS-1.9 nm</b>
pulse sequence	VACP echo	VACP echo	VACP echo	VACP echo
number of scans	16548	13447	14417	15814
pl $90^\circ$ $^1\text{H}$ , $\mu\text{s}$	4.43	4.43	4.43	4.43
$\tau_1$ , $\mu\text{s}$	64.52	64.52	64.52	64.52
pl $180^\circ$ $^{111}\text{Cd}$ , $\mu\text{s}$	4.0	4.0	4.0	4.0
$\tau_2$ , $\mu\text{s}$	24.52	24.52	24.52	24.52
ct, ms	2.0	0.5	2.0	0.5
sw, kHz	100	100	100	100
rd, s	5.0	5.0	5.0	5.0

The IUPAC recommended reference compound for  $^{111}\text{Cd}$  and  $^{113}\text{Cd}$  is  $\text{Me}_2\text{Cd}$ .<sup>29</sup> However, due to its high toxicity and special handling precautions needed, other inorganic reference

compounds are often used, both as solid or liquid materials and in aqueous solutions. For comparison of experimental results in this work with those given in different literature sources, all chemical shifts were referenced to a 0.1 M aqueous  $\text{Cd}(\text{ClO}_4)_2$  standard using the conversion data summarized in Table 4.15.

**Table 4.15:** Literature data on the chemical shifts used for conversion to the scale with 0.1 M aqueous solution of  $\text{Cd}(\text{ClO}_4)_2$  set as a standard ( $\delta = 0$ ).

	$\text{Me}_2\text{Cd}_{(\text{liq})}$	3 M aq $\text{CdSO}_4$	0.1 M aq $\text{Cd}(\text{ClO}_4)_2$	1 M aq $\text{Cd}(\text{NO}_3)_2$	$3\text{CdSO}_4 \cdot 8\text{H}_2\text{O}_{(\text{s})}$	$\text{Cd}(\text{NO}_3)_2 \cdot 4\text{H}_2\text{O}_{(\text{s})}$
$\delta$ , ppm	643	5	0	-17	-58 <sup>a</sup>	-100
reference	[47]	[45]		[45]	[48]	[48]
used for scale conversion in	[46]	[44]		[38]	[26]	[43,50]

<sup>a</sup> The chemical shift is shown for the low-frequency resonance of crystalline  $3\text{CdSO}_4 \cdot 8\text{H}_2\text{O}$ .

#### 4.5 References and Notes

- (1) Alivisatos, A. P. *J. Phys. Chem.* **1996**, *100* (31), 13226.
- (2) Nirmal, M.; Brus, L. *Acc. Chem. Res.* **1999**, *32* (5), 407.
- (3) Soloviev, V. N.; Eichhöfer, A.; Fenske, D.; Banin, U. *J. Am. Chem. Soc.* **2000**, *122* (11), 2673.
- (4) Soloviev, V. N.; Eichhöfer, A.; Fenske, D.; Banin, U. *J. Am. Chem. Soc.* **2001**, *123* (10), 2354.
- (5) Collier, C. P.; Vossmeier, T.; Heath, J. R. *Annu. Rev. Phys. Chem.* **1998**, *49*, 371.
- (6) Turk, T.; Resch, U.; Fox, M. A.; Vogler, A. *J. Phys. Chem.* **1992**, *96* (9), 3818.
- (7) Dehnen, S.; Eichhöfer, A.; Fenske, D. *Eur. J. Inorg. Chem.* **2002**, No. 2, 279.
- (8) Corrigan, J. F.; DeGroot, M. W. In *The chemistry of nanomaterials: synthesis, properties and applications* / C. N. R. Rao, A. Müller, A. K. Cheetham (eds.); Weinheim: Wiley-VCH; Chichester: John Wiley, 2004; Vol. 2, pp 418–451.
- (9) Corrigan, J. F.; Fuhr, O.; Fenske, D. *Adv. Mater.* **2009**, *21* (18), 1867.
- (10) Fuhr, O.; Dehnen, S.; Fenske, D. *Chem. Soc. Rev.* **2013**, *42* (4), 1871.
- (11) Müller, A.; Fenske, D.; Kögerler, P. *Curr. Opin. Solid State Mater. Sci.* **1999**, *4* (2), 141.
- (12) Dance, I. G. *Polyhedron* **1986**, *5* (5), 1037.
- (13) Krebs, B.; Henkel, G. *Angew. Chem.-Int. Ed. Engl.* **1991**, *30* (7), 769.
- (14) Dance, I.; Fisher, K. *Prog. Inorg. Chem. Vol 41* **1994**, *41*, 637.
- (15) Arnold, J. In *Progress in Inorganic Chemistry, Vol 43*; Karlin, K. D., Ed.; John Wiley & Sons Inc: Hoboken, 1995; Vol. 43, pp 353–417.
- (16) Bu, X.; Zheng, N.; Feng, P. *Chem.-Eur. J.* **2004**, *10* (14), 3356.
- (17) Feng, P.; Bu, X.; Zheng, N. *Acc. Chem. Res.* **2005**, *38* (4), 293.
- (18) Vaqueiro, P. *Dalton Trans.* **2010**, *39* (26), 5965.

- (19) Ueyama, N.; Sugawara, T.; Sasaki, K.; Nakamura, A.; Yamashita, S.; Wakatsuki, Y.; Yamazaki, H.; Yasuoka, N. *Inorg. Chem.* **1988**, *27* (4), 741.
- (20) Vittal, J. J.; Dean, P. A. W.; Payne, N. C. *Can. J. Chem.-Rev. Can. Chim.* **1992**, *70* (3), 792.
- (21) Dance, I. G.; Choy, A.; Scudder, M. L. *J. Am. Chem. Soc.* **1984**, *106* (21), 6285.
- (22) Lee, G. S. H.; Craig, D. C.; Ma, I.; Scudder, M. L.; Bailey, T. D.; Dance, I. G. *J. Am. Chem. Soc.* **1988**, *110* (14), 4863.
- (23) Zheng, N. F.; Bu, X. H.; Lu, H. W.; Zhang, Q. C.; Feng, P. Y. *J. Am. Chem. Soc.* **2005**, *127* (34), 11963.
- (24) Vittal, J. J. *Polyhedron* **1996**, *15* (10), 1585.
- (25) Choy, A.; Craig, D.; Dance, I.; Scudder, M. *J. Chem. Soc.-Chem. Commun.* **1982**, No. 21, 1246.
- (26) Lee, G. S. H.; Fisher, K. J.; Vassallo, A. M.; Hanna, J. V.; Dance, I. G. *Inorg. Chem.* **1993**, *32* (1), 66.
- (27) Summers, M. F. *Coord. Chem. Rev.* **1988**, *86*, 43.
- (28) Yesinowski, J. P. In *Solid State NMR*; Chan, J. C. C., Ed.; Springer-Verlag Berlin: Berlin, 2012; Vol. 306, pp 229–312.
- (29) Harris, R. K.; Becker, E. D.; De Menezes, S. M. C.; Goodfellow, R.; Granger, P. *Pure Appl. Chem.* **2001**, *73* (11), 1795.
- (30) *Transition metal nuclear magnetic resonance*; Pregosin, P. S., Ed.; Studies in inorganic chemistry; Elsevier: Amsterdam, Netherlands; New York, USA, 1991.
- (31) Murphy, P. D.; Stevens, W. C.; Cheung, T. T. P.; Lacelle, S.; Kurtz, D. M.; Gerstein, B. C. *J. Am. Chem. Soc.* **1981**, *103* (15), 4400.
- (32) Lacelle, S.; Stevens, W. C.; Kurtz, D. M.; Richardson, J. W.; Jacobson, R. A. *Inorg. Chem.* **1984**, *23* (7), 930.
- (33) Strickler, P. *J. Chem. Soc. -Chem. Commun.* **1969**, No. 12, 655.
- (34) Eckert, H. *Curr. Opin. Solid State Mater. Sci.* **1996**, *1* (4), 465.
- (35) Levchenko, T. I.; Kübel, C.; Wang, D.; Najafabadi, B. K.; Huang, Y.; Corrigan, J. F. *Chem. Mater.* **2015**, *27* (10), 3666.
- (36) Herron, N.; Calabrese, J.; Farneth, W.; Wang, Y. *Science* **1993**, *259* (5100), 1426.
- (37) Ingham, B. *Crystallogr. Rev.* **2015**, *21* (4), 229.
- (38) Bendova, M.; Puchberger, M.; Schubert, U. *Eur. J. Inorg. Chem.* **2010**, No. 21, 3299.
- (39) Matheis, K.; Eichhöfer, A.; Weigend, F.; Ehrler, O. T.; Hampe, O.; Kappes, M. M. *J. Phys. Chem. C* **2012**, *116* (25), 13800.
- (40) Wu, T.; Zhang, Q.; Hou, Y.; Wang, L.; Mao, C.; Zheng, S.-T.; Bu, X.; Feng, P. *J. Am. Chem. Soc.* **2013**, *135* (28), 10250.
- (41) Hagen, K. S.; Holm, R. H. *Inorg. Chem.* **1983**, *22* (21), 3171.
- (42) Note, that here lies a potential source of ambiguity for the notation  $ax,ax$ : since two faces share a common edge in a tetrahedron,  $ax,ax$  disposition of two vicinal substituents at the edge with respect to one face of the nanocluster automatically defines this pair as  $eq,eq$  with respect to the other face. We state that two vicinal substituents at the edge cadmium site are in  $ax,ax$  disposition with respect to that nanocluster face, where one of these substituents also belongs to  $ax,ax$  pair at the vertex cadmium site.

- (43) Ratcliffe, C. I.; Yu, K.; Ripmeester, J. A.; Zaman, M. B.; Badarau, C.; Singh, S. *Phys. Chem. Chem. Phys.* **2006**, *8* (30), 3510.
- (44) Nolle, A. *Z. Naturforschung Sect. - J. Phys. Sci.* **1978**, *33* (6), 666.
- (45) Kostelnik, R. J.; Bothner-By, A. A. *J. Magn. Reson.* **1974**, *14* (2), 141.
- (46) Herron, N.; Wang, Y.; Eckert, H. *J. Am. Chem. Soc.* **1990**, *112* (4), 1322.
- (47) Cardin, A. D.; Ellis, P. D.; Odom, J. D.; Howard, J. W. *J. Am. Chem. Soc.* **1975**, *97* (7), 1672.
- (48) Mennitt, P. G.; Shatlock, M. P.; Bartuska, V. J.; Maciel, G. E. *J. Phys. Chem.* **1981**, *85* (14), 2087.
- (49) Løver, T.; Henderson, W.; Bowmaker, G. A.; Seakins, J. M.; Cooney, R. P. *Inorg. Chem.* **1997**, *36* (17), 3711.
- (50) Li, M.; Ouyang, J.; Ratcliffe, C. I.; Pietri, L.; Wu, X.; Leek, D. M.; Moudrakovski, I.; Lin, Q.; Yang, B.; Yu, K. *Acs Nano* **2009**, *3* (12), 3832.
- (51) Wang, R.; Calvignanello, O.; Ratcliffe, C. I.; Wu, X.; Leek, D. M.; Zaman, M. B.; Kingston, D.; Ripmeester, J. A.; Yu, K. *J. Phys. Chem. C* **2009**, *113* (9), 3402.
- (52) Yu, K.; Ouyang, J.; Zaman, M. B.; Johnston, D.; Yan, F. J.; Li, G.; Ratcliffe, C. I.; Leek, D. M.; Wu, X.; Stupak, J.; Jakubek, Z.; Whitfiel, D. *J. Phys. Chem. C* **2009**, *113* (9), 3390.
- (53) Piveteau, L.; Ong, T.-C.; Rossini, A. J.; Emsley, L.; Coperet, C.; Kovalenko, M. V. *J. Am. Chem. Soc.* **2015**, *137* (43), 13964.
- (54) Boles, M. A.; Ling, D.; Hyeon, T.; Talapin, D. V. *Nat. Mater.* **2016**, *15* (2), 141.
- (55) Anderson, D. H.; Corll, J. A. *Bull. Am. Phys. Soc.* **1966**, *11*, 482.
- (56) Wu, G. *Chem. Phys. Lett.* **1998**, *298* (4–6), 375.
- (57) Bruno, I. J.; Cole, J. C.; Edgington, P. R.; Kessler, M.; Macrae, C. F.; McCabe, P.; Pearson, J.; Taylor, R. *Acta Crystallogr. Sect. B-Struct. Sci.* **2002**, *58*, 389.
- (58) Macrae, C. F.; Edgington, P. R.; McCabe, P.; Pidcock, E.; Shields, G. P.; Taylor, R.; Towler, M.; van De Streek, J. *J. Appl. Crystallogr.* **2006**, *39*, 453.
- (59) Macrae, C. F.; Bruno, I. J.; Chisholm, J. A.; Edgington, P. R.; McCabe, P.; Pidcock, E.; Rodriguez-Monge, L.; Taylor, R.; van de Streek, J.; Wood, P. A. *J. Appl. Crystallogr.* **2008**, *41*, 466.
- (60) Peersen, O. B.; Wu, X.; Kustanovich, I.; Smith, S. O. *J. Magn. Reson. A* **1993**, *104* (3), 334.

## Chapter 5

### Superstructures of Nanoscopic CdSe: Solvothermal Routes to a Superlattice of Large Nanoclusters and a Nanoporous Single Crystal

#### 5.1 Introduction

The assembly of nanoscale building blocks (*e.g.*, metallic or semiconductor nanoparticles) into ordered superstructures is a major goal of modern materials chemistry.<sup>1-5</sup> Exploiting the size-dependent quantum-confinement properties of nanoparticles, these superstructures can reach tens of micrometers in size, making them suitable for the creation of functional components for electronic and optoelectronic applications.<sup>6-9</sup>

Secondary structures can be built in a number of ways, depending, for instance, on the presence or absence of auxiliary linkers or the nature of the forces holding the superstructure together. Thus, uniform crystalline nanoparticles and nanoclusters stabilized by a surface passivating ligand shell can self-assemble into superlattices<sup>10</sup> held together by various non-covalent interactions and forces.<sup>11</sup> Among them, molecular crystals of monodisperse group 12-16 semiconductor nanoclusters stabilized by phenyl chalcogenolate ligands are well-ordered (cubic) superlattices formed *via* Coulomb or van der Waals interactions between neighboring nanoclusters. The largest structurally characterized examples of such nanoclusters are  $[\text{Cd}_{54}\text{Se}_{32}(\text{SPh})_{48}(\text{H}_2\text{O})_4]^{4-}$  and  $[\text{Cd}_{54}\text{S}_{28}(\text{SPh})_{52}(\text{dmf})_4]$ , containing water and N,N'-dimethylformamide (*dmf*) ligands along with  $\text{PhS}^-$ .<sup>12,13</sup> The connection between building blocks in superlattices is typically reversible, even with a relatively stronger cluster-cluster interaction, such as hydrogen bonding (*e.g.*, between  $[\text{Cd}_{32}\text{S}_{14}(\text{SCH}_2\text{CH}(\text{OH})\text{CH}_3)_{36}(\text{H}_2\text{O})_4]$  nanoclusters in a double-layer three-dimensional superstructure).<sup>14</sup> Thus, dissolving the crystals can disassemble superlattices without changing the core and ligand shells of individual frameworks.

Much stronger cluster-cluster interactions include the covalent attachment of inorganic frameworks without auxiliary linkers into one-, two- and three-dimensional superstructures. For crystalline faceted nanoscale constituents, direct covalent attachment is possible by vertex-sharing or face fusion. Thus, the chalcogenolate stabilizing ligands at the vertices of

metal chalcogenide nanoclusters can also act as bridging intercluster linkers between outer metal atoms, resulting in the formation of extended, ordered structures.<sup>15</sup> Examples of one-point cluster–cluster connections formed by vertex-sharing include  $[\text{Cd}_{17}\text{S}_4(\text{SPh})_{26}(\text{py})]$  nanoclusters connected in one-dimensional chains;<sup>13</sup> two-dimensional frameworks of six-member rings formed by  $[\text{Cd}_{17}\text{S}_4(\text{SPhMe-4})_{27}(\text{SH})]^{2-}$ ;<sup>16</sup> and  $[\text{Cd}_{17}\text{S}_4(\text{SCH}_2\text{CH}_2\text{OH})_{26}]$  crystallizing as a three-dimensional superstructure with the double diamond topology.<sup>17</sup>

In the case of face fusion, superstructure formation is often mediated by the spontaneous arrangement of adjacent crystalline primary building blocks sharing a common crystallographic orientation.<sup>18–21</sup> Next, new covalent bonds form, joining certain facets of crystalline particles and resulting in the irreversible assembly of superstructures with complex morphology and single crystal-like properties.<sup>22</sup> It has been proposed that, in many cases, superstructure formation by face fusion is enabled by adsorption–desorption equilibria in the stabilizing (organic) shell on primary building blocks.<sup>23</sup> Surfactants or macromolecules showing facet-specific adsorption may play a decisive role in triggering fusion and determining the geometry of the resulting superstructure by making certain crystalline facets reactive. This formation mechanism has been frequently observed and is well understood in the non-classical crystallization of metal chalcogenide one-dimensional superstructures (*i.e.*, nanowires or nanorods from pre-formed nanoparticles).<sup>24–27</sup> There are significantly fewer examples of two-dimensional superstructures formed through oriented attachment.<sup>28,29</sup>

Hybrid, covalently assembled superstructures, in which nanodimensional inorganic building blocks are joined by polydentate organic ligands, form a large, diverse family with a vast variety of structural types.<sup>30,31</sup> Of particular interest among recently reported superstructures are coordination polymers,<sup>32</sup> in which bi-, tri- or tetradentate N-containing (*e.g.*, pyridyl- or imidazole-based) ligands attached to vertices create ordered links between tetrahedral metal chalcogenide nanoclusters.<sup>33,34</sup> Thus, tetrahedral  $[\text{Cd}_{32}\text{S}_{14}(\text{SPh})_{36}\text{L}_{4/2}]$  are assembled by the flexible, bidentate ligand  $\text{L} = 4,4'$ -trimethylenedipyridine in either one-dimensional, doubly bridged chains<sup>35</sup> or two-dimensional superstructures with alternating singly and doubly bridged clusters in layers.<sup>36</sup>

The collective properties of nanocluster assemblies are partly inherited from their constituent cluster frameworks and partly arise from synergistic interactions between

superstructure components. Thus, emerging properties may be induced by the electronic, plasmonic and magnetic coupling between building blocks.<sup>37</sup>

Here, we report the preparation of two distinct regular superstructures using the same mononuclear cadmium selenophenolate precursor. First, a superlattice of monodisperse  $(\text{Me}_4\text{N})_4[\text{Cd}_{54}\text{Se}_{32}(\text{SePh})_{48}(\text{dmf})_4]$  nanoclusters (**6**) was crystallized as cubic crystals after solvothermal treatment at 200 °C in DMF. A second superstructure – porous CdSe single crystal (**7**) – was isolated as red hexagonal prisms among the products of the solvothermal treatment under similar conditions but in the presence of cetyltrimethylammonium bromide (CTAB). To illustrate the structures of both materials, the results of single crystal and powder X-ray diffraction, selected area electron diffraction (SAED) and electron microscopy characterization are discussed. Particular attention is paid to evaluation of the optical properties (including emission) of the two superstructures and their comparison with previously known systems. Crystallization by oriented attachment of nanoparticles is proposed as a possible formation mechanism for porous CdSe monocrystal hexagonal prisms.

## 5.2 Results and Discussion

Although cadmium chalcogenolates are among the most widely used of the single source precursors for the preparation of CdE (E = S, Se, Te) nanoparticles and molecular nanoclusters, only a few explored synthetic routes involved mononuclear  $[\text{Cd}(\text{EPh})_4]^{2-}$ .<sup>38</sup> In our experiments, heating solutions of colourless  $[\text{Me}_4\text{N}]_2[\text{Cd}(\text{SePh})_4]$  in DMF at 200 °C for 1 day results in a solution colour change to orange-yellow as solvothermal conversion of the precursor occurs with formation of polynuclear cadmium selenophenolate species. Visual observations were supported by UV–vis absorption spectra of the reaction solutions, showing the presence of intense excitonic absorption bands (see discussion below), which is evidence for the formation of monodisperse species of a particular size. Rapid crystallization occurs from these solutions after opening reaction autoclaves, yielding large (up to 0.5 mm in size), transparent, yellow, cubic crystals (**6**), which are typically found to be cracked to some extent. Characterization using single-crystal X-ray diffraction shows that **6** represents a cubic superlattice of monodisperse nanoclusters possessing a  $\text{Cd}_{54}\text{Se}_{80}$  core (Figure 5.1). This core is built up from a relatively large fragment of a regular cubic CdSe framework and four hexagonal CdSe cages in four corners (completing the shape of the tetrahedron) – a new



member of capped supertetrahedral cluster family, represented by previously reported  $[\text{Cd}_{17}\text{S}_4(\text{SPh})_{28}]^{2-}$  /  $[\text{Cd}_{17}\text{Se}_4(\text{SePh})_{28}]^{2-}$ ;  $[\text{Cd}_{32}\text{S}_{14}(\text{SPh})_{36}(\text{dmf})_4]$  /  $[\text{Cd}_{32}\text{Se}_{14}(\text{SePh})_{36}(\text{PPh}_3)_4]$ ; and  $\text{Cd}_{54}\text{S}_{28}(\text{SPh})_{52}(\text{dmf})_4$  /  $[\text{Cd}_{54}\text{Se}_{32}(\text{SPh})_{48}(\text{H}_2\text{O})_4]^{4-}$  with a similar build-up principle.<sup>12,13,39–42</sup> In the crystalline core of nanoclusters **6** the edge length of the tetrahedron is 2.17 nm (taking the center of the Cd–O bond as the vertex). The height of such a tetrahedron is 1.77 nm and the diameter of the sphere having the same volume as this tetrahedron (the equivalent spherical diameter) is 1.32 nm; both values can be used for comparison with nanoparticles of different shapes.<sup>43</sup> Molecular nanoclusters **6** form a superlattice in the space group  $P\bar{4}3m$  with a unit cell parameter 24.412(6) Å (see Appendix B), very close to the cell constant of previously reported  $[\text{Cd}_{54}\text{Se}_{32}(\text{SPh})_{48}(\text{H}_2\text{O})_4]^{4-}$  which contains a thiolate ligand shell (P23 and 24.0656(7) Å, respectively).<sup>12</sup> Substantial disorder of the surface organic ligands (which has been often observed in single-crystal structures based on large monodisperse CdS or CdSe nanoclusters; see, for instance, refs. 12,13,44) did not allow for full characterization of the stabilizing shell of **6** by single-crystal X-ray diffraction. However, a set of auxiliary analyses, including Raman spectroscopy, indicates  $\text{PhSe}^-$  as surface-stabilizing ligand (see discussion below). The distinct feature of the superlattice in **6** is the presence of large intercluster voids (reaching up to a half of unit cell volume), not containing any heavy atoms but only crystallization solvent molecules and/or charge-balancing species. A related structure with large voids was previously reported by Herron for the smaller nanocluster  $[\text{Cd}_{32}\text{S}_{14}(\text{SPh})_{36}(\text{dmf})_4]$ .<sup>41</sup>

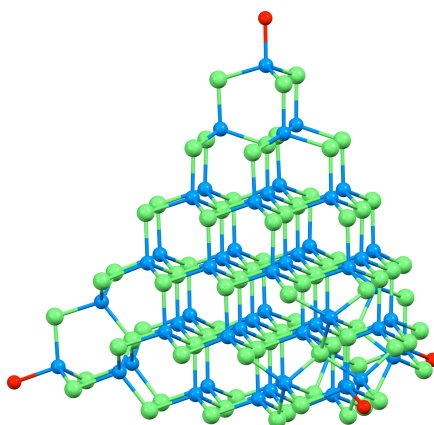


**Figure 5.1:**  $\text{Cd}_{54}\text{Se}_{80}$  core structure of **6**. Four O atoms at vertexes belong to *dmf* ligands. Cd sites are shown as blue; Se, green; O, red.

PXRD patterns for **6**, obtained for freshly prepared crystals (with some mother liquor) ground under paraffin oil, match the corresponding patterns calculated using single-crystal X-ray diffraction data (Figure 5.2, patterns *b* and *a*, respectively), confirming phase purity of the material. A small shift towards low angles ( $2\theta$  0.1-0.2°) of the reflections for measured diffraction patterns versus calculated ones was observed previously (see, for example, ref. 45) and can be explained by the effect of thermal expansion (PXRD measurements done at room temperature vs. 110 K for single crystal data collection for **6**). In the low-angle region of PXRD patterns, of note is a strong and sharp reflection at  $2\theta$  4.13°, together with much weaker and broader ones at 5.82, 7.11 and 8.25° (in accordance with primitive cubic unit cell). From the position of the first reflection, the corresponding interplanar spacing  $d$  of 2.48 nm was calculated using the Bragg equation. In the wide-angle region, sharp and quite intense peaks (matching with calculated values) are displayed together with very broad and unresolved ones.

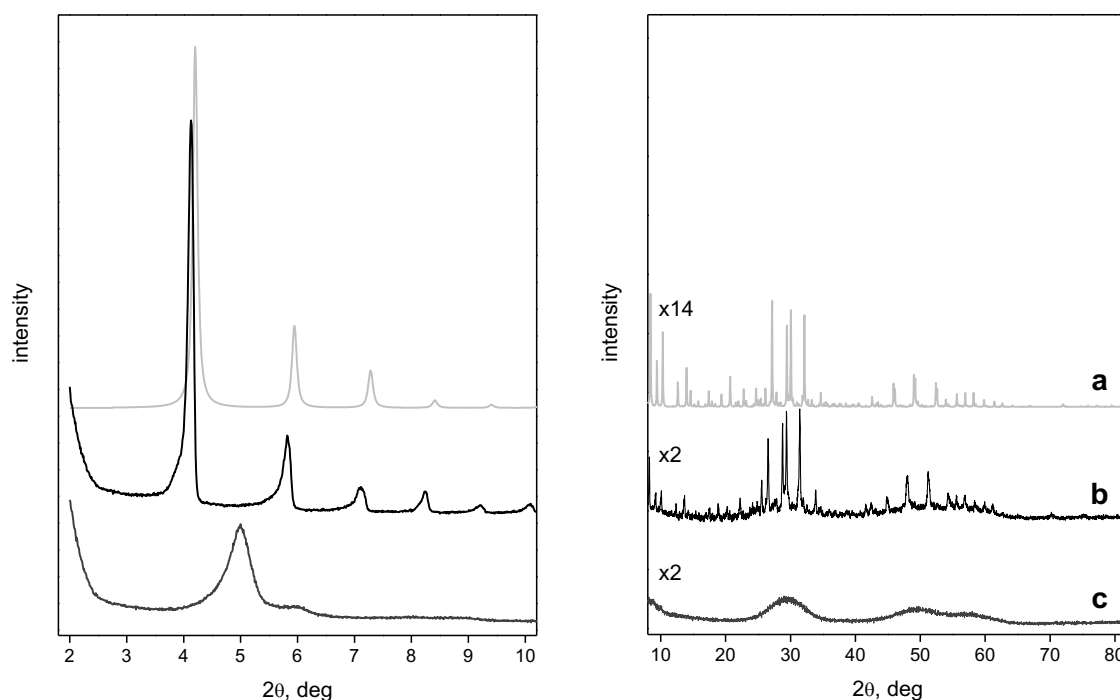


**Figure 5.2:** Measured (fresh material in paraffin oil, **b**; dried material, **c**) and simulated (**a**) powder X-ray diffraction patterns (Co K $\alpha$  radiation) for **6**: low-angle region, *left*; wide-angle region, *right*. Pattern **b** was corrected for paraffin oil background. Wide-angle region is scaled  $\times 2$  for patterns **b** and **c**, and  $\times 14$  for the pattern **a**; the data are shown with ordinate axis offset for clarity.

Upon isolation and vacuum-drying of the crystals of **6**, cracking progresses to noticeable fracturing into smaller pieces; this process may reflect substantial changes in the superlattice, most probably due to removal of crystallization solvent. First observed by the naked eye and optical microscopy (Figure 5.3, *left*), the cracking spans to the micrometer scale, with multiple defects in block fragments of the dried material **6** seen on its SEM images (Figure 5.3, *center*). Despite high electron beam sensitivity of **6**, TEM images were obtained for thin areas close to the crystal edge (wet preparation method), showing continuous domains of ordered superlattice of monodisperse nanoclusters (with the CdSe core appearing as dark regions and the PhSe<sup>-</sup> shell as lighter spaces) with a measurable lattice parameter 2.05 nm (Figure 5.3, *right*). This value for the dried material **6** is substantially smaller than a unit cell parameter 2.48 nm, found from powder X-ray diffraction data for solvated crystals of **6**.

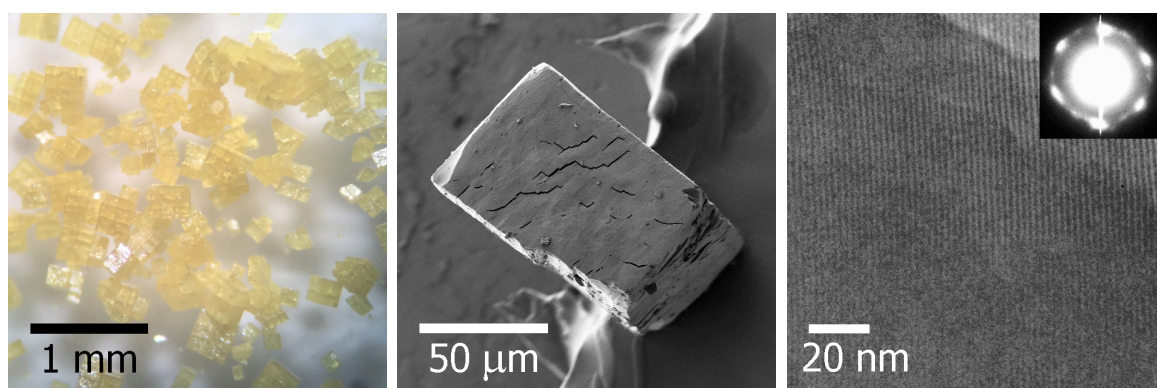


**Figure 5.3:** Microscopy images of dried **6**: optical micrograph, taken by a digital camera through the objective of an optical microscope (*left*), SEM (*center*) and TEM (*right*). *Inset*: low-angle SAED reflections of **6**.

Low-angle SAED reflections of **6** are in agreement with the presence of hexagonal superlattice with d-spacing close to that measured from TEM (Figure 5.3, *right, inset*). PXRD measurements on dried samples of **6** (see Figure 5.2, pattern *c*) confirmed formation of a new superlattice arrangement as well: from the position of the first low-angle reflection at  $2\theta$  5.00° a corresponding interplanar spacing  $d$  of 2.05 nm was calculated. Quantitative comparison of the peak intensities for fresh versus dried samples of **6** is complicated, as different sample preparation techniques were used for collecting the diffraction patterns. Overall however, the intensity of low-angle peaks for the dried

material **6** is noticeably lower and the peaks themselves are less sharp, reflecting a decrease of order upon superlattice rearrangement. Although the broad and low intensity nature of the weak, low-angle peaks (around  $\sim 6, 8$  and  $9^\circ$ ) complicates the analysis, (new) hexagonal superlattice can be suggested. In the wide-angle region of the PXRD patterns for dried **6** (Figure 5.2, pattern *c*) only broad peaks are found (as previously noted for dried  $[\text{Cd}_{32}\text{Se}_{14}(\text{SePh})_{36}(\text{PPh}_3)_4]$  superlattice);<sup>46</sup> these do nonetheless illustrate the relation of the internal structure of **6** with bulk cubic and hexagonal structures of CdSe (see below). The breadth of the wide-angle peaks in PXRD patterns for dried **6** (Figure 5.2, pattern *c*) is substantially different from PXRD patterns for freshly prepared crystals **6**, where both sharp and broad peaks appear (Figure 5.2, pattern *b*).

The broadening of peaks in a diffraction pattern of nano-scale crystalline materials is typically attributed to the effect of crystallite size (after accounting for other sources of broadening, *e.g.*, instrumental factors).<sup>47,48</sup> Indeed, calculations of the mean size of the crystalline domains using the Scherrer equation (average for the 220 and 311 reflections, assuming cubic CdSe cell is the main crystal structure motif for nanocluster core; shape factor  $K = 0.9$ ) for the dried material **6** give a value of 1.55 nm, which is close to the size determined from X-ray crystallography (*e.g.*, tetrahedron height and the equivalent spherical diameter are 1.77 and 1.32 nm, respectively). The absence of sharp reflections in the wide-angle region of PXRD patterns for the dried material **6** is consistent with the superlattice rearrangement with decrease in its long range order. We observed similar rearrangement for large (54 or more metal atoms) CdS clusters but not for smaller ones.<sup>49</sup>

X-ray diffraction (single crystal and powder) and electron microscopy provide concrete data for both the nature of the individual building blocks and their secondary structure in material **6**: monodisperse nanoclusters with  $\text{Cd}_{54}\text{Se}_{80}$  core form a primitive cubic superlattice. We observed that crystallization begins only after opening (to inert atmosphere) the autoclave in which the solvothermal synthesis was performed. This is unusual, because, typically, the main reaction product crystallizes either in the process of cooling reaction solutions to room temperature or immediately after the cooling is finished. It is possible that release of gaseous by-products from solvothermal conversion (*e.g.*,  $\text{NMe}_3$ ) upon opening the autoclave changes some properties of the solution and thus triggers crystallization of material **6**. Upon

isolation and drying, the ordered superlattice in **6** persists but its parameters are found to be substantially different from those of the freshly isolated material. Thus, rearrangement from cubic to hexagonal superlattice with a unit cell length decrease for 17% is observed probably due to removal of crystallization solvent. As far as we know, no such significant structure rearrangement was previously followed using PXRD for metal chalcogenide nanoclusters. The rearrangement is expected to be the distinctive feature of the superlattices of large nanoclusters, with high (cubic) symmetry and spacious intercluster voids.

Analysis of the stabilizing organic shells of the nanoparticles (including ligands identification and quantification) is often a complex task which requires a set of analytical techniques to be applied.<sup>50</sup> Raman spectroscopy allowed extending characterization of material **6** as observed bands can be assigned to the vibrations of bonds in both the Cd<sub>54</sub>Se<sub>80</sub> core and ligand shell. Thus, in the low-frequency region of Raman spectra of **6** a broad, medium-strong band at 201 cm<sup>-1</sup> (Figure 5.4) appears, close to the one of the most intense bands in bulk CdSe at 210 cm<sup>-1</sup> (the bulk longitudinal optical phonon mode)<sup>51</sup> and can be assigned to the stretching vibrations of interior Cd–Se bonds<sup>46</sup> in the Cd<sub>54</sub>Se<sub>80</sub> core. The broadness and asymmetry (a low-frequency shoulder at ~193 cm<sup>-1</sup>) of the peak can be related with a contribution from surface optical phonon mode or other confinement-induced effects.<sup>52,53</sup> The size dependence of the optical phonon frequency of nano-scale crystalline solids was previously described theoretically<sup>54,55</sup> and observed experimentally as a shift to lower wavelength with CdSe nanoparticle size decrease (see, for instance, refs. 56–59). Several strong bands in characteristic aromatic areas (*e.g.*, at 3052 cm<sup>-1</sup> due to aromatic C–H stretch vibrations and 1574 cm<sup>-1</sup> due to aromatic C–C stretch vibrations) as well as the medium-strong band at 666 cm<sup>-1</sup> due to Se–C stretch vibrations<sup>60</sup> are in agreement with PhSe<sup>-</sup> ligands present on the surface of nanoclusters **6**. Only weak bands (*e.g.*, at 2992 and 2940 cm<sup>-1</sup>) can be found in the area characteristic for aliphatic C–H stretching. The weak aliphatic signal may originate from residual lattice solvent (DMF) or coordinated *dmf* in the stabilizing shell of nanoclusters **6** at four apexes similar to previously reported cadmium sulfide nanoclusters [Cd<sub>32</sub>S<sub>14</sub>(SPh)<sub>36</sub>(*dmf*)<sub>4</sub>] and [Cd<sub>54</sub>S<sub>28</sub>(SPh)<sub>52</sub>(*dmf*)<sub>4</sub>].<sup>13,41</sup> Also, charge-balancing species (*e.g.*, [Me<sub>4</sub>N]<sup>+</sup>) may be present in crystalline packing of anionic nanoclusters to achieve overall neutral system, as it was reported for [Cd<sub>54</sub>Se<sub>32</sub>(SPh)<sub>48</sub>(H<sub>2</sub>O)<sub>4</sub>]<sup>4-</sup>.<sup>12</sup>

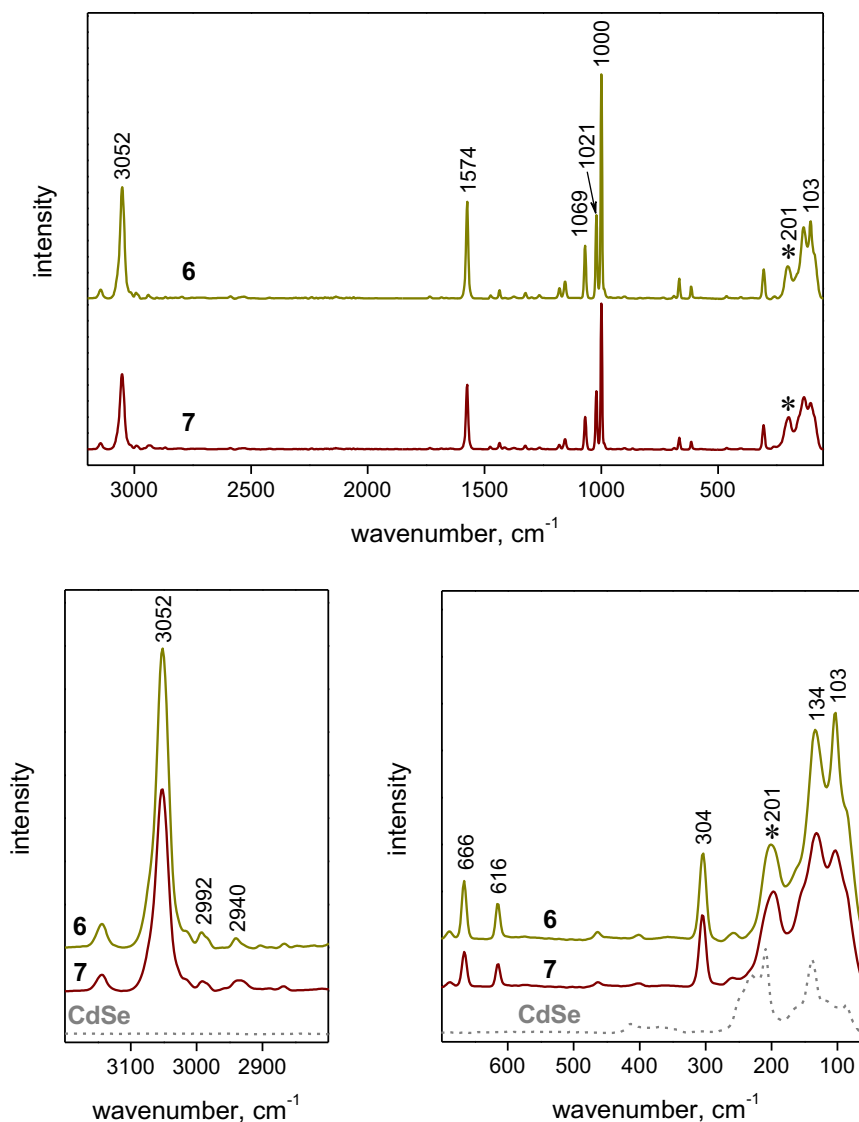


**Figure 5.4:** Raman spectra of **6** and **7**: *top*, general view; *left*, enlarged high-frequency part; *right*, enlarged low-frequency part. Raman spectrum of bulk CdSe (dash grey line) is shown for comparison. All spectra are corrected for background and normalized by the band labelled with asterisk \*; ordinate axis offset was applied for clarity).

Crystalline samples of **6** show a ~36% weight loss between 275 and 450 °C (an abrupt step centered around 318 °C), as determined using TGA (Figure 5.5). By analogy with thermal decomposition of smaller nanoclusters  $(\text{Me}_4\text{N})_4[\text{Cd}_{10}\text{S}_4(\text{SPh})_{16}]$ ,<sup>61</sup> this major weight loss can be attributed to the elimination of surface selenophenolate groups and the formation of bulk CdSe. The initial gradual weight loss of 3.46% observed between 20

and 275 °C in TGA for **6** can be attributed to the removal of residual lattice solvent, a loss of weakly bonded apex ligands or/and counter ions. Indeed, experimental data agree well with a calculated weight loss (3.53%) for the elimination of four tetramethylammonium counterions and *dmf* ligands at four vertexes from the nanocluster with the molecular formula  $(\text{Me}_4\text{N})_4[\text{Cd}_{54}\text{Se}_{32}(\text{SePh})_{48}(\text{dmf})_4]$ . Further heating ( $> 600$  °C) leads to sublimation of CdSe, as was proven by additional experiments. From the weight loss observed between 275 and 450 °C, it is possible to derive ratios between Cd/Se and  $\text{Se}^{2-}/\text{PhSe}^-$  present in nanoclusters **6**, with the approximation that all  $\text{PhSe}^-$  is eliminated in the form of diphenyl selenide ( $\text{Ph}-\text{Se}-\text{Ph}$ ). Cd/Se ratio (0.672 : 1) found using the experimental weight loss fits well the calculated Cd/Se ratio (0.675 : 1) for nanocluster core composition  $\text{Cd}_{54}\text{Se}_{80}$ , revealed by single crystal X-ray diffraction. From the experimental  $\text{Se}^{2-}/\text{PhSe}^-$  ratio (0.52 : 1), the amount of surface selenophenolate groups is higher than it is expected for  $(\text{Me}_4\text{N})_4[\text{Cd}_{54}\text{Se}_{32}(\text{SePh})_{48}(\text{dmf})_4]$  (calculated  $\text{Se}^{2-}/\text{PhSe}^-$  ratio 0.67 : 1), being closer to the one in the neutral nanocluster  $[\text{Cd}_{54}\text{Se}_{28}(\text{SePh})_{52}(\text{dmf})_4]$  (calculated  $\text{Se}^{2-}/\text{PhSe}^-$  ratio 0.54 : 1). The molecular formula of the neutral  $[\text{Cd}_{54}\text{Se}_{28}(\text{SePh})_{52}(\text{dmf})_4]$  nanocluster is derived by analogy with the neutral  $[\text{Cd}_{54}\text{S}_{28}(\text{SPh})_{52}(\text{dmf})_4]$ , described by Schubert and co-workers.<sup>13</sup> These possess a larger number of  $\mu_3$ - versus  $\mu$ -SePh moieties with an additional ligand at each of four faces (besides those on edges), resulting in an overall neutral CdSe framework.

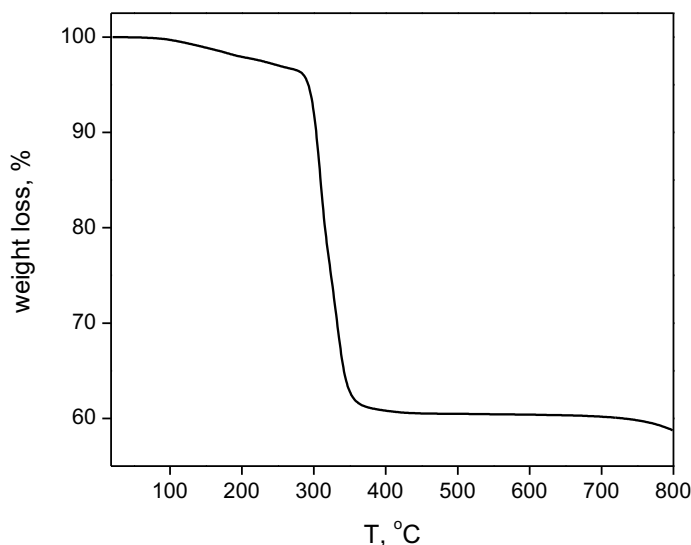


**Figure 5.5:** TGA curve for **6** under  $\text{N}_2$  flow during 1 °C/min ramp.

Electrospray ionization mass spectrometry of **6** dissolved in DMF or acetonitrile in a negative ion mode revealed the intense, sharp peak at  $m/z$  5620.7 with another two of lower intensity at 4254.4 and 8354.2 (Figure 5.6). The observed peaks are in a good agreement with doubly, triply and fourfold charged species corresponding to the unfragmented  $[\text{Cd}_{54}\text{Se}_{32}(\text{SePh})_{48}(\text{dmf})_4]^{n-}$  (calculated  $m/z$  are 8190.2, 5460.1 and 4095.1, respectively).

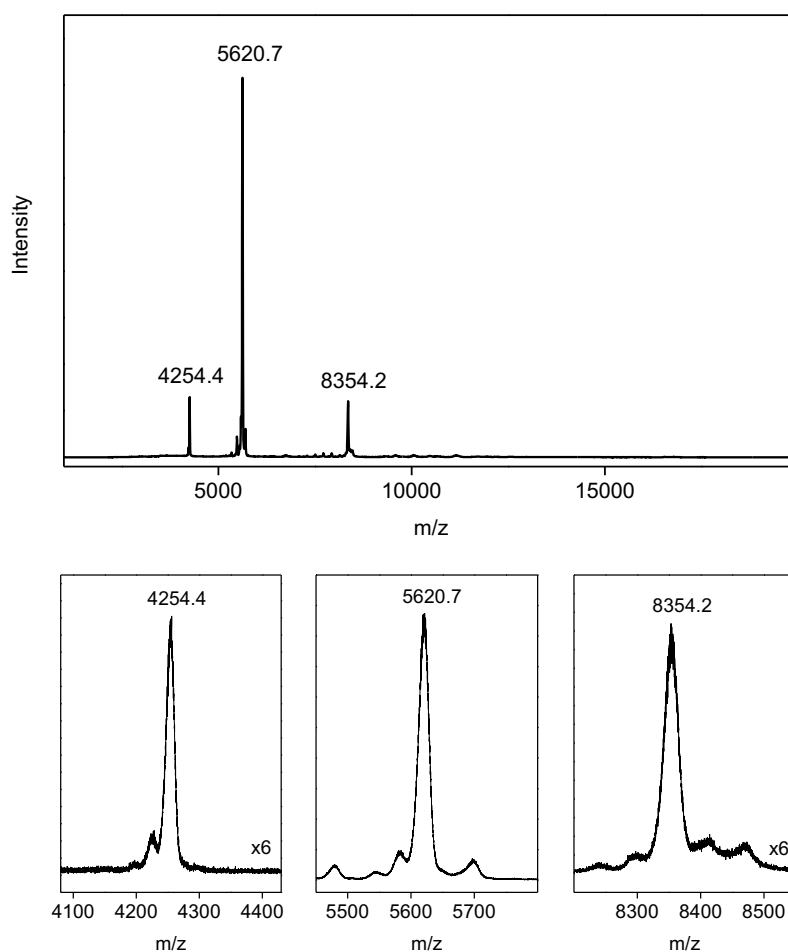


**Figure 5.6:** Negative ion mode electrospray mass spectrum of **6** dissolved in DMF (*top*) and enlarged areas around three the most intense signals (*bottom*).

Similar fragments (*i.e.*, weak broad peak at  $m/z \sim 8300$ ) were also found in positive ion mode, along with even weaker peak at  $m/z \sim 16800$  presumably corresponding to the (singly charged) unfragmented anion. The small, constant discrepancy between proposed molecular formula and observed  $m/z$  is most probably related with ion uptake ( $\text{Na}^+$  and  $\Gamma^-$ ) from the calibrant. Several other peaks of much lower intensity in a negative ion mode



appear to result from fragmentation of the original core. It is interesting that under conditions used for the analysis of **6**, no significant presence was found for ionic fragments that arise from lattice plane cleavage in the cluster core, previously observed for  $[\text{Cd}_{32}\text{S}_{14}(\text{SPh})_{36}(\text{dmf})_4]$  and suggested as general fragmentation pattern for larger nanoclusters under electrospray ionization conditions.<sup>62</sup>

Using energy dispersive X-ray (EDX) spectroscopy for the analysis of cubic crystals of dried **6**, the Cd/Se atomic ratio is found to be 0.74 : 1 which is reasonably close to the 0.675 : 1 expected for  $(\text{Me}_4\text{N})_4[\text{Cd}_{54}\text{Se}_{32}(\text{SePh})_{48}(\text{dmf})_4]$  and  $[\text{Cd}_{54}\text{Se}_{28}(\text{SePh})_{52}(\text{dmf})_4]$ . Elemental analysis (C, H, N, S) is in agreement with such formulations as well. Thus, a set of auxiliary analyses allowed to confirm the presence of  $\text{PhSe}^-$  as surface-stabilizing ligand for **6**. The results of Raman, TGA, mass, elemental and EDX analyses are consistent with molecular formula  $(\text{Me}_4\text{N})_4[\text{Cd}_{54}\text{Se}_{32}(\text{SePh})_{48}(\text{dmf})_4]$ , while neutral  $[\text{Cd}_{54}\text{Se}_{28}(\text{SePh})_{52}(\text{dmf})_4]$  nanocluster can not be excluded.

The fragments of cubic crystals of dried **6** display distinct luminescence in the solid state; a combination of optical microscopy and luminescence imaging confirms that emission is clearly observed at room temperature, homogeneously distributed from every part of the sample (Figure 5.7). The confocal fluorescence microscopy images are pseudocolored red; the real color of emitted light is discussed below. Since an absence of room temperature emission was reported for related, smaller cadmium chalcogenide nanoclusters both in the solid state and in solution,<sup>41,46</sup> the optical properties of **6** were examined more closely.

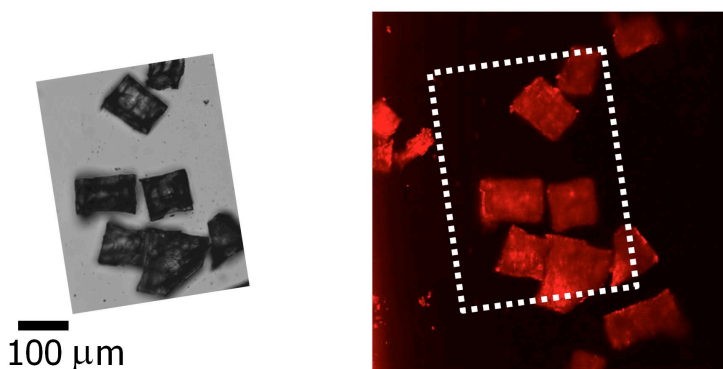


**Figure 5.7:** Transmission optical (*left*) and confocal fluorescent microscopy (*right*) images of fragments of cubic crystals of **6**. The confocal fluorescence microscopy images are pseudocolored red.

Similar to previously reported cadmium chalcogenide nanoclusters, clusters **6** can be re-dissolved in some polar solvents, breaking interactions between nanoclusters in the superlattice while leaving intact individual frameworks.<sup>12,41</sup> It also was reported previously that keeping cadmium chalcogenide nanoclusters dissolved in strongly coordinating solvent for > 24 h or performing additional treatments, like sonication or heating of the solution, may modify the nanoclusters themselves. The changes may vary from partial ligand exchange<sup>63</sup> to significant cluster core rearrangement.<sup>64</sup> To avoid any changes in nanocluster composition, all our measurements of optical properties were done for solutions prepared by stirring at room temperature immediately after re-dissolving crystalline samples.

The UV–vis absorption spectra of solutions of **6** in DMF (Figure 5.8) show the presence of sharp and narrow excitonic features. The lowest energy absorption band is observed at 410 nm (fwhm 22 nm). The peak width for monodisperse nanoclusters in **6** is related with effects other than distribution of sizes, *e.g.*, electron-phonon coupling or trapping to surface states.<sup>65</sup> The peaks at shorter wavelengths (*i.e.*, 376 and ~310 nm; fwhm ~40, and ~30 nm, revealed upon deconvolution) are attributed to the excited states of the excitons on the same CdSe nanoclusters. The first two absorption peaks are assigned to 1S(e)-1S<sub>3/2</sub>(h), 1S(e)-2S<sub>3/2</sub>(h), transitions, respectively; while the third peak can be assigned to the 1P(e)-1P<sub>3/2</sub>(h), 1S(e)-2S<sub>1/2</sub>(h) or 1P(e)-1P<sub>1/2</sub>(h) transitions or their combination.<sup>66,67</sup> The ambiguity in assignment of the higher energy peaks is related with the size dependence of relative positions and intensities of the transitions in the strong confinement regime (when the particle radius is a few times smaller than the exciton Bohr radius, which is 5.6 nm for CdSe).<sup>67</sup>

The effect of cluster composition (for a given Cd<sub>x</sub>E<sub>y</sub>(E'Ph)<sub>z</sub> cluster size, where E, E' = S, Se, Te) was systematically followed previously for smaller frameworks. In the case of dichloroethane solutions of [Cd<sub>10</sub>E<sub>4</sub>(E'Ph)<sub>12</sub>L<sub>4</sub>] (L = P<sup>n</sup>Pr<sub>3</sub> or P<sup>n</sup>Pr<sub>2</sub>Ph) and acetonitrile solutions of [Cd<sub>17</sub>E<sub>4</sub>(E'Ph)<sub>28</sub>]<sup>2-</sup>, the lowest-energy excitonic peak shows a red shift upon changing from sulfur (E = E' = S) to the heavier chalcogenide and chalcogenolate ligands through various mixed species (*e.g.*, E = Se, E' = S) to pure selenium- or tellurium-containing clusters (E = E' = Te).<sup>45,68</sup> Along this line, a shift toward longer wavelength is

observed from  $[\text{Cd}_{54}\text{S}_{32}(\text{SPh})_{48}(\text{H}_2\text{O})_4]^{4-}$  through  $[\text{Cd}_{54}\text{Se}_{32}(\text{SPh})_{48}(\text{H}_2\text{O})_4]^{4-}$  <sup>12</sup> to **6** (*i.e.*,  $[\text{Cd}_{54}\text{Se}_{32}(\text{SePh})_{48}(\text{dmf})_4]^{4-}$ ), with the low-energy excitonic peak positions found at 353, 393 and 410 nm, respectively, in DMF solutions.

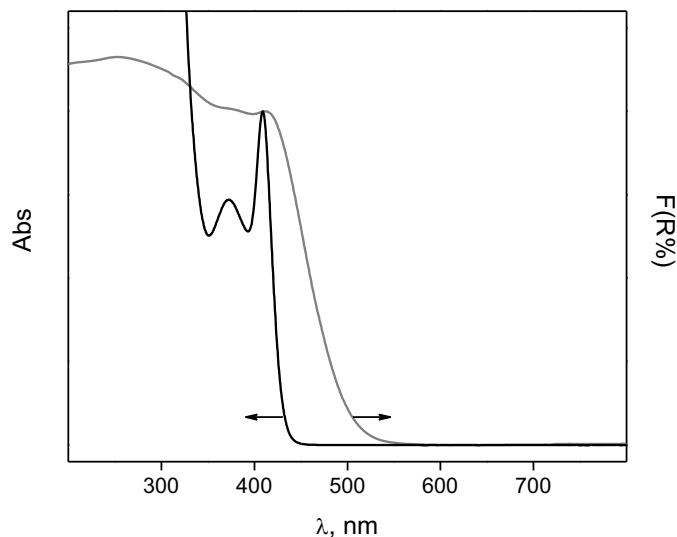


**Figure 5.8:** UV–vis absorption spectrum of **6** re-dissolved in DMF (normalized) and diffuse reflection spectrum of solid material **6** (processed using the Kubelka–Munk function and normalized).

The main features in the UV–vis absorption spectrum of **6** in DMF essentially match with those of reactions solutions prior to crystallization (*i.e.*, a distinct peak at  $\sim 414$  nm with shoulder at  $\sim 376$  nm, see Figure 5.9), although the latter are broader, slightly red-shifted and a distinct tail to longer wavelengths can be discerned. After crystallization is complete the peak at  $\sim 414$  nm and shoulder at  $\sim 377$  nm are no longer present in the spectra of the mother liquor (Figure 5.9). Remaining, however, are weak, broad bands at 438 and  $\sim 465$  nm suggesting that larger CdSe species (probably having a distribution of sizes) are also present. Due to a lack of monodispersity these species would not proceed further, while nanoclusters **6** crystallize into their superlattice, forming a pure solid phase.

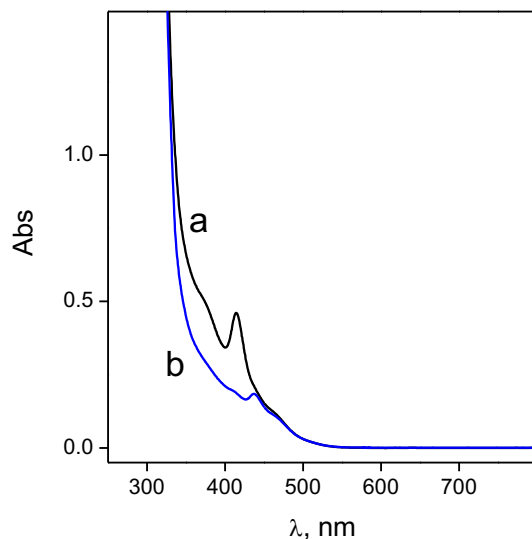


**Figure 5.9:** UV-vis absorption spectra of DMF-diluted mother liquor before (a) and after (b) crystallization of **6**.

While material **6** dissolves most readily in DMF (solubility  $\sim 6$  mg/ml), it also can be dissolved in acetonitrile (solubility  $< 0.1$  mg/ml). The UV-vis absorption spectrum of **6** dissolved in acetonitrile is essentially identical to that in DMF (Figure 5.10). However, the lower absorption onset for this solvent itself allowed for another band at 245 nm to be observed, associated with transitions within the aryl ring of the surface  $\text{PhSe}^-$  ligands. Unlike highly coordinating DMF in which cluster core rearrangement was reported previously for smaller CdS and CdSe nanoclusters, acetonitrile is less likely to cause such changes. An absence of any significant difference in absorption bands position or width in the UV-vis spectra of **6** in DMF and acetonitrile suggests that the structures do not change considerably upon dissolution. In agreement with this, mass spectra of **6** re-dissolved in DMF and acetonitrile show the presence of identical ionic species. The molar extinction coefficients  $\epsilon$  at the lowest-energy absorption peak was found  $\sim 127,000 \text{ M}^{-1}\cdot\text{cm}^{-1}$  in DMF, suggesting that the first transition is strongly allowed. The value of  $\epsilon$  for **6** is comparable with those reported previously for smaller cadmium chalcogenide nanoclusters, for instance,  $84,500 \text{ M}^{-1}\cdot\text{cm}^{-1}$  in THF solution for  $[\text{Cd}_{32}\text{S}_{14}(\text{SPh})_{36}(\text{dmf})_4]^{41}$  and  $52,000 \text{ M}^{-1}\cdot\text{cm}^{-1}$  in acetonitrile solution for  $[\text{Cd}_{32}\text{Se}_{14}(\text{SePh})_{36}(\text{PPh}_3)_4]^{43}$ . Strong size dependence of  $\epsilon$  at the lowest-energy absorption peak was also found previously for crystalline CdS, CdSe and CdTe nanoparticles, which increases supralinearly with increasing particle diameter.<sup>69,70</sup>

The fact that the position of the absorption bands is insensitive to change of solvent polarity (as with transition from DMF to acetonitrile, relative polarity changes from 0.386 to 0.460)<sup>71</sup> indicates that the ground state or the corresponding excited state have a vanishingly small dipole moment. This observation, together with the large oscillator strength, is in agreement with characteristics of an excitonic transition.<sup>41</sup>

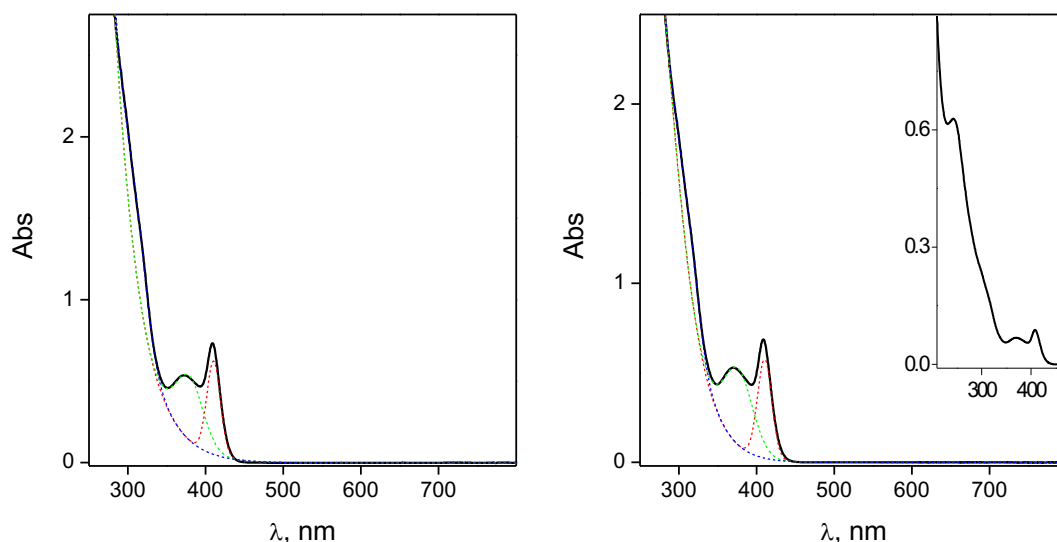


**Figure 5.10:** UV-vis absorption spectra of **6** re-dissolved in DMF (*left*) and acetonitrile (*right*). *Inset:* the spectrum of dilute solution of **6** in acetonitrile. Dashed lines show multi-peak fitting (Gaussian function).

In the UV-vis diffuse reflectance spectra of solid **6**, the lowest-energy absorption peak is broader, and an onset of the peak is shifted toward a longer wavelength in comparison to solution data (Figure 5.8). A similar relation between the UV-vis absorption spectra of solid and dissolved material was reported previously for smaller CdS nanoclusters and attributed to weak cluster-cluster interaction present in the superlattice.<sup>14,41</sup>

Low-temperature ( $T = 77$  K) emission spectra of **6** in DMF show a distinct and rather broad (fwhm 72 nm) band at 509 nm (Figure 5.11). This emission maximum is red shifted in comparison with the previously reported emission for smaller  $[\text{Cd}_{32}\text{Se}_{14}(\text{SePh})_{36}(\text{PPh}_3)_4]$ , where the emission band was observed at 480 nm (fwhm  $\sim 65$  nm) while measured in Nujol suspension at  $T = 8$  K.<sup>46</sup> The peak in the emission spectrum of **6** is asymmetric, with a tail toward higher wavelengths, and the peak shape

and position changes a little ( $< 8$  nm for the latter) when the wavelength is varied from the red edge to blue excitation (Figure 5.12). This lack of wavelength dependence provides additional evidence for the purity and homogeneity<sup>72,73</sup> of the species **6**, having the same nature of the emitting state. Several peaks are resolved in the corresponding low-temperature photoluminescence excitation spectra: a distinct narrow absorption band at 394 nm and weaker ones at 368 and 324 nm. These bands match the excitonic transitions observed in UV-Vis absorption spectra of **6**.

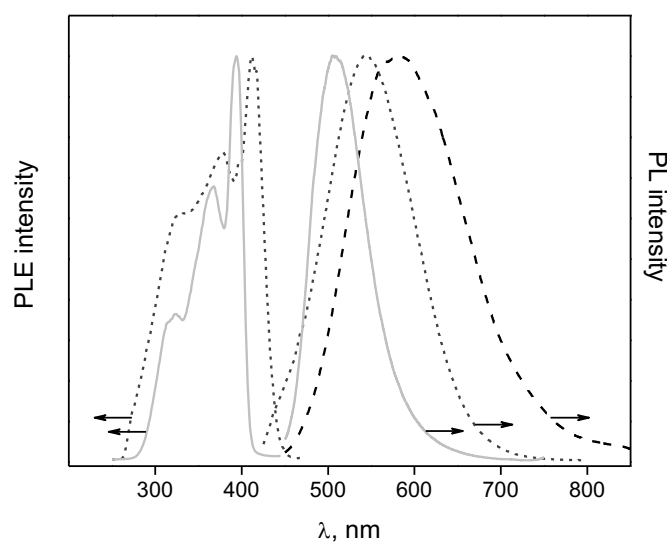


**Figure 5.11:** Normalized PL and PLE spectra of **6** re-dissolved in DMF, obtained at 77 K (solid lines) and at room temperature (short dash lines); PL spectrum of **6** in solid state, obtained at room temperature (dash line). For the spectra in solution, the excitation wavelength for PL spectra corresponds to the low-energy band in corresponding PLE; the monitoring wavelength for PLE spectra – to the PL maximum. For solid state PL spectrum, the excitation wavelength was 405 nm.

Unlike previously reported smaller CdSe nanoclusters (for which no detectable emission was observed above 150–200 K due to fast nonradiative decay processes),<sup>46</sup> solutions of **6** also exhibit prominent emission at room temperature. Here, emission is observed at 545 nm, shifted toward a longer wavelength in comparison to the low-temperature spectrum, with a larger fwhm of 123 nm (Figure 5.11). Such increased linewidth can be explained in terms of thermal broadening. In comparison with the low-temperature data, room temperature emission also has a weak shoulder at shorter wavelength ( $\sim 440$  nm), which suggests that competing transitions may take place for solutions of **6** at room temperature.

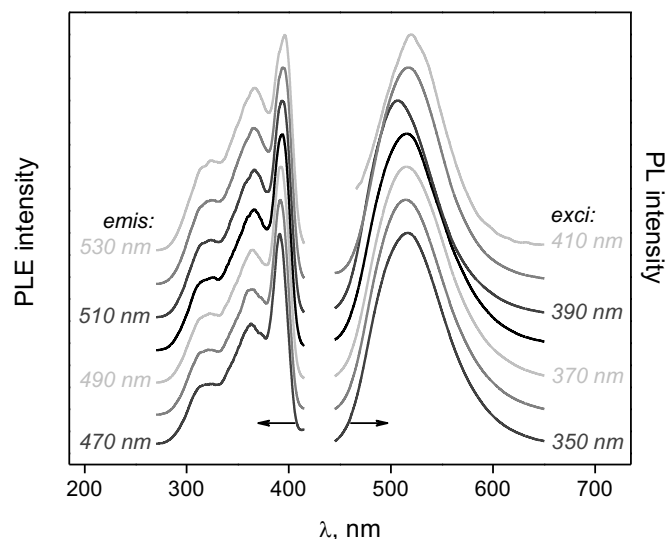


**Figure 5.12:** Normalized PL and PLE spectra of **6** re-dissolved in DMF, obtained at different excitation and detection wavelengths with 10 nm step. All measurements were performed at 77 K. The spectra are shown with ordinate axis offset; for those with low intensity signal line smoothing was applied for clarity.

With increases in concentration of **6** in DMF solutions, the intensity of emission increases as well, while peak position, width, and shape remain the same (Figure 5.13). The room-temperature excitation spectrum shows a distinct relatively narrow absorption band at 412 nm and weaker ones at 378 and ~328 nm; all peaks are red-shifted in comparison to those in the low-temperature spectra (Figure 5.11). With increase of concentration of **6** in DMF solutions, not only does the intensity of excitation band increases but the ratio between the three absorption bands also changes and additional narrow features (*i.e.*, at 418 and 397 nm denoted by asterisk \* Figure 5.13) gradually become resolved. The substructure of the low-energy band in PLE spectra was reported previously for CdSe nanoparticles and assigned to the band-edge exciton splitting (LO-phonon substructure) due to particle's crystalline structure, nonspherical shape and electron-hole exchange interaction enhanced by quantum confinement.<sup>66,74,75</sup> Noteworthy that resolving such fine structure in the PLE spectra of CdSe nanoparticles with sizes comparable to nanocluster size in **6** (*e.g.*, in examined series of samples the smallest mean effective diameter was ~3 nm from TEM<sup>75</sup> vs. the tetrahedron height for **6** 1.77 nm) required special experiments to be conducted (*e.g.*, transient differential absorption or fluorescence line narrowing

spectroscopy at 10 K) to reduce line-broadening inhomogeneity (by size, shape and surface chemistry) of the nanoparticles.<sup>66,74–77</sup> In contrast, in the room temperature PLE spectra of monodisperse nanoclusters **6** the additional, narrow features are well resolved.

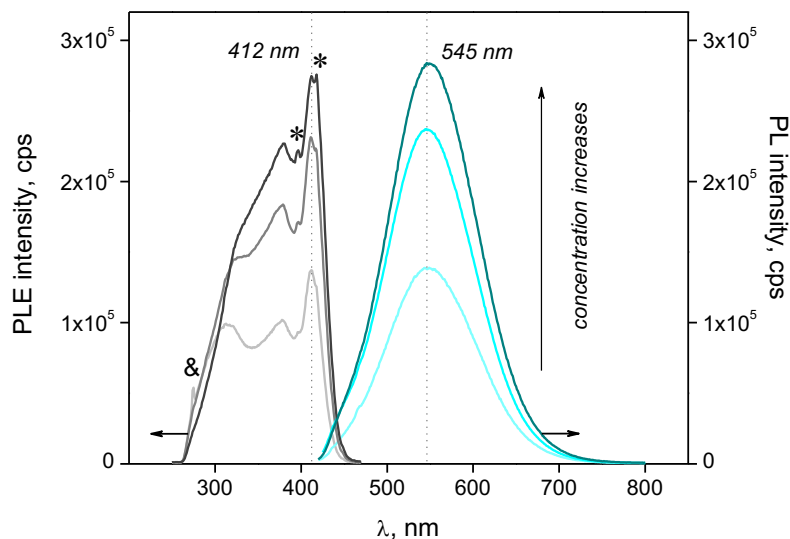


**Figure 5.13:** Room-temperature PL and PLE spectra of **6** re-dissolved in DMF, obtained for 2.2, 4.2 and  $5.7 \cdot 10^{-6}$  M solutions: the asterisk \* denotes the narrow features in the low-energy absorption band better resolved at higher concentrations. The excitation wavelength for PL spectra was 412 nm; the monitoring wavelength for PLE spectra was 548 nm. The ampersand & denotes harmonic vibration and/or solvent peaks.

Solid-state emission spectra of **6** show a distinct broad (fwhm 151 nm) band at 582 nm (Figure 5.11), supporting previous observations using confocal fluorescent microscopy and confirming that pronounced green emission at room temperature is inherent to material **6** itself, and does not come from any new species arising from possible changes in solution. The red shift of the emission maximum in the solid state, in comparison to its position for **6** in DMF solution (both at room temperature), is in agreement with the weak cluster-cluster interactions present in the superlattice.

Emission bands in the PL spectra of CdSe nanoclusters and nanoparticles, reported previously, were generally assigned to 1) band edge fluorescence or 2) deep trap emission.<sup>78,79</sup> Emission of both types can also be observed in the same spectrum (see, for instance, ref. 80). The band edge emission (recombination of free charge carriers) is characterized by narrow



peak shape, a small red shift from the absorption band, and a short lifetime. For both low and room temperature PL/PLE measurements for **6**, the emission is considerably red shifted from the lowest energy excitation: 115 and 133 nm, respectively. A comparable shift (~107 nm) was observed previously in PL/PLE spectra of  $[\text{Cd}_{32}\text{Se}_{14}(\text{SePh})_{36}(\text{PPh}_3)_4]$  obtained in Nujol suspension at  $T = 8 \text{ K}$ .<sup>46</sup> On the basis of the broad line width of the emission and the significant shift to the red, the emission observed for **6** likely originates from the radiative recombination of charge carriers, trapped on the surface selenophenolate  $\text{PhSe}^-$  ligands (“trapped emission”), previously suggested for smaller nanoclusters.<sup>43,46</sup> An assignment of the emission to transitions related with phenylchalcogenolate ligands was further supported by a significant blue shift of the PL maximum for the nanoclusters with the same size and core composition but having thiophenolate *vs.* selenophenolate ligands.<sup>81</sup> The corresponding excited state is not detected in the absorption spectrum since it has a low oscillator strength (as a forbidden transition). For monodisperse nanoclusters the broad line width for the emission peak can be explained by 1) inhomogeneous distribution of surface coverage by selenophenolate ligands in any given nanocluster and by 2) existence of multiple conformational isomers for a given nanocluster. The latter explanation is supported by the observed lower line width for the emission spectrum obtained at  $T = 77 \text{ K}$ , in agreement with decreasing of rotational flexibility of ligands in a frozen solution/glass. The temperature effect (rather than different nature of absorption or emission) also explains the red shift observed for both excitation and emission bands of **6**.

An assignment of the broad emission band of smaller CdSe nanoclusters as trapped emission was supported by time-resolved PL measurements, which showed non-exponential emission decay (distributed kinetics) on the microsecond time scale.<sup>46,82</sup> Calculated mean decay time  $\tau$  (in Nujol suspension at  $T = 10 \text{ K}$ ; data approximation using stretched exponential function  $\exp[-(t/\tau)^\beta]$ ) was found to decrease from 10.0 to 0.78  $\mu\text{s}$  with nanocluster size increase from  $(\text{Pr}_4\text{N})_2[\text{Cd}_4(\text{SePh})_6\text{Cl}_4]$  to  $[\text{Cd}_{32}\text{Se}_{14}(\text{SePh})_{36}(\text{PPh}_3)_4]$ , respectively.<sup>46</sup> Significantly longer  $\tau$  were found at  $T = 20 \text{ K}$  for the nanoclusters with the same size and core composition but having thiophenolate *vs.* selenophenolate ligands, which provides an additional argument in favour of the involvement of surface phenylchalcogenolate ligands in the PL mechanism.<sup>81</sup> Time-

resolved PL measurements for **6** at room temperature in micro- and millisecond time scales ( $1.2 \cdot 10^{-7}$ – $1.5 \cdot 10^{-3}$  s interval) show that the decay process is very complex and can be roughly fit as a sum of several exponential decay functions (Figure 5.14, *top left*). Most of the emission decays with  $\tau_1 = 0.33 \mu\text{s}$  (and overall data were approximated as third order exponential decay  $\sum_{n=1}^3 A_n \cdot \exp[-(t/\tau_n)]$ ). This value of  $\tau$  for **6** (*i.e.*,  $[\text{Cd}_{54}\text{Se}_{32}(\text{SePh})_{48}(\text{dmf})_4]^{4-}$ ) is smaller than previously published  $0.78 \mu\text{s}$  for  $[\text{Cd}_{32}\text{Se}_{14}(\text{SePh})_{36}(\text{PPh}_3)_4]$  and fits the trend of  $\tau$  decrease with tetrahedral CdSe nanocluster size increase.<sup>46</sup> The key difference with previously reported smaller CdSe frameworks consists in the existence of other decay components with much longer life times (*i.e.*,  $\tau_2 = 15.6$  and  $\tau_3 = 190 \mu\text{s}$ ). To check if any faster (than  $\sim 1 \cdot 10^{-7}$  s) processes can be revealed as well, additional time-resolved PL measurements are performed for **6** in the nanosecond time scale (Figure 5.14, *center left*). Fluorescence decay measurements, along with fluorescence-lifetime imaging microscopy (Figure 5.14, *bottom left*), show that in this time scale major emission intensity decay corresponds to  $\tau = 3.6$  ns. In general, the decay for **6** over the entire time scale is found to be multiexponential, with at least 2–3 components of lifetime in each time window. Such a broad range of lifetimes was observed previously for cadmium chalcogenide systems at low temperatures (for example, see ref. 83) and discussed in terms of simultaneous radiative and nonradiative transitions between deeply trapped charge carriers, occurring with participation of various vibrational modes (multiphonon relaxation). Nonradiative relaxation for semiconductor nanoparticles and nanoclusters may include different processes that contribute to complex decay kinetics (*e.g.*, Auger recombination, Förster resonance energy transfer, thermal escape and ligand-induced charge transfer),<sup>84–87</sup> the large number of possible relaxation pathways complicates the analysis. Overall, long-lived components in the time-resolved PL decay traces for **6** are consistent with the trapped emission associated with forbidden states involving the selenophenolate  $\text{PhSe}^-$  surface ligands, although the possibility of radiative recombination *via* other defect states can not be excluded.

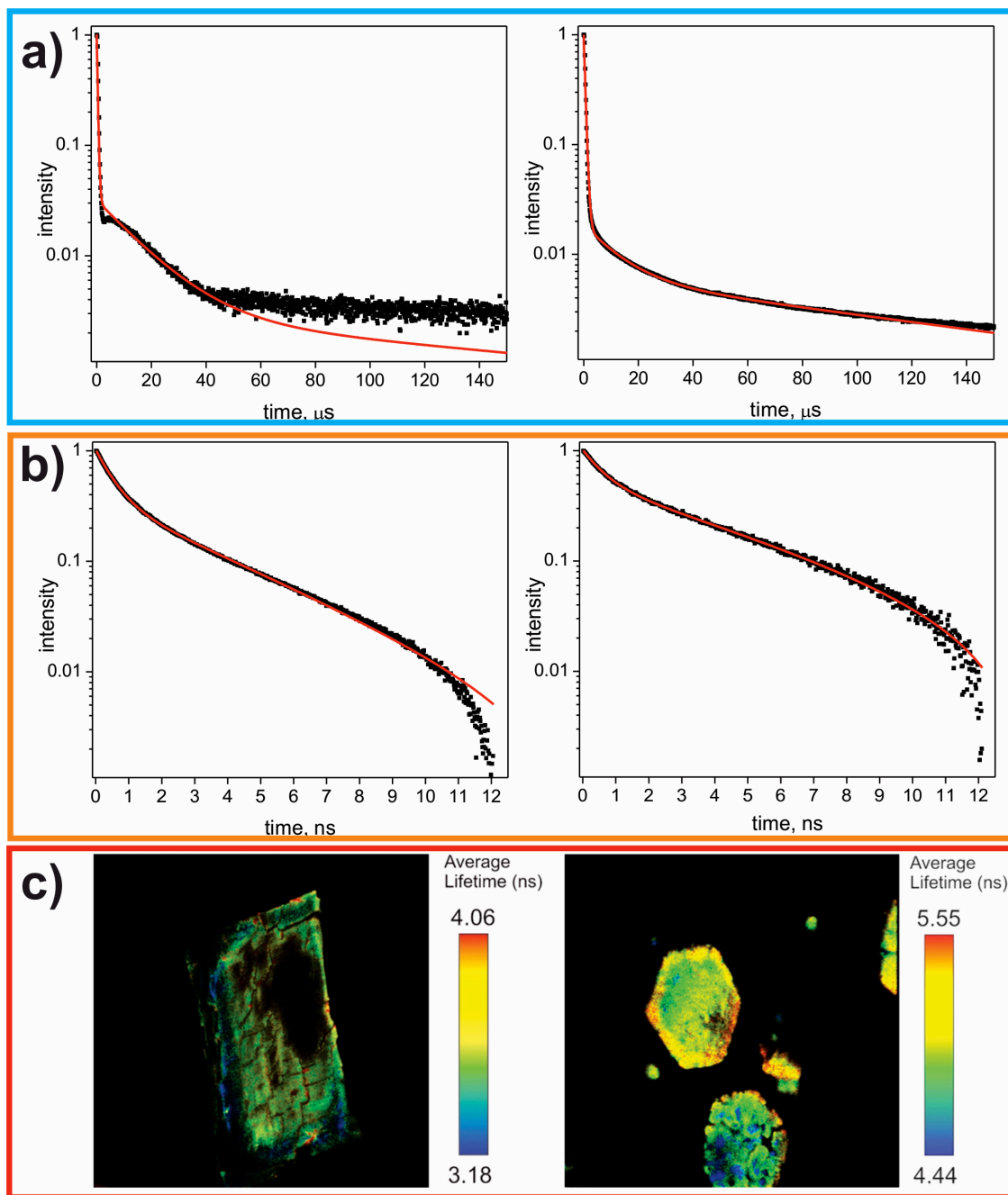


**Figure 5.14:** Normalized time-resolved PL decay traces for **6** (left) and **7** (right): microsecond (a) and nanosecond (b) time scales. All measurements were performed at room temperature. Solid lines show the fits to a sum of the exponential decay functions. Fluorescence-lifetime imaging microscopy (FLIM) micrographs (c), showing lifetime distributions for **6** (left) and **7** (right).

The room-temperature emission of **6**, not observed for smaller members of capped supertetrahedral cluster family,<sup>46</sup> can be considered from the point of view of composition evolution upon the cluster size increase in the homologues series. As nonradiative relaxation in  $[\text{Cd}_{17}\text{Se}_4(\text{SePh})_{24}\text{L}_4]^{2+}$  and  $[\text{Cd}_{32}\text{Se}_{14}(\text{SePh})_{36}\text{L}_4]$  ( $\text{L} = \text{PPh}_2\text{Pr}$  and  $\text{PPh}_3$ , respectively) at room temperature was proposed to occur through vibrating modes of the bridging selenophenolate ligands ( $\mu\text{-SePh}^-$ ) at the nanocluster edges,<sup>46,82</sup> the increase of the cluster size while progressing toward  $[\text{Cd}_{54}\text{Se}_{32}(\text{SePh})_{48}\text{L}_4]^{4-}$  may diminish this effect due to decreasing the fraction of surface sites. Thus, change in nanoclusters composition in capped tetrahedral cluster family can be followed in the case of different Se sites (Table 5.1): surface-to-core ratio ( $\mu\text{-SePh}^- / \mu_4\text{-Se}^{2-}$  sites) decreases from 6 : 1 to 2.4 : 1 in Cd17Se and Cd54Se, respectively. For the latter cluster, relaxation from the excited state through selenophenolate ligands vibrations may become less influential, and emission (slow radiative transitions involving trapped states) is observed. This hypothesis is consistent with previous observations that the temperature at which the emission of nanoclusters reduces to the background level increases progressively with increasing nanocluster size from  $(\text{Pr}_4\text{N})_2[\text{Cd}_4(\text{SePh})_6\text{Cl}_4]$  through  $[\text{Cd}_{10}\text{Se}_4(\text{SePh})_{12}(\text{PPr}_3)_4]$  and  $[\text{Cd}_{17}\text{Se}_4(\text{SePh})_{24}(\text{PPh}_2\text{Pr})_4]^{2+}$  to  $[\text{Cd}_{32}\text{Se}_{14}(\text{SePh})_{36}(\text{PPh}_3)_4]$ .<sup>46</sup> Then, larger members of capped supertetrahedral cluster family possess surface  $\mu_3\text{-Se}^{2-}$  sites. Surface ligand-to-ligandless ratio ( $\mu\text{-SePh}^- / \mu_3\text{-Se}^{2-}$  sites) decreases from 9 : 1 to 4 : 1 in Cd32Se and Cd54Se, respectively. Such differences in surface composition may also contribute to emission properties of **6**. Moreover, it was observed experimentally and confirmed by theoretical calculations at DFT and TDDFT levels for tetrahedral CdE nanoclusters belonging to different families, that the influence of ligands on the photophysical properties becomes less pronounced with increasing cluster sizes (see, for example, ref. 88).

**Table 5.1:** Composition of the members of capped tetrahedral nanocluster series.

Cluster formula	Number of $\mu_4\text{-Se}^{2-}$ sites (tetrahedral)	Number of $\mu_3\text{-Se}^{2-}$ sites (tri-coordinated pyramidal)	Number of edge $\mu\text{-SePh}^-$ sites (bridging)
$[\text{Cd}_{17}\text{Se}_4(\text{SePh})_{24}\text{L}_4]^{2+}$	4	0	24
$[\text{Cd}_{32}\text{Se}_{14}(\text{SePh})_{36}\text{L}_4]$	10	4	36
$[\text{Cd}_{54}\text{Se}_{32}(\text{SePh})_{48}\text{L}_4]^{4-}$	20	12	48

Examination of the optical properties of **6** allowed to reveal both similarities and differences from the trends for structurally-related smaller cadmium chalcogenide nanoclusters reported previously. Thus, comparison of UV–vis absorption, diffuse reflectance and PLE spectra of **6** with those of smaller members of capped super-tetrahedral cluster family shows, that low-energy peak positions are consistent with systematical shift due to quantum confinement effect. This can be illustrated by the red shift of the low-energy excitonic peak maximum in UV–vis spectra from 341 and 373 to 410 nm with nanoclusters size increase from  $[\text{Cd}_{17}\text{Se}_4(\text{SePh})_{28}]^{2-}$  and  $[\text{Cd}_{32}\text{Se}_{14}(\text{SePh})_{36}(\text{PPh}_3)_4]^{45,46}$  to **6** (*i.e.*,  $[\text{Cd}_{54}\text{Se}_{32}(\text{SePh})_{48}(\text{dmf})_4]^{4-}$ ), respectively. Unlike smaller family members, room temperature PL spectra of **6** in DMF solutions, as well as its room temperature solid state PL spectra, show the presence of distinct emission with maxima at 545 and 582 nm, respectively. Based on considerable red shift from excitation maximum, broad line width and long-lived components in multiexponential emission decay, observed emission was attributed to deep trap states related to surface selenophenolate  $\text{PhSe}^-$  ligands. CdSe nanoparticles (average diameter  $\sim 4$  nm) with phenylchalcogenolate ligands were also previously reported to show broad long-lived trapped emission at 77 K while no emission at room temperature; in the latter case relaxation was assigned to a combination of hole transfer to the ligand (more efficient at higher temperature and for the ligands in the row  $\text{PhS}^- < \text{PhSe}^- < \text{PhTe}^-$ ) and of phonon-assisted nonradiative decay pathways.<sup>89</sup> In contrast, room temperature trapped emission (broad band at 604 nm) was reported for much smaller CdSe nanoparticles with thiophenolate ligands.<sup>90</sup> Generally, a complex relationship between nanocluster/nanoparticle size, shape, surface structure and relaxation pathways in the system may exist; the surface science of nanoscale objects represents the area of active scientific research where many phenomena are still far from being fully understood.<sup>91</sup> Further investigation (*e.g.*, quantum yield experiments) will be necessary for better understanding of observed unprecedented room temperature emission of **6** and the exact mechanism for “unquenching” in the presence of  $\text{PhSe}^-$  surface ligands.

It was shown previously, that  $\text{Br}^-$  ions in reaction solutions influences the thermally induced condensation of the sulfur complex  $[\text{Me}_4\text{N}]_2[\text{Cd}(\text{SPh})_4]$  in DMF, resulting in the formation of larger (in comparison to additive-free synthesis) monodisperse CdS

nanoclusters, arranged into cubic superlattices.<sup>63</sup> In a similar fashion, the addition of CTAB to solutions of  $[\text{Me}_4\text{N}]_2[\text{Cd}(\text{SePh})_4]$  was found to have a marked affect on the size and arrangement of the CdSe particles generated under solvothermal conditions.

Solvothermal treatment of  $[\text{Me}_4\text{N}]_2[\text{Cd}(\text{SePh})_4]$  in the presence of CTAB yields a solid product, which comprises two distinct materials: relatively large brick-red hexagonal prisms (**7**), which sediment readily from the mixture, and fine, shapeless, orange aggregates, which remain suspended in the mother liquor or pure DMF unless centrifuged. Material **7** was separated, dried, and examined more closely.

Despite the fact that hexagonal prisms demonstrate some characteristics of a single crystal (*e.g.*, they are well-faceted and show single crystalline behavior in polarized light), multiple attempts of single-crystal X-ray characterization for fresh **7** were not successful: the samples display diffuse scattering streaks rather than clearly discernible Bragg reflections. Although a regular pattern can be observed from the X-ray scattering (Figure 5.15), the data are insufficient to derive additional information on the structure of material **7**.

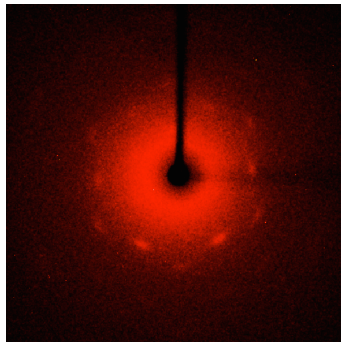


**Figure 5.15:** Snapshot of X-ray diffraction image of a single hexagonal prism from **7**.

Optical microscopy and subsequent SEM examination of dried **7** revealed that all well faceted hexagonal prisms have similar proportions. According to SEM (Figure 5.16), the size of majority of the prisms is approximately 50  $\mu\text{m}$  (distance between opposite corners of the hexagonal base) and about the same in height. Much smaller ( $< 10 \mu\text{m}$ ) and larger ( $> 70 \mu\text{m}$ ) prisms are also seen but relatively rare. High resolution SEM of selected hexagonal prisms allows more details to be observed: while the surface of some prisms is relatively smooth (Figure 5.17, *left*), in other prisms it is partially or entirely roughened

(Figure 5.17, *center and right*). Larger defects, such as cracks and cavities, are also seen. Cracks are observed exclusively on the hexagonal bases; smaller hexagonal prisms seem to contain fewer defects. Specific localization of the continuous defects may suggest that the nature of cracking in **7** (presumably, shrinkage cracking, see below) is different from that suggested for material **6**.

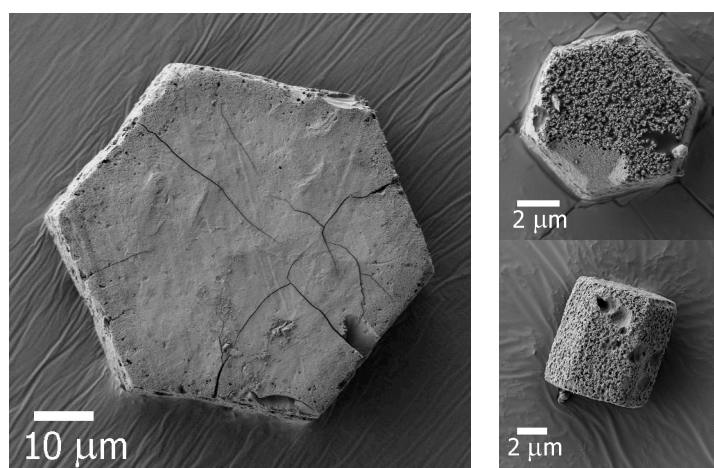


**Figure 5.16:** SEM images of representative hexagonal prisms in **7**. Top (*left and top right*) and side (*bottom right*) views are shown.



**Figure 5.17:** High resolution SEM images of surface of selected hexagonal prisms in **7**.

In the low-angle PXRD patterns for dried **7** a sharp but not very intense reflection is found at  $2\theta$   $2.68^\circ$ , and a weak, broad one is observed at  $5.38^\circ$  (*i.e.*, at double the angle of the main diffraction peak) (Figure 5.18). Low-angle PXRD reflections provide evidence of long-range order present in hexagonal prisms. The lowest angle reflection is shifted substantially towards the lower values due to a larger unit cell, in comparison to that of

dried **6**. Thus the calculated interplanar spacing  $d$  for **7** is 3.83 nm, whereas for **6** it is only 2.05 nm. In the wide-angle region of the PXRD patterns for **7** reflections are narrower in comparison to those in the patterns for **6**. It is interesting that some features characteristic of the hexagonal CdSe structure can be discerned (e.g., 100 and 101 reflections around  $2\theta$  30°). However, no sign of the 103 reflection for the hexagonal CdSe is observed, which argues in favour of the cubic CdSe structure. Substantial breadth of reflections in the wide-angle region complicates the analysis of the internal crystalline structure in this case, as it was described previously for CdSe nanoparticles (see, for instance, ref. 92) and many other nanodimensional objects.<sup>93</sup> Calculations of the mean size of the crystalline domains using the Scherrer equation for the dried material **7** give a value of 2.26 nm, which is larger than 1.55 nm in the case of **6**.

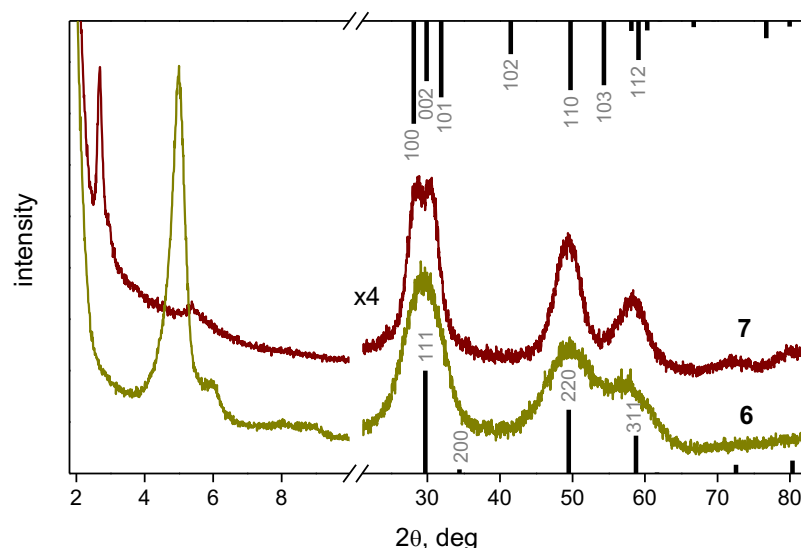


**Figure 5.18:** Powder X-ray diffraction patterns (Co K $\alpha$  radiation) of dried materials **6** and **7** and their relation with the patterns for bulk cubic (bottom stick representation) and hexagonal (top stick representation) CdSe structures. Difference in the intensity of reflections in part caused by different sample preparation techniques used in case of materials **6** and **7**. Wide-angle region is scaled  $\times 4$  for both samples; the data are shown with ordinate axis offset for clarity. Reference structures are from the database of the International Centre for Diffraction Data: hexagonal CdSe no. 04-011-9600; cubic CdSe no. 03-065-2891.

Unlike **6**, which is soluble both in DMF and acetonitrile, even prolonged stirring of **7** in DMF does not result in solutions with any detectable UV–vis absorption bands. The



UV–vis diffuse reflectance spectra of solid **7** (Figure 5.19) are essentially structureless with only very broad bands at  $\sim 475$  and  $405$  nm. An onset of the absorption is more gently sloping and shifted toward a longer wavelength in comparison to the diffuse reflectance spectra of **6**. Both red shift of absorption onset and negligibly small solubility of **7** in comparison with **6** is consistent with the larger size of constituent elements in **7**, also derived from PXRD patterns.

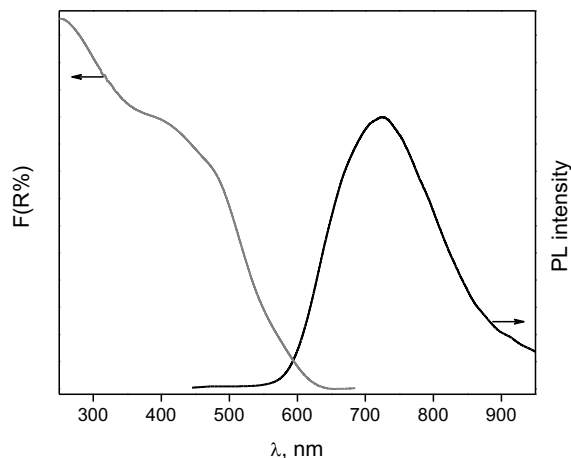


**Figure 5.19:** UV–vis diffuse reflection spectrum of solid material **7** (processed using the Kubelka–Munk function and normalized); room temperature solid state PL spectrum of **7** (normalized). For solid state PL spectrum, the excitation wavelength was  $405$  nm.

Raman spectra of **7** (Figure 5.4) contain very similar bands as those observed for **6**, showing the general similarity in composition of these two materials. For instance, bands at  $197\text{ cm}^{-1}$  due to interior Cd–Se bonds,  $666\text{ cm}^{-1}$  due to surface Se–C bonds, and  $3052\text{ cm}^{-1}$  due to aromatic C–H bonds can be assigned, confirming the supposition that **7** represents crystalline CdSe with  $\text{PhSe}^-$  ligands on its surface. The difference between **6** and **7** consists in the relative intensities of the Raman bands. To facilitate their comparison, the Raman spectra of **6** and **7** were normalized to the intensity of the band at  $\sim 200\text{ cm}^{-1}$  (assigned as stretching vibrations of interior Cd–Se bonds). Such normalization allows for evaluation of surface/interior group ratio; it can be concluded that the relative intensity of any bands related with organic ligands is smaller for **7** in comparison with **6**. A representative example is the band at  $666\text{ cm}^{-1}$  due to surface Se–C bonds: decrease in intensity of this band from **6** to **7** is in agreement with the decrease in

the overall selenophenolate to selenide ( $\text{PhSe}^-/\text{Se}^{2-}$ ) ratio. Since there are no aliphatic C–H Raman bands of high intensity present in the spectra of **7** (*i.e.*, bands at 2992 and 2935  $\text{cm}^{-1}$  are very weak), it is more likely that neither CTAB nor any possible products of its decomposition are “ensnared” inside the prisms or on their surface. Similarly to this, there is hardly any residual solvent (DMF) in **7** present. Overall, it can be suggested that the organic component in hexagonal prisms is mainly  $\text{PhSe}^-$  groups.

Site-specific EDX spectroscopy analysis of hexagonal prisms in **7** confirms the composition  $[\text{Cd}_x\text{Se}_y(\text{SePh})_z]$ ; the Cd/Se atomic ratio was found to be 1.06 : 1 which is reasonable value for continuous CdSe network. Unlike this, the Cd/Se atomic ratio for **6** was found to be essentially smaller (0.74 : 1) which reflects the presence of nanocluster constituents having anionic facets. No Br was found in a detectable amount in **7** by EDX analysis which suggests that the halide may facilitate fusion of lower-nuclearity cadmium selenophenolate intermediates leading to growth of larger constituents (similar as it was previously concluded for related CdS systems),<sup>63</sup> while not being present in the final product. Halogen-containing additives were also recently found to influence both the kinetics and thermodynamics of CdSe nanoparticles growth, presumably *via* unequal participation of  $\text{Hal}^-$  in dynamic absorption/desorption processes on different crystalline facets; in this case halide ligands were then clearly detected in purified samples.<sup>94</sup> An absence of  $\text{Hal}^-$  in **7** (and in **6** as well) is a significant result since halide ligands are known to influence emission of cadmium chalcogenide nanoclusters and nanoparticles.<sup>95–97</sup>

The hexagonal prisms of dried **7** show clearly visible red luminescence at room temperature; on the confocal fluorescence microscopy images bright emission is observed from all hexagonal prisms regardless of their size (Figure 5.20, *top*). Apparent uneven brightnesses of emission is assumed to originate mainly from differing orientations of the hexagonal prisms (lying flat on a base, or flat on a side, or tilted at some angle, see Figure 5.20, *top*). For a single prism, nearly homogeneous emission is observed from any spot on each side (*e.g.*, the hexagonal base, Figure 5.20, *bottom*).

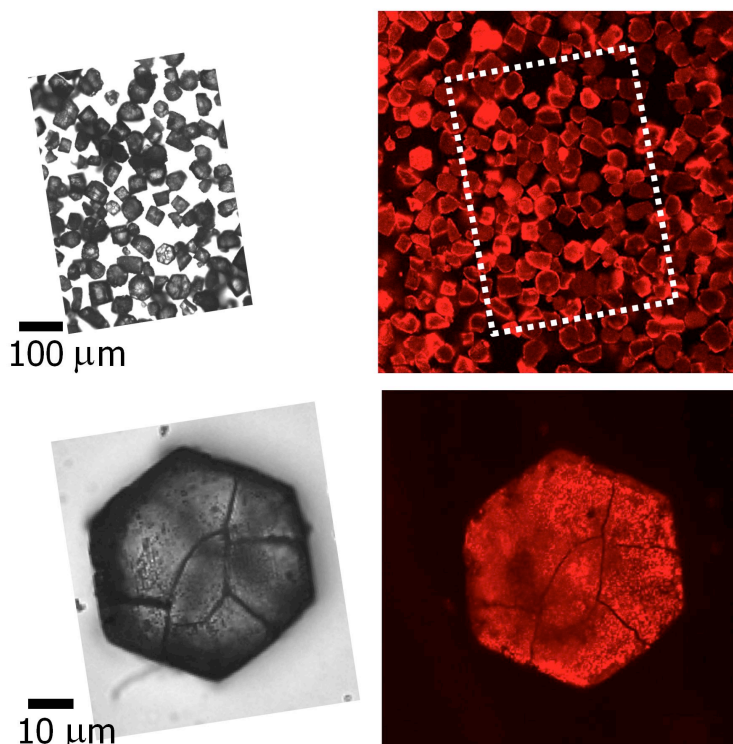


**Figure 5.20:** Transmission optical (*left*) and confocal fluorescent microscopy (*right*) images of hexagonal prisms of **7**: multiple (*top*) and single (*bottom*). The confocal fluorescence microscopy images are pseudocolored red.

The emission spectra of dried **7** show a distinct broad (fwhm 185 nm) band at 725 nm (Figure 5.19), attributed to trapped emission. A remarkable red-shift in comparison with solid state emission maximum for **6** (observed at 582 nm) may suggest the difference in surface chemistry between these two samples (which is consistent with the difference in their organic ligand shells, observed by Raman spectroscopy). The difference in optical properties may also be related with the fact that the structure of materials **6** and **7** is remarkably different (as revealed by powder X-ray diffraction measurements). Time-resolved PL measurements show that decay traces for **7** (Figure 5.14, *top right* and *center right*) are substantially different from those for **6** in both nano-, micro- and millisecond time scales. Thus, obtained data for the long-living processes fit a third order exponential decay with  $\tau_1$ ,  $\tau_2$  and  $\tau_3$  being 0.54, 12.0 and 132  $\mu$ s, respectively. In the nanosecond time scale, a major emission intensity decay for **7** corresponds to  $\tau = 5.0$  ns, while the lifetime distribution is similar to observed for **6**. The complexity of the decay processes does not allow for the strict attribution of the relaxation pathways for **7**, as the set of observations can be explained by different scenarios. For

instance, slower room temperature decay on the nanosecond scale for **7** in comparison with **6** may be related with difference in fast phonon-assisted nonradiative decay<sup>89</sup> due to different sample structure (presumably, continuous CdSe network for **7** vs. superlattice of non-covalently bonded nanoclusters for **6**). Similar rates of emission decay for **7** and **6** on the microsecond time scale may refer to radiative and nonradiative transitions due to trapped states related with the same surface ligands for both samples (*i.e.*,  $\text{PhSe}^-$ ; lifetimes  $> 100 \mu\text{m}$ ).<sup>89</sup> Then, considerably faster decay for **7** in comparison with **6** on a millisecond time scale may be related to a smaller  $\text{PhSe}^-/\text{Se}^{2-}$  ratio in the case of **7**.

Knowing the internal organization within the hexagonal prisms was assumed to be the key for better understanding the optical properties of material **7**. Since very similar composition and optical properties were observed for smaller and larger hexagonal prisms found in **7**, the difference in sample size seems not to be induced by the difference in nature of the material. As fewer defects were usually found with the smaller prisms, it makes them more convenient for sample preparation for electron microscopy examination. A relatively small ( $\sim 3.2 \mu\text{m}$  between opposite corners of hexagonal base) hexagonal prism was localized in **7** under a SEM (Figure 5.21, *left*) and used for sample preparation by FIB milling. Note that the sample of **7** selected was not separated from the accompanying by-product, and thus also contains some shapeless aggregates. A thin slice was obtained perpendicular to the main axis of the hexagonal prism (Figure 5.21, *right*). An assumption is made that such a slice is representative of the elements throughout the internal structure of the hexagonal prism.

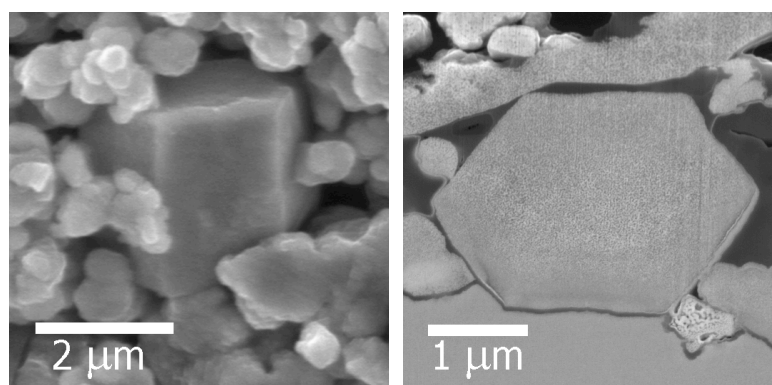


**Figure 5.21:** SEM images of small hexagonal prism **7** surrounded by shapeless aggregates (*left*) and of the thin slice, prepared from the same hexagonal prism by selective material ablation using FIB (*right*). On the right image the sample is tilted, and cross-section of the prism (close to regular hexagon) appears to be distorted.

STEM and TEM examination of the as-prepared slice reveal that the inner part of the hexagonal prism is heterogeneous (Figure 5.22, *left*). Due to the intergrowth nature of the internal structure, specific particle sizes are not discernible for the visible constituent elements, which appear as brighter regions on STEM and as darker regions on TEM images (Figure 5.22, *center* and *right*, respectively). No obvious pattern can be found for the constituent elements; with electron microscopy imaging looking at a two-dimensional projection, the exact internal structure of the prism **7** in three dimensions can hardly be unraveled without special experiments (*e.g.*, electron tomography and/or three-dimensional modeling). Intriguing is that clear gradients in the size of constituent elements can be seen from lateral face to the center of the prism (Figure 5.22, *center*), while in the localized areas (*e.g.*, central part only or small fragment closer to the edge only) the constituent elements appear to be approximately the same in size. The obtained images can be interpreted in two alternative ways: 1) the prism is composed of individual CdSe nanoparticles of different size (a size gradient from smaller particles at the surface to larger ones at the center); or 2) the prism represents continuous three-dimensional network of solid CdSe material (an inorganic phase thickness gradient changing in nano scale from thinner walls at the surface to thicker ones at the center). In both cases CdSe domains alternate with other domains that are more transparent to the electron beam (most likely, organics). The key difference between these two interpretations is whether CdSe forms a discrete (nanoparticles) or continuous (interconnected walls) phase.

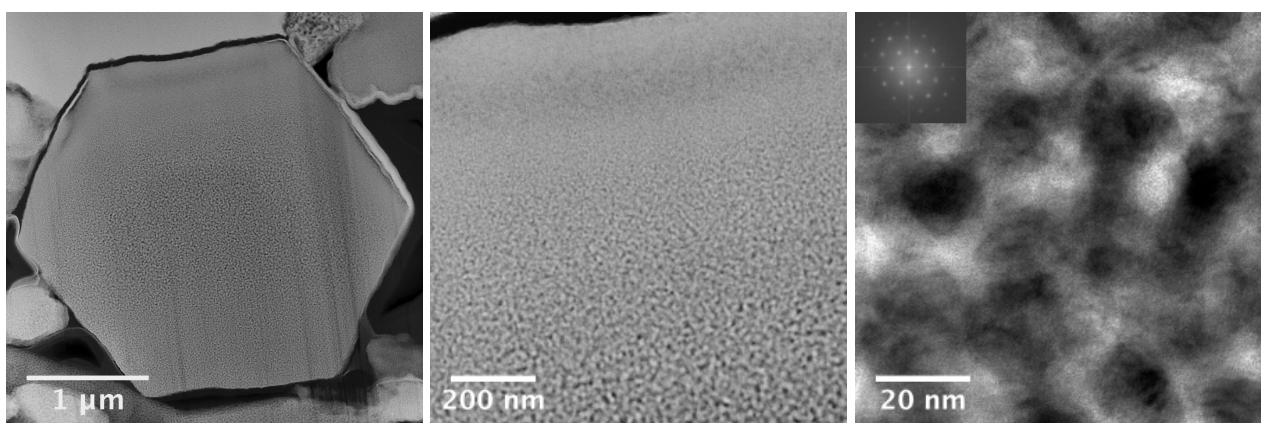


**Figure 5.22:** STEM images of thin slice through hexagonal prism **7**: general view (*left*); gradient from face to center shown from top to bottom (*center*). TEM image of central part of hexagonal prism (*right*). Insert: Fourier transform of TEM image showing reflections due to crystalline CdSe structure.

The hexagonal prism appears to be crystalline with visible rows of atoms (Figure 5.22, *right*). Fourier transform of the TEM images of the central part of the hexagonal prism shows individual spots due to a coherent crystalline CdSe structure throughout the (continuous) examined areas (Figure 5.22, *right, inset*); similar results were also obtained while analyzing TEM images of other parts of the prism. The electron diffraction patterns, obtained for several parts inside the prism, contain well-separated reflections, indicating an identical orientation of a CdSe crystalline lattice (Figure 5.23), as if the hexagonal prism would be a single crystal with a pore-like structure. Additional bright-field and dark-field TEM images are in agreement with single-crystal-like behaviour of **7** (Figure 5.24), as uniform crystalline lattice orientation can be observed through the whole slice of hexagonal prism.

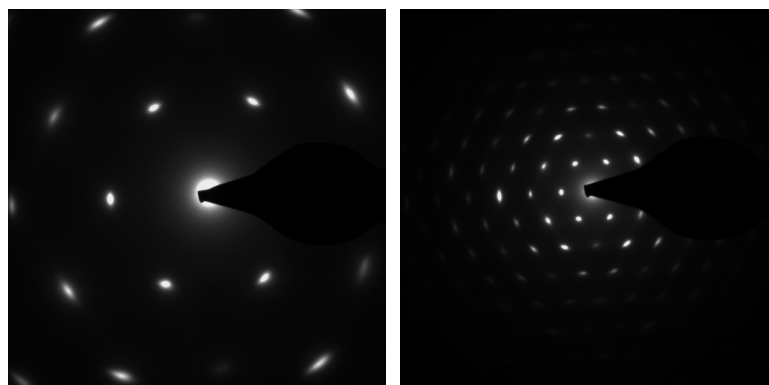


**Figure 5.23:** SAED of the thin slice of hexagonal prism **7**: low-angle (*left*) and wide-angle (*right*) reflections, characterizing the long-range order and CdSe crystalline lattice of the inorganic phase, respectively.

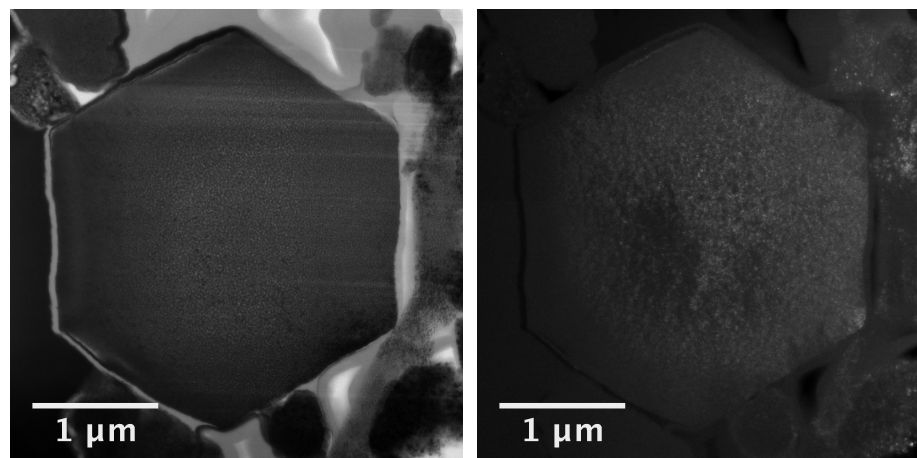


**Figure 5.24:** Bright-field (*left*) and dark-field (*right*) TEM of the thin slice of hexagonal prism **7**.

A perfect alignment of the CdSe crystalline lattice throughout continuous domains in apparently heterogeneous formation could only be possible when there is a strong interaction (connection) between constituent components. Thus, different degrees of partial alignment of an intramolecular crystalline lattice are usually observed in superlattices of individual nanoclusters, as only relatively weak (*e.g.*, van der Waals) cluster-cluster interactions hold the order in secondary structure. In the wide-angle electron diffraction patterns of such superlattices, segmented rings are typically observed. Dried **6** and related superlattices of larger CdS nanoclusters<sup>63,98</sup> represent such a case. Unlike in the case of nanocluster superlattice, individual reflections are seen in the wide-angle electron diffraction patterns for **7**. Hence, both TEM and SEAD provide evidence in favor of a three-dimensional crystalline CdSe network in **7**, interspaced with a second phase (most probably, organic matter). A superstructure represented with a single crystal having complex morphology was reported by Nogami *et al.*,<sup>99,100</sup> with crystalline Pt primary particles (~5 nm in size) assembled into porous secondary structures in the shape of cubes (20–80 nm in length) in such a way that they have a coherent crystalline structure, as confirmed by TEM and SAED.

The presence of a three-dimensional crystalline CdSe network provides background for explaining the optical properties of material **7**. Thus, the substantial red shift of solid state emission maximum in comparison with **6** (for which the same origin of radiative transitions, *i.e.*, trapped emission related with surface  $\text{PhSe}^-$  ligands, can be suggested) can be rationalized taking into account different surface curvature and larger surface-to-volume ratio in **7** vs. **6**. The larger size of constituent elements in **7** vs. **6** would not likely cause such a red shift, as trapped emission was previously reported to be virtually size-independent.<sup>46</sup> The difference in structures for **7** and **6** will also qualitatively explain the difference in emission decay of these materials, as a continuous network would have, for instance, different parameters for phonon-assisted nonradiative decay vs. superlattice of individual nanoclusters. The difference in positions of the medium-strong band in Raman spectra, assigned to the stretching vibrations of interior Cd–Se bonds (197 and 201  $\text{cm}^{-1}$  for **7** and **6**, respectively) argues in favor of such an interpretation.

A three-dimensional crystalline CdSe network in **7** could potentially be disordered or possess secondary (with respect to crystalline lattice) order. In the latter case such ordered secondary structure can be referred to as a mesostructure, *i.e.*, material with the properties intermediate between amorphous and crystalline solids and comprising constituent elements with sizes between 2 and 50 nm.<sup>101–103</sup> Despite the apparent lack of regular pattern seen on electron microscopy images, the right geometrical shape of the hexagonal prisms is most probably related to intricate internal periodicity. The presence of reflections in the low-angle region of the PXRD patterns for **7** also suggests that certain long range order exists. Additional examination (*e.g.*, electron tomography) may help to gain more information about the internal structure of the hexagonal prisms.

Vapour phase, solution-based and solid-state preparation of crystalline micro- and nanoparticles possessing a shape of hexagonal platelets or hexagonal prisms was reported previously for many metal chalcogenide systems, including d-block (*e.g.*, Ni, Cu or Cd)<sup>104–110</sup> and main group metals (*e.g.*, In, Sn or Sb)<sup>111–116</sup> as well as multinary systems (*e.g.*, Bi-Sb and Yb-Sb).<sup>117,118</sup> In the majority of cases the growth of anisotropic particles is related with the inherent anisotropy of a crystal structure (*e.g.*, the shape is dictated by the trigonal unit cell) or different reactivity of crystal facets (including the facet-specific adsorption of ligands), while some exceptions are also known. For instance, STEM and SAED examination of solvothermally-prepared single crystalline Sb<sub>2</sub>Te<sub>3</sub> hexagonal nanoplatelets and several intermediates (isolated upon process quenching at different reaction times) revealed apparently amorphous intermediate possessing hexagonal shape.<sup>119</sup> Micrometer sized particles in the shape of hexagonal platelets representing a superlattice of nearly monodisperse CdSe nanoparticles were also reported.<sup>120</sup> To the best of our knowledge, no CdSe hexagonal prisms having heterogeneous (porous) single crystal structure have been reported.

A supposition can be made that the three-dimensional crystalline CdSe network in **7** is created by fusion of pre-formed crystalline CdSe nanoparticles. Results of analyses (Appendix B) of the orange material lacking a distinctive shape, present among the products of solvothermal synthesis along with red hexagonal prisms **7**, support this. The



orange material is found to be non-regular aggregates of polydisperse CdSe nanoparticles (larger than nanoclusters in **6**) with stabilizing organic shell of primarily  $\text{PhSe}^-$  ligands.

Particle-mediated crystallization *via* oriented attachment mechanism was previously discussed as a possible (non-classical) pathway of crystalline materials formation.<sup>18–22</sup> This mechanism assumes irreversible self-assembly of nanometer-sized crystalline building blocks into continuous superstructure by alignment and fusion of appropriate crystal facets. An atomic matching of the facets in a process of such connection leads to the formation of iso-oriented crystalline lattice in continuous homo- or heterogeneous material.<sup>121,122</sup> In the first case the process results in conventional crystals, while in the second it results in crystalline mesostructures, such as porous single crystals and sponge crystals.<sup>123</sup> Oriented attachment is different from nanocluster self-assembly into an ordered superlattice in the strength of the cohesive forces, which are covalent cluster-cluster bonding in the first case and non-covalent interactions (*e.g.*, electrostatic or van der Waals) in the second case. In turn, oriented attachment is different from random aggregation (coalescence) by the presence of strong alignment preference for crystalline nanoparticles fusion.<sup>124</sup> A few examples of three-dimensional crystalline mesostructures achieved by oriented attachment for group 12-16 compounds include self-assembly of ~5 nm ZnO crystalline nanoparticles into highly uniform ZnO mesoporous ellipsoids with length and width up to 190 and 111 nm, respectively.<sup>125</sup>

Similar to these, the formation of hexagonal prisms **7** may occur through several consecutive steps (Figure 5.25): 1) growth of crystalline faceted CdSe nanoparticles, stabilized by  $\text{PhSe}^-$  ligands; 2) assembly and alignment of primary CdSe nanoparticles into metastable formation (kept together by relatively weak forces, like van der Waals) with iso-oriented crystalline lattices of individual building blocks; 3) docking and fusion of oriented primary CdSe nanoparticles into continuous solid CdSe network with remnants of original organic stabilizers (*i.e.*,  $\text{PhSe}^-$  ligands). In other words, upon the oriented attachment the individual nanoparticles build up *walls* of continuous solid CdSe network (seen as brighter regions on STEM and as darker regions on TEM images, Figure 5.22). The resulting three-dimensional network retains the size-related properties of its nanodimensional constituents, as thickness of the CdSe walls is related to the

dimensions of primary CdSe nanoparticles. According to this scheme, the cracking of hexagonal prisms **7** is rather related with network shrinkage accompanying formation of mesoporous nanomaterials<sup>126</sup> than removal of crystallization solvent from non-covalently bonded nanocluster superlattice, as it is proposed for **6**.

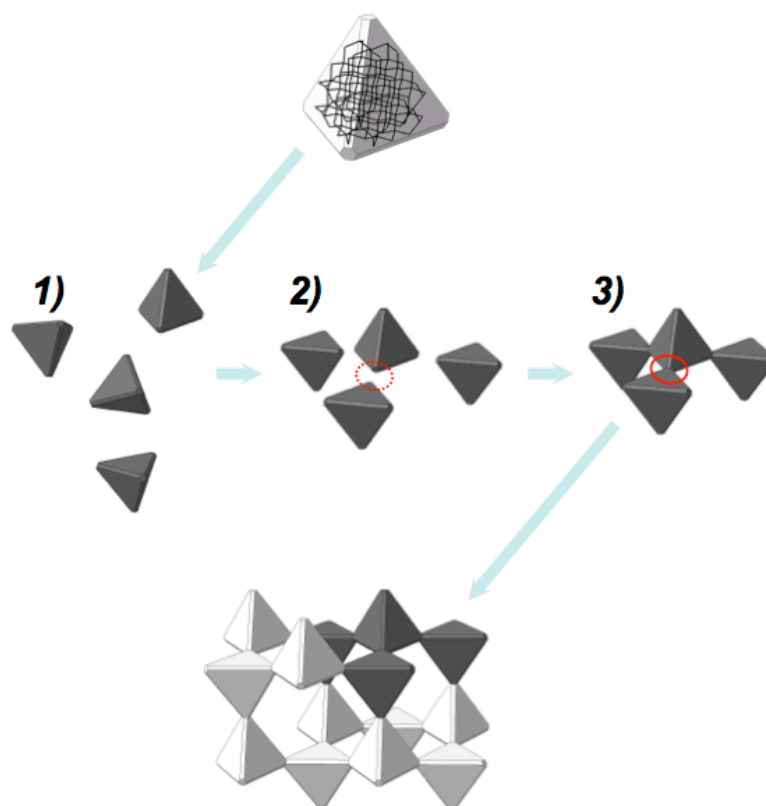


**Figure 5.25:** Schematic representation of a possible pathway for stepwise formation of the three-dimensional CdSe network in hexagonal prisms **7**: 1) growth of primary crystalline nanoparticles; 2) assembly and alignment into metastable formation (cohesive forces act between particular crystalline facets – pointed out on the scheme with dotted line oval); 3) docking and fusion of iso-oriented primary nanoparticles into continuous solid CdSe network (covalent bonds formation between particular crystalline facets – pointed out on the scheme with solid line oval).

*Top:* crystalline CdSe core is shown for the primary truncated tetrahedral nanoparticle, used for the model. *Bottom:* the dark-grey colour highlighting used to show the place of an arbitrary chosen self-assembled fragment in continuous three-dimensional CdSe network. See text for further details.

While the synthetic pathway towards **6** allows for considerable variation of selected reaction parameters (*e.g.*, precursor concentration, volume of solution, solvothermal treatment duration and temperature), the preparation of **7** as well-faceted hexagonal prisms is much more demanding in terms of reproducing most favorable reaction conditions, otherwise a similar red product but lacking distinct morphological features is obtained (Figure 5.26). This observation may be explained with high sensitivity of oriented attachment pathway (especially on assembly, alignment and fusion steps) to reaction conditions changes.

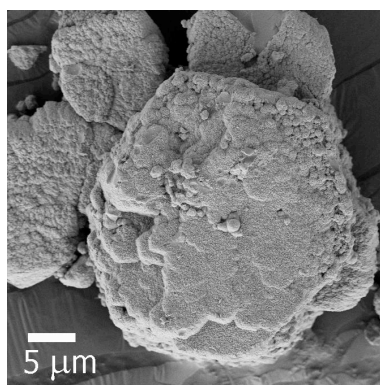


**Figure 5.26:** SEM images of red material (heavily distorted hexagonal prisms) prepared under conditions similar to those for **7** but smaller ratio between precursor and additive was used.

Unlike **6** where nanoclusters are derived from tetrahedra, the shape of the primary nanoparticles, participating in the formation of hexagonal prisms **7**, is most probably more complex. The fact to be taken into consideration is that the fusion of triangular faces of tetrahedra will not result in formation of porous three-dimensional network. TEM examination of both hexagonal prisms **7** and the accompanying orange material does not allow definite conclusions to be made. Truncated polyhedral shapes (*e.g.*, cubes with different level of truncation) was proposed previously for crystalline nanoparticles forming superstructures *via* oriented attachment.<sup>100,127</sup> The shape of truncated tetrahedra was concluded previously for large CdS nanoclusters prepared under solvothermal conditions.<sup>98</sup> In the case of CdSe nanoparticles participating in the formation of **7**, a reasonable assumption also includes the shape of truncated tetrahedra. These faceted nanoparticles are structurally related to capped supertetrahedral CdSe nanoclusters but missing the capping

hexagonal cages at all vertexes, resulting in purely cubic CdSe framework (see a model on Figure 5.25). Alignment and fusion of such truncated tetrahedral CdSe nanoparticles is supposed to occur by hexagonal facets (at missing vertexes), leading to porous crystalline (cubic) CdSe secondary structure. The fusion of matching facets of truncated tetrahedral nanoparticles explains the perfect alignment of CdSe crystalline lattice throughout the continuous regions of the secondary structure of **7**. The formation of the three-dimensional CdSe network by fusion of large truncated tetrahedral nanoparticles is consistent with relatively low organic ligand content for **7** in comparison with **6**, revealed by Raman spectroscopy. From these analyses it also follows that the organic component in the heterogeneous structure **7** is mainly surface  $\text{PhSe}^-$  ligands of the CdSe network. As the size of visible constituent elements (corresponding to CdSe wall thickness) is not the same throughout the hexagonal prisms but has clearly discernible gradient from larger to smaller from center to surface on TEM images, it is apparent, that the primary nanoparticles participating in three-dimensional CdSe network formation in **7** have some polydispersity (unlike nanoclusters in **6**, which are all identical to each other). To understand the wall thickness gradient in the prisms, it can be suggested that the majority of the primary nanoparticles took part in the self-assembly process via fusion into the three-dimensional crystalline CdSe network. However, the similarity of the constituent component size seen on higher resolution electron microscopy images of selected parts of the hexagonal prism (*e.g.*, only in the center or only localized area closer to the edge) allows to propose that the primary nanoparticles of the same size tend to self-assemble simultaneously, forming distinct areas in the secondary structure (Figure 5.27). The wall thickness gradient can originate from the successive self-assembly (largest first, then progressively smaller and smaller) due to the size-selective solubility.

To complete the picture, the orange material lacking a distinctive shape can be viewed as some portion of the primary CdSe nanoparticles building blocks found in **7**, for which self-assembly step has not occurred in the same way as it happened during hexagonal prism formation. Consequently, fusion into a continuous network by oriented attachment was not possible for this portion of the primary nanoparticles, and they mostly flocked together as a polycrystalline material. The absence of a fusion step is consistent with possibility to dissolve the orange material (at least in part) in DMF, while red hexagonal prisms **7** are insoluble.

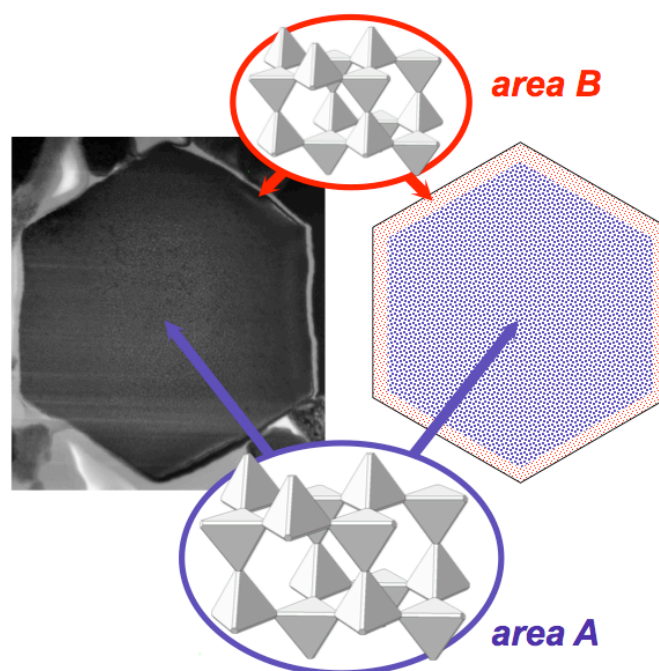


**Figure 5.27:** Schematic representation of a possible nature for the CdSe wall thickness gradient in hexagonal prisms **7**: the size of primary CdSe nanoparticles in the center (*area A*) is larger than the size of nanoparticles near the edge (*area B*). See text for further details.

### 5.3 Conclusions

Two distinct superstructures of nanoscopic CdSe were prepared using solvothermal conversion of the same cadmium selenophenolate precursor  $[\text{Me}_4\text{N}]_2[\text{Cd}(\text{SePh})_4]$ . The first is a superlattice of monodisperse CdSe nanoclusters and the second – unique porous CdSe single crystal. Nanoclusters were crystallized as cubic crystals ( $\leq 0.5$  nm in size) after solvothermal treatment at 200 °C in DMF. Molecular formula  $(\text{Me}_4\text{N})_4[\text{Cd}_{54}\text{Se}_{32}(\text{SePh})_{48}(\text{dmf})_4]^{4-}$  was proposed for this material based on single crystal X-ray diffraction and a set of auxiliary analyses (including Raman spectroscopy and TGA). Some peculiarities of this large nanocluster superlattice (including triggered-by-autoclave-opening crystallization and superlattice rearrangement upon drying) were observed. UV–vis absorption and PLE spectra of nanoclusters  $[\text{Cd}_{54}\text{Se}_{32}(\text{SePh})_{48}(\text{dmf})_4]^{4-}$ , comparing with those of smaller members of the same capped supertetrahedral cluster family, are consistent with the previously established trends, as they show systematical

shift of the low-energy peak positions due to quantum confinement effect and composition change. In contrast to this, results of PL spectra of nanoclusters  $[\text{Cd}_{54}\text{Se}_{32}(\text{SePh})_{48}(\text{dmf})_4]^{4-}$  are rather unexpected, as distinct room temperature emission is observed both in solutions and in solid state. Detailed examination (including time-resolved PL measurements) points to the conclusion that the emission is associated with forbidden states involving the selenophenolate  $\text{PhSe}^-$  surface ligands (trapped emission), which is unusual to be detected at room temperature. Further experiments will help to elucidate the nature for observed “unquenching” in presence of  $\text{PhSe}^-$  surface ligands in  $[\text{Cd}_{54}\text{Se}_{32}(\text{SePh})_{48}(\text{dmf})_4]^{4-}$  nanoclusters.

A second CdSe superstructure was isolated as red hexagonal prisms ( $\leq 70 \mu\text{m}$  in size) among the products of the solvothermal treatment under similar conditions but with addition of CTAB. The presence of three-dimensional CdSe network having a coherent crystalline structure inside hexagonal prisms was concluded based on powder X-ray diffraction, SAED and electron microscopy imaging. As it was revealed by Raman spectroscopy, an organic component of in the network is represented with  $\text{PhSe}^-$  ligands on surface. Self-assembly *via* oriented attachment of crystalline nanoparticles is discussed as the most probable mechanism of formation of porous CdSe single crystal hexagonal prisms. Neither  $\text{Br}^-$  nor any long-tail alkylammonium residues were detected in the final product. The role of  $\text{Br}^-$  in the superstructure growth may lie in facilitating the fusion of lower-nuclearity intermediates during the solvothermal process with formation of primary nanoparticles as well as in subsequent fusion of oriented nanoparticles into continuous CdSe network. Red hexagonal prisms also exhibit distinct trapped emission at room temperature; maximum in solid state PL spectrum is remarkably red-shifted in comparison with that for  $[\text{Cd}_{54}\text{Se}_{32}(\text{SePh})_{48}(\text{dmf})_4]^{4-}$  nanoclusters superlattice. The difference in optical properties of two prepared superstructures is attributed to their unlike morphology.

Obtained results give an insight into the solvothermal preparation of nanoscopic CdSe materials with intriguing structure and unprecedented optical properties. This information may potentially help in tuning properties and rationally designing architecture of functional materials targeting application in electronics and optoelectronics.

## 5.4 Experimental Section

### 5.4.1 Syntheses

All synthetic and handling procedures were carried out under an atmosphere of high-purity dried nitrogen using standard double manifold Schlenk line techniques and a MBraun Labmaster 130 glovebox.

Solvents were purchased from Caledon. Tetrahydrofuran (THF) was dried by passing through packed columns of activated alumina using a commercially available MBraun MB-SP Series solvent purification system. Acetonitrile and methanol were dried and distilled over  $\text{CaH}_2$ . Water, acetonitrile and  $N,N'$ -dimethylformamide (DMF) were deoxygenated using Schlenk and cannula techniques by sparging with nitrogen. Diphenyl diselenide,  $\text{Ph}_2\text{Se}_2$ ; anhydrous cadmium chloride,  $\text{CdCl}_2$ ; tetramethylammonium chloride,  $\text{Me}_4\text{NCl}$ ; and hexadecyltrimethylammonium bromide, CTAB, were purchased from Sigma-Aldrich; sodium (sticks in mineral oil) was from Alfa Aesar. All solid reagents were reagent ( $\geq 98\%$ ) grade or higher and were not further purified.

**NaSePh** was synthesized by a modification of the published procedures<sup>128,129</sup> by reduction of  $\text{Ph}_2\text{Se}_2$  with sodium in THF and product re-crystallization from acetonitrile.  $\text{Ph}_2\text{Se}_2$  (5 g; 16 mmol) was dissolved in the small volume of THF (40–50 ml). Resulting transparent orange solution was added to freshly cut into small pieces sodium sticks (0.81 g; 35.2 mmol) and the mixture was stirred vigorously using magnetic stirrer for 6–8 h. Catalytic amount of naphthalene allows easier initiation and reaction rate enhancement: after < 15 min reaction mixture had turned cloudy, progressively accumulating large amount of fine white precipitate of NaSePh. Precipitate was isolated by filtration (with Celite®) and dried under vacuum on filter. Crude product was dissolved by running warm acetonitrile (~100 ml) through the filter and collecting the filtrate. Product was isolated by filtration and dried under vacuum. This procedure can be successfully scales up to  $\times 10$  times retaining relatively high yield (~85%).

**(Me<sub>4</sub>N)<sub>2</sub>[Cd(SePh)<sub>4</sub>]** was synthesized by a modification of published procedure for  $(\text{Et}_4\text{N})_2[\text{Cd}(\text{SPh})_4]$ <sup>130</sup> by reaction of  $\text{CdCl}_2$  with NaSePh and  $\text{Me}_4\text{NCl}$  in acetonitrile.  $\text{CdCl}_2$  (0.37 g; 2 mmol) was mixed using magnetic stirrer with deoxygenated water

(1.1 ml) and acetonitrile (5 ml); resulting emulsion/suspension was heated up with stirring until homogeneous transparent solution was obtained. NaSePh (1.79 g; 10 mmol) was dissolved in acetonitrile (30 ml), then warm solution of CdCl<sub>2</sub> was added in small portions and stirred for 30 min (producing a lot of white fluffy precipitate of NaCl). Resulting suspension was combined with a suspension of Me<sub>4</sub>NCl (0.438 g; 4 mmol) in acetonitrile (50 ml), stirred for 1–2 h and filtered with Celite®. (Washing residue on filter by extra portion of acetonitrile (5–10 ml) helps to increase the product yield.) The volume of the filtrate was then reduced under vacuum in about 5 times until incipient crystallization; the solution was gently warmed almost to boiling and then cooled slowly to –20° C. The white crystalline product was isolated by rapid filtration on air, washed with cold acetonitrile and methanol and dried under vacuum. This procedure can be successfully scaled up to ×10 times. Product was re-crystallized from acetonitrile (solubility in boiling solvent ~0.07 g/ml). Yield 90%, after re-crystallization 82%.

Solubility of (Me<sub>4</sub>N)<sub>2</sub>[Cd(SePh)<sub>4</sub>] at room temperature in acetonitrile ~0.016 g/ml; in DMF ~0.14 g/ml.

Syntheses of CdSe nanoscopic superstructures **6** and **7** were performed in a sealed reactor (autoclave) at controlled temperature and increased pressure using DMF (solvothermal conditions). The reagents were mixed and sealed in autoclaves under inert atmosphere in the glovebox; heating the sealed autoclaves in an oven was performed under ambient atmosphere, while product isolation was performed under inert atmosphere.

*Preparation of 6* can be achieved using a range of selected reaction parameters (such as precursor concentration, volume of solution, duration and temperature of solvothermal treatment). Typical synthetic procedure was as follows: (Me<sub>4</sub>N)<sub>2</sub>[Cd(SePh)<sub>4</sub>] (1.062 g; 1.20 mmol) was combined with DMF (5 ml) in a 30 mL glass bottle and mixed with magnetic stirrer for 15–30 min resulting colourless solution over a small amount of undissolved precursor. The bottle was sealed in a stainless steel autoclave and placed into preheat oven at 200 °C for 24 h. The oven was then opened, and the sealed autoclave was allowed to cool naturally to ambient temperature over ~2 h. The autoclave was opened and reaction solution (turbid orange-yellow liquid) was immediately filtered (0.22 μm,



PTFE 100/pk membrane, Dikma Technologies Inc.) and left undisturbed at room temperature. Yellow cubic crystals of **6** rapidly grow (mainly over the period 2–24 h; after several days or even few weeks more identical crystals may appear). The crystals with some mother liquor were used for single-crystal and powder X-ray diffraction (“fresh **6**”); for other analyses material was isolated and dried (“dry **6**”) as follows. The crystals were collected by centrifugation at 4000 rpm for 5 min, quickly washed with small portion of acetonitrile and several times with copious amount of methanol, then dried under vacuum for 1–2 h. Mass yield ~0.05 g.

**6** can also be prepared as the main product using different precursor concentration. Thus, similar procedure but taking less  $(\text{Me}_4\text{N})_2[\text{Cd}(\text{SePh})_4]$  (0.664 g; 0.75 mmol and less) allows for delayed crystallization of **6**, with solid phase becoming noticeable in > 6 h. Similar procedure but using extra  $(\text{Me}_4\text{N})_2[\text{Cd}(\text{SePh})_4]$  (1.150 g; 1.30 mmol and more) results in appearance of solid by-product, which is already present in the reaction mixture upon cooling down and opening the autoclave after solvothermal treatment, while crystallization of **6** starts in a few hours. (This by-product, fine orange material, shows broad diffraction patterns corresponding to nanocrystalline CdSe in wide-angle region of PXRD. For by-product solution in DMF low-energy absorption band was found at ~465 nm (fwhm ~60 nm). On the basis of the empirical formula proposed by Yu *et al.*,<sup>69</sup> this would correspond to CdSe nanoparticles with average diameter 2.06 nm. Based on PXRD and UV–vis absorption spectroscopy, the orange by-product was assumed to be a mixture of CdSe nanoparticles larger than **6**.) Longer time for the solvothermal treatment (*i.e.*, 2, 4, and 6 days) also results in increased amount of orange by-product coming along with **6**. Temperature of the solvothermal treatment can be decreased (*e.g.*, 190 and 180 °C) still producing **6** as the main product.

*Preparation of 7.* The procedure for the preparation of **7** was generally similar to that used for **6** except particular modifications. Thus, solvothermal synthesis in this case was performed in Teflon bottles sealed with Teflon tape; attempts to reproduce synthesis in glass bottle resulted in less morphologically sophisticated product.  $(\text{Me}_4\text{N})_2[\text{Cd}(\text{SePh})_4]$  (1.51 g; 1.71 mmol) was combined with DMF (5 ml) and mixed with magnetic stirrer for 15–30 min resulting colourless solution over noticeable amount of undissolved precursor.

CTAB (0.311 g; 0.85 mmol) was added and stirrer for another 15–30 min producing white suspension. The bottle was sealed in a stainless steel autoclave and placed into preheat oven at 200 °C for 48 h. The oven was then opened, and the sealed autoclave was allowed to cool naturally to ambient temperature over ~2 h. The autoclave was left undisturbed for another 48 h and then opened; very turbid orange liquid and brick-red heavy solid product (often attached to inside walls and bottom of Teflon bottle) were typically found. Brick-red solid (the main product) was separated from orange solid by-product using multiple washing with DMF: the red fraction is insoluble in DMF and sediments quickly, while the orange fraction is slightly soluble in DMF and stays suspended unless centrifugated. Brick-red solid was washed well with MeOH and dried under vacuum for 1–2 h. Mass yield 0.03–0.06 g.

#### 5.4.2 Single-Crystal X-ray Diffraction

Crystals of **6** suitable for single-crystal X-ray diffraction were taken directly from the reaction solutions, selected under Paratone N oil, and mounted on a Mitegen polyimide micromount. All X-ray measurements were made on a Bruker Kappa Axis Apex2 diffractometer in a nitrogen stream at 110 K. Graphite-monochromated Mo K $\alpha$  radiation ( $\lambda = 0.71073 \text{ \AA}$ ) was used for the measurements. The unit cell dimensions were determined from a symmetry constrained fit of 9603 reflections with  $6.02^\circ < 2\theta < 37.72^\circ$ . The data collection strategy was a number of  $\omega$  and  $\phi$  scans, which collected data up to  $37.714^\circ$  ( $2\theta$ ). The frame integration was performed using the SAINT program (Bruker AXS Inc., version 2013.8). The resulting raw data were scaled and absorption corrected using a multiscan averaging of symmetry equivalent data using the SADABS program (Bruker AXS Inc., version 2012.1).

The structure of **6** was solved by using a dual space methodology in the SHELXT program (Bruker AXS Inc., version 2014). All nonhydrogen atoms were obtained from the initial solution. The structural model was fit to the data using full matrix least-squares based on  $|F^2|$ . The calculated structure factors included corrections for anomalous dispersion from the usual tabulation. The structure was refined using the SHELXL-2014 program package from the SHELXTL suite of crystallographic software.<sup>131</sup> All of the Cd, Se, and O atoms were refined anisotropically. The apex ligands (probably, DMF) could

not be found in the residual electron density except for the Cd-bonded O atom. No C atoms belonging to phenyl rings were distinguished near any of Se atoms on the tetrahedron edges. The residual electron density was treated as a diffused contribution without specific atomic positions using the program package PLATON (Squeeze).<sup>132</sup> For the structure of **6**, PLATON calculates a void volume of 10675 Å<sup>3</sup> containing 3347 electrons. Graphic plots and simulated powder patterns (peak shape parameter 0.1°) were produced using the Mercury program suite.

### 5.4.3 Characterization

Elemental analysis (CHNS) was performed by Laboratoire d'Analyse Élémentaire de l'Université de Montréal (Quebec, Canada). The values of nitrogen found for **6** were less than the minimum detection limit (0.3%). Results are reported as an average of two measurements.

Calcd for Cd<sub>54</sub>S<sub>80</sub>C<sub>316</sub>H<sub>316</sub>N<sub>8</sub>O<sub>4</sub> ((Me<sub>4</sub>N)<sub>4</sub>[Cd<sub>54</sub>Se<sub>32</sub>(SePh)<sub>48</sub>(dmf)<sub>4</sub>): C, 22.76; H, 1.91; N, 0.67%

Calcd for Cd<sub>54</sub>S<sub>80</sub>C<sub>324</sub>H<sub>288</sub>N<sub>4</sub>O<sub>4</sub> ([Cd<sub>54</sub>Se<sub>28</sub>(SePh)<sub>52</sub>(dmf)<sub>4</sub>): C, 23.32; H, 1.74; N, 0.34%

Found for **6**: C, 23.67; H, 1.64; N, 0.28%

Powder X-ray diffraction (PXRD) patterns of the samples were obtained using a Rigaku Rotaflex RU-200 BVH rotating-anode X-ray diffractometer with a Co K $\alpha$  ( $\lambda = 1.79026$  Å) radiation. X-ray generator (Rigaku Rotaflex RTP 300 RC) was operated at 45 kV and 160 mA, with monochromation being achieved using a curved crystal, diffracted beam, and graphite monochromator. The normal scan rate of 10° 2 $\theta$ /min for the instrument is equivalent to 0.5° on conventional diffractometers. X-rays were collimated using 1° divergent and scatter slits and a 0.15 mm receiving slit. The samples (in the form of thick crystals suspension in Paratone N oil or a fine powder) were placed on a standard glass holder and measured from 2 to 82° 2 $\theta$  with a scan rate of 2° 2 $\theta$ /min and a sampling interval of 0.02°. Low-angle parts (from 2 to 12° 2 $\theta$ ) were additionally measured with the a scan rate of 0.5° 2 $\theta$ /min and a sampling interval of 0.01°.

Optical micrograph images were taken using Zeiss Stemi 2000 optical microscope.

SEM imaging and energy-dispersive X-ray (EDX) spectroscopy analysis were performed using a LEO (Zeiss) 1540XB FIB/SEM system. Prior to imaging, a thin film of amorphous

osmium metal was deposited on the samples using a Filgen osmium plasma coater OPC80T to prevent charging and reduce damage from the electron beam during imaging.

TEM images and selected area electron diffraction (SAED) patterns were acquired using an image aberration corrected Titan 80-300 (FEI) operated at an acceleration voltage of 300 kV and equipped with an S-UTW EDX detector (EDAX) and a US1000 CCD camera (Gatan). STEM images were acquired using a high-angle annular dark field (HAADF) detector with a nominal spot size of 0.14 nm. Imaging was performed in dark-field and bright-field transmission electron microscopy (DF and BF TEM, respectively) and HAADF-STEM modes; the electron beam current/exposure time used for analysis was limited to minimize morphological changes in the samples. The SAED patterns were processed using the Digital Micrograph (Gatan) script PASAD.

Two different procedures, 1) dry dispersing and 2) focused ion beam (FIB) milling, were applied to prepare solid samples for morphological and compositional characterization by electron microscopy.

In the dry preparation method, a small amount of solid material was dispersed directly onto a holey carbon copper TEM grid coated with an additional 2 nm carbon film (Quantifoil). This method was used, for instance, to prepare samples of 6.

In the FIB preparation method, thin slices (lamellae) of the material under study were prepared: a Strata 400s DualBeam FIB (FEI) was used for in situ lift-out in a focused ion beam (FIB) system with parallel SEM imaging. The solid material was first covered with a protective carbon coating. A platinum protective coating was added (thick layer) at the target location, and the lamella was lifted after applying FIB milling and attached to a lift-out microscopy grid (Omicron). The lamella was further thinned to a thickness of 50–100 nm. The initial cutting was performed using 30 kV Ga<sup>+</sup> ions with final polishing at 5 kV. This method was used, for instance, to prepare samples of 7.

FT Raman spectra were recorded on a Bruker RFS 100/S FT Raman spectrometer equipped with a Nd<sup>3+</sup>/YAG laser operating at a wavelength of 1064 nm and a liquid nitrogen-cooled Ge detector. Typical laser powers ranged from 50 to 400 mW at the sample (fine powder in

a glass capillary). 1024 spectra were averaged for each sample; the resolution used was  $2\text{ cm}^{-1}$ . Spectra were corrected for background using OPUS software.

Thermal gravimetric analyses (TGA) were conducted on a Q600 SDT TA instrument: samples of about 15 mg were placed in an alumina crucible with a lid and heated at a rate of  $1\text{ }^{\circ}\text{C}/\text{min}$  from room temperature to  $800\text{ }^{\circ}\text{C}$  under nitrogen flow ( $100\text{ mL}/\text{min}$ ).

Mass spectra were recorded on a Bruker micrOTOF II instrument (electrospray ionization) in  $1000\text{--}20000\text{ m/z}$  range.

Fluorescence images were collected on a Zeiss LSM510 META Multiphoton Confocal Laser Scanning Microscope equipped with an AxioCam HRm CCD camera, using a  $488\text{ nm}$  excitation line from an Argon laser and air ( $\times 20$ ,  $0.5\text{ NA}$ ) or oil immersion ( $\times 63$ ,  $1.4\text{ NA}$ ) objectives. The emission of the samples (crystals on glass substrate) was collected above  $505\text{ nm}$  using a longpass filter.

Solution UV–vis absorption spectra were acquired using a Varian Cary 50 Bio or Scan UV–vis spectrometers at  $25\text{ }^{\circ}\text{C}$  in  $1\text{ cm}$  quartz cells against pure solvent. To obtain saturated solutions, solid sample ( $1\text{--}30\text{ mg}$ ) was stirred with deoxygenated solvent ( $1\text{--}10\text{ mL}$ ) for about  $15\text{ min}$  under nitrogen atmosphere. Such solutions, if necessary, were then diluted by pure solvent and/or filtered through a syringe filter ( $0.22\text{ }\mu\text{m}$ , PTFE  $100/\text{pk}$  membrane, Dikma Technologies Inc.). The multipeak fitting of the spectra was carried out with Gaussian function using OriginPro 9.1 software.

UV–vis diffuse reflectance spectra of the solid samples were recorded using a Shimadzu UV–vis–NIR spectrophotometer UV-3600 with an integrating sphere attachment ISR-3100. Barium sulfate was used as reflectance standard and as the diluting matrix for the finely ground samples. To compare with absorption spectra, diffuse reflectance spectra were converted to the Kubelka–Munk function and normalized.

Photoluminescence (PL) and photoluminescence excitation (PLE) spectra were acquired using a Photon Technology International Inc. Quanta Master (QM) fluorescence spectrofluorometers equipped with xenon lamps. QM 4 and 7 were used for low- and room temperature measurements, respectively. Room temperature measurements were performed

using DMF solutions (prepared as described above for UV–vis absorption spectroscopy) in conventional 1 cm quartz cells. For measurements carried out at 77 K, frozen samples were obtained by using DMF solutions dropped into a quartz Dewar vessel containing liquid nitrogen, where solid glassy droplets sank into quartz cell coupled with the vessel.

Fluorescence lifetime imaging microscopy (FLIM) experiments were carried out on a Leica confocal fluorescence microscope (TCS SP2, Wetzlar, Germany) equipped with a time-correlated single-photon counting (TCSPC) module (PicoHarp 300, PicoQuant). Samples were excited at 800 nm with a pulsed Ti:sapphire laser system (Mira 900, Coherent) with a repetition rate of 76 MHz. Fluorescence signal was collected through an oil immersion objective (x63, 1.32 NA), the scanning area for the image was set to  $512 \times 512$  pixels and the emission was collected below 750 nm.

Solid state PL spectra and time-resolved PL decay data were acquired at room temperature using the experimental setup designed by Zalloum *et al.*<sup>133</sup> An excitation beam from laser diode (US-Lasers, Inc.) with wavelength  $405 \pm 10$  nm and power output of 120 mW was filtered using a low pass (405 nm) filter. The emitted fluorescence was filtered using a long pass (450 nm) filter and analyzed using a HRS-BD1-200 Mightex Spectrometer equipped with CCD multichannel detector with entrance slit size 10  $\mu\text{m}$  and wavelength range 300–1050 nm. Calibration and data processing were performed with custom-made code using Matlab (version 2014) software.

Schematic diagram of the setup used in time-resolved PL decay measurements is shown in Figure 5.28. A focusing lens directs emitted light towards the R7400U-20 Hamamatsu photomultiplier tube (PMT) with a spectral range of 300–900 nm, and peak sensitivity at 630 nm. The PMT signal was read by a 14 bit precision digital oscilloscope Cleverscope CS320A with averaging by 128 curves. The rise and the fall times of the laser intensity were approximately 250 ns, which determines the system resolution since the PMT response is much faster. The laser on and off periods were 2 ms in duration, sufficiently long to bring the excitation of the sample into equilibrium, and to allow the emitted light to decay to the noise floor of the PMT. TRPL data were collected using homemade LabVIEW software (National Instruments) and analyzed using OriginPro 9.1 software.

To prepare samples for solid state PL measurements, a small amount of solid material was suspended in 1–2 ml of EtOH. One drop of such a suspension was placed on a cleaned microscopy glass slide or Si wafer and allowed to evaporate; procedure was repeated until desired density of coverage was achieved. Then the substrate with a sample was thoroughly dried, finally under vacuum.

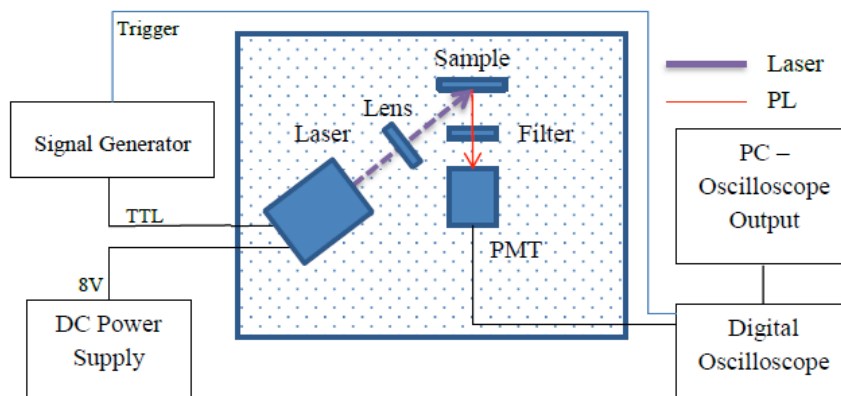


**Figure 5.28:** Schematic of the experimental setup used for TRPL measurements.

## 5.5 References

- (1) Vanmaekelbergh, D. *Nano Today* **2011**, 6 (4), 419.
- (2) Gao, Y.; Tang, Z. *Small* **2011**, 7 (15), 2133.
- (3) Talapin, D. V. *Mrs Bull.* **2012**, 37 (1), 63.
- (4) Hanrath, T. *J. Vac. Sci. Technol. A* **2012**, 30 (3), 30802.
- (5) Huang, M. H.; Thoka, S. *Nano Today* **2015**, 10 (1), 81.
- (6) Xu, L.; Ma, W.; Wang, L.; Xu, C.; Kuang, H.; Kotov, N. A. *Chem. Soc. Rev.* **2013**, 42 (7), 3114.
- (7) Talapin, D. V.; Lee, J.-S.; Kovalenko, M. V.; Shevchenko, E. V. *Chem. Rev.* **2010**, 110 (1), 389.
- (8) Nozik, A. J.; Beard, M. C.; Luther, J. M.; Law, M.; Ellingson, R. J.; Johnson, J. C. *Chem. Rev.* **2010**, 110 (11), 6873.
- (9) Yang, J.; Choi, M. K.; Kim, D.-H.; Hyeon, T. *Adv. Mater.* **2016**, 28 (6), 1176.
- (10) Collier, C. P.; Vossmeier, T.; Heath, J. R. *Annu. Rev. Phys. Chem.* **1998**, 49, 371.
- (11) Bishop, K. J. M.; Wilmer, C. E.; Soh, S.; Grzybowski, B. A. *Small* **2009**, 5 (14), 1600.
- (12) Zheng, N. F.; Bu, X. H.; Lu, H. W.; Zhang, Q. C.; Feng, P. Y. *J. Am. Chem. Soc.* **2005**, 127 (34), 11963.
- (13) Bendova, M.; Puchberger, M.; Schubert, U. *Eur. J. Inorg. Chem.* **2010**, No. 21, 3299.
- (14) Vossmeier, T.; Reck, G.; Schulz, B.; Katsikas, L.; Weller, H. *J. Am. Chem. Soc.* **1995**, 117 (51), 12881.

- (15) Feng, P.; Bu, X.; Zheng, N. *Acc. Chem. Res.* **2005**, 38 (4), 293.
- (16) Yang, X.-L.; Zhang, J.; Ren, S.-B.; Li, Y.-Z.; Huang, W.; Du, H.-B.; You, X.-Z. *Inorg. Chem. Commun.* **2010**, 13 (11), 1337.
- (17) Vossmeier, T.; Reck, G.; Katsikas, L.; Haupt, E.; Schulz, B.; Weller, H. *Science* **1995**, 267 (5203), 1476.
- (18) Niederberger, M.; Cölfen, H. *Phys. Chem. Chem. Phys.* **2006**, 8 (28), 3271.
- (19) Zhang, Q.; Liu, S.-J.; Yu, S.-H. *J. Mater. Chem.* **2009**, 19 (2), 191.
- (20) Bahrig, L.; Hickey, S. G.; Eychemüller, A. *Crystengcomm* **2014**, 16 (40), 9408.
- (21) Lu, C.; Tang, Z. *Adv. Mater.* **2016**, 28 (6), 1096.
- (22) De Yoreo, J. J.; Gilbert, P. U. P. A.; Sommerdijk, N. A. J. M.; Penn, R. L.; Whitelam, S.; Joester, D.; Zhang, H.; Rimer, J. D.; Navrotsky, A.; Banfield, J. F.; Wallace, A. F.; Michel, F. M.; Meldrum, F. C.; Cölfen, H.; Dove, P. M. *Science* **2015**, 349 (6247), aaa6760.
- (23) Tang, Z. Y.; Kotov, N. A.; Giersig, M. *Science* **2002**, 297 (5579), 237.
- (24) Cho, K. S.; Talapin, D. V.; Gaschler, W.; Murray, C. B. *J. Am. Chem. Soc.* **2005**, 127 (19), 7140.
- (25) Koh, W.; Bartnik, A. C.; Wise, F. W.; Murray, C. B. *J. Am. Chem. Soc.* **2010**, 132 (11), 3909.
- (26) Li, Z.; Sui, J.; Li, X.; Cai, W. *Langmuir* **2011**, 27 (6), 2258.
- (27) Sarkar, S.; Acharya, S.; Chakraborty, A.; Pradhan, N. *J. Phys. Chem. Lett.* **2013**, 4 (19), 3292.
- (28) Wang, Z.; Schliehe, C.; Wang, T.; Nagaoka, Y.; Cao, Y. C.; Bassett, W. A.; Wu, H.; Fan, H.; Weller, H. *J. Am. Chem. Soc.* **2011**, 133 (37), 14484.
- (29) Boneschanscher, M. P.; Evers, W. H.; Geuchies, J. J.; Altantzis, T.; Goris, B.; Rabouw, F. T.; van Rossum, S. a. P.; van der Zant, H. S. J.; Siebbeles, L. D. A.; Van Tendeloo, G.; Swart, I.; Hilhorst, J.; Petukhov, A. V.; Bals, S.; Vanmaekelbergh, D. *Science* **2014**, 344 (6190), 1377.
- (30) Sanchez, C.; Soler-Illia, G.; Ribot, F.; Lalot, T.; Mayer, C. R.; Cabuil, V. *Chem. Mater.* **2001**, 13 (10), 3061.
- (31) Cheetham, A. K.; Rao, C. N. R.; Feller, R. K. *Chem. Commun.* **2006**, No. 46, 4780.
- (32) Vaqueiro, P. *Dalton Trans.* **2010**, 39 (26), 5965.
- (33) Zhang, Q.; Bu, X.; Lin, Z.; Wu, T.; Feng, P. *Inorg. Chem.* **2008**, 47 (21), 9724.
- (34) Chen, Z.; Luo, D.; Luo, X.; Kang, M.; Lin, Z. *Dalton Trans.* **2012**, 41 (14), 3942.
- (35) Zheng, N. F.; Bu, X. H.; Lu, H. W.; Chen, L.; Feng, P. Y. *J. Am. Chem. Soc.* **2005**, 127 (43), 14990.
- (36) Zheng, N.; Bu, X.; Lauda, J.; Feng, P. *Chem. Mater.* **2006**, 18 (18), 4307.
- (37) Kagan, C. R.; Murray, C. B. *Nat. Nanotechnol.* **2015**, 10 (12), 1013.
- (38) Garcia-Rodriguez, R.; Hendricks, M. P.; Cossairt, B. M.; Liu, H.; Owen, J. S. *Chem. Mater.* **2013**, 25 (8), 1233.
- (39) Lee, G. S. H.; Craig, D. C.; Ma, I.; Scudder, M. L.; Bailey, T. D.; Dance, I. G. *J. Am. Chem. Soc.* **1988**, 110 (14), 4863.
- (40) Eichhöfer, A.; Hampe, O. *J. Clust. Sci.* **2007**, 18 (3), 494.
- (41) Herron, N.; Calabrese, J.; Farneth, W.; Wang, Y. *Science* **1993**, 259 (5100), 1426.
- (42) Behrens, S.; Bettenhausen, M.; Deveson, A. C.; Eichhöfer, A.; Fenske, D.; Lohde, A.; Woggon, U. *Angew. Chem.-Int. Ed. Engl.* **1996**, 35 (19), 2215.



- (43) Soloviev, V. N.; Eichhöfer, A.; Fenske, D.; Banin, U. *J. Am. Chem. Soc.* **2000**, *122* (11), 2673.
- (44) Beecher, A. N.; Yang, X.; Palmer, J. H.; LaGrassa, A. L.; Juhas, P.; Billinge, S. J. L.; Owen, J. S. *J. Am. Chem. Soc.* **2014**, *136* (30), 10645.
- (45) Matheis, K.; Eichhöfer, A.; Weigend, F.; Ehrler, O. T.; Hampe, O.; Kappes, M. M. *J. Phys. Chem. C* **2012**, *116* (25), 13800.
- (46) Soloviev, V. N.; Eichhöfer, A.; Fenske, D.; Banin, U. *J. Am. Chem. Soc.* **2001**, *123* (10), 2354.
- (47) Warren, B. E. *X-ray diffraction*; Addison-Wesley series in metallurgy and materials; Addison-Wesley Pub. Co: Reading, Massachusetts, 1969.
- (48) Klug, H. P.; Alexander, L. E. *X-ray diffraction procedures for polycrystalline and amorphous materials*, 2d ed.; Wiley: New York, 1974.
- (49) Levchenko, T. I.; Huang, Y.; Corrigan, J. F. **Unpublished results**.
- (50) Morris-Cohen, A. J.; Malicki, M.; Peterson, M. D.; Slavin, J. W. J.; Weiss, E. A. *Chem. Mater.* **2013**, *25* (8), 1155.
- (51) *Landolt-Börnstein: Numerical Data and Functional Relationships in Science and Technology - New Series. II-VI and I-VII Compounds; Semimagnetic Compounds.* Rössler, U. (Ed.); Condensed Matter; Springer: Berlin, 1999; Vol. 41B.
- (52) Rolo, A. G.; Vasilevskiy, M. I. *J. Raman Spectrosc.* **2007**, *38* (6), 618.
- (53) Lin, C.; Kelley, D. F.; Rico, M.; Kelley, A. M. *Acs Nano* **2014**, *8* (4), 3928.
- (54) Richter, H.; Wang, Z. P.; Ley, L. *Solid State Commun.* **1981**, *39* (5), 625.
- (55) Campbell, I. H.; Fauchet, P. M. *Solid State Commun.* **1986**, *58* (10), 739.
- (56) Trallero-Giner, C.; Debernardi, A.; Cardona, M.; Menendez-Proupin, E.; Ekimov, A. I. *Phys. Rev. B* **1998**, *57* (8), 4664.
- (57) Dzhagan, V. M.; Valakh, M. Y.; Raevskaya, A. E.; Stroyuk, A. L.; Kuchmiy, S. Y.; Zahn, D. R. T. *Nanotechnology* **2008**, *19* (30), 305707.
- (58) Nien, Y.-T.; Zaman, B.; Ouyang, J.; Chen, I.-G.; Hwang, C.-S.; Yu, K. *Mater. Lett.* **2008**, *62* (30), 4522.
- (59) Lin, C.; Gong, K.; Kelley, D. F.; Kelley, A. M. *J. Phys. Chem. C* **2015**, *119* (13), 7491.
- (60) Ueyama, N.; Sugawara, T.; Sasaki, K.; Nakamura, A.; Yamashita, S.; Wakatsuki, Y.; Yamazaki, H.; Yasuoka, N. *Inorg. Chem.* **1988**, *27* (4), 741.
- (61) Farneth, W. E.; Herron, N.; Wang, Y. *Chem. Mater.* **1992**, *4* (4), 916.
- (62) Gaumet, J. J.; Khitrov, G. A.; Strouse, G. F. *Nano Lett.* **2002**, *2* (4), 375.
- (63) Levchenko, T. I.; Kübel, C.; Wang, D.; Najafabadi, B. K.; Huang, Y.; Corrigan, J. F. *Chem. Mater.* **2015**, *27* (10), 3666.
- (64) Bendova, M.; Puchberger, M.; Pabisch, S.; Peterlik, H.; Schubert, U. *Eur. J. Inorg. Chem.* **2010**, No. 15, 2266.
- (65) Alivisatos, A. P.; Harris, A. L.; Levinos, N. J.; Steigerwald, M. L.; Brus, L. E. *J. Chem. Phys.* **1988**, *89* (7), 4001.
- (66) Bawendi, M. G.; Wilson, W. L.; Rothberg, L.; Carroll, P. J.; Jedju, T. M.; Steigerwald, M. L.; Brus, L. E. *Phys. Rev. Lett.* **1990**, *65* (13), 1623.
- (67) Ekimov, A. I.; Hache, F.; Schanneklein, M. C.; Ricard, D.; Flytzanis, C.; Kudryavtsev, I. A.; Yazeva, T. V.; Rodina, A. V.; Efros, A. L. *J. Opt. Soc. Am. B-Opt. Phys.* **1993**, *10* (1), 100.

- (68) Eichhöfer, A.; Aharoni, A.; Banin, U. *Z. Für Anorg. Allg. Chem.* **2002**, 628 (11), 2415.
- (69) Yu, W. W.; Qu, L. H.; Guo, W. Z.; Peng, X. G. *Chem. Mater.* **2003**, 15 (14), 2854.
- (70) Gong, K.; Zeng, Y.; Kelley, D. F. *J. Phys. Chem. C* **2013**, 117 (39), 20268.
- (71) Reichardt, C.; Welton, T. *Solvents and solvent effects in organic chemistry*, 4th ed.; Wiley-VCH: Weinheim: Chichester, 2010.
- (72) Bawendi, M. G.; Carroll, P. J.; Wilson, W. L.; Brus, L. E. *J. Chem. Phys.* **1992**, 96 (2), 946.
- (73) Hoheisel, W.; Colvin, V. L.; Johnson, C. S.; Alivisatos, A. P. *J. Chem. Phys.* **1994**, 101 (10), 8455.
- (74) Norris, D. J.; Bawendi, M. G. *J. Chem. Phys.* **1995**, 103 (13), 5260.
- (75) Norris, D. J.; Efros, A. L.; Rosen, M.; Bawendi, M. G. *Phys. Rev. B* **1996**, 53 (24), 16347.
- (76) Norris, D. J.; Sacra, A.; Murray, C. B.; Bawendi, M. G. *Phys. Rev. Lett.* **1994**, 72 (16), 2612.
- (77) Norris, D. J.; Bawendi, M. G. *Phys. Rev. B* **1996**, 53 (24), 16338.
- (78) Brus, L. *IEEE J. Quantum Electron.* **1986**, 22 (9), 1909.
- (79) Henglein, A. *Chem. Rev.* **1989**, 89 (8), 1861.
- (80) Bowers, M. J.; McBride, J. R.; Rosenthal, S. J. *J. Am. Chem. Soc.* **2005**, 127 (44), 15378.
- (81) Aharoni, A.; Eichhöfer, A.; Fenske, D.; Banin, U. *Opt. Mater.* **2003**, 24 (1–2), 43.
- (82) Soloviev, V. N.; Eichhofer, A.; Fenske, D.; Banin, U. *Phys. Status Solidi B-Basic Res.* **2001**, 224 (1), 285.
- (83) Chestnoy, N.; Harris, T. D.; Hull, R.; Brus, L. E. *J. Phys. Chem.* **1986**, 90 (15), 3393.
- (84) Klimov, V. I.; Mikhailovsky, A. A.; McBranch, D. W.; Leatherdale, C. A.; Bawendi, M. G. *Science* **2000**, 287 (5455), 1011.
- (85) Mork, A. J.; Weidman, M. C.; Prins, F.; Tisdale, W. A. *J. Phys. Chem. C* **2014**, 118 (25), 13920.
- (86) Morello, G.; De Giorgi, M.; Kudera, S.; Manna, L.; Cingolani, R.; Anni, M. *J. Phys. Chem. C* **2007**, 111 (16), 5846.
- (87) Sharma, S. N.; Pillai, Z. S.; Kamat, P. V. *J. Phys. Chem. B* **2003**, 107 (37), 10088.
- (88) Nguyen, K. A.; Pachter, R.; Day, P. N.; Su, H. *J. Chem. Phys.* **2015**, 142 (23), 234305.
- (89) Buckley, J. J.; Couderc, E.; Greaney, M. J.; Munteanu, J.; Riche, C. T.; Bradforth, S. E.; Brutchey, R. L. *Acs Nano* **2014**, 8 (3), 2512.
- (90) Dolai, S.; Dass, A.; Sardar, R. *Langmuir* **2013**, 29 (20), 6187.
- (91) Boles, M. A.; Ling, D.; Hyeon, T.; Talapin, D. V. *Nat. Mater.* **2016**, 15 (2), 141.
- (92) Bawendi, M. G.; Kortan, A. R.; Steigerwald, M. L.; Brus, L. E. *J. Chem. Phys.* **1989**, 91 (11), 7282.
- (93) Ingham, B. *Crystallogr. Rev.* **2015**, 21 (4), 229.
- (94) Meyns, M.; Iacono, F.; Palencia, C.; Geweke, J.; Coderch, M. D.; Fittschen, U. E. A.; Gallego, J. M.; Otero, R.; Juarez, B. H.; Klinke, C. *Chem. Mater.* **2014**, 26 (5), 1813.

- (95) Adams, R. D.; Zhang, B.; Murphy, C. J.; Yeung, L. K. *Chem. Commun.* **1999**, No. 4, 383.
- (96) Greaney, M. J.; Couderc, E.; Zhao, J.; Nail, B. A.; Mecklenburg, M.; Thornbury, W.; Osterloh, F. E.; Bradforth, S. E.; Brutchey, R. L. *Chem. Mater.* **2015**, *27* (3), 744.
- (97) Kim, W. D.; Kim, J.-H.; Lee, S.; Lee, S.; Woo, J. Y.; Lee, K.; Chae, W.-S.; Jeong, S.; Bae, W. K.; McGuire, J. A.; Moon, J. H.; Jeong, M. S.; Lee, D. C. *Chem. Mater.* **2016**, *28* (3), 962.
- (98) Levchenko, T. I.; Kübel, C.; Huang, Y.; Corrigan, J. F. *Chem.-Eur. J.* **2011**, *17* (51), 14394.
- (99) Nogami, M.; Koike, R.; Jalem, R.; Kawamura, G.; Yang, Y.; Sasaki, Y. *J. Phys. Chem. Lett.* **2010**, *1* (2), 568.
- (100) Cao, Y.; Yang, Y.; Shan, Y.; Fu, C.; Long, N. V.; Huang, Z.; Guo, X.; Nogami, M. *Nanoscale* **2015**, *7* (46), 19461.
- (101) Antonietti, M.; Ozin, G. A. *Chem.-Eur. J.* **2004**, *10* (1), 28.
- (102) Kanatzidis, M. G. *Adv. Mater.* **2007**, *19* (9), 1165.
- (103) Shi, Y.; Wan, Y.; Zhao, D. *Chem. Soc. Rev.* **2011**, *40* (7), 3854.
- (104) Liu, X.; Hu, R.; Chai, L.; Li, H.; Gu, J.; Qian, Y. *J. Nanosci. Nanotechnol.* **2009**, *9* (4), 2715.
- (105) Chu, L.; Zhou, B.; Mu, H.; Sun, Y.; Xu, P. *J. Cryst. Growth* **2008**, *310* (24), 5437.
- (106) Kumar, P.; Singh, K.; Srivastava, O. N. *J. Cryst. Growth* **2010**, *312* (19), 2804.
- (107) Zhang, X.; Zhang, D.; Tang, H.; Ji, X.; Zhang, Y.; Tang, G.; Li, C. *Mater. Res. Bull.* **2014**, *53*, 96.
- (108) Castro-Guerrero, C. F.; Deepak, F. L.; Ponce, A.; Cruz-Reyes, J.; Del Valle-Granados, M.; Fuentes-Moyado, S.; Galvan, D. H.; Jose-Yacamán, M. *Catal. Sci. Technol.* **2011**, *1* (6), 1024.
- (109) Wang, J.; Feng, H.; Chen, K.; You, T. *Mater. Lett.* **2013**, *104*, 87.
- (110) Lang, D.; Liu, F.; Qiu, G.; Feng, X.; Xiang, Q. *Chempluschem* **2014**, *79* (12), 1726.
- (111) Park, K. H.; Jang, K.; Son, S. U. *Angew. Chem.-Int. Ed.* **2006**, *45* (28), 4608.
- (112) Zhu, Y.; Chen, Y.; Liu, L. *J. Cryst. Growth* **2011**, *328* (1), 70.
- (113) Wang, W. Z.; Poudel, B.; Yang, J.; Wang, D. Z.; Ren, Z. F. *J. Am. Chem. Soc.* **2005**, *127* (40), 13792.
- (114) Shi, W.; Zhou, L.; Song, S.; Yang, J.; Zhang, H. *Adv. Mater.* **2008**, *20* (10), 1892.
- (115) Schulz, S.; Heimann, S.; Friedrich, J.; Engenhorst, M.; Schierning, G.; Assenmacher, W. *Chem. Mater.* **2012**, *24* (11), 2228.
- (116) Liang, Y.; Wang, W.; Zeng, B.; Zhang, G.; Huang, J.; Li, J.; Li, T.; Song, Y.; Zhang, X. *J. Alloys Compd.* **2011**, *509* (16), 5147.
- (117) Ren, W.; Cheng, C.; Xu, Y.; Ren, Z.; Zhong, Y. *J. Alloys Compd.* **2010**, *501* (1), 120.
- (118) Hanifehpour, Y.; Joo, S. W. *J. Nanomater.* **2014**, 452659.
- (119) Saltzmann, T.; Bornhoeft, M.; Mayer, J.; Simon, U. *Angew. Chem.-Int. Ed.* **2015**, *54* (22), 6632.
- (120) Talapin, D. V.; Shevchenko, E. V.; Kornowski, A.; Gaponik, N.; Haase, M.; Rogach, A. L.; Weller, H. *Adv. Mater.* **2001**, *13* (24), 1868.
- (121) Cölfen, H.; Antonietti, M. *Angew. Chem. Int. Ed.* **2005**, *44* (35), 5576.

- (122) Zhang, H.; De Yoreo, J. J.; Banfield, J. F. *Acs Nano* **2014**, *8* (7), 6526.
- (123) Zhou, L.; O'Brien, P. *Small* **2008**, *4* (10), 1566.
- (124) Thanh, N. T. K.; Maclean, N.; Mahiddine, S. *Chem. Rev.* **2014**, *114* (15), 7610.
- (125) Liu, Y.; Wang, D.; Peng, Q.; Chu, D.; Liu, X.; Li, Y. *Inorg. Chem.* **2011**, *50* (12), 5841.
- (126) Dutta, S.; Wu, K. C.-W.; Kimura, T. *Chem. Mater.* **2015**, *27* (20), 6918.
- (127) Evers, W. H.; Goris, B.; Bals, S.; Casavola, M.; de Graaf, J.; van Roij, R.; Dijkstra, M.; Vanmaekelbergh, D. *Nano Lett.* **2013**, *13* (6), 2317.
- (128) Liotta, D.; Markiewicz, W.; Santiesteban, H. *Tetrahedron Lett.* **1977**, No. 50, 4365.
- (129) Ley, S. V.; O'Neil, I. A.; Low, C. M. R. *Tetrahedron* **1986**, *42* (19), 5363.
- (130) Hagen, K. S.; Stephan, D. W.; Holm, R. H. *Inorg. Chem.* **1982**, *21* (11), 3928.
- (131) Sheldrick, G. M. *Acta Crystallogr. Sect. A* **2008**, *64*, 112.
- (132) Spek, A. L. *J. Appl. Crystallogr.* **2003**, *36* (1), 7.
- (133) Zalloum, O. H. Y.; Flynn, M.; Roschuk, T.; Wojcik, J.; Irving, E.; Mascher, P. *Rev. Sci. Instrum.* **2006**, *77* (2), 23907.

## Chapter 6

### Conclusions and Future Directions

#### 6.1 Summary of the synthetic approach: Towards elucidating the mechanism of precursor conversion and finding parameters that govern product structure formation

This thesis reports results on developing a novel approach for the preparation of nanoscopic CdE materials (where E = S or Se). The synthetic approach utilizes conversion of a single source cadmium phenylchalcogenolate precursor  $(\text{Me}_4\text{N})_2[\text{Cd}(\text{EPh})_4]$  in polar organic solvent (*e.g.*, DMF) under solvothermal conditions. Generally, the combination of elevated temperature ( $\leq 200\text{ }^\circ\text{C}$ ) and pressure during solvothermal synthesis is known to allow for increased solubility of reagents and products, speeding up reactions and facilitating crystallization of the product.<sup>1</sup> In this research, the formation of cadmium phenylchalcogenolate intermediate(s) and growth of large  $\text{Cd}_x\text{E}_y(\text{EPh})_z$  clusters was found to be accompanied by the appearance of methylphenyl chalcogenide  $\text{Ph-E-Me}$  and diphenyl chalcogenide  $\text{Ph-E-Ph}$  (Chapter 2). The latter by-product is especially important, because its formation from  $\text{PhE}^-$  occurs with  $\text{E}^{2-}$  release, which is necessary to build up large cluster cores. It was proposed that the presence in reaction mixture of volatile by-products (*e.g.*, trimethylamine  $\text{Me}_3\text{N}$ ) also plays an important role in growth of large  $\text{Cd}_x\text{E}_y(\text{EPh})_z$  clusters (Chapter 5). Performing the reaction in the absence/presence of an alkylammonium halide additive allowed for tuning the diameter of monodisperse nanocluster constituents and directing their self-assembly into micrometer-sized superparticles with different morphologies. It was established that the presence of halide  $\text{Hal}^-$  rather than the nature of  $\text{R}_4\text{N}^+$  governs the growth of a larger cluster core (Chapters 2, 3). Neither  $\text{Hal}^-$  nor residual  $\text{R}_4\text{N}^+$  were found to be present in significant amounts in the resulting nanoscopic CdE materials. Synthetic parameters, such as precursor concentration, time and temperature of the solvothermal treatment and cooling rate were optimized for selected preparation procedures.

## 6.2 New materials prepared

The efficiency of solvothermal conversion of the  $(\text{Me}_4\text{N})_2[\text{Cd}(\text{EPh})_4]$  precursor in the preparation of tetrahedral CdE clusters was illustrated with the crystallization and single crystal X-ray diffraction characterization of  $[\text{Cd}_{54}\text{S}_{32}(\text{SPh})_{48}(\text{dmf})_4]^{4-}$  (**2**) and  $[\text{Cd}_{54}\text{Se}_{32}(\text{SePh})_{48}(\text{dmf})_4]^{4-}$  (**6**), as described in Chapters 2 and 5, respectively. Both molecular clusters have an inorganic core with equivalent spherical diameter of  $\sim 1.3$  nm and form superlattices in the cubic space group  $P-43m$  with the crystal size reaching up to 0.5 mm (edge length).

Chapter 2 describes the preparation of monodisperse clusters of phenylchalcogenolate-stabilized CdS with an inorganic core of 1.9 nm in diameter (**1**). PXRD and electron microscopy provide information on the self-assembly of constituent clusters into superparticles (5–25  $\mu\text{m}$  in size) having a continuous cubic superlattice with a lattice parameter 2.9 nm. While this material, close to the predicted Cd84, has some similarities with superlattices of previously reported tetrahedral Cd32 and Cd54 clusters, several structural features demonstrate the significance of **1** as a transition point from known families of smaller CdS clusters to unexplored larger ones. The shape of neutral clusters in **1** is, most probably, close to truncated tetrahedral, and their surfaces are less rich in  $\text{PhS}^-$ ; the secondary structure of **1** is more complex, with three different orientations for the constituent nanoclusters in 3D superparticles.

Chapters 2 and 3 describe the preparation of even larger frameworks, *i.e.*, monodisperse clusters of phenylchalcogenolate-stabilized CdS with inorganic cores of 2.3 nm in diameter (**4** and **5**), self-assembled into very similar superstructures upon solvothermal conversion of  $(\text{Me}_4\text{N})_2[\text{Cd}(\text{SPh})_4]$  in the presence of  $[\text{Me}_4\text{N}]\text{Br}$  and CTAB, respectively. Composed of the largest characterized monodisperse CdS nanoscale frameworks reported to date, continuous cubic superlattice with a lattice parameter 3.4 nm – in the case of **4** and **5** – resembles the superlattice observed for the smaller clusters in **1**. With the proposed formula  $[\text{Cd}_{130}\text{S}_{103}(\text{SPh})_{54}]$ , **5** is close to predicted tetrahedral Cd123, while the cluster shape is changed further from that of the regular tetrahedron inherent to smaller CdS frameworks.

Along with the crystalline superlattices of progressively larger molecular CdE clusters (1–2, 4–6), the developed method allowed for the preparation of new superstructures of nanoscopic CdE with fascinating morphology (3, 7). Thus, it is reported in Chapter 2 that upon solvothermal treatment of  $(\text{Me}_4\text{N})_2[\text{Cd}(\text{SPh})_4]$  in the presence of  $[\text{Me}_4\text{N}]\text{Cl}$  as an additive, 2.3 nm CdS clusters are formed along with larger nanoparticles that are self-assembled into spherical superparticles 0.5–2.0  $\mu\text{m}$  in size (3). The size-selective segregation upon self-assembly results in the formation of either homogeneous (*H*-spheres, composed of randomly attached 2.3 nm CdS nanoparticles) or core–shell superparticles (*CS*-spheres, having a gradient of CdS nanoparticles ranging in size from 2.5 nm at the surface to 20 nm in the center).

An even more unusual superstructure, a porous CdSe single crystal (7), was isolated as hexagonal prisms (up to 70  $\mu\text{m}$  in size) among the products of the solvothermal treatment of  $(\text{Me}_4\text{N})_2[\text{Cd}(\text{SePh})_4]$  in the presence of CTAB. Self-assembly of a 3D CdSe network – having a coherent crystalline structure throughout the continuous region inside of the hexagonal prisms – was proposed to occur *via* oriented attachment of primary crystalline CdSe nanoparticles in Chapter 5. Additional examination, such as electron tomographic reconstruction, would help to gain more information about the internal structure of the hexagonal prisms, elucidating the mechanism of its formation and creating the background for the future application.

### 6.3 New properties reported

The characterization of superstructures of nanoscopic materials, such as 3D superlattices of large metal and semiconductor clusters, is problematic due to challenges with growing quality single crystals. For such systems valuable structural information can be obtained using complementary characterization techniques, electron microscopy and tomography and SSNMR spectroscopy.

Electron microscopy (including TEM, STEM and SEM) imaging was used to obtain structural information on the superstructures of nanoscopic CdE materials. Thus, despite high electron beam sensitivity of the material, TEM images were obtained for thin areas close to the crystal edge of 6, showing continuous domains of an ordered superlattice of

monodisperse nanoclusters with a measurable lattice parameter 2.05 nm (Chapter 5). Moreover, parameters for the 3D superlattices of monodisperse CdS clusters with inorganic cores of 1.9 and 2.3 nm in diameter were determined; the results are in good agreement with the parameters calculated from PXRD data (Chapters 2 and 3). It must be noted that HR TEM images obtained for the discrete crystalline clusters in both 1.9 and 2.3 nm CdS systems do not allow a definite conclusion about clusters shape to be made. Choosing an optimal sample preparation method (*i.e.*, wet/dry dispersing *vs.* focused ion beam milling and mounting to the microscopic grid) was shown to be crucial to reveal representative structure features of superstructures of nanoscopic CdE materials (Chapters 2 and 5). Tomographic reconstruction was successfully used to visualize 3D superstructure of 2.3 nm CdS clusters and to define more accurately structural parameters of this material (Chapter 3).

As detailed in Chapter 4, systematic  $^{111}\text{Cd}$  SSNMR experiments were performed in order to correlate X-ray crystallographic data from literature sources with SSNMR parameters of a set of materials, varying from molecular crystals of small complexes  $[\text{Cd}(\text{SPh})_4]^{2-}$  and  $[\text{Cd}_4(\text{SPh})_{10}]^{2-}$  to the superlattices of large monodisperse clusters  $[\text{Cd}_{54}\text{S}_{32}(\text{SPh})_{48}(\text{dmf})_4]^{4-}$  and 1.9 nm CdS (*i.e.*, materials **2** and **1**, respectively). Systematic data analysis allowed for assigning individual resonances or resonance groups to particular types of cadmium sites, having chemically and/or crystallographically different coordination environments. For large CdS frameworks, such as **1** and **2**, cadmium resonances were found to form three groups. This result is unusual, since for related systems with size polydispersity and composition variations, such as CdS or CdSe nanoparticles protected with an organic ligand shell, typically only two groups of resonances were observed. Obtained generalized information can be used for the interpretation of  $^{111}\text{Cd}$  SSNMR data for large CdS cluster and nanoparticles, for which crystal structure analysis remains inaccessible.

Comparison of the PXRD patterns for freshly prepared and dried superlattices of large CdE clusters revealed an interesting superstructure re-arrangement (Chapters 4 and 5) that was not observed for the smaller frameworks.



The optical properties, including UV–vis absorption and photoluminescence studies under various conditions were examined for all prepared materials (Chapters 2, 3, and 5), which allowed for the observations of unexpected results. In particular, a distinct, room temperature emission was observed both in solution and in the solid state for **6** (Chapter 5), while an absence of such emission was reported previously for smaller tetrahedral CdSe clusters. Further investigation (*e.g.*, quantum yield experiments) will be necessary for better understanding of the unprecedented room temperature emission of **6** and the exact mechanism for “unquenching” in the presence of  $\text{PhSe}^-$  surface ligands for large CdSe clusters.

#### 6.4 Future Directions

The synthetic approach using solvothermal conversion of mononuclear metal phenylchalcogenolate precursor  $(\text{Me}_4\text{N})_2[\text{M}(\text{EPh})_4]$ , where M represents metal and E – chalcogen, can potentially be extended to Te systems targeting ordered superlattices of large  $[\text{Cd}_x\text{Te}_y(\text{TePh})_z]$  clusters, presumably emitting in near-IR wavelength range. Similar kind of mononuclear metal phenylchalcogenolate precursors can also be used to attempt the solvothermal preparation of other binary ME and ternary MM'E systems to synthesize diverse nanoscopic materials with tailored photophysical properties. In this vein, an incorporation into large molecular MM'Se clusters of specific dopants, such as Mn or Cu ions.

More challenging would potentially be developing solvothermal approach to nanoscopic materials in systems other than group 12-16; in particular, to superlattices of monodisperse  $\text{Zn}_3\text{P}_2$  clusters. The high natural abundance, relatively low cost and danger to environment of  $\text{Zn}_3\text{P}_2$  makes such materials promising candidates for optoelectronic technologies application and underpins the necessity in finding new synthetic approaches.

#### 6.5 References

- (1) Qian, Y. T.; Gu, Y. L.; Lu, J. In *The chemistry of nanomaterials: synthesis, properties and applications* / C.N.R. Rao, A. Müller, A.K. Cheetham (eds.); Weinheim: Wiley-VCH; Chichester: John Wiley, 2004; Vol. 1, pp 170–207.

## Appendix A

**Figure A1:** UV-Vis spectra

**Table A1:** Summary of crystal data

**Figure A2:** SEM images illustrating different stages of FIB preparation for the sample of **1**.

**Figure A3:** SEM images illustrating different stages of FIB preparation for the sample of **3**.

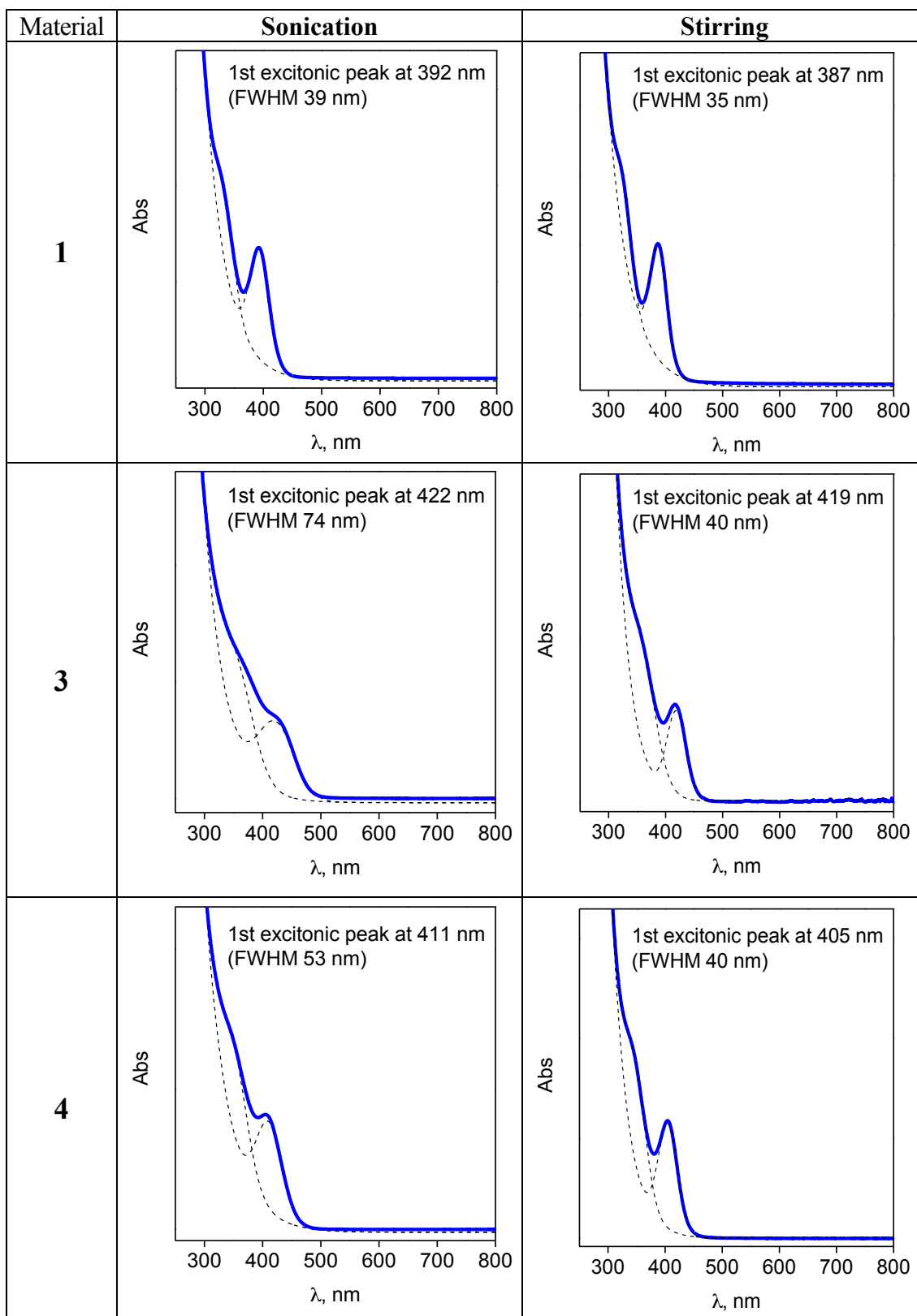


**Figure A1:** UV-Vis spectra of DMF solutions, obtained by re-dissolving of solid materials **1**, **3**, and **4** using sonication or stirring methods. Dashed lines: the multi-peak fitting (Gaussian function).

**Table A1:** Summary of crystal data for **2**.

Formula	C <sub>240</sub> Cd <sub>54</sub> O <sub>4</sub> S <sub>80</sub>
Formula weight, <i>g/mol</i>	11580.83
Crystal dimensions, <i>mm</i>	0.100 × 0.091 × 0.072
Crystal color and habit	colourless cubic
Crystal system	cubic
Space group	<i>P</i> -43 <i>m</i>
Temperature, K	110
<i>a</i> , Å	23.976(8)
<i>b</i> , Å	23.976
<i>c</i> , Å	23.976
$\alpha$ , °	90
$\beta$ , °	90
$\gamma$ , °	90
<i>V</i> , Å <sup>3</sup>	13783(13)
Number of reflections to determine final unit cell	9369
Min & max 2θ for cell determination, °	5.1, 45.82
<i>Z</i>	1
F(000)	5344
$\rho$ , <i>g/cm</i>	1.395
$\lambda$ , Å (Mo K $\alpha$ )	0.71073
$\mu$ , <i>cm</i> <sup>-1</sup>	2.359
Diffractometer type	Bruker Kappa Axis Apex2
Scan type(s)	phi and omega scans
Max 2θ for data collection, °	46.036
Measured fraction of data	0.782
Number of reflections measured	239970
Unique reflections measured	3606
<i>R</i> <sub>merge</sub>	0.0745
Number of reflections included in refinement	3606
Cut off threshold expression	<i>I</i> > 2sigma( <i>I</i> )
Structure refined using	full matrix least-squares using <i>F</i> <sup>2</sup>
Weighting scheme	$w = 1/[\text{sigma}^2(F_o^2) + (0.2000P)^2]$ , where $P = (F_o^2 + 2F_c^2)/3$
Number of parameters in least-squares	100
<i>R</i> <sub>1</sub>	0.1334
<i>wR</i> <sub>2</sub>	0.3504
<i>R</i> <sub>1</sub> (all data)	0.1979
<i>wR</i> <sub>2</sub> (all data)	0.4430
GOF	1.795
Maximum shift/error	0.000
Min & max peak heights on final $\Delta F$ Map ( <i>e</i> /Å)	-2.182, 9.545

where:  $R_1 = \sum(|F_o| - |F_c|) / \sum F_o$ ;  $wR_2 = [ \sum w(F_o^2 - F_c^2)^2 / \sum w F_o^4 ]^{1/2}$

GOF =  $[ \sum w(F_o^2 - F_c^2)^2 / (\text{No. of reflns.} - \text{No. of params.}) ]^{1/2}$

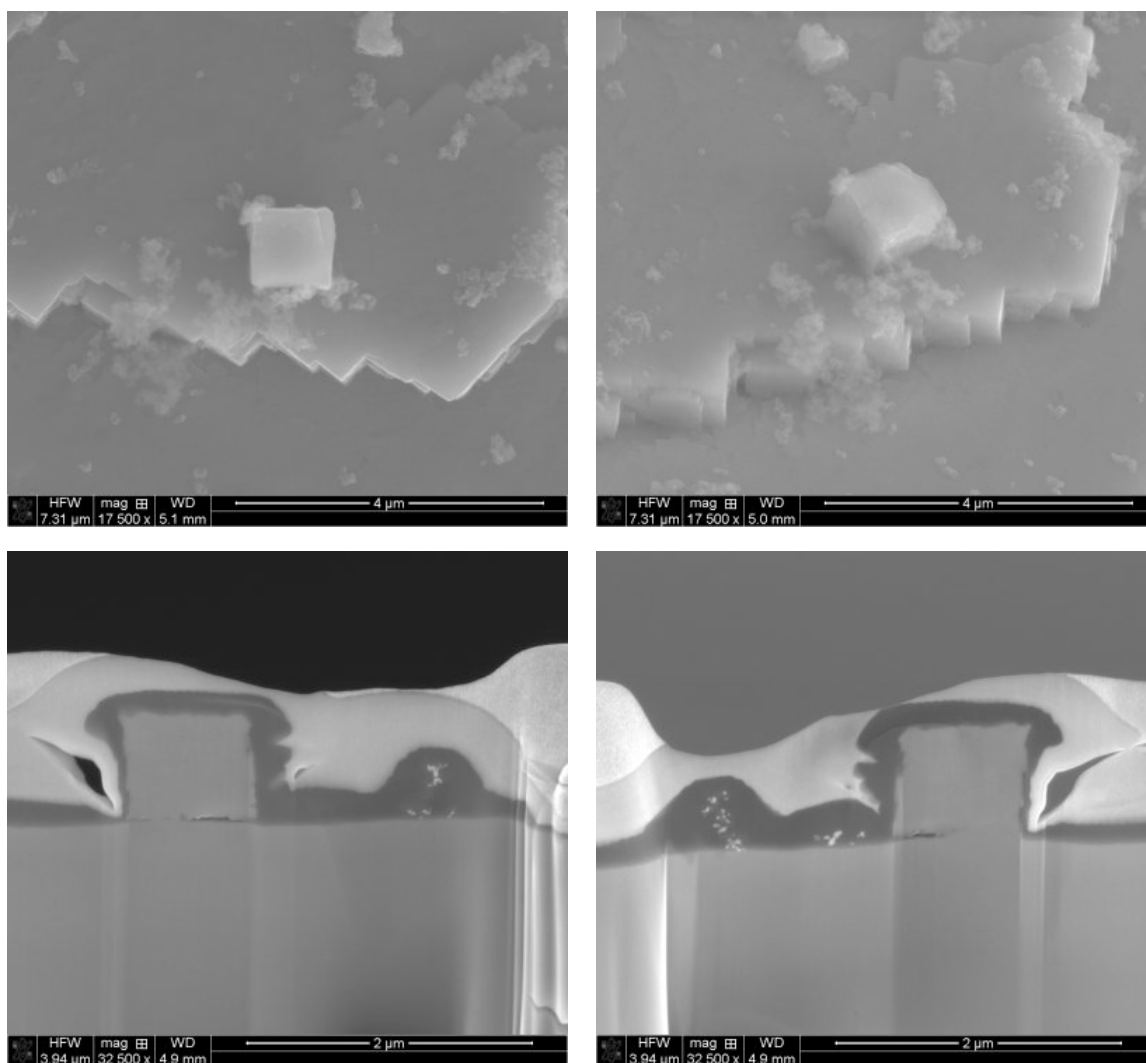


**Figure A2:** SEM images illustrating different stages of FIB preparation for the sample of 1.

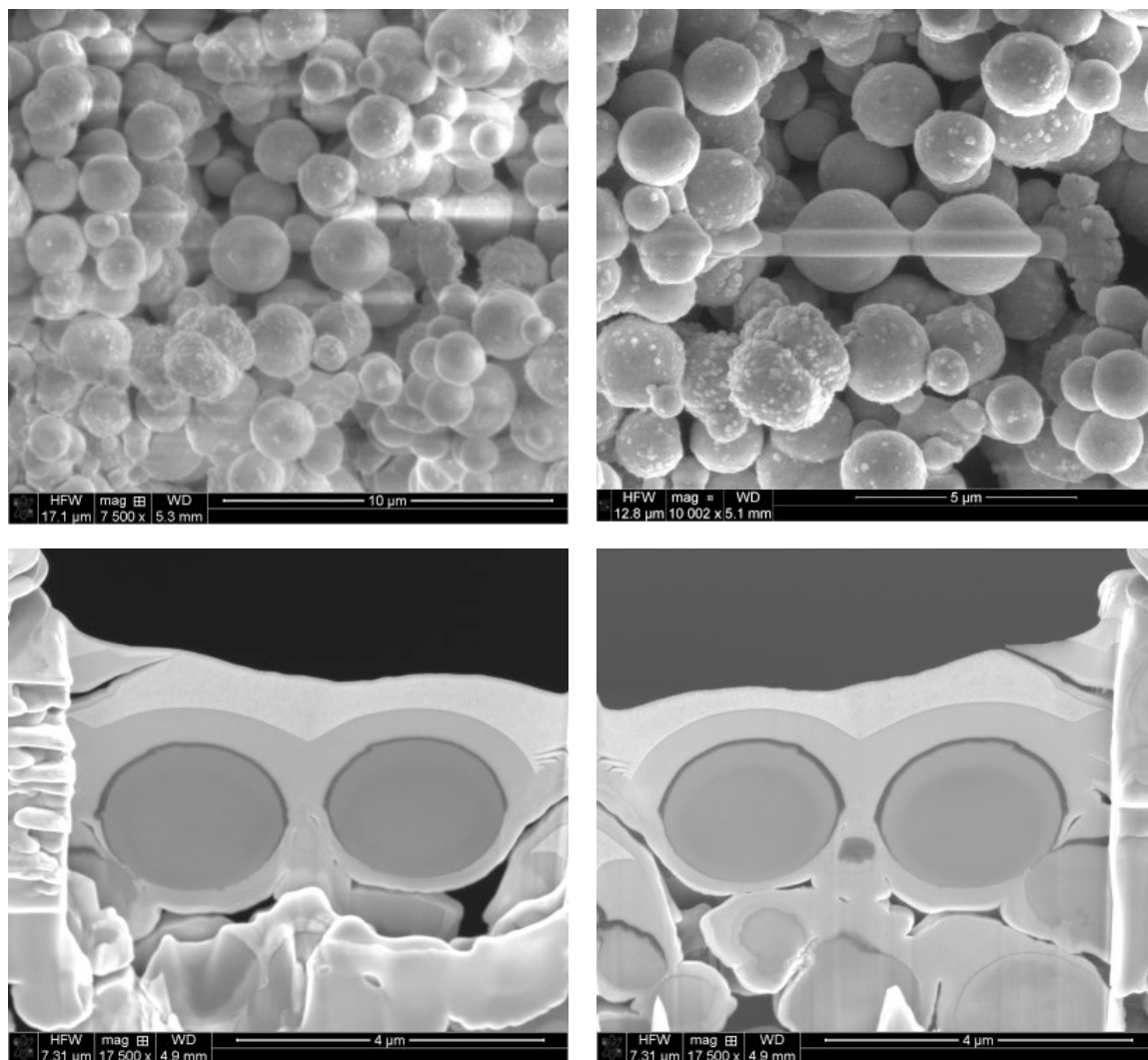


**Figure A3:** SEM images illustrating different stages of FIB preparation for the sample of 3.

## Appendix B

**Table B1:** Summary of crystal data for **6**.

Characterization of orange material (“**8**”) coexisting with red hexagonal prisms **7**:

**Figure B1:** Powder X-ray diffraction pattern (Co K $\alpha$  radiation) of separated, washed and dried material **8** and its relation with the patterns for bulk cubic (bottom stick representation) and hexagonal (top stick representation) CdSe structures.

**Figure B2:** UV–vis absorption spectrum of **8** re-dissolved in DMF. Multi-peak fitting (Gaussian function) is shown by dashed lines.

**Figure B3:** STEM image of **8**: general view (left) and enlarged fragment (right).

**Figure B4:** Wide-angle SAED of **8**, obtained from the different areas.

**Figure B5:** Bright-field (left) and dark-field (right) TEM images of **8**: aggregates with randomly (top) and coherently (bottom) oriented crystalline lattices of constituent nanoparticles.

**Table B1:** Summary of crystal data for **6**.

Formula	Cd <sub>54</sub> O <sub>4</sub> Se <sub>80</sub>
Formula weight, <i>g/mol</i>	12450.40
Crystal dimensions, <i>mm</i>	0.268 × 0.208 × 0.134
Crystal color and habit	yellow cubic
Crystal system	cubic
Space group	<i>P</i> -43 <i>m</i>
Temperature, K	110
<i>a</i> , Å	24.412(6)
<i>b</i> , Å	24.412
<i>c</i> , Å	24.412
$\alpha$ , °	90
$\beta$ , °	90
$\gamma$ , °	90
<i>V</i> , Å <sup>3</sup>	14549(10)
Number of reflections to determine final unit cell	9603
Min & max 2θ for cell determination, °	6.02, 37.72
<i>Z</i>	1
F(000)	5344
$\rho$ , <i>g/cm</i>	1.421
$\lambda$ , Å (Mo K $\alpha$ )	0.71073
$\mu$ , <i>cm</i> <sup>-1</sup>	6.933
Diffractometer type	Bruker Kappa Axis Apex2
Scan type(s)	phi and omega scans
Max 2θ for data collection, °	37.714
Measured fraction of data	0.992
Number of reflections measured	49900
Unique reflections measured	2187
<i>R</i> <sub>merge</sub>	0.0517
Number of reflections included in refinement	2187
Cut off threshold expression	<i>I</i> > 2sigma( <i>I</i> )
Structure refined using	full matrix least-squares with <i>F</i> <sup>2</sup>
Weighting scheme	$w = 1/[\text{sigma}^2(F_o^2) + (0.0100P)^2]$ , where $P = (F_o^2 + 2F_c^2)/3$
Number of parameters in least-squares	72
<i>R</i> <sub>1</sub>	0.1109
<i>wR</i> <sub>2</sub>	0.2345
<i>R</i> <sub>1</sub> (all data)	0.1717
<i>wR</i> <sub>2</sub> (all data)	0.2694
GOF	7.278
Maximum shift/error	0.000
Min & max peak heights on final $\Delta F$ Map ( <i>e</i> <sup>-</sup> /Å)	-1.801, 1.610

where:  $R_1 = \Sigma(|F_o| - |F_c|) / \Sigma F_o$ ;  $wR_2 = [ \Sigma( w( F_o^2 - F_c^2 )^2 ) / \Sigma( w F_o^4 ) ]^{1/2}$

GOF =  $[ \Sigma( w( F_o^2 - F_c^2 )^2 ) / (\text{No. of reflns.} - \text{No. of params.}) ]^{1/2}$



### Characterization of orange material (“8”) coexisting with red hexagonal prisms 7

No peaks are found in the low-angle region of the PXRD for **8**; the wide-angle region of PXRD patterns for **8** is consistent with crystalline nanometer-sized CdSe (Figure B1). The reflections become stronger and sharper in comparison with **7** and especially **6**. The mean size of the crystalline domains by the Scherrer equation in the case of **8** is 2.52 nm, which is larger than 2.26 and 1.55 nm for the dried **7** and **6**, respectively.

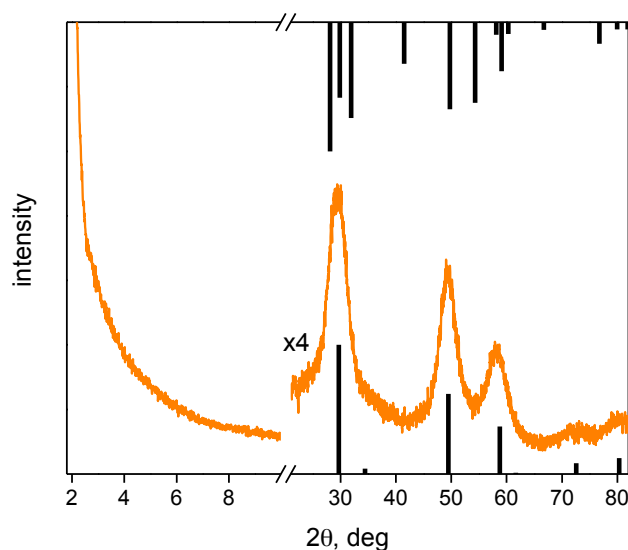


**Figure B1:** Powder X-ray diffraction pattern (Co K $\alpha$  radiation) of separated, washed and dried material **8** and its relation with the patterns for bulk cubic (bottom stick representation) and hexagonal (top stick representation) CdSe structures. Reference structures are from the database of the International Centre for Diffraction Data: hexagonal CdSe no. 04-011-9600; cubic CdSe no. 03-065-2891.

Solubility of **8** in DMF ( $\sim 0.5$  mg/ml) is substantially lower than solubility of **6** in the same solvent. It is possible, that only some fractions from the sample of **8** go into solution; in contrast, **7** was found to be virtually insoluble. In the UV–vis absorption spectra of **8** in DMF (Figure B2), weak excitonic features are observed; peaks at 494 and 419 nm (fwhm for the low-energy peak  $\sim 63$  nm) are found upon the multipeak fitting. These excitonic peaks are shifted to higher wavelengths in comparison with **6** (where the low-energy absorption maximum found at 410 nm), which is in agreement with having species of larger size in **8**. On the basis of the empirical formula proposed by Yu *et al.*<sup>1</sup>,

the low energy absorption peak at 494 nm for **8** would correspond to CdSe nanoparticles with average diameter 2.29 nm. The breadth of the peaks suggests that material **8** is not composed of a homogeneous distribution of clusters of similar size and shape. Such clusters are unlikely to crystallize into regular superlattice or self-assemble *via* oriented attachment into continuous superstructure.

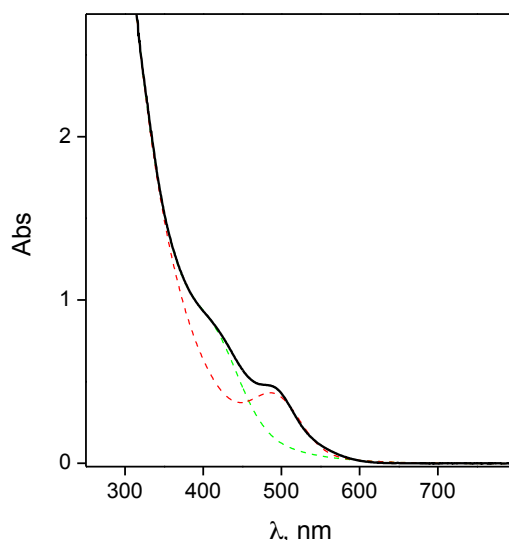


**Figure B2:** UV-vis absorption spectrum of **8** re-dissolved in DMF. Multi-peak fitting (Gaussian function) is shown by dashed lines.

This is in agreement with the results of TEM and STEM, as imaging revealed several distinct types of constituents present in material **8**: 1) discrete polydisperse nanoparticles; 2) nanoparticles of comparable size, apparently fused into complex aggregates or even network-like structure (Figure B3). The largest network fragments are much smaller in size in comparison with network forming hexagonal prisms in **7** and (unlike those prisms) have no a distinctive shape. While for some (larger) nanoparticles straight edges can be discerned, no definite conclusion about shape of individual nanoparticles is possible based on electron microscopy images of material **8**. Both discrete and fused nanoparticles in **8** have visible lattice fringes; wide angle SAED confirms crystalline CdSe (hexagonal) lattice present (Figure B4). Unlike **7**, showing individual reflections in agreement with coherent lattice orientation throughout continuous areas of the sample, well-distinguished rings with some streaks can be found in wide-angle SAED of **8**. Difference in SAED for particular areas in the sample of **8** (*i.e.*, predomination of either rings or streaks, see

Figure B4, left and right, respectively) may reflect different size of constituent elements (relatively smaller or larger randomly oriented crystalline nanoparticles, respectively). Alternatively, some nanoparticle aggregates or small network fragments may have similar orientation of crystalline lattice. The later explanation is also supported by the bright-field and dark-field TEM images of different nanoparticle aggregates in **8**, showing coherent orientation of crystalline lattices of constituent nanoparticles in selected fragment (Figure B5, bottom).

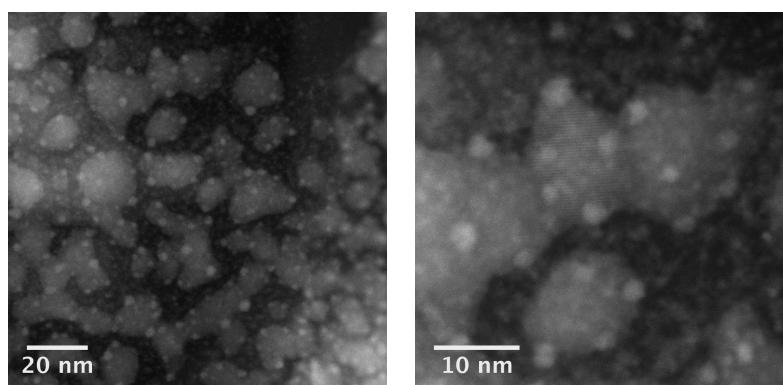


**Figure B3:** STEM image of **8**: general view (left) and enlarged fragment (right).

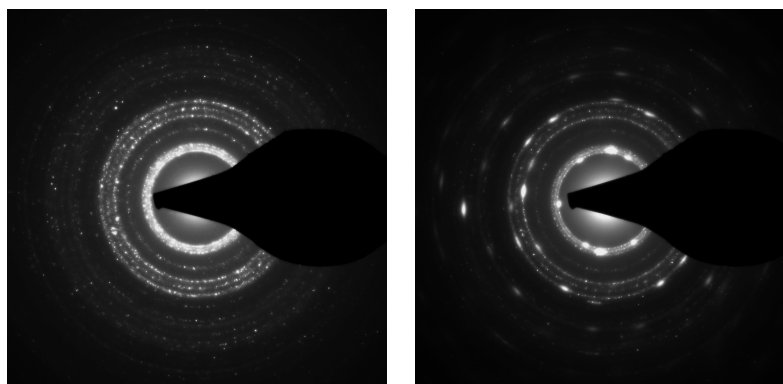


**Figure B4:** Wide-angle SAED of **8**, obtained from the different areas.

The electron microscopy and PXRD data for dried material **8**, as well as optical properties of re-dissolved material **8** show that the constituents are polydisperse CdSe nanoparticles substantially larger than nanoclusters in **6**; no continuous areas of regular secondary structure are produced. This means that  $\text{Br}^-$  indeed promotes further growth of CdSe nanoparticles, though conditions for larger monodisperse nanocluster formation and crystallization into regular superlattice are yet to be found.

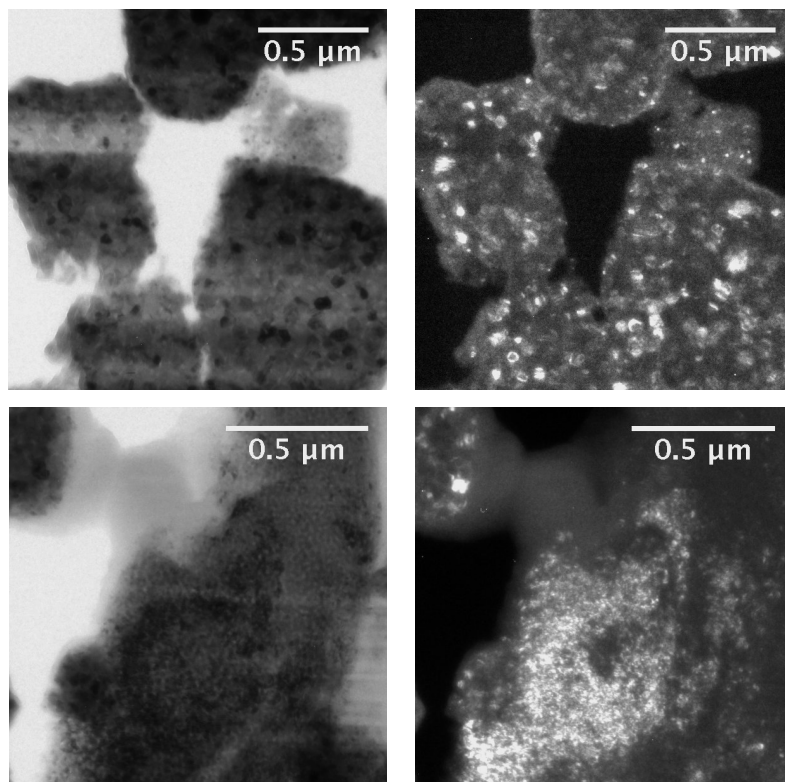


**Figure B5:** Bright-field (left) and dark-field (right) TEM images of **8**: aggregates with randomly (top) and coherently (bottom) oriented crystalline lattices of constituent nanoparticles

### References

- (1) Yu, W. W.; Qu, L. H.; Guo, W. Z.; Peng, X. G. *Chem. Mater.* **2003**, *15* (14), 2854.

## Curriculum Vitae

<b>Name:</b>	<b>Tetyana I. Levchenko</b>
<b>Post-secondary Education and Degrees:</b>	<p>National Taras Shevchenko University Kyiv, Ukraine 1995-1999 B.A.</p> <p>National Taras Shevchenko University Kyiv, Ukraine 1999-2000 M.Sc.</p> <p>The University of Western Ontario London, Ontario, Canada 2009-2010 M.Sc. Candidate</p> <p>The University of Western Ontario London, Ontario, Canada 2010-2016 Ph.D. Candidate</p>
<b>Honours and Awards:</b>	<p>The University of Western Ontario Graduate Research Scholarship – WGRS 2009-2012</p> <p>The University of Western Ontario A Special International Research Award – ASPIRE 2011</p> <p>Natural Sciences and Engineering Research Council (NSERC) Doctoral Post Graduate Scholarship 2012-2014</p>
<b>Related Work Experience:</b>	<p>Laboratory Engineer Institute of Surface Chemistry Kyiv, Ukraine 2000-2003</p> <p>Junior Research Associate Institute of Surface Chemistry Kyiv, Ukraine 2003-2009</p> <p>Teaching Assistant The University of Western Ontario London, Ontario, Canada 2009-2014</p> <p>Research Assistant The University of Western Ontario London, Ontario, Canada 2009-2015</p>

### **Publications:**

**Levchenko, T.I.**; Huang, Y.; and Corrigan, J.F. Large metal chalcogenide clusters and their ordered superstructures *via* solvothermal and ionothermal syntheses. *Part of the series Structure and Bonding*, Springer Berlin Heidelberg, **2016** (51 pages). Published on-line, DOI: 10.1007/430\_2016\_5

Azizpoor Fard, M.; **Levchenko, T.I.**; Cadogan, C.; Humenny, W.J.; Corrigan, J.F. Stable -ESiMe<sub>3</sub> complexes of Cu(I) and Ag(I) (E=S, Se) with NHCs: Synthons in ternary nanocluster assembly. *Chem. Eur. J.* **2016**, 22 (13), 4543-4550.

Azizpoor Fard, M.A.; Willans, M.J.; Khalili Najafabadi, B.; **Levchenko, T.I.**; Corrigan, J.F. Polydentate chalcogen reagents for the facile preparation of Pd-2 and Pd-4 complexes. *Dalton Trans.* **2015**, 44 (17), 8267-8277.

**Levchenko, T.I.**; Kübel, C.; Wang, D.; Khalili Najafabadi, B.; Huang, Y.; and Corrigan, J.F. Controlled solvothermal routes to hierarchical 3D superparticles of nanoscopic CdS. *Chem. Mater.* **2015**, 27 (10), 3666-3682.

**Levchenko, T.I.**; Kübel, C.; Huang, Y.; and Corrigan, J.F. From molecule to materials: Crystalline superlattices of nanoscopic CdS clusters. *Chem. Eur. J.* **2011**, 17 (51), 14394-14398.

**Levchenko, T.**; Plyuto, Yu.; and Kovtyukhova, N. Functionalisation of the template-free and template-structured silica films synthesised on glass substrates by sol-gel technique. *J. Sol-Gel Sci. Technol.* **2007**, 43 (3), 269-274.

**Levchenko, T.I.**; Plyuto, Yu.V.; Gozhenko, V.V.; and Grechko, L.G. Red-Ox transformations of silver ions and nanoparticles within mesoporous silica thin films. *Nanosystems, nano-materials, nanotechnologies.* **2004**, 2, 1231-1248, *in Russian*.

Zaporozhets, O.A.; Ivanko, L.S.; **Levchenko, T.I.**; and Sukhan, V.V. Influence of matrix properties on chemical and analytical characteristics of solid-phase analytical reagent. *Bulletin of Kyiv State University.* **2000**, 37, 30-33, *in Ukrainian*.

### **Research Presentations:**

**Levchenko, T.I.**; Kübel, C.; Huang, Y.; Corrigan, J.F. Controlled Solvothermal Routes to Hierarchical 3D Superparticles of Nanoscopic CdS. *Fallona Interdisciplinary Showcase*, London, December **2014**.

**Levchenko, T.I.**; Corrigan, J.F.; Huang, Y.; Kübel, C. A Novel Solvothermal Route to 3D Superstructures of Nanoscopic CdS. *CAMBR Distinguished Lecturer and Research Day*, London, November **2012**.

**Levchenko, T.I.**; Corrigan, J.F.; Huang, Y.; Kübel, C. From Molecule to Materials: Crystalline Superlattices of Nanoscopic CdS and CdSe. *24th Canadian Material Science Conference*, London, June **2012**.

**Levchenko, T.I.**; Corrigan, J.F.; Huang, Y.; Kübel, C. From Molecule to Materials: Crystalline Superlattices of Nanoscopic CdS. *CAMBR Distinguished Lecturer and Research Day*, London, June **2011**.

**Levchenko, T.I.**; Kübel, C.; Corrigan, J.F.; Huang, Y. From Molecule to Materials: Crystalline Superlattices of Nanoscopic CdS. *94rd Canadian Society for Chemistry Conference and Exhibition*, Montreal, June **2011**.

**Levchenko, T.I.**; Kübel, C.; Corrigan, J.F.; Huang, Y. Crystalline Superlattices of Nanoscopic CdS. *International Conference on Frontier Topics in "Nanostructures and Condensed Matter Theory"*, London, March **2011**.

**Levchenko, T.I.**; Corrigan, J.F.; Huang, Y.; Kübel, C. From Molecule to Materials: Crystalline Superlattices of Nanoscopic CdS. *43rd Inorganic Discussion Weekend*, Windsor, November **2010**.

**Levchenko, T.I.**; Corrigan, J.F.; Huang, Y. Cadmium Thiophenolate Complexes as Precursors to Mesostructured CdS. *93rd Canadian Society for Chemistry Conference and Exhibition*, Toronto, May-June **2010**.